Material characterization leading to predictive drilling tool for carbon fibre reinforced composite material using FEM

MATERIAL CHARACTERIZATION LEADING TO PREDICTIVE DRILLING TOOL FOR CARBON FIBRE REINFORCED COMPOSITE MATERIAL USING FEM

BY

PATRICK WILLIAM HALE, M. Sc.

A THESIS

SUBMITTED TO THE DEPARTMENT OF MECHANICAL ENGINEERING

AND THE SCHOOL OF GRADUATE STUDIES

OF MCMASTER UNIVERSITY

IN PARTIAL FULFILMENT OF THE REQUIREMENTS

FOR THE DEGREE OF

DOCTOR OF PHILOSOPHY

Doctor of Philosophy (2024)	McMaster University
Mechanical Engineering	Hamilton, Ontario, Canada

TITLE:	Material characterization leading to predictive drilling tool for carbon fibre reinforced composite material using FEM
AUTHOR:	Patrick William Hale M. Sc., Mechanical Engineering University McMaster University, Hamilton, Canada
SUPERVISOR:	Dr. Eu-Gene Ng
NUMBER OF PAGES:	xxii, 293

To my wife, Alisa and my son, Lando.

Abstract

Utilizing carbon fiber reinforced polymers (CFRP) in design offers advantages including as mass reduction, increased stiffness, enhanced corrosion resistance, improved sound damping, and vibration absorption. The notable strength-to-weight ratio of CFRP has driven its adoption over traditional materials like aluminum and steel in various industries such as aerospace, automotive, and sports. The assembly of "Stack-ups," which are layered assemblies of CFRP and metal components, becomes crucial as CFRP increasingly replaces metallic parts in high mechanical loading structural situations. The high thrust force involved in machining fiber reinforced polymers (FRPs) causes a peel-up and push-out effect on the workpiece, leading to delamination of the plies. This study developed an FE tool to simulate the drilling of FRPs effectively, aiming to validate tool design and enhance the cutting process.

Modeling the impact of fiber orientation in CFRP material on mechanical behavior is essential for optimizing component design and manufacturing. To reduce the exhaustive experimental work related to CFRP material characterization Abaqus Explicit is used to predict the tensile material response through fracture. FEA analyses included mesh size, mass/time scaling, failure models, and cohesive surfaces. Experimental results with the new fixturing-rig show consistent gauge region failure, regardless of fiber orientation. Puck's model accurately predicts fracture force and

displacement for parallel fiber orientation. 45 and 90-degree orientations, maximum strain and LaRCO2 models offer better accuracy. Most apparent, was the criticality of cohesive surfaces to predict the nonlinear loading response observed experimentally. Simulations for various fiber layup orientations indicate similar force-displacement signatures, with a notable reduction in failure force at angles between parallel and 45 degrees.

Simulating CFRP mechanical properties under three-point bending to understand cohesive interactions between plies in a laminate was investigated; this capability critical to effectively model the peel-up and push-out problem observed when drilling. A parametric FEA study investigated the affect of mesh size, mass/time scaling, failure models (Hashin, MCT, LaRC02, Maximum Strain, Puck), and cohesive surfaces versus loading response. Experimental results with a larger radius punch show failure on the intended bottom side, facilitating Aramis strain camera recording. Effective mass/time scaling reduces computation time while maintaining accuracy. For perpendicular fiber orientation, all failure models exhibit a similar force-displacement rate. Minimal difference exists among 0-degree models, except for a 4.18% underprediction by LaRC02. At 45 and 90 degrees, Maximum Strain and LaRCO2 models prove more accurate and converge well. The study underscores the need for cohesive surfaces to predict nonlinearity in loading responses for non-parallel bending setups.

A 3D drilling model is developed discussing significance of modelling techniques and considerations. The removal of failed elements creates periodic voids between the workpiece and tool, underlining the importance of proper mesh development. Accurate, computationally efficient models with element lengths of 50-75 μm near the expected failure region were emphasized. Using a discrete rigid body yielded a 42.1%

reduction in memory requirements and a 2.81x reduction in time step compared to deformable bodies with rigid constraints. Mass scaling led to over tenfold computation time reduction with a mere 5.3% mass change. Increasing viscosity parameters improved the loading response of CFRP laminate during high-speed drilling. Strain rate strengthening, aligned with literature, increased the load profile by 10.9%. Friction in the CFRP drilling model showed less sensitivity than estimated, with a 4.4% standard deviation.

The FE model once confidently developed, was compared to experiments. The prediction aligned well with experiments, accurately predicting thrust force differences between CD854 and CD856 drills. The CD856 exhibited reduced inter-ply damage, highlighting the advantage of double-angle drill geometry. The CD854's "spur" cutting edge geometry improved hole quality. The "Stack-up" drilling model effectively predicted thrust force transitions between UD-CFRP and Aluminum layers, confirming the CD854's reduced thrust force when drilling Aluminum, as described by the tool manufacturer Sandvik.

Overall, these studies underscore the importance of advanced modeling techniques, in understanding and optimizing the behavior of composite materials like CFRP in various applications. These studies offer valuable insights into the complexities and factors influencing machining and assembly processes, thereby contributing to the progression of materials and manufacturing methodologies.

Acknowledgements

I would like to extend genuine gratitude to my supervisor, Dr. Ng, for their invaluable direction and commitment, which have been essential in shaping this thesis into a meaningful contribution. Your guidance and support have been crucial throughout this process.

I would also like to thank Dr. Bruhis for their dedication and assistance during the critical testing stages. Your expertise and attention to detail were essential in ensuring the rigor and accuracy of this work.

I am grateful to my thesis committee members, Dr. Veldhuis and Dr. Wu, for their thoughtful feedback. Your insights have enhanced the quality and scope of this research.

A special thanks to my colleagues, Dr. Donal Finnerty and Dr. Keyvan Hosseinkhani, for their unwavering support and the much-needed distractions throughout the challenging grind of research.

I am deeply grateful for the unwavering support of those who have stood by me throughout this journey. To my wife, Alisa, for her endless patience and encouragement, and to my son, Lando, for always reminding me of what truly matters. I am also sincerely thankful to my parents, family, and friends, whose support has been essential in allowing me to achieve this milestone.

Nomenclature

σ	Stress
ϵ	Strain
E	Young's Modulus
v	Poisson' Ratio
G	Shear Moduli
f, m, c	Fibre, Matrix, Composite
σ_{11}	Longitudinal (Fibre) Stress
σ_{22}, σ_{33}	Transverse (Matrix) In-Plane Stress, Transverse Out-of-Plane Stress
σ_{12}, σ_{13}	Longitudinal In-Plane Shear Stress, Longitudinal Out-of-Plane Shear Stress
σ_{23}	Transverse Shear Stress
X_T	Longitudinal Tensile Strength
X_C	Longitudinal Compressive Strength
Y_T	Transverse Tensile Strength
Y_C	Transverse Compressive Strength
S_L	Longitudinal Shear Strength
S_T	Transverse Shear Strength
α	Hashin Damage Model; Contribution of Shear Variable ($0 \leq \alpha \leq 1$)
α	Exponential Softening of Damage Models
σ_{eq}	Equivalent Stress
$\hat{\sigma}$	Effective Stress Tensor
σ_0	Reference Stress
ϵ_0	Reference Strain
$\dot{\epsilon}_0$	Reference Strain Rate
u_n	Normal Separation
u_t	Tangential Separation
δ_n	Maximum Normal Separation
δ_t	Maximum Tangential Separation

T_n	Normal Traction
T_t	Tangential Traction
G_{Ic}	Mode I Fracture Energy
G_{TIc}	Mode II Fracture Energy
R_a	Average Surface Roughness (μm)
V_f or ϕ_f	Fibre Volume Fraction
V_m or ϕ_m	Matrix Volume Fraction
θ	Fibre Orientation ($^\circ$)
ρ	Density (Kg/m^3)
L^C	Characteristic Length
I_j^m, j = 1,2,3,4	Trans-Isotropic Invariants Matrix Average Stress State
I_i^f, i=1,4	Trans-Isotropic Invariants Fibre Avgerage Stress State
A_i^m, A_i^f	Adjustable Coefficients
F_i, F_{ij}	Failure Coefficients Defined by Strengths
p	Slope of Fracture Envelope
H	Helix Angle ($^\circ$)
D	Damage Variable

List of Abbreviations

CDM	Continuum Damage Mechanics
CFRP	Carbon Fibre Reinforced Polymer
CODAM	Composite Damage Model
CZM	Cohesive Zone Model
FD	Fibre Damage
FE	Finite Element
FRP	Fibre Reinforced Polymer
HAZ	Heat Affected Zone
HM	High Modulus
MD	Matrix Damage
RVE	Representative Volume Element
WWFE	World Wide Failure Exercise
3PBT	Three Point Bending Test
4PBT	Four Point Bending Test

Contents

List of Tables

List of Figures

Chapter 1

Introduction

Thomas Edison and Joseph Swan created the first carbon fibres by burning bamboo and cotton. This was not for use in an airplane, but to create the original filaments used in the invention of a light bulb near the end of the 19^{th} century. With the creation of tungsten filaments, carbon fibres were no longer useful for creating light and soon forgotten [1].

Carbon fibre composites have long been thought of as a revolutionary material. "The New Steel-Carbon-fiber-reinforced plastics: the materials that may revolutionize aircraft design" was the title of a 1968 journal describing advantageous material characteristics [2]. By incorporating carbon fibre reinforced polymers (CFRP) into a design one can reduce the mass of a part, increase stiffness, improve corrosion resistance, improve sound damping and vibration, facilitate complex aerodynamic shapes and absorb substantial energy in failure events. Most incentivizing is the strength-to-weight ratio which has been the motivation to replace conventional workpiece materials such as aluminum and steel across numerous industries including, aerospace, automotive and sport.

Pioneering research done by Roger Bacon in 1958 created high-performance carbon fibers. Production process realizations involving “hot-stretching" by Schalamon created a ten-fold production increase when creating fibres from Rayon [3]. In 1961, research using polyacrylonitrile (PAN) by Dr. Akio Shindo led to the development of different modulus fibre. A high modulus (HM) for structural design and low modulus fiber that is widely popular in sporting equipment [4]. In 1970, limited mostly to aerospace applications, carbon fibre cost approximately \$150/lb. With the inclusion of sporting goods, automotive, industrial and wind energy applications the price has fallen to \$10/lb, a trend expected to continue. Zoltek, a leading global manufacturer of carbon fibre materials states growth globally will continue for carbon fibre tow from 46,000 tons in 2011 to 140,000 tons in 2020 [1].

Composites are made of two or more constituents that are combined to form an improved material [5]. One material is strong and stiff acting as the reinforcement. The other, identified as the matrix envelopes the reinforcement and is generally more ductile and tough [6]. Aerospace and defence sectors are increasing the use of CFRP year over year. In the 1980's the Boeing 757/767 was less than 5% by weight made from CFRP. In contrast, the Boeing 787 Dreamliner is almost 50% by weight [7]. The largest aircraft in the world is the Airbus 380, which is 25% by weight made from composites. The A380 is also the first aircraft that has a CFRP centre wing box that reduces this components weight by up to one and a half tonnes [8]. These advancements will create fuel savings of 12-20% [9, 11, 10]. In the automotive industry growth is evident. Originally CFRP was incorporated in Class-A cars only such as the Bugatti Veyron. Today Audi, with Voith are working towards 100-150 units per day producing a rear wall for an A8 that will save 50% of the components weight [12].

As utilization of CFRP increases across many sectors difficulties continue to exist pertaining to cost. The cost breakdown of carbon fibre is significantly dominated by the manufacturing cost at 53% and of that, 51% is the precursor [13]. Precursor is the carbon filament in CFRP fibre and is made from PAN, rayon or petroleum pitch. Although CFRP has advantageous material characteristics including formability, the parts require various machining processes to meet design and quality requirements. Processes that must be optimized and improved constantly to drive costs down.

“Stack-ups" are multiple layer assemblies of CFRP and metal components. In aerospace as CFRP replaces more metallic components in high mechanical loading structural situations assembly of these multi layer interactions becomes critical. Frequently “Stack-ups" incorporate Titanium and Aluminum in a variety of layups. When CFRP parts are incorporated as structural components into an assembly they need to be mechanically joined. Exact part production for CFRP components is difficult in comparison to conventional machining of metal parts. Hole drilling, frequently at assembly location, is used to facilitate the assembly. However, drilling “Stack-ups" is very cumbersome. Aluminum has a high strength-to-weight ratio and remains an ideal material choice for many aerospace and automotive applications. Aluminum is not a difficult material to machine, but can be subject to adhesion problems when machining creating built-up edge (BUE) on the cutting edge. Specific machining parameters regarding cutting feeds and speeds, tool coatings and coolants must be selected for proper machining of a specific Aluminum alloy [14]. Titanium and CFRP are considered difficult materials to machine. Titanium is subject to high cutting temperatures which causes diffusion and dissolution tool wear [15]. The hardness, and high strength in CFRP induce significant wear, dulling the tool rapidly leading to poor machinability and quality of the workpiece [16, 17].

The machining process becomes more cumbersome due to the different cutting mechanisms between the materials. When machining metal a shearing mechanism generates a continuous or serrated chip [18]. The fracture mechanism with CFRP is a brittle crack growth significantly effected by the fibre layup in the anisotropic material. Using a quick stop device, Koplev et al. studied the fracture mechanism of fibre reinforced polymers (FRP) describing the various differences in comparison to machining with metal [19]. Sakuma et al. describes the effect on cutting forces, surface finish and tool wear all highly dependent on fibre orientation [20, 21, 22]. Shown by altering the tool geometry and the fibre orientation when machining determines the failure mechanism albeit tension, compression, bending or buckling.

Sheffler describes the numerous considerations when drilling “Stack-ups". Parameters that directly effect material quality and surface requirements including tool design, cutting parameters and paths, coolants and coatings, swarf control, etc. [23]. The dissimilar materials require a compromise of machining considerations that exaggerates the difficulty of machining these materials and therefore negatively impacts the workpiece quality and tool life. Research on tool geometries and cutting parameters has progressed the understanding of drilling these hard, high strength composites [24]. The understanding of the fracture mechanism of CFRP, the heat transfer between materials, the tool wear and the frictions developed all must progress to make informative tool design advancements [25]. Thrust force is considered to correlate to the observed tool wear. The experimental studies indicated the thrust force is significantly affected by feed rate, cutting speed and tool wear leading to the development of an empirical model [26]. Experiments with CFRP tend to be destructive and therefore become costly. Finite element modelling has been extensively used to progress the understanding of machining.

Advancements regarding CFRP processing are continuously being made offering greater productivity and improved surface quality/integrity. Developments regarding the understanding of fracture of CFRP and advancements in tool materials, design, cutting parameters and other process factors continue to improve the viability of CFRP across multiple industries. This research attempts to delineate the significance of FE modelling of CFRP and validate the effect drill geometries have when machining CFRP. Understanding the fracture mechanisms in CFRP drilling will allow the selection of the right tool for each application of CFRP drilling. Efficiency in all aspects of the process from design, manufacture, install, certification and maintenance are crucial. This is realized in most aspects although fundamental understanding of the fracture, friction and failure mechanics is still in its infancy.

1.1 Objectives

This research was carried out to progress the understanding of CFRP material characterization with FE modelling, to improve productivity and quality of machined CFRP. In doing so, machining of CFRP will continue to become more effective facilitating its use in more applications. Specific objectives of research were to:

- Simulate the mechanical properties of CFRP to fracture. Finite element solver ABAQUS Explicit will be used to perform a sensitivity analysis regarding element type, mesh convergence, scaling techniques, damage initiation and evolution methods were studied with its respective limitations in a tensile loading configuration. A tensile test rig that could induce fracture at the specimen gauge section consistently to validate the model.

- Evaluate different failure models, which include Hashin, MCT, LaRC02, maximum strain, Tsai-Wu, Tsai-Hill, Christensen and Puck. The fibre orientations investigated to be investigated were parallel, 45 deg and perpendicular to the tensile loading condition. The significance of modelling multiple ply layups using cohesive surface interactions will also be investigated.

- Model the mechanical properties up to fracture for CFRP laminates under three-point bending loading configuration and to gain understanding on the cohesive interaction between plies and validate mechanical properties and predictive capability of the FE model. Fibre orientations to be investigated were parallel, 45° and perpendicular to the structure axial direction.

- Develop a 3D macro-Finite Element (FE) model to accurately predict the effects of drill tip geometry on hole entry and exit quality. The macro-mechanical material model will be developed treating the Fiber Reinforced Plastic (FRP) as an Equivalent Homogeneous Material (EHM). To reduce computational time, numerical analysis will be performed to investigate the influence of mass scaling, bulk viscosity, friction, strain rate strengthening and cohesive surface modelling. Consideration will be made to minimize the dynamic effects in the FE prediction. Experimental work will be carried out to investigate the effect of drill tip geometry on drilling forces, hole quality and to validate the FE results. The geometry of the drills used were either double-point angle or a “candle-stick” profile.

1.2 Outline of Thesis

The thesis includes the following chapters:

Chapter 2 provides a comprehensive literature review of work completed by researchers regarding FEM and machining of CFRP. The content is supplementary to the literature review present in the three journal papers in the subsequent chapters. The review includes descriptions of experiments, modelling techniques employed by researchers and limitations of the work. Any limitations or gaps in knowledge promote further research.

Chapter 3 presents work published in Materials Today Communications. The title of the paper is “Non-linear material characterization of CFRP with FEM utilizing cohesive surface considerations validated with effective tensile test fixturing". This work experimentally tested CFRP samples using an improved fixturing setup. FE research resulted in effective modelling of the CFRP at various fibre-layup orientations utilizing cohesive surface interactions between plies with damage capability. The cohesive surface interaction created the ability to capture the nonlinear loading response observed in experiments, frequently not considered nor implemented in FE models. The FE model proved effective when predicting the response to loading of multi-fibre orientations and the effect of various laminate thicknesses.

Chapter 4 presents work published in Modelling and Simulation in Materials Science and Engineering journal. The title of the paper is “Three-point bending analysis with cohesive surface interaction for improved delamination prediction and application of CFRP composites". This research experimentally tested CFRP samples at various fibre-layup orientations using an increased diameter punch, three-point bending setup. The research effectively modelled the CFRP utilizing cohesive surface interactions between plies with damage capability, demonstrating improved prediction of the loading response. The FE model proved effective when predicting the response to loading of multi-fibre orientations, cross-ply layups and the effect of various span lengths.

Chapter 5 presents work published in the journal Materials. The title of the paper is “3D Finite Element Model on Drilling of CFRP with Numerical Optimization and Experimental Validation". This work effectively developed 3D drilling models of CFRP predicting the effectiveness of different drill geometries, validated by experiments. The 3D drilling model accurately predicts the thrust force and hole quality generated by the two different drills. Results highlight the improvement in predicted results with the inclusion of cohesive surface modelling.

Chapter 6 communicates work continued from the 3D drilling model, focusing on Stack-Ups involving CFRP laminated by Aluminum.

Chapter 7 outlines specific conclusions from the body of work and describes areas of focus for continued work in the future. Figure 1.1 illustrates the layout of the thesis.

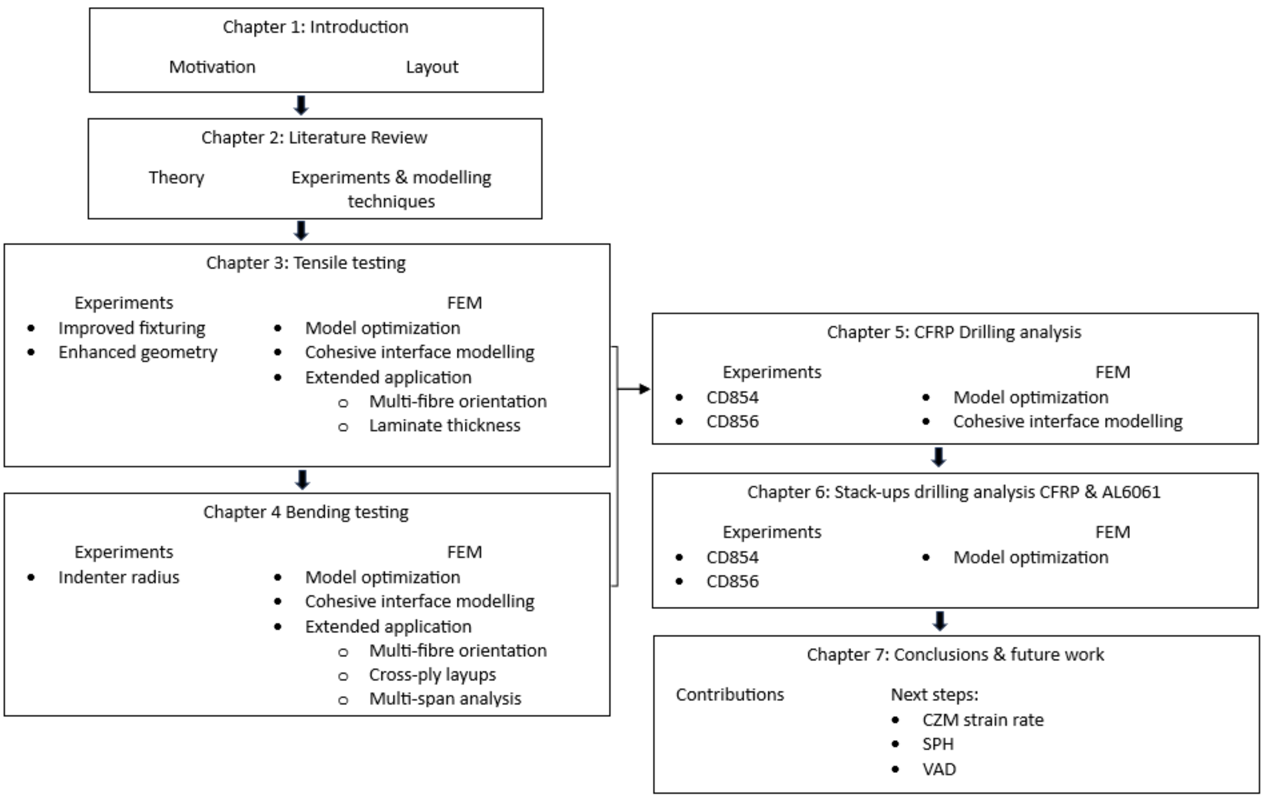

Figure 1.1: Thesis layout

Chapter 2

Theory & Literature Review

2.1 Overview

The literature review provided in this chapter focuses on information pertaining to CFRP testing, modelling and machining. Description of composite materials, most specifically CFRPs are provided. Experiments completed for specific material characterization are described including any shortcomings of certain experimental setups. The various modelling techniques that exist for FEM and the effectiveness of these techniques are outlined in detail.

2.2 Materials

A composite material is made from two or more different constituents. The reinforcement phase has high rigidity and is subject to the majority of the loading. Reinforcements are generally long fibres, short fibres, particles or whiskers. The continuous matrix constituent is generally tough and envelopes the fibre reinforcement.

The matrix provides protection from the environment, distributes the applied load and will determine the form of the part, binding it together [7].

The three standard classifications for composite materials are ceramic matrix composites (CMCs), metal matrix composites (MMCs) and polymer matrix composites (PMCs). Depending on the application, the reinforcement material may be particle-reinforced involving large particle or dispersion-strengthened; fibre-reinforced involving continuous, discontinuous, aligned or random fibres; or structural laminates or sandwich panels [27]. Shown in Figure 2.1 a) is a composite made of continuous fibres reinforced in a matrix. Figure 2.1 b) illustrates the strength of a composite in comparison to its individual constituents.

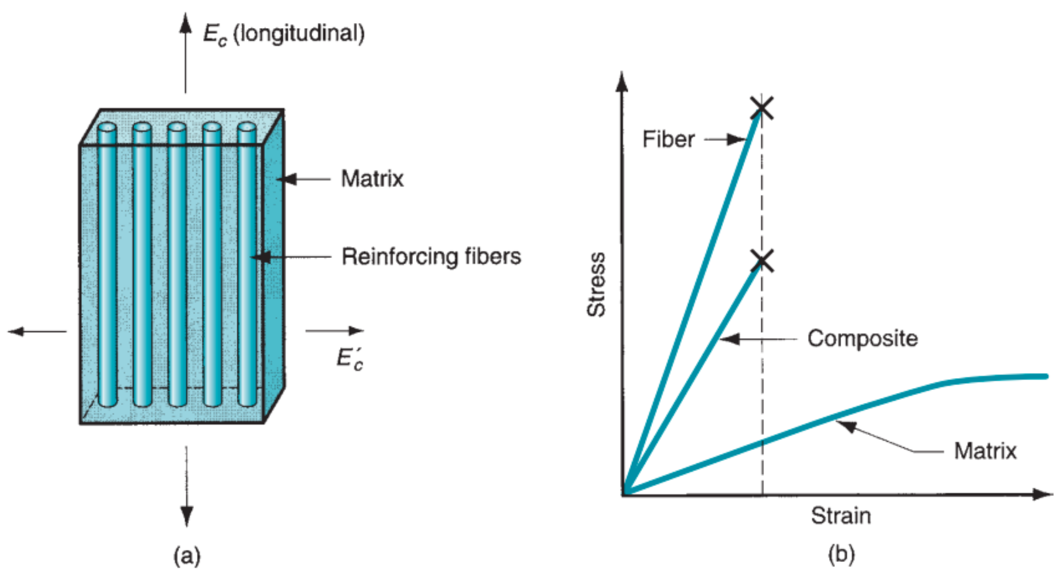

Figure 2.1: a) Fibre reinforced composite structure b) Constituent force [28]

Polymer matrix composites are synonymous with fibre reinforced plastics (FRPs). FRP composites are described as unidirectional (UD) or woven. Unidirectional refers to the fibre layup orientation being arranged in one direction. Shown in Figure 2.2, woven FRPs involve weaves with the intersection of fibre in various patters and various angles to promote laminate function.

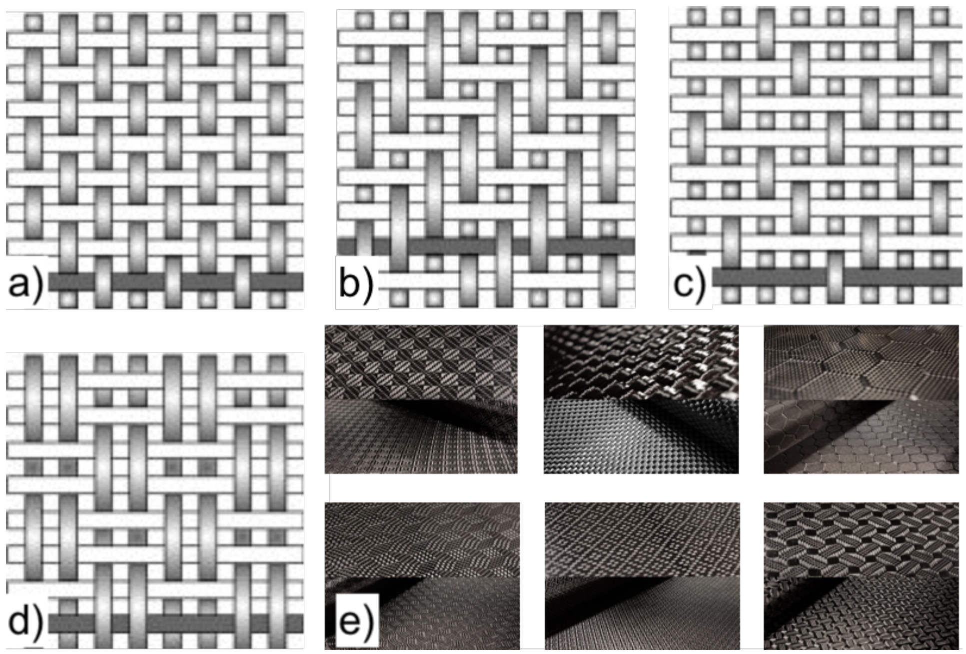

Figure 2.2: CFRP weaves: a) Plain b) Twill c) Satin d) Basket e) Various [30, 29]

A plain weave involves each bundle of fibre passing under then over a perpendicular bundle of fibres. The 2x2 twill weave involves a bundle passing over and then under 2 bundles of fibre, however this is staggered in the perpendicular direction. The 3 harness-satin weave shown involves a 3 over 1 under pattern; satin weaves can be done in 3 over 1, 4 over 1, 5 over 1 etc. The basket weave is similar to the plain weave however it involves two bundles passing over and then under. In Figure 2.2 e) specialty weaves such as Rook, Grandmaster, Wasp, Labyrinth, Atomic and Roswell are shown and are generally selected for aesthetic reasons.

The most common fibre reinforcement with PMCs are carbon, glass and aramid (also known as Kevlar), with a small usage involving Boron and polyethylene fibres

[11]. Glass fibres are classified into eight classifications that categorize key physical properties including: (A) higher durability, strength and electric resistivity; (C) higher corrosion resistance; (D) low dielectric constant; (E) higher strength and electriacal resistivity; (AR) Alkali resistance; (R) higher strength and acid corrosion resistance; (S) highest tensile strength; (S-2) high strength, modulus and stability [31]. Aramid fibres are organic fibres in the aromatic polyamide family resulting in high strength, toughness, high modulus and thermal stability[32]. Carbon fibre is most frequently made from a raw material called polyacrylonitrile (PAN), know as the precursor. The precursor is subject to a stabilizing process whereby the fibre is subject to air at 200-300 °C. The fibres bond with oxygen transforming the linear atomic bonds to more stable ladder bonding. The stabilizing process can use heated chambers, hot rollers or other gases to promote the stabilization process. Post stabilization, the fibres are heated to 1000-3000 °C for several minutes in a gas mixture absent of oxygen. This prevents the fibres from burning and causes them to vibrate violently forcing the non-carbon elements to be expelled as gases. This focuses the bonding of the carbon atoms more densely and aligns the crystal with the fibre axis. To increase adhesion with epoxies, the carbonized fibre surfaces are subject to a controlled oxidation. This allowing for better chemical bonding and etches the surface that creates a roughness that increases the mechanical bonding qualities of the fibre. The fibres are coated to add protection from winding processes, increase bonding characteristics and to size the fibres [1].

The matrix material is crucial to the composite function. It is a thermoset or thermoplastic resin material which binds the fibre-reinforcement. A thermoset resin involves a chemical reaction altering the molecular structure of the resin during curing, which is irreversible. The thermoplastic resin is reversible by adding heat, the material will transform between solid and liquid phase. With respect to design, this can have advantages and disadvantages, however with most applications only one type is appropriate. Composites used in industry are generally limited to the following resins: polyester, vinyl-ester, epoxy and high-temperature thermosetting resins phenolic, cyanate-ester and bismaleide [27]. Table 5.1 and 2.2 detail the physical and mechanical properties of the fibre reinforcement and matrix.

Table 2.1: Typical fibre reinforcement properties [27, 32, 34, 33]

Fibre property	Carbon fibre	Glass fibre	Aramid fibre
Density (kg/m^3)	1600	2100	1400
Diameter (μm)	4-10	3-20	12
Longitudinal modulus (GPa)	145	45	76
Transverse modulus (GPa)	10	12	5.5
Tensile strength (MPa)	1240-2000	1020-2500	1380
Elongation at fracture (%)	0.5-1.0	1.8-3.3	1.8

Table 2.2: Typical matrix material properties [34, 35]

Matrix property	Epoxy	Polyester
Density (kg/m^3)	1100.0-1400.0	1200.0-1500.0
Modulus of elasticity (GPa)	3.0-6.0	2.0-4.5
Tensile strength (MPa)	35-100	40-90
Compressive strength (MPa)	100-200	90-250
Elongation at fracture (%)	1.0-6.0	2.0

Between the fiber and matrix, regardless of the layup, is a region referred to as the interface, or interfacial bonding. The interface refers to the three-dimensional boundary between the fiber and matrix, playing a crucial role in governing the properties of composites. This is because the fiber–matrix interaction happens at the interface. There are three primary mechanisms through which this interaction can occur: mechanical coupling or micromechanical interlocking between the two materials, physical coupling such as van der Waals forces or electrostatic interactions, and covalent bonding facilitated by a coupling agent [36]. Between instances in the finite element modelling cohesive interactions can be developed to mimic the interfacial bonding.

This research focuses on the material characterization and machining of unidirectional carbon fibre epoxy laminates (UD-CFRP).

2.3 Fundamentals of FRPs: Empirical & Theoretical Representations

The inherent advantages of FRP materials are the specific strength and stiffness, that can be customized to produce varying sized structures, as one piece or assembled parts. This is possible by controlling the fibre orientation and stacking of the laminated plies. The abundance of options to customize a FRP, create a similar abundance of difficulties to analyze the response of the part when subject to a load. FRPs heterogeneous properties create additional complexities when producing analytical models in comparison to standard isotropic engineering materials. In the most basic of approaches, damage in a FRP involves interactions of fibre cracking, matrix failure and delamination as shown in Figure 2.3.

The machining process becomes especially difficult due to the different cutting mechanisms involved as the fibre orientation changes. When machining metal a shearing mechanism generates a continuous or serrated chip. The serrated, saw-toothed chips generally occur when machining hardened steels, super-alloys, and titanium

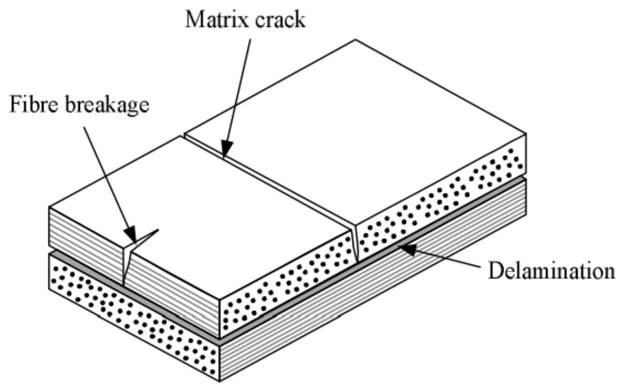

Figure 2.3: FRP failure [37]

alloys machined at low cutting speeds. This serrated chip can also occur in ductile materials if machined at high speeds resulting in instability and poor quality [18].

The fracture mechanism with FRPs involve a brittle crack growth significantly affected by the fibre layup in the anisotropic material. Using a quick stop device (QSD) to study the cutting region, Koplev et al. identified the fracture phenomenon when machining FRPs [19]. Shown in Figure 2.4, altering the tool geometry and the fibre orientation when machining determines the failure mechanism albeit tension, compression, bending or buckling. Koplev et al. describes when machining perpendicular to the fibre the surface is destroyed 0.3 mm below the surface versus minimal damage when machining parallel to fibres. Sakuma et al. describes the effect on cutting forces, surface finish and tool wear all highly dependent on fibre orientation [21]. Arola et al. [20] and Kaw [22] made similar experimental observation regarding the effects of fiber orientation.

A FRP can be represented in a variety of ways within a finite element software. Consideration must be made to accurately represent the composite structure while maintaining a reasonable amount of computational expense. At a microscopic level,

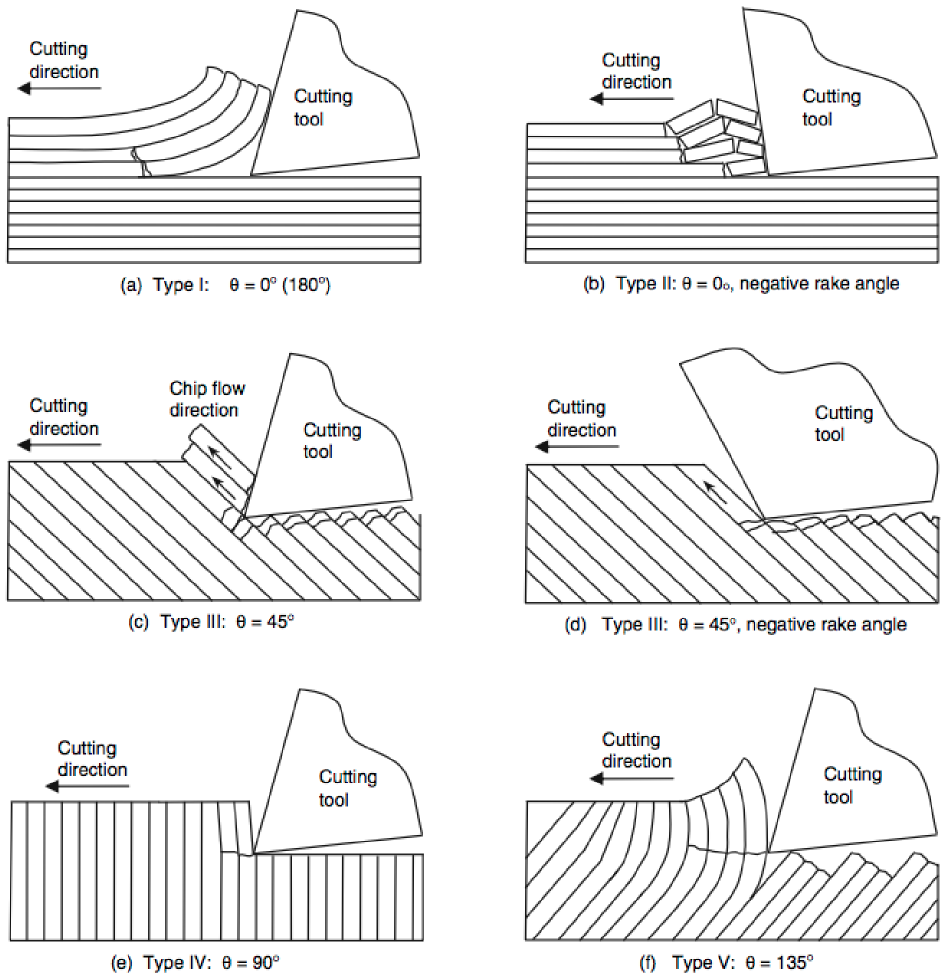

Figure 2.4: Cutting mechanism for various fibre orientations [7]

when a FRP is subjected to load, damage would initiate with micro-cracks at the interface between the matrix and the fibre. These micro-cracks grow causing interlaminar delamination followed by macro-cracks in the matrix. As this continues, macro-level failure occurs in the fibre [38]. To increase the understanding of the highly complex mechanical behavior of FRP composites, numerical models at different scales have been developed with different loading conditions. There are three distinct scales: micro, macro and meso.

Micro-scale analyses incorporate separate model volumes for the fibre and matrix. The interface between these constituents is also considered. Micro-scale models successfully predict properties of the laminate at a macro scale and can model damage initiation. However, such approach are unable to predict damage evolution because there is no additional volume representing the undamaged region of the FRP part experiencing the onset of failure [37].

A macro-scale model represents the component homogeneously with anisotropic material properties. This is referred to as an equivalent homogeneous material (EHM). It does not include individual plies, nor the cohesive interaction between plies and therefore cannot capture delamination. By neglecting the sub-laminate plies computational efficiency can be gained facilitating greater complexities to be included. Complexities such as alternative failure criteria, damage evolution techniques, more complex frictions and contact interactions, wear and erosion considerations, etc. In addition to the inability to capture delamination between plies, the damage evolution through the representative volume is averaged throughout the critical area depending on the progressive damage relationship [39, 40]. The majority of progressive damage models involve the matrix damage preceding fibre damage, which leads to failure in the structure. In a variety of loading conditions, especially with unidirectional composites, matrix damage will determine structure failure. This is a significant limitation in the functionality of numerous failure models at a macro-scale.

At the macro-scale (laminate) level, rather than a single instance with homogenized anisotropic properties, a numerical technique can facilitate the ply layup. If the FRP is not unidirectional, where the orientation of the fibres per ply are parallel, an analytical manipulation of the volume will more accurately represent the anisotropic nature of the FRP structure. This is achieved by subdividing the instance into a number of plies and allowing the properties of the plies to vary; properties such as fibre orientation, material, thickness [37, 38].

The meso-scale (lamina) is an alternative, where the laminate is modelled by the stacking of individual plies. The ply is an individual instance with homogeneous properties dependent on the ply orientation. The plies are then laminated together, incorporating a stacking sequence and orientation if required, with the ability to consider the interface between the plies [39, 40]. A surface interaction with specific cohesive behavior and damage modelling can be considered. The ability to simulate delamination failure is possible. Most crucial, the cohesive interaction allows the FE model to capture softening in the structure as damage progresses and can therefore predict a nonlinear loading response frequently not predicted due to the highly stiff, elastic properties of the fiber-dominating failure evolution. Alternatively, each of the laminated plies can be connected using cohesive elements versus a surface contact. This involves an additional instance between each pair of FRP plies. The cohesive elements are modelled with similar material and failure properties as with the contact surface setup. Due to the additional, generally thin, instances computational time suffers. A representation of the different scales of modelling are illustrated in Figure 2.5.

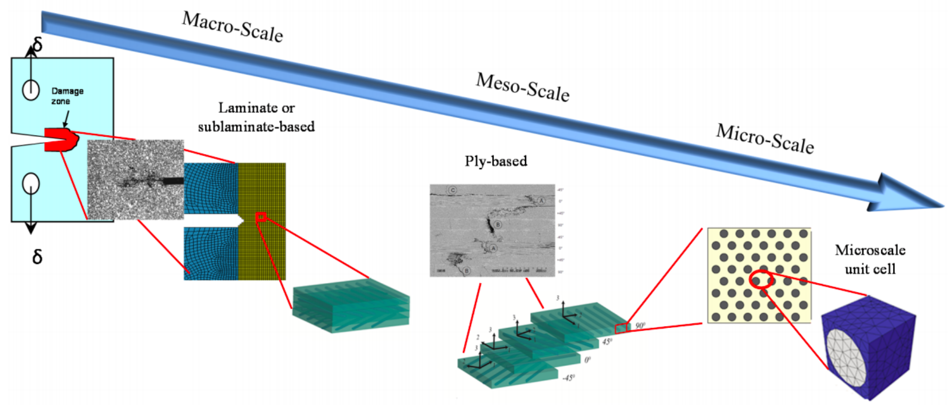

Figure 2.5: Multi-scale FRP studies [37]

FE modelling has been successfully utilized to model the complexities of FRP instances for numerous applications such as structural analyses, fluid dynamic studies or damage studies, each with their own significance [20, 41, 42, 43, 44, 45, 46, 48, 49, 50, 51, 52, 53, 54, 47, 55]. Damage initiation and evolution prediction is used to model the material response when FRPs are subject to loads exceeding the elastic limit. To guarantee reliable, accurate simulations FE research must be based on theoretical studies and validated by experimental work. Finite element modelling must resolve the local load balancing of a section to determine the global response of a system in terms of its mass, damping and stiffness. This global response is represented by Equation 2.1:

$$[M]\{\ddot{u}\} + [C]\{\dot{u}\} + [K]\{u\} = \{f(t)\} \tag{2.1}$$

which is a combination of acceleration, $\ddot{u}$, velocity, $\dot{u}$, displacement, u and the resulting force vectors, $f(t)$.

In all FE analyses there are two pairs of parameters that distinctly identify the type of analysis: static versus dynamic and linear versus non-linear. A static analysis is one where the inertial forces can be ignored (also includes quasi-static). These analyses can be linear or nonlinear. In a static analysis the load is divided into increments. In each increment, the external forces applied must be balanced by the internal forces of deformation.

A dynamic analysis is one which the inertia effects must be considered and therefore parameters are affected by time. There are three categories for dynamic analyses: transient fidelity, moderate dissipation and quasi-static [39]. Transient fidelity require minimal energy dissipation to accurately model the vibrational response of a system. An example of a transient fidelity analysis would be the study of an automobile suspension. The moderate dissipation analyses involve studies where energy is dissipated by plasticity, viscous damping and other effects such is the case for impact and forming analyses. In a quasi static analysis only the final static response is of interest and the inertial effects can be used to settle unstable responses [39]. Bulk forming including drawing, rolling, stretching and extrusions involving contact and large deformations are examples of quasi-static simulations. The greatest advantage to quasi-static analyses is taking advantage of negligible inertial effects [49]. This allows for increased loading rates and mass scaling with minimal effect on the prediction; this consideration is advantageous for efficient material testing simulations.

If an analysis remains in the linear-elastic range of a material response a linear material response is adequate, requiring Young's modulus, Poisson's ratio and density. This is appropriate for many analyses in engineering design, such as structural components that must avoid any plastic deformation.

Alternatively, if a analysis will exceed the yield point of a material, experience damage and possibly require element erosion, then a non-linear response is required. Nonlinearities exist in material behaviour, but can also exist due to large-displacements and boundary nonlinearities such as contacts and friction [40]. Many real-world analyses are non-linear. One should maximize the plasticity of a material in a forming application, or try to reduce the energy required to promote shear failure in a metal cutting process.

There are two distinct methods of integration in FE models, implicit and explicit. Explicit integration uses the central difference method that assumes linear changes in one increment to predict the kinematic conditions of another. The central difference rule integrates the equations of motion explicitly through time, solving the dynamic equilibrium shown in Equation 2.2:

$$M\ddot{u} = P - I \tag{2.2}$$

where M is the nodal mass matrix, P is the externally applied forces and I are the internal element forces. The accelerations at the beginning of the current increment are calculated as:

$$\ddot{u} = (M)^{-1} \cdot (P - I)|_{(t)} \tag{2.3}$$

The acceleration $\{\ddot{u}\}$ at increment n is shown in Equation 2.4:

$$\{\ddot{u}\} = \frac{\{\dot{u}\}_{n+1/2} - \{\dot{u}\}_{n-1/2}}{\Delta t} \tag{2.4}$$

where $\{\dot{u}_{n+1/2}\}$ and $\{\dot{u}_{n-1/2}\}$ define the velocity at the next half increment and the previous, respectively to the elapsed time between the two increments, Δt. The central difference method can then be applied to determine the velocities at these half steps by relation of the nodal displacement as shown in Equations 2.5 and 2.6 respectively:

$$\{\dot{u}\}_{n+1/2} = \frac{u_{n+1} - u_n}{\Delta t} \tag{2.5}$$

$$\{\dot{u}\}_{n-1/2} = \frac{u_n - u_{n-1}}{\Delta t} \tag{2.6}$$

The velocities are integrated through the step and added to the displacements at the beginning of the increment to determine the displacement at the end of the increment, shown in Equation 2.7.

$$u|_{(t+\Delta t)} = u|_{(t)} + \Delta t|_{(t+\Delta t)} \dot{u}|_{(t+\frac{\Delta t}{2})} \tag{2.7}$$

The time increment is small enough to assume constant acceleration. The acceleration of the node is determined by its mass and the net force acting on it and does not require solving for the acceleration, resulting in a computationally inexpensive process. With the nodal displacements known, the incremental strain and strain rate can be determined across the element. With strain determined, stresses can be computed using the element stiffness and the process is repeated [39].

The implicit formulation equilibrium is also defined by Equation 2.2. However, the implicit method uses a direct solution method to determine the nodal accelerations, which is computationally expensive. To do this, the full Newton iterative solution method is used, known as the Newton-Raphson method. With a nonlinear problem, each increment will require several iterations to resolve the error within a certain tolerance, c_j. Each iteration requires the solution of a set of simultaneous variables shown in Equation 2.8 [39]:

$$\hat{K}_j c_j = P_j - I_j - M_j \ddot{u}_j \tag{2.8}$$

where $\hat{K}_j$ is the effective stiffness matrix. The iterations for a given time step continue until parameters such as displacement corrections and force residuals are within the tolerance. Solving an implicit analysis requires significant computational time per increment and due to the large system of linear equations are quite expensive with respect to computational hardware; disk space and memory. Implicit analysis also have significant difficulty resolving the highly discontinuous contact conditions present [39]. As such, the highly dynamic machining of FRPs can only be effectively solved using an explicit analysis.

2.3.1 Meshing techniques

A critical aspect of a FE model is the ability to converge efficiently and avoiding severe mesh distortion leading to an aborted simulation. There are three classic methods to represent motion in FEM: the Lagrangian method, where the mesh moves with the material; the Eulerian method, where material moves through a fixed mesh; and more recently, an Arbitrary Lagrangian-Eulerian description [56].

The Eulerian description is regularly used in Computational Fluid Dynamics (CFD) and requires the flow of material to be defined [56]. For a fluid or energy flow simulation that may be acceptably known. However, for other analyses such as crack path prediction, or newly surface generations, the purpose of the study may be that separation prediction and therefore the Eulerian method is not preferred. The Eulerian description does have the advantage of avoiding excessive element distortion as the mesh is fixed [56].

In the Lagrangian approach, the mesh is attached to the body of study and elements are allowed to move relative to the original position based on the deformation induced. This has the advantage of no predefined flow regions. The Lagrangian approach is susceptible to excessive element distortion near the separation region, may require frequent remeshing and as a result can be computationally expensive [56].

The Arbitrary Lagrangian Eulerian (ALE) is an adaptive mesh technique that combines the Lagrangian and Eulerian formulations incorporating advantages of both. The ALE mesh is neither attached to the material nor spatially fixed. It allows the mesh to flow with the material and severe distortion of elements can be avoided. The ALE description utilizes Lagrangian and Eulerian aspects implemented on one mesh. The ALE representation has been successfully implemented on 2D orthogonal cutting analyses [57], however implementing Eulerian boundaries of an ALE setup in a 3D machining model is not possible. To accomplish this, a Coupled Eulerian Lagrangian (CEL) analysis that incorporates Eulerian and Lagrangian instances within the same model must be setup. A single Eulerian part is created and acts as the domain of the model. Materials are assigned to different Lagrangian regions and those without material assignment are treated as a void [39, 54, 47, 58]. However, for CEL element failure criteria cannot be incorporated into the mechanical behavior resulting in unavoidable severe element distortion. As a result, the Lagrangian formulation was used. In Figure 2.6 the three meshing approaches are illustrated [59].

Fortunately, CFRP experiences a highly elastic-brittle failure. Elements exceeding critical strengths experience a damage evolution procedure that leads to element deletion. The Lagrangian representation is an effective approach when consideration is made for element type, seeding, stacking, hourglass control and adaptive meshing; these specific modelling considerations will be described in section 2.3.3.

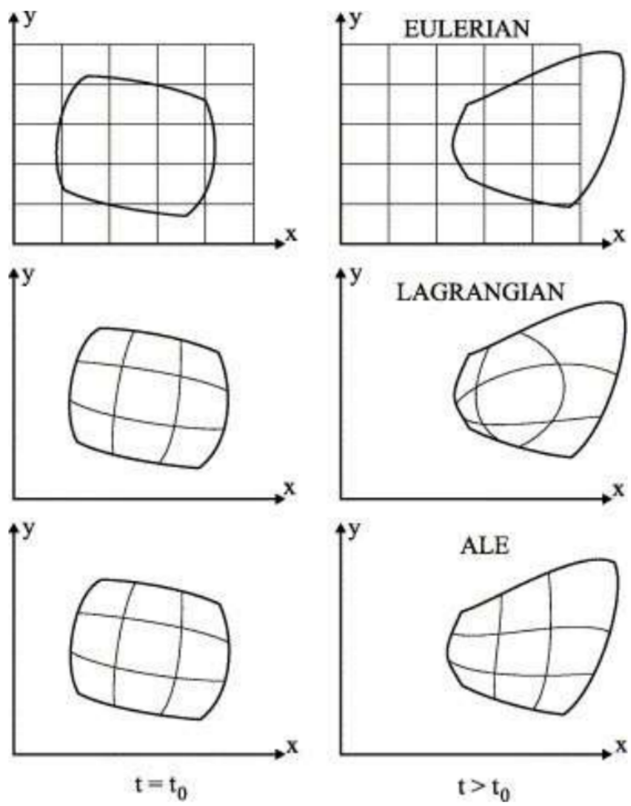

Figure 2.6: Meshing approach [59]

2.3.2 Elements

The element type selected for a FE model affects the material properties and additional analysis parameters required for the given setup. In addition to material properties, structural elements such as beam elements, require a cross-sectional area and moments of inertia to solve the 3D governing equations. Shell elements used in the stacking of plies require a laminating sequence to develop the anisotropic information for the material. Continuum 3D elements do not require any additional information as the material properties and mesh provide all required information [40].

The available elements for a FE model of FRPs are conventional and continuum shell elements and 3D solid elements. Conventional shell elements are used to represent a 3D object by a 2D flat/curved surface. Conventional shell elements can be thin or thick. Thin shell elements assume the transverse shear deformations to be zero, which is not a suitable assumption for thick composites. Thick composites' shear deformation is not zero as a result of enforcing first-order shear deformation theory (FSDT). FSDT is based on a straight line relationship perpendicular to the surface of the shell, through its thickness. As the shell deforms it will rotate about the mid-surface, but remain straight. From the rotation about the middle of the surface the shear deformation for thick shells can be determined [60].

Continuum shell elements use the shell thickness similar to the formulation using the element thickness for a solid 3D elements, but apply the FSDT. The limitation of these elements are the inability to have any rotational degrees of freedom. Limited to translational movement, the elements may not accurately predict a bending response [61]. Continuum shell elements can predict contact better than shell elements as it is a two-sided contact as a result of the element thickness. Solid, continuum elements can be used in linear and nonlinear analysis that involve contact, plasticity, large deformations, heat transfer, acoustic and other electromagnetic models.

Shown in Figure 2.7, an element can be first-order with nodes at the end of the element, or second-order incorporating additional nodes at the mid-point of the element; increasing a hexahedral element from eight to twenty, or a tetradral from four to ten. Second-order elements can model curved surfaces with fewer elements and improve accuracy for bending dominated problems, however have an increased computational time expense.

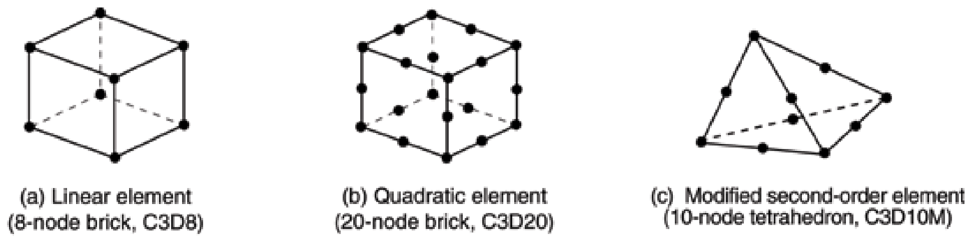

Figure 2.7: Element types [39]

Reduced integration uses a lower-order integration for the element stiffness. The mass and force distribution is still fully-integrated, but this will reduce the integration points in a quadratic brick element from 27 to 8 [39]. An unwanted effect of reduced integrartion can be hourglassing shown in Figure 2.8. In a first-order linear brick element, hourglassing can occur because the single integration point can facilitate strains that are all zero that can create distorted a mesh. This is not physically possible in reality and hourglass control must be implemented.

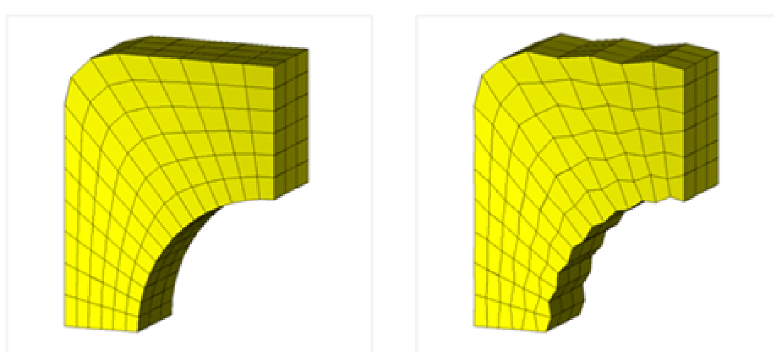

Figure 2.8: Hourglassing [62]

2.3.3 Material modelling

Unlike many engineering materials CFRPs are non isotropic. Properties including stiffness, strength and toughness vary depending on the principal directions of the material. The degree of anisotropy in a CFRP depends on the layup. The four layups for FRPs are unidirectional (UD), woven, multi-axial and random. A UD layup is one which the fibre orientation remains parallel with each additional ply. For a mutiaxial (cross-ply) layup the fibre orientation will change depending on a stacking sequence, specifically designed for the intended part function. The woven plies weave the bundles of the fibres in a specific pattern to attain desired strength, stiffness and aesthetic appeal.

The constitutive equations relating stress (σ) to strain (ϵ) are defined by 3D Hooke's law shown in Equation 2.9:

$$\sigma_{ij} = C_{ijkl}\epsilon_{kl} \tag{2.9}$$

where C_{ijkl} is the 3D stiffness tensor. For anisotropic materials the fourth-order stiffness tensor with 81 components, reduces to 36 independent components, as the stress and strain tensors are symmetric and can be written in a 6x6 matrix. Using the inverse of the stiffness matrix $[C]$, known as the compliance matrix $[S]$, the strain components can be determined [40].

An orthotropic material has three planes of symmetry that coincide with the coordinate planes requiring nine constants to describe this material. E_1, E_2, E_3, v_{12}, v_{13}, v_{23}, G_{12}, G_{13}, G_{23} identify the Young's modulus, Poisson's ratio and Shear modulus in a local material orientation with 1, 2, and 3 representing the fibre (longitudinal), matrix (transverse) and through thickness direction. Depending on the nature of the layup, additional symmetry in properties can be gained resulting in a transversely isotropic material; $E_2 = E_3,\ v_{12} = v_{13},\ G_{12} = G_{23},\ G_{23} = \frac{E_2}{2(1+v_{23})}$. A compliance matrix, shown in Equation 2.10, is used to evaluate the relationship between stress and strain, shown in Equation 2.11:

$$[S'] = \begin{bmatrix} \frac{1}{E_1} & \frac{-v_{21}}{E_2} & \frac{-v_{31}}{E_3} & 0 & 0 & 0 \\ \frac{-v_{12}}{E_1} & \frac{1}{E_2} & \frac{-v_{32}}{E_3} & 0 & 0 & 0 \\ \frac{-v_{13}}{E_1} & \frac{-v_{23}}{E_2} & \frac{1}{E_3} & 0 & 0 & 0 \\ 0 & 0 & 0 & \frac{1}{G_{23}} & 0 & 0 \\ 0 & 0 & 0 & 0 & \frac{1}{G_{13}} & 0 \\ 0 & 0 & 0 & 0 & 0 & \frac{1}{G_{12}} \end{bmatrix} \tag{2.10}$$

$$\epsilon' = S'\sigma' \tag{2.11}$$

where the $()'$ denotes the laminate coordinate system. Equation 2.10 includes 12 constants, but only 9 independent material terms. In a UD layup, the fibre orientation provides a plane of symmetry and the transversly isotropic material can be described by five constants as the composite is in a state of plane stress [40].

Using the Rule of Mixtures, the elastic properties of an FRP composite can be estimated based on the volume fraction of the constituents. Equation 2.12 and 2.13 show the Young's modulus for the longitudinal and transverse direction respectively. Equation 2.14 and 2.15 shows the Halpin-Tsai formulation for the shear modului respectively. Equation 2.16 and 2.17 shows the Poisson's ratio based on the Rule of mixtures respectively [63]:

$$E_1 = (1-f)E_m + fE_f \tag{2.12}$$

$$E_2 = E_3 = E_m \frac{(1+\xi\eta f)}{(1-\eta f)} \tag{2.13}$$

$$G_{12} = G_{21} = G_{13} = G_{31} = \frac{G_m(1+\xi\eta f)}{(1-\eta f)} \tag{2.14}$$

$$G_{23} = \frac{E_2}{2(1+\nu_{23})} \tag{2.15}$$

$$\nu_{12} = (1-f)\nu_m + f\nu_f \tag{2.16}$$

$$\nu_{23} = 1 - \nu_{21} - \frac{E_2}{3K} \tag{2.17}$$

where f represents the fibre volume fraction and subscripts 1, 2, 3, m and f refer to longitudinal, transverse (2 and 3), matrix and fibre. Equation 2.18 shows the relationship between the fibre and matrix Young's modulus to determine η, the reinforcement constant assumed to be unity [64]. Equation 2.19 shows the relationship to determine the bulk moduli (K) using the rule of mixtures. Equation 2.20 and 2.21 shows the bulk moduli for fibre and matrix respectively [63].

$$\eta = \frac{(\frac{E_f}{E_m}-1)}{(\frac{E_f}{E_m}+\xi)} = \frac{(\frac{G_f}{G_m}-1)}{(\frac{G_f}{G_m}+\xi)} \tag{2.18}$$

$$K = \left[\frac{f}{K_f} + \frac{(1-f)}{K_m} \right]^{-1} \tag{2.19}$$

$$K_f = \frac{E_f}{3(1-2\nu_f)} \tag{2.20}$$

$$K_m = \frac{E_m}{3(1-2\nu_m)} \tag{2.21}$$

The stacking of plies allows the laminate to be custom tailored for a particular function. The relationships just described are used to determine the laminate response to a given load configuration. If the loading surpasses the strength of the laminate a designer should understand how the laminate will progress through damage evolution.

2.3.3.1 Failure models

The damage of a composite laminate is a complex phenomenon with many failure modes concurrently interacting. With respect to the multiscale approach described earlier - micro, meso and macro - failure in a FRP at the ply level involves fibre breakage, matrix failure or fibre-matrix failure at the interface of cohesion [65]. These failure modes result in interlaminar or intralaminar failure modes at the laminate level and are illustrated in Figure 2.9. Intralaminar damage describing damage within a ply, such as the fibre debonding from the matrix. Interlaminar damage describing damage between plies, such as delamination between plies.

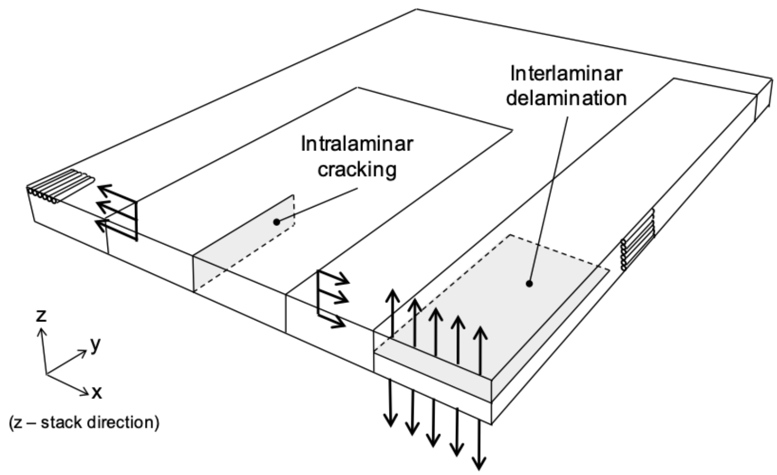

Figure 2.9: Interlaminate versus intralaminate failure [66]

Within the FE framework many failure models exist to predict the loading response, onset of damage and evolution to fracture for a FRP. Two types describe the failure criteria models, non-physics and physics based. Non-physics based failure criteria are mathematical functions creating an envelope based on interpolating experimental results. The prediction of the specific failure mode is not of concern at the laminate level. Physics-based failure criteria attempt to predict the failure based on the physical mechanics of the process at the lamina level [65].

Motivation behind non-physics failure criteria is the efficient implementation into FE models. However, with increasing computational power more complex, physically driven criteria have become the norm. Direct laminate failure envelope theories include Maximum Stress, Maximum Strain, Maximum Shear Stress and others. In 1986, Nahas reviewed failure and post failure theories for laminated composites comparing 30 theories categorized as limit failure theories, interaction failure theories, tensor polynomial failure theories and direct laminate failure theories [67]. Tsai and

Wu developed a stress-based failure criteria that does not distinguish different failure modes, specifically relating to the composite constituents [68]. Using a quadratic formulation, which generated a smoother failure envelope, Tsai-Wu prediction agreed better with the experimental data. Naresh described the Tsai-Wu theory as the simplest of the tensor polynomial theories, however it does require bi-axial experimental test data, which was not easy to carry out [69].

To predict damage initiation many physics based models have been developed, most utilizing the groundbreaking work by Hashin. Failure indices are developed to predict the physical failure modes and are defined as shown in Equation 2.22:

$$I_F = \frac{stress}{strength} \tag{2.22}$$

which predicts the onset of damage initiation when the ratio is greater than one. Hashin failure criteria suggests four modes of failure: fibre tension, fiber compression, matrix tension, and matrix compression. The failure indices for these four modes are shown in Eqautions 2.23 to 2.26:

$$I_{Fft}^2 = (\frac{\sigma_1}{F_{1t}})^2 + \alpha(\frac{\sigma_{12}}{F_{12}})^2 \ , \ if \ \sigma_1 >= 0 \tag{2.23}$$

$$I_{Ffc}^2 = (\frac{\sigma_1}{F_{1c}})^2 \ , \ if \ \sigma_1 <= 0 \tag{2.24}$$

$$I_{Fmt}^2 = (\frac{\sigma_2}{F_{2t}})^2 + (\frac{\sigma_{12}}{F_{12}})^2 \ , \ if \ \sigma_2 >= 0 \tag{2.25}$$

$$I_{Fmc}^2 = (\frac{\sigma_2}{2F_4})^2 + [(\frac{F_{2c}}{2F_4})^2 - 1]\frac{\sigma_2}{F_{2c}} + (\frac{\sigma_{12}}{F_{12}})^2 \ , \ if \ \sigma_2 <= 0 \tag{2.26}$$

where $_{ft}$ and $_{fc}$ describe fibre tension and compression, and $_{mt}$ and $_{mc}$ represent matrix tension and compression [40]. The variable α controls the contribution of shear on fibre failure [70]. With the four primary failure modes outlined, their effect on the stiffness of the laminate at the meso-scale is determined by Continuum Damage Mechanics (CDM). CDM calculates the stiffness degradation of the laminate, represented as an effective stiffness. This is accomplished by assuming a homogeneous dispersion of cracks/damage in a continuum and associates this to an effective mechanical response [71]. The damage variable D, represents the loss of stiffness, shown in Equation 2.27. The loss of stiffness results from the accumulated damage resulting in a theoretical reduction of area due to the micro-cracks and is illustrated in Figure 2.10.

$$D = 1 - E/\widetilde{E} \tag{2.27}$$

In Figure 2.10 a) $\widetilde{E}$ represents the Young's modulus without stiffness degradation and $\widetilde{A}$ is the nominal area. Figure 2.10 b) represents the actual configuration with a decreased area due to damage and the nominal Young's modulus. The FE model utilizing CDM as shown in Figure 2.10 c), which uses the nominal geometry, an increased effective stress $\widetilde{\sigma}$ and decreased effective stiffness E. Finally, the principal of energy equivalence defines the elastic strain energy in configurations b) and c) as equal, resulting in Equations 2.28 and 2.29 respectively:

$$\sigma = \widetilde{\sigma}[1 - D] \tag{2.28}$$

$$\widetilde{\epsilon} = \epsilon[1 - D] \tag{2.29}$$

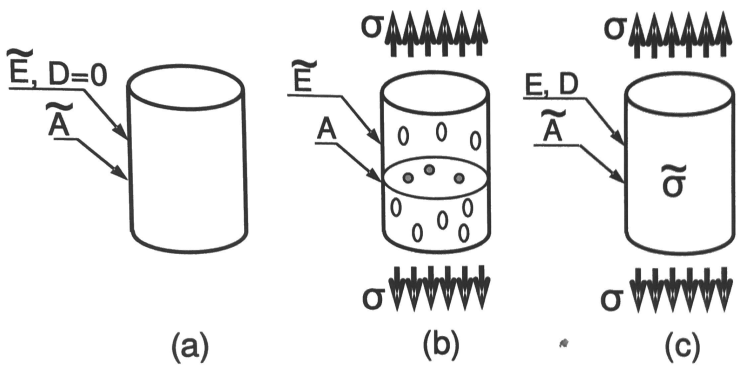

Figure 2.10: Continuum damage mechanics [40]

The effective normal and shear stresses act on an equivalent undamaged material and therefore represent the same strain as the damaged material. This is computed as shown in Equation 2.30:

$$\sigma_e = M\sigma \tag{2.30}$$

where M represents the matrix of damage parameters initiated by a failure index and shown in Equation 2.31:

$$[M] = \begin{bmatrix} \frac{1}{1-d_f} & 0 & 0 \\ 0 & \frac{1}{d_m} & 0 \\ 0 & 0 & \frac{1}{1-d_s} \end{bmatrix} \tag{2.31}$$

Until a failure index indicates damage, the M matrix is equal to an identity matrix and the effective stress remains equal to stress as no damage is present. Once a failure index is initiated the equivalent stress and strains in the element are determined by Equations 2.32 to 2.39 for the four indices outlined by Hashin failure criteria:

Fibre tension ($\widetilde{\sigma_{11}} \geq 0, \epsilon_{11} \geq 0$),

$$\delta_e^{ft} = L^c\sqrt{\langle\epsilon_{11}\rangle^2 + \alpha\epsilon_{12}^2} \tag{2.32}$$

$$\sigma_e^{ft} = \frac{\langle\sigma_{11}\rangle\langle\epsilon_{11}\rangle + \alpha\sigma_{12}\epsilon_{12}}{\delta_e^{ft}/L^c} \tag{2.33}$$

Fibre compression ($\tilde{\sigma_{11}} < 0, \epsilon_{11} < 0$),

$$\delta_e^{fc} = L^c\langle-\epsilon_{11}\rangle \tag{2.34}$$

$$\sigma_e^{fc} = \frac{\langle-\sigma_{11}\rangle\langle-\epsilon_{11}\rangle + (-\sigma_{11})}{\delta_e^{fc}/L^c} \tag{2.35}$$

Matrix tension ($\tilde{\sigma_{22}} \geq 0, \epsilon_{22} \geq 0$),

$$\delta_e^{mt} = L^c\sqrt{\langle\epsilon_{22}\rangle^2 + \epsilon_{12}^2} \tag{2.36}$$

$$\sigma_e^{mt} = \frac{\langle\sigma_{22}\rangle\langle\epsilon_{22}\rangle + \sigma_{12}\epsilon_{12}}{\delta_e^{mt}/L^c} \tag{2.37}$$

Matrix compression ($\tilde{\sigma_{22}} < 0, \epsilon_{22} < 0$),

$$\delta_e^{mc} = L^c\sqrt{\langle-\epsilon_{22}\rangle + \epsilon_{12}^2} \tag{2.38}$$

$$\sigma_e^{mc} = \frac{\langle-\sigma_{22}\rangle\langle-\epsilon_{22}\rangle + \sigma_{12}\epsilon_{12}}{\delta_e^{mc}/L^c} \tag{2.39}$$

where $\langle\ \rangle$ represents the Macaulay bracket operator. The Macaulay bracket operator ensures the equivalent displacements and stress is calculated as it incorporates the positive portion of the parameter, computed as shown in Equation 2.40 [40]:

$$\langle x \rangle = \frac{1}{2}(x + |x|) \tag{2.40}$$

Using the equivalent displacements, the tensile and compressive damage in the matrix and fibre are determined and tracked independently ($d_f^t, d_f^c, d_m^t, d_m^c,$) based on the relationship shown in Equation 2.41:

$$d = \frac{\delta_e^F(\delta_e - \delta_e^0)}{\delta_e(\delta_e^F - \delta_e^0)} \tag{2.41}$$

where δ_e^0 is the displacement at the initiation at damage and δ_e^F is the displacement at failure. The remaining damage variable for shear (d_s) is determined using Equation 2.42:

$$d_s = 1 - [(1 - d_f^t)(1 - d_f^c)(1 - d_m^t)(1 - d_m^c)] \tag{2.42}$$

Damage can progresses from its initiation through to failure on the range $0 \leq d \leq 1$ as $\delta_e^0 \leq \delta_e \leq \delta_e^F$ and is illustrated in Figure 2.11.

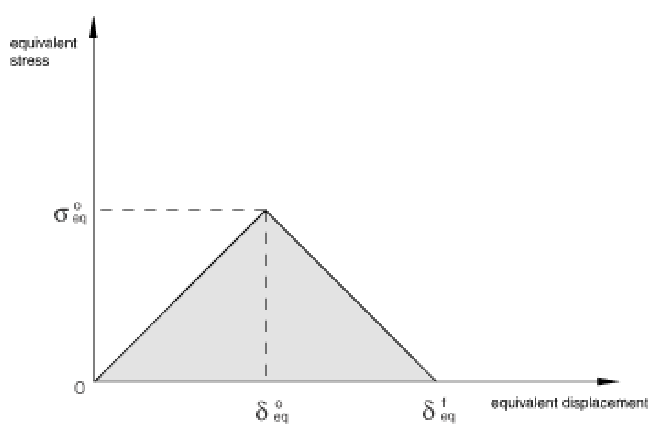

Figure 2.11: Damage evolution [39]

The damaged, degrading stiffness matrix C_d is shown in Equation 2.43. Equations 2.43 and 2.44 are used to determine the resulting stress after the equivalent displacements have been used to calculate the strain. This follows the original relationship of Hooke's law, now updated with stiffness degradation due to the damage, shown in Equation 2.45:

$$[C_d] = \frac{1}{D}\begin{bmatrix} (1-d_f)E_1 & (1-d_f)(1-d_m)v_{21}E_1 & 0 \\ (1-d_f)(1-d_m)v_{12}E_2 & (1-d_m)E_2 & 0 \\ 0 & 0 & (1-d_s)G_{12}D \end{bmatrix} \tag{2.43}$$

$$D = 1 - [(1-d_f)(1-d_m)v_{12}v_{21}] \tag{2.44}$$

$$\sigma = [C_d]\epsilon \tag{2.45}$$

FRP laminate failure is initiated by matrix damage. When the laminate is loaded in tension or compression, perpendicular to the fibre orientation the fibre-matrix cohesion interface fails. In compression, this failure results in a shear band. If the loading of the FRP is focused parallel to the fibre orientation, fibre damage will dominate the failure prediction. When the applied load is in tension and parallel to the fiber orientation, decohesion of the fibre-matrix interface will occur followed by fibre breakage. If the applied force acting parallel to the fibres generates compressive stress, the fibre-matrix cohesion fails leading to a kinking in the laminate. Interlaminar failure, known as delamination is common for Uni-directional (UD) composites. In frequent load configurations the normal and shear stress exceed the weaker resin-rich interlaminar area, leading to decohesion of the plies [65].

To model the interlaminar delamination a significant modelling consideration to the representation of the laminate must be made. A macro-scale representation, with a single instance using a representative volume element (RVE) can determine the matrix and fibre damage independently in a representative sense, but cannot facilitate delamination [40]. To represent the interlaminar delamination a meso-scale representation is required. Individual ply instances must be modelled with a cohesive response between the plies. Many factors can facilitate delaminations including manufacturing imperfections, fatigue, low velocity impacts, stress concentrations due to geometrical and material discontinuities, or due to high interlaminar stresses [40]. Interlaminar fracture strength is described by mode I opening, mode II shear and mode III tearing conditions, as illustrated in Figure 2.12.

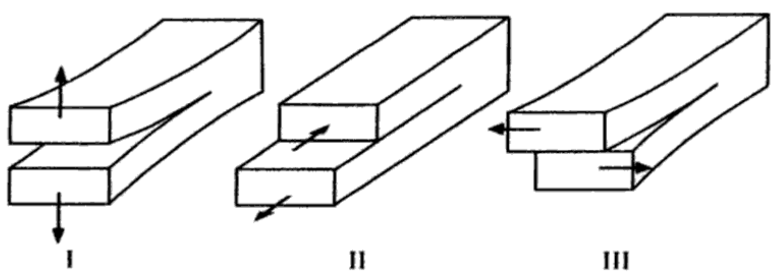

Figure 2.12: Crack propagation modes: I-opening, b) II-shear, c) III-tearing [72]

The cohesive zone model (CZM) uses a stress - displacement approach (σ versus δ) known as traction separation, versus the standard engineering stress-strain approach (σ versus ϵ). To model the interlaminar cohesive interaction continuum cohesive elements or cohesive surfaces can be used. Illustrated in Figure 2.13 are the three zones created to represent the cohesion: the non-damaged elastic zone, the damage initiated zone and the stress-free fully damaged zone.

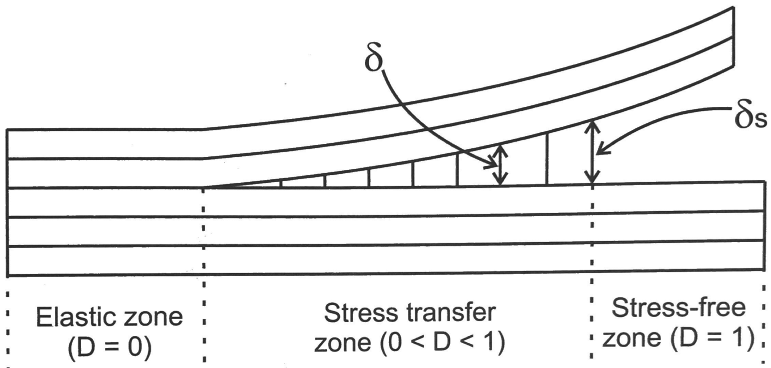

Figure 2.13: CZM crack propagation [40]

The three zones allows for damage progression, such that the stress between the laminates is not fully lost when damage is initiated. Secondly, because the displacement is initially zero as there is no cohesive damage, strain cannot define the deformation. The behaviour of this cohesive interface is linear-elastic and is represented by Equation 2.46:

$$\sigma_i = K_i \delta_i \tag{2.46}$$

where $i = I, II, III$ denoting the three modes of deformation at the interface. Similar to the composite stiffness degradation, the traction stiffness follows Equation 2.47:

$$K_i = (1 - D_i)\widetilde{K_i} \tag{2.47}$$

where $\widetilde{K_i}$ is the stiffness undamaged and D_i is the damage variable. This stiffness is different than the Young's modulus (E) or shear modulus (G) with units $[N/mm^3]$. The stiffness value is non-physical, relatively insensitive and is used to prevent model inconsistencies ranging in magnitude from 10^6 to 10^{12} [61].

The damage initiation criteria is based on a stress or separation in the contact. This is achieved by defining a maximum stress or separation (MAXS or MAXU), or using a quadratic interpretation for the stress or separation (QUADS or QUADU). The maximum stress and separation criteria are shown in Equation 2.48 and 2.49 respectively:

$$max\left\{\frac{\langle t_n\rangle}{t_n^0}, \frac{t_s}{t_s^0}, \frac{t_t}{t_t^0}\right\} = 1 \tag{2.48}$$

$$max\left\{\frac{\langle \delta_n\rangle}{\delta_n^0}, \frac{\delta_s}{\delta_s^0}, \frac{\delta_t}{\delta_t^0}\right\} = 1 \tag{2.49}$$

where t represents the stress and t^0 represents the critical value where cohesive damage would be initiated. In the case, the Macaulay bracket insures that a compressive displacement or stress state does not initiate contact damage. The quadratic formulation of the stress and separation criteria is shown in Equation 2.50 and 2.51 respectively:

$$\left\{\frac{\langle t_n\rangle}{t_n^0}\right\}^2 + \left\{\frac{t_s}{t_s^0}\right\}^2 + \left\{\frac{t_t}{t_t^0}\right\}^2 = 1 \tag{2.50}$$

$$\left\{\frac{\langle \delta_n\rangle}{\delta_n^0}\right\}^2 + \left\{\frac{\delta_s}{\delta_s^0}\right\}^2 + \left\{\frac{\delta_t}{\delta_t^0}\right\}^2 = 1 \tag{2.51}$$

Cohesive damage evolution is the process of degrading the cohesive stiffness and requires two definitions. First, providing the effective separation at failure, δ_m^f, relative to the effective separation at the initiation of damage for the cohesion, δ_m^0. Secondly, by specifying the energy dissipated at failure, G^C. The energy dissipation definition identifies the magnitude of the evolution of damage and can follow a linear softening or exponential relationship. The linear and exponential softening of the damage evolution for traction separations are expressed in Equation 2.52 and 2.53 respectively:

$$D = \frac{\delta_m^f(\delta_m^{max} - \delta_m^0)}{\delta_m^{max}(\delta_m^f - \delta_m^0)} \tag{2.52}$$

$$D = 1\left\{\frac{\delta_m^0}{\delta_m^{max}}\right\}\left\{1 - \frac{1 - exp(\alpha(\frac{\delta_m^{max} - \delta_m^0}{\delta_m^f - \delta_m^0}))}{1 - exp(-\alpha)}\right\} \tag{2.53}$$

where α is a non-dimensional parameter that controls the rate of the exponential evolution [39]. Damage evolution based on energy is determined by the area under the traction separation curve. The damage evolution of the cohesive interaction based on the fracture energy can be modelled using a tabular description, the Power law, or the Benzeggagh-Kenane (BK) form. The Power law form and BK fracture energy relationships are given in Equation 2.54 and 2.55 [39] respectively:

$$\left\{\frac{G_n}{G_n^C}\right\}^\alpha + \left\{\frac{G_s}{G_s^C}\right\}^\alpha + \left\{\frac{G_t}{G_t^C}\right\}^\alpha = 1 \tag{2.54}$$

$$G_n^C + (G_s^C - G_n^C)\left\{\frac{G_S}{G_T}^\eta\right\} = G^C \tag{2.55}$$

The Power Law form requires critical fracture energies in the normal (G_n^C), primary (G_s^C) and secondary (G_t^C) shear directions to be specified; in addition, α which defines the power of the relationship. The BK relationship requires G_n^C, G_t^C and a cohesive property parameter η to be specified; where $G_S = G_s + G_t, G_T = G_n + G_S$ [39]. When separation is focused in the primary and secondary shear directions ($G_s^C = G_t^C$) BK is effective [73]. Alternative to cohesive surface interactions, cohesive elements can be used to model these regions. Cohesive elements require partitioned sections or individual instances in which the cohesive properties are applied. Due to the 3D nature of the instance a finite-thickness is known. Rather than the traction-separation criteria for surface based cohesion, the cohesive elements use a continuum macroscopic property to model the constitutive response [39]. Properties include stiffness and strength that are determined experimentally. The cohesive elements are capable of modelling through-thickness strain, two transverse shear strains and all six stress components. The cohesive zone with a finite thickness is modelled using a continuum constitutive (σ versus ϵ) behaviour, in contrast to the zero thickness cohesive elements that is based on the traction-separation constitutive behaviour (σ versus δ) [40]. Special considerations must be taken when using cohesive elements together with contact interactions that can lead to degradation of the stable time increment, or convergence issues in an implicit analysis. Ullah et al. [55], performed large deflection bending tests on woven CFRP laminates and compared with FE simulations. The FE models had cohesive elements capability. Results showed that mesh size of the cohesive zone element and stiffness have significant effect on the simulation. Computational time was affected by two unique material properties. Furthermore, Ullah et. al. also found that interface parameters has to be specifically calibrated and specify correctly otherwise model will be terminated preternaturally, long computation times and to avoid solution oscillations. In an Explicit FE analysis the stable time increment is commonly significantly less than other elements in the model due to the small element length (cohesive thickness), high stiffness and comparatively low density [39]. To mitigate these concerns the cohesive modelling in this research implements cohesive surface interactions.

With delamination, the drill movement of a distance dX is associated with the work done by the thrust force, F_A. This deflects the ply while promoting the inter-laminar crack. The energy related to this is represented by Equation 2.56 [24]:

$$G_{IC}dA = F_A dX - dU \tag{2.56}$$

where dU is the strain energy, dA is the increase in delamination crack area and G_{IC} is the mode I crack propagation energy per unit area. The drilling induced delamination is a function of the applied thrust force. Exceeding a critical amount, F_A, which the uncut thickness of the laminate cannot withstand causes delamination. Figure 2.14 illustrates the mechanism outlined by Equation 2.57 [24]:

$$F_A = \pi\sqrt{32G_{IC}M} = \pi\left[\frac{8G_{IC}Eh^3}{3(1-v^2)}\right]^{1/2} \tag{2.57}$$

where E is the Young's modulus, v is the Poisson's ratio and M is the stiffness per unit width of the fibre-reinforced polymer (FRP). The relationship for M is given by Equation 2.58 [24]:

$$M = \frac{Eh^3}{12(1-v^2)} \tag{2.58}$$

A result of the thrust force, is the pure bending of the laminate causing delamination. The change in area, dA, is calculated in Equation 2.59 depending on the radius of delamination, a [24]:

$$dA = \pi(a+da)(a+da) - \pi a^2 = 2\pi a da \tag{2.59}$$

By identifying the critical thrust force causing delamination, with respect to uncut

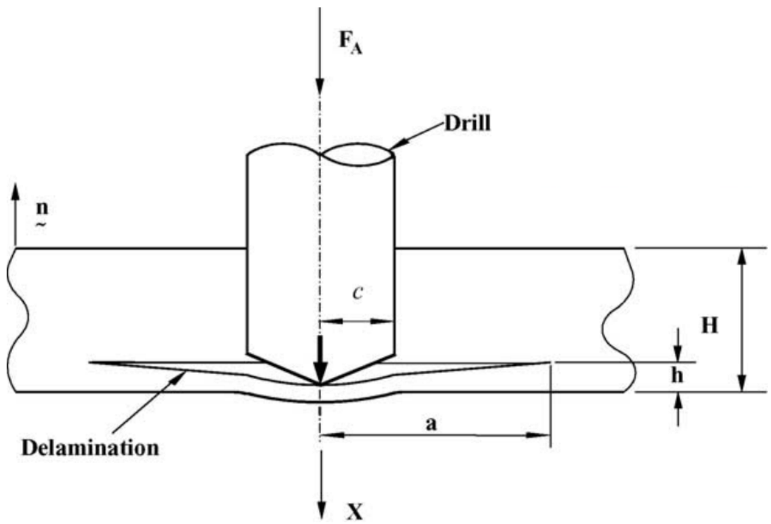

Figure 2.14: Delamination cause by twist drill [24]

thickness of the laminate, the feed rate should be modified throughout the progression of the cut [24, 74]. Most effectively with an aggressive feed at initiation to promote material removal rate (MRR) and a reduced feed to mitigate delamination near the exit of the cut.

2.3.4 Experiment and modelling relating to material characterization and subtractive machining

2.3.4.1 Tensile test configurations

There are abounding benefits to CFRP composites, most specifically the high strength to weight ratio and the ability to customize a part for a particular function. As described, there are equally as many considerations that must be made to ensure an effective, optimized part is created. To promote the knowledge and understanding of FRPs experimental tests and numerical modelling have been studied extensively.

Designers have been provided this information regarding material properties for different loading configurations to ensure a successful part is created.

The anisotropic nature of FRP composites needs to be efficiently understood and characterized. The near infinite combinations of fibre types, matrix types, fibre arrangements and loading configurations is an intensive undertaking. UD-FRP composites are transversely isotropic and can be described by five material properties $(E_1, E_2, \nu_{12}, \nu_{23}, G_{12})$. Numerical modelling and FE simulations have greatly reduced the experimental testing required to characterize an FRP. Experiments are time consuming and costly, but necessary to determine material parameters used to accurately represent a CFRP sample for design calculations and end use. The American Society for Testing and Materials (ASTM) outlines numerous tests to characterize FRP materials: D3039/D3039M-17 for tensile properties used by [41, 75], D7264/D7264M-15 for flexural properties, D8066/D8066M-17 for compression testing, etc. [76].

The designated acceptable failure locations of the tensile test by ASTM are shown in Figure 2.15. Many modes of failure illustrated are not useful if the measurement tools are not capturing the failure in the chosen gauge section. Any failure that is not designated with a second character Gage (G) would be outside the intended failure region and unable to capture the strain at failure. Wong et al. and Coguill and Adams, report damage first initiating in the tabbed region rather than the intended gauge region [78, 77]. Coguill and Adams studied tabs and specimen geometry extensively describing no one specimen configuration can be optimal for ultimate tensile performance of unidirectional specimens [79]. Numerous fixturing techniques and sample geometries have been studied including rectangular, wishbone, notched and the disc geometry created by Arcan to improve testing repeatability.

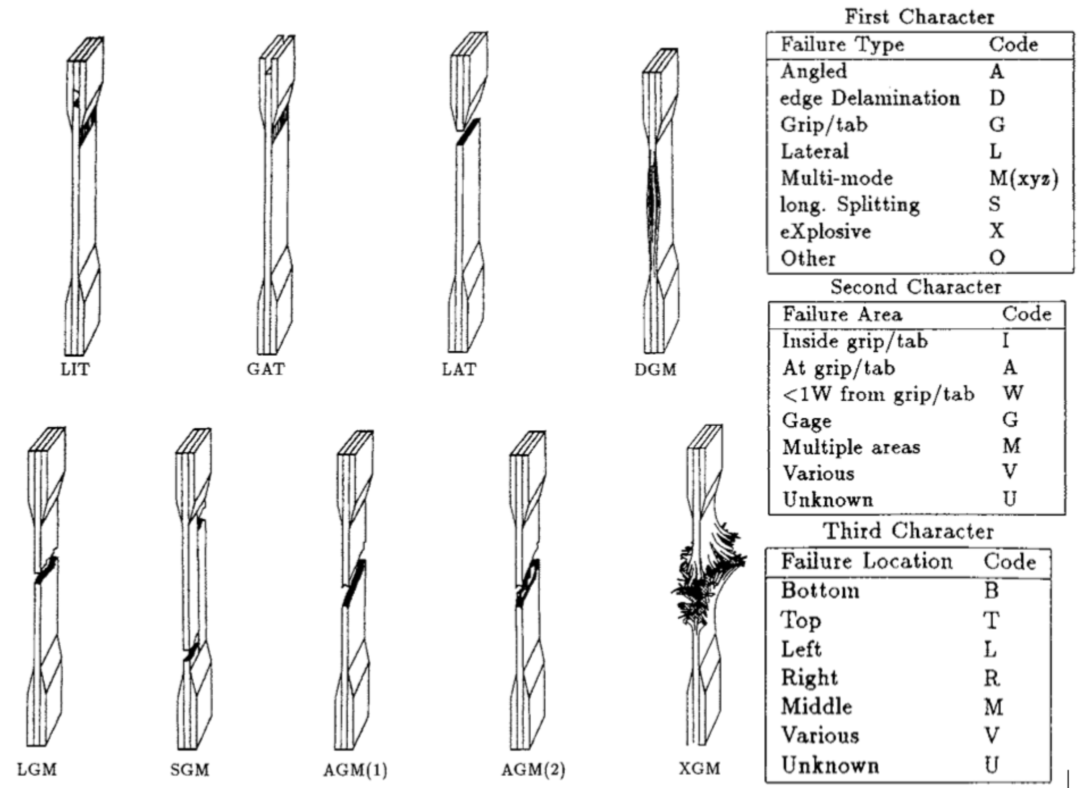

First Character

Failure Type	Code
Angled	A
edge Delamination	D
Grip/tab	G
Lateral	L
Multi-mode	M(xyz)
long. Splitting	S
eXplosive	X
Other	O

Second Character

Failure Area	Code
Inside grip/tab	I
At grip/tab	A
<1W from grip/tab	W
Gage	G
Multiple areas	M
Various	V
Unknown	U

Third Character

Failure Location	Code
Bottom	B
Top	T
Left	L
Right	R
Middle	M
Various	V
Unknown	U

Figure 2.15: Tensile test failure codes [76]

Common serrated wedge grips unfortunately induce concentrated compressive damage on the sample due to the significant gripping force required when loading the CFRP samples to fracture. ASTM-D3039 describes adding tabs as needed [76]. An exhaustive 74 page report titled Tabbing Guide for Composite Test Specimens exists to provide information regarding tab design and application [80]. A NASA supported report by Worthem tested five geometries to reduce stresses leading to unintended failure between the gauge section and the tab region. It concluded tab materials must be selected with great consideration to adhesion and toughness versus stiffness that will lead to nonlinearity in response [81]. Mehar et al. describes tab design as an art that affects coupon strength [82]. Sadeghian et al. uses epoxy tabs to prevent premature failure near coupon ends [83] although others note steel, aluminum, carbon fibre and epoxy as possible options [84, 85]. UD fibre reinforced polymers (FRP) are susceptible to notch sensitivity due to the great longitudinal strength, but comparatively low shear strength.

To avoid inefficient or unusable testing researchers have adapted ASTM methods and other methods in literature to improve material characterization. When unidirectional (UD) CFRP is loaded parallel to the fibres in a tensile test, the loads experienced can be ten orders greater than when loaded perpendicular to the fibre. Significant gripping pressure is required for these tests to prevent slipping during the loading, frequently resulting in compressive damage on the CFRP samples in the gripping area prior to failure in the gauge region. A modified wishbone geometry was implemented to control failure location in work by Kobayashi et al. used to test enhanced strengths resulting from creep at high temperatures [86].

Despite the ideal material properties of a CFRP composite they are quite susceptible to damage caused during manufacturing, assembly, or in service. Zappalorto and Carraro worked to quantify the stress concentration factor of orthotropic plates, thus improving the understanding of notch sensitivity and controlling the location of failure [87].

Hallett and Wisnom tests progressive damage using a double-edge-notched geometry to control and correlate failure at the notch for multiple cross-ply layups [88] Hallett et al. described the failures due to notches highly dependent on size and layup, very complex and not possible to characterize using analytical techniques based on fracture mechanics or average stress criterion. Hallett et al. continued this work modelling using FEM capturing delamination and ply splitting while considering mode II damage [89].

Lapczyk and Hutado studied a new energy based damage evolution law with Hashin's failure initiation criteria to predict notch sensitivity. Energy based damage evolution is generally dissipated proportional to the volume of the failed element, rather than the area of the fractured surface. As meshes are refined the energy dissipated reduces to zero. This common mesh sensitivity issue can be minimized using a crack band model that uses a characteristic element length and preserves the fracture energy. Damage softening convergence issues were alleviated using viscous regulation [90].

Creatively in 1977, Arcan et al. developed a unique disc geometry that when loaded in tension, at 0° with respect to the primary fibre direction would determine in-plane shear and is shown in Figure 2.16 [91]. This work motivated by the previous conventional "rail-shear method" that was highly influenced by gripping procedures, or the "picture-frame method" that did not produce a homogeneous stress state. Limitations of the Arcan disc geometry include the significant material required per test due to the geometry in comparison to the gauge section. Additionally, setup angles greater than 45° cannot achieve plane stress in the gauge region due to stress concentrations. Therefore the test cannot be used to determine normal stresses in the longitudinal and transverse directions.

Hajjar and Haj-Ali used a modified Arcan fixture to determine the non-linear shear response up to failure by mimicking the Arcan fixture, but including a gripping section requiring a reduced geometry for the test [92]. Tessmer et al. used the modified geometry for combined loading situations to determine the out-of-plane response [93]. Nikbakht and Choupani used the modified Arcan geometry to test pure mode I,

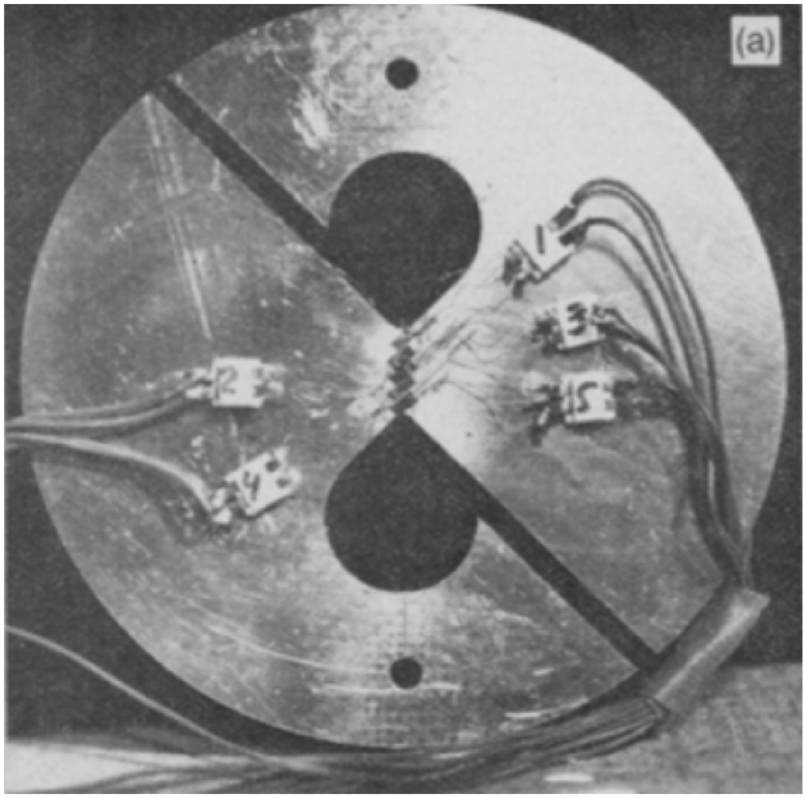

Figure 2.16: Arcan method to produce uniform plane-stress states [91]

pure mode II and a full range of mixed mode setups to characterize the interlaminar strength of the carbon-epoxy composite; the interlaminar specimen is tougher in shear versus a tensile loading condition [94].

When a unidirectional (UD) CFRP coupon is loaded in tension a non-linear response is observed resulting from damage in the matrix and the interface between the matrix and fibres or plies. This nonlinearity increases as the angle between fibre orientation and the loading direction of the UD-CFRP is increased. Frequently, a CFRP material response is modelled as linear-elastic, followed by damage initiation and evolution based on time, displacement, or energy; omitting the non-linear response observed experimentally [96, 41, 95]. This representation is not sufficient as it neglects the inter-ply interactions and the pre-failure damage in the matrix that contributes to a nonlinear response. Precision of FEM versus analytical formulations and trade off between average method and complete layup are outlined in [97]. As the name implies, the average method averages the composites anisotropic properties throughout the volume. The average method of a symmetrical multi-ply layup will more accurately represent a laminate versus a cross-ply UD layup.

Classical laminate theory (CLT) is the fundamental method for calculating response of multi-ply inhomogeneous layups. The stiffness response of a ply, based on its orientation and anisotropic properties is determined and transformed from the ply level to the laminate coordinate system. This allows one instance to mathematically represent a multi-ply layup oriented in any stacking sequence. In FE software, a composite layup can facilitate a cross-ply layup of a single instance requiring the ply thickness, orientation and elastic material properties; negating the requirement of multi-instance assemblies with tied constraints or partitioned geometries.

In an implicit FE analysis pre-failure nonlinearity can be incorporated in the FE model to better predict a UD laminates nonlinear softening response, a result of the nonlinear longitudinal shear [33]. This prediction generates a four-segment picewise linear representation with three discrete reductions in the shear moduli. In an explicit anslysis, to accurately capture the non-linear response of the CFRP coupon, the inclusion of multi-ply layups, with cohesive interaction between plies capable of damage, must be modelled.

2.3.4.2 Bending test configurations

Described in an International Organization for Standardization (ISO) document "Plastics-Determination of flexural properties" [98], tensile tests are quite cumbersome for brittle materials. Techniques to improve repeatability in fracture location, minimize tabbing-effect or alternative gripping methods are required. Three-point bending tests are preferred due to advantages in sample production, testing repeatability, negated grip sensitivity and predictable failure location.

Huang et al. [99] used cohesive elements to model three-point bending using material properties from [100], however no description of the layup, cohesive element geometry or implementation, nor comparison to experimental tests was provided. Ullah et al. [34] studied woven composites under large-deflection and compared experimental results to a 2D FE model highlighting the interface zone cohesive elements were highly sensitive to mesh and stiffness magnitudes. Ullah et al. incorporated three layers of cohesive elements parallel to the plies and a cohesive layer in the transverse direction through the thickness of the laminate; no other literature was found incorporating a cohesive layer through the thickness of the laminate. The predicted delamination and force-deflection represent the experiments well, but the application of real-world, three-dimensional, dynamic loading was suggested to cause issues [34, 55, 101]. Petrescu et al. [102] used various span lengths to determine flexural modulus of the CFRP laminate, noting bending tests should be used preferentially for brittle materials for which tensile tests are difficult. Petrescu et al. referred to the modulus as interchangeable to the Young's modulus but did not provide any description as to why. Naresh et al. study experimentally the effect of fibre orientation (0°, 45°and 90°) and two cross-ply layups in bending using CFRP and GFRP. Naresh et al. described fibre-matrix debonding for the 0°, 45°and 90°setups and increased flexural strain due to delamination hindering crack propagation for cross-ply layups [69]. Niezgoda and Derewonko [38] created a two-stage, macro-micro scale FE model using brick elements for the resin and beam elements to represent the fibre constituent. Approximately a 60% reduction in elements is created with the two-stage model, however differences in strain prediction between the models and the effort required to setup the analysis presents significant challenges. Mujika describes an inflated flexural modulus for three and four point bending tests resulting from a decreased span due to rotations at supports. Mujika describes greater inflation error for four point bending tests due to the additional span increase resulting from the loading noses. Testing the same specimen using three-point and four point bending setups resulted in a 5% difference, that reduced to below 1% when corrected for span length. The over estimated flexural modulus creates a design risk using inaccurate material information [103].

2.3.4.3 Drilling

CFRP requires modelling in tension, bending and shear setups to accurately and efficiently predict material response and failure in common loading configurations. Finite element modelling (FEM) of machining processes involves higher strain rates, complex tool design and various material interactions requiring specific modelling considerations. Vijayaraghvan outlines numerous considerations in modelling multilayer material machining including: material modelling, contact, fracture criteria, adaptive meshing, element types, tool modelling [104].

Significant experimental work has been carried out studying the effectiveness of drilling CFRP materials, including reviews completed by Panchagnula et al. outlining the significance of process monitoring to ensure hole quality [105, 106]. Panchagnula et al. reiterates the generated force, cutting mechanism and delamination damage created when drilling FRPs are directly related to cutting speed, feed and tool geometry. Experimentally, Liu et al. specifically studied the drilling of composite laminates, highlighting the variation between materials' elastic modulus resulting in deviations in drilled hole diameters [107]. Bhatnagar et al. used Iosipescu shear tests and orthogonal cutting experiments to characterize chip formation for various fibre orientations in hope of future use in more complex cutting operations such as drilling [108]. Bhatnagar et al. concluded the principal stress was always in the direction of the longitudinal fiber, creating a chip formation process transverse to this axis.

Sandvik tool manufacturer outlines surface roughness for drilling compisite metal stacks must achieve $3.2\mu m$ or less and 1.6 μm or less for titanium or aluminum alloys [109]. A Mapal (Aalen, Germany) business unit manager of aerospace and composites, Dr. Peter Mueller-Hummel, outlines holes drilled in metal for aerospace structures must achieve H7 tolerances, ± 12 μm. When drilling composites this is relaxed to H8 tolerances, ± 18 μm and even H9, ± 30 μm, referencing the ISO 286-1:2021 Geometrical product specifications standard [110].

Conventional drilling experiments carried out by Merino-Perez et al. investigate cutting speed and CFRP constituents, identify the significant importance of the matrix on the material response due to strain rate and thermal effects [111]. Aspinwall et al. studied the effect of machining inputs when drilling CFRP, and concluded that drill geometry and feed rate are the main contributing factors relating to tool life and thrust force. Two of the geometries investigated and the relationship between tool life and process parameters are shown in Figure 2.17 [112].

Karpat et al. compared drill designs experimentally and highlighted that double

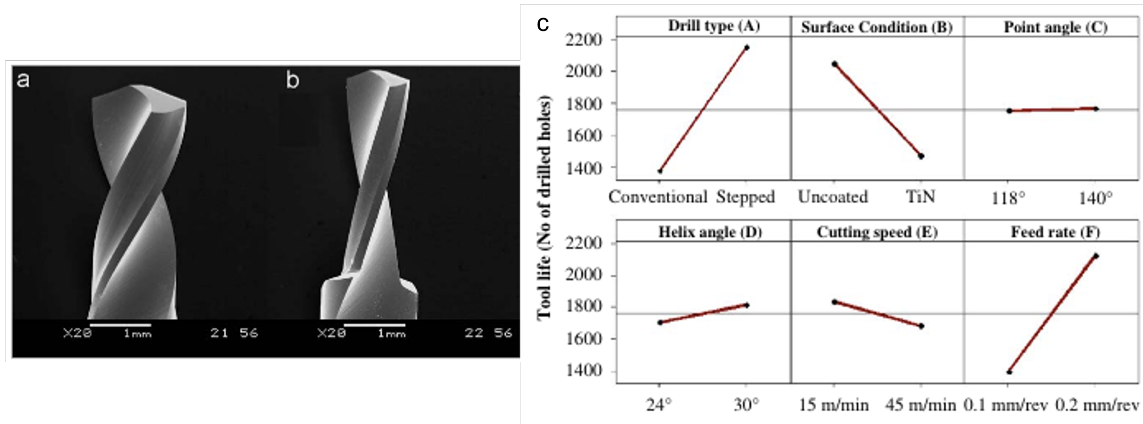

Figure 2.17: a) Conventional twist drill b) Stepped drill c) Tool life versus process parameters [112]

point drill angles with long primary edge length showed lower thrust force at exit. However, the tool exhibited increased wear and confirms better tool performance at lower feeds [113]. Wang et al. studied the effect of tool wear in drilling CFRP, describes rapid dulling due to brittle nature of CFRP can be significantly reduced with ultra-hard diamond coating, however aluminum titanium nitride (AlTiN) did not, due to its oxidation during drilling. Insignificant change in torque after 80 holes, however 3.5 times the thrust force with wear on uncoated and AlTiN coated [114]. Faraz et al. studied the effect of cutting edge rounding (CER) to predict and prevent increase drill loads and maintain hole quality, versus more common flank wear monitoring [115].

Aspinwall et al. studied different stepped drill geometries noting a reduction in thrust force attributed to the reduced chisel edge [112]. Won [116] demonstrated that as the feed rate increased from 0.1 to 0.7 mm/rev for a 1/4" twist drill the thrust force increased nearly 5 times in magnitude; a feed rate greater than 0.1 mm/rev resulted in a thrust force greater than the critical force causing delamination damage. However, with the pre-drill thrust force increased only marginally and remained well under the critical thrust force value even at feeds of 0.7 mm/rev, as shown in Figure 2.18.

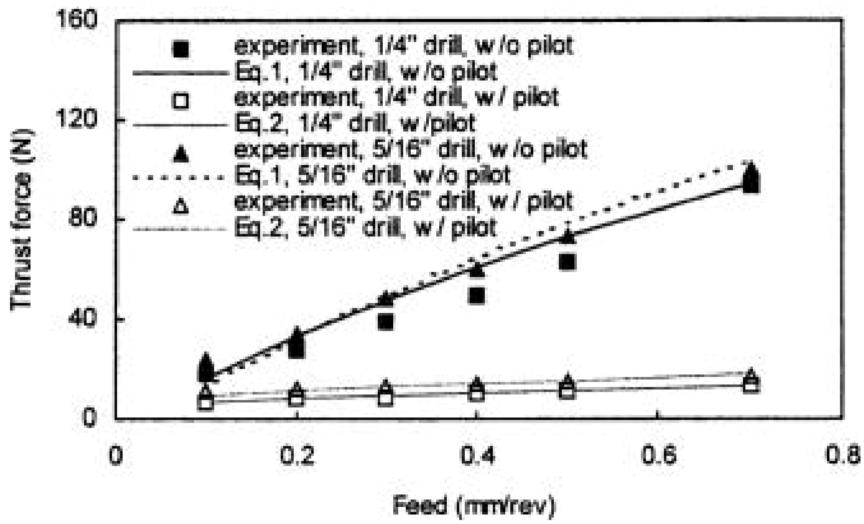

Figure 2.18: Measured thrust forces versus feed rate [116]

Tsao and Hocheng continued this investigation identifying a process window for pre-drilled holes relating the ratio of the chisel edge length to pre-drilled hole diameter. As a result the critical thrust is reduced with a pre-drilled hole, therefore allowing for more assertive feed rates to be used [117]. Jain et al. preformed experiments regarding the reduced feed that support Hocheng et al. work. Jain et al. [118] found 40-60% of the thrust force is created by the chisel edge and demonstrated by reducing the chisel width edge thrust force and thereby delamination was greatly reduced. Further improvements focused on reducing the effect of the chisel edge of the drill to minimize thrust force were preformed by Won who studied the effect on forces with and without pre-drilled holes [116]. The pilot hole was shown to reduce thrust force significantly allowing for use of much higher feed force. Lissek et al. describes delamination is the most critical damage when drilling CFRP [106].

Xu and Mansori preformed experiments outlining machining quality when trimming CFRP/Ti stacks relies highly on fibre orientaiton and tool wear [119]. Zitoune et al. preformed experimental tests on drilling stacks and determined thrust force of aluminum and titanium to be 2-3 times higher than CFRP and high feed rates increase circularity [120]. Phadnis et al. experimentally drilled Aluminum with CFRP stacks and compared with an FEA model developed, concluding low feed rate, high cutting speeds reduced thrust force and torque, shown in Figure 2.19 [48]. Brinksmeier et al. experimentally studied the drilling of multi-layer composites consisting of CFRP, Titanium and Aluminum alloys and concluded improved drill geometries, coatings and minimum quantity lubrication is critical [121].

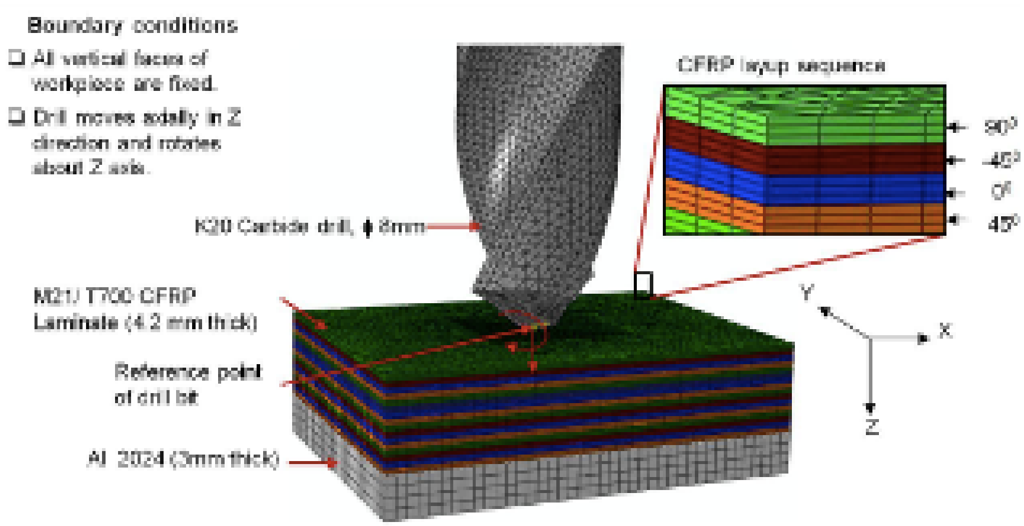

Figure 2.19: FE model setup with boundary conditions of Aluminum and CFRP stack-up [48]

Shyha et al. [122] investigated hole quality utilizing one drill geometry with various coatings, coolant environments, cutting speeds and feed settings in addition to a dual level speed program, doubling the speed for Aluminum and CFRP versus the Titanium. Two cutting environments were investigated, which were wet, high pressure coolant and spray mist coolant. Shyha et al. determined wet, high pressure coolant generated undersized holes between 14 to 20 um when compared to 120 um with spray mist coolant. Park et al. [16] concluded that polycrystalline diamond (PCD) drills were superior to tungsten carbide (WC) drill. However, major chipping was noticed at the cutting edges when drilling titanium due to brittle nature of PCD. CFRP abraded the cutting edge, and titanium extended the flank wear due to carbide grain pullout when the titanium adhesion was removed. Drilling Titanium, CFRP and Aluminum Shyha et al. [123] demonstrated low cutting speed and feed under wet conditions were most ideal (less than 20/40 m/min & 0.05 mm/rev). This feed is recommended for drilling stacks by multiple drill manufacturers including Sandvik [109]. However, this cutting speed was 1.5-3 times less than commonly recommended. Although tool life demonstrated 310 drilled holes, material removal has decreased and therefore reduced productivity.

Kahwash et al. [124] highlights the current practice of modelling the cutting process of CFRPs describing significant work on 2D orthogonal cutting due to its simplicity from modelling assumptions and computational advantage. Kahwash et al. outlines the need for more comprehensive modelling research with emphasis on multi-scale and mesh-free methods. Multi-scale methods attempt to obtain large scale solutions accurately without determining all small scale details. The small scale information is captured within each element and then coupled to the global stiffness matrix of the large scale. Mesh-free methods use discretized unconnected nodes, unlike solving the partial differential equations of the nodes connected by elements and is shown in Figure 2.20. The motivation for this modelling technique is the reduction in remeshing due to large deformations and element distortion present with machining simulations.

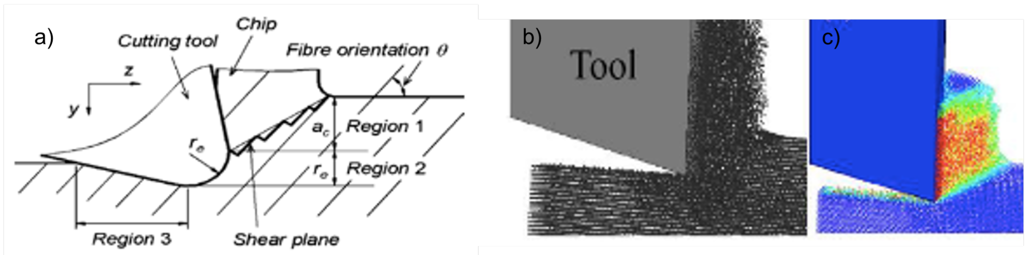

Figure 2.20: a) 2D orthogonal cutting setup b) Mesh-free 3D view c) Mesh-free FEM effective plastic-strain [124]

Arola and Ramulu produced preliminary 2D orthogonal models involving graphite epoxy material, highlighting the significant potential of FE modelling for FRP machining acquiring good correlation between cutting force prediction and experiments, but not with thrust force prediction [20]. 2D FE orthogonal models were investigated additionally by Dandekar et al. [44], Abena et al. [125] and Gobivel et al. [45, 126] focusing on separate matrix, fibre and cohesive interface phases. Dandekar et al. was able to predict fiber debonding, fiber damage and cutting forces, but results had limitations depending on fiber angle. Matrix damage such as cracking or redistribution of load was not captured. Abena et al. developed a fiber-matrix interface that could predict compressive cohesive, shear and tension failure depending on the 2D orthogonal setup, however mesh sensitivity and prediction of thrust force need more development. Gobivel et al. developed a thermal-mechanical 3D model of the 2D orthogonal cutting process investigating cryogenic cooling of workpiece versus heating pre-treatments. Cryogenic cooling developed brittle failure modes in both the fiber and matrix, versus the pre-heating developing a thermal softening of the matrix material. Although cutting force was decreased with higher heating pre-treatments, the surface roughness increased, a relationship dominated by fiber orientation.

Mahdi et al. studied mesh sensitivity, plane stress versus strain assumption and rake angle concluding the rake angle had minimum effect, but succesfully demonstrated the effect of fibre angle when machining FRPs [50]. Lasri et al. used a progressive failure stiffness degradation scheme when modelling 2D orthogonal machining to gain understanding on subsurface damage and its contribution on chip formation [127]. A hybrid 2D orthogonal cutting model involving CFRP and Titanium was created by Xu et al. [119]. The inclusion of an interface zone between the constituents proved to have significant effect on delamination magnitude and fibre/matrix failure.

Phadnis et al. compared drilling experiments to FEM model. Using X-ray microtomography, drill entry and exit delamination damage was investigated [128]. Although exaggerated, the outer region of the damage predicted in the FEA resembled experiments and is shown in Figure 2.21. The concern is the significant element removal of the failed cohesive elements at exit.

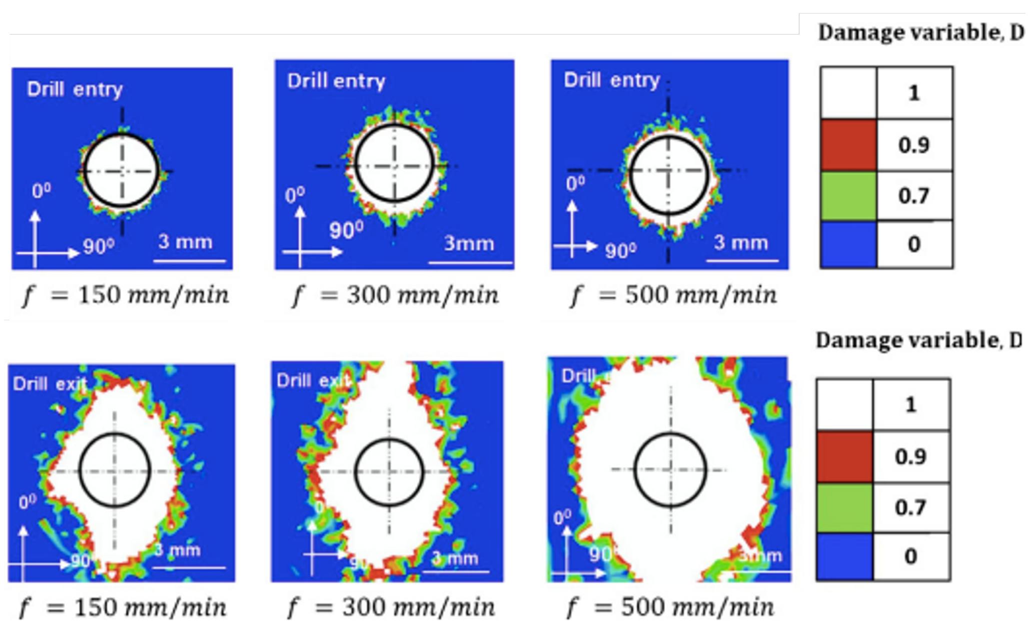

Figure 2.21: Predicted damage at drill entry and exit [128]

A 3D model was created to represent the 2D orthogonal cutting of CFRP with a macro-mechanical setup that does not consider matrix-fibre interface, by He et al. [129]. A strong variance in predicted cutting forces was described when using different failure criteria including Hashin and Max Stress. Max Stress predicted cutting force reasonably where Hashin underestimated significantly. However, thrust force was significantly under predicted, 75% difference from experiments. He et al. [129] described the thrust force predictions an order of magnitude less than experiments. No element removal or chip formation was captured. Lasri et al. [127] describes good prediction of cutting force, but inability to predict thrust force in comparison to experimental data. The model captures damage modes, however does not show the removal of elements, nor the progression of chip evacuation; only the initiation as shown in Figure 2.22. Lasri et al. uniquely describes minimal strain rate dependence and a bouncing back effect reducing the overall depth of cut [127].

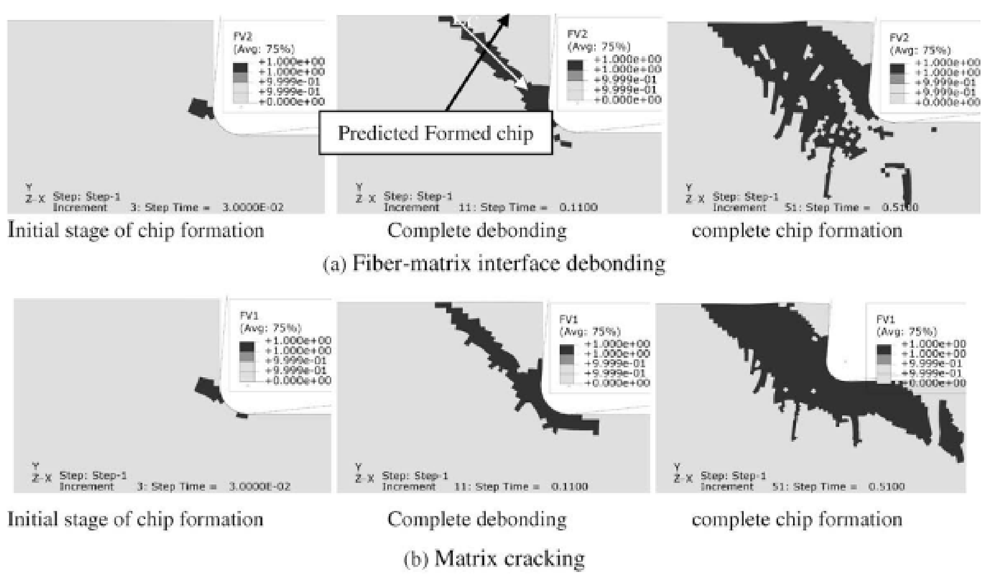

Figure 2.22: Predicted damage initiation, chip initiation and chip formation [127]

3D orthogonal and drilling model produced by Usui et al. [46] captured delamination in various fibre orientations by using cohesive zone elements mapped to fracture planes defined by the Miller indices. The orthogonal cutting model predicts chip formation for the various fibre orientations, however no no experimental validation is provided. Usui et al. noted the thrust force continually increasing throughout the drilling simulation. This contrary to the steady output observed experimentally. Usui et al. suggested this was due to a deflecting workpiece and progressing damage zone as the fault; these factors are not conveyed with any basis. Zenia et al. developed 3D orthogonal and drilling models with an elasto-plastic damage model applied in the transverse and in-plane shear. This was accomplished by a VUMAT, that predicts interply damage and chip formation [130].Giasin et al. created a 3D drilling model of a hybrid material made of stacked glass fibre/epoxy prepreg with aluminum sheets. The model predicted torque within 0.83-17.9% and thrust force within 3.2-53.2% [49]. The FE model provided torque measurment within 18% and thrust within 52%. Isbilir et al. used the Johnson-Cook constitutive model to simulate the drilling of Titanium alloy (Ti6Al4V) to successfully predicted thrust force, reasonably predict torque, but was not able to capture the burr height [131].

2.3.5 Framework for experiments and FE analysis

A description of the current practices in experiments and modelling has been outlined. CFRP composite constituents, manufacturing process, assemblies and maintenance continue to improve. At the same time, demand and application of CFRP increases. Efficient material characterization is a necessity, requiring continual research and development for more effective means. Orthogonal cutting models have been extensively covered in literature due to the comparative simplicity versus a 3D machining process and reduced computational demand when modelling. The isotropic nature of metals reduces complexity of experimental testing and finite element modelling, leading to an accelerated progression of modelling techniques including Eulerian, Lagrangian, Adaptive-Lagrangian-Eulerian (ALE), Coupled-Eulerian-Lagrangian, and mesh-free techniques including smoothed-particle-hydrodynamics (SPH). The orthotropic nature of CFRP composites increases complexity in material characterization and testing. Drilling experiments have been investigated, determining ideal cutting parameters, coatings, coolants, tool design and have led to the development of analytical models and techniques to prevent delamination and improve hole quality. Assembly requirements of Stack-ups involving the layering of CFRP with aluminum and titanium, in various configurations, has lead to the development of one-shot drilling analyses. To develop an effective one-shot-drilling process through a multi-material layup, research is needed to synergize the copious amount of knowledge across these areas to develop an effective meso-scale predictive model.

Author	FE Scale			Analysis
	Micro	Meso	Macro	
Mehar et al. [82]		x		Fibre content vs. orientation tensile test (FE & exp.) (damage and CZM not discussed)
Krishnamoorthy, K. & Sasikumar, T. [75]			x	FE tabbed tensile tests (exp.) (damage and CZM not discussed)
Zitoune et al. [132]				Behaviour of drilled versus moulded holes in UD-CFRP (exp.)
Nirbhay et al. [41]		x		Cross-ply FE tensile tests (damage and CZM not discussed)
Wong et al. [78]		x		Anti-symmetric cross-ply CFRP tensile test w/ CZM & damage
Sadeghian et al. [83]				Nonlinear behaviour of cross-ply layups in tensile testing configuration (exp.)
Belingardi et al. [85]				Tab vs. tensile strength (exp.)
Faulstich de Paiva et al. [84]				Tensile testing of woven CFRP laminates (exp.)
Zappalorto, M. & Carraro, P.A. [87]				Analytical formulation for stress concentration in tension
Shahbazi, M. [37]		x		Notched composite laminates interface damage modelling (exp.)
Hallett, S. & Wisno, M.R. [133, 88]				2D cross-ply notched tensile tests (FE & exp.)
Arcan et al. [91]				Disc geometry for plane-stress states for FRP (exp.)
Nikbakht, M. & Choupani, N. [94]		x		Interlaminar fracture toughness using Arcan geometry (FE & exp.)
El-Hajjar, R. & Haj-Ali, R. [92]				Modified Arcan for thick-section in-plane shear (exp.)
Lapczyk, I. & Hurtado, J.A. [90]		x		FE blunt notched tensile loading w/ CZM using crack band model (exp. [134])
Kwon et al. [95]				Analytical prediction model of strain rate on tensile properties (exp.)
Gilioli et al. [135]		x	x	Macro, meso & meso w/ CZM tensile tests on CFRP (FE & exp.)
Iannucci et al. [136]		x		Thickness effect on tensile strength with interface CZM (FE & exp.)

Author	FE Scale			Analysis
Naresh et al. [69]				Shear (ILSS) and bending experiments UD & cross-ply (exp.) versus analytical CLT
Ullah et al. [34, 55]		x		2D large-deflection bending of woven CFRP with CZE (exp.)
Daghigh et al. [42]			x	Tensile and 3 pt. bending w/o interface CZM (FE vs. exp. from literature)
Marzi et al. [137]		x		Reinforced double cantilever beam & reinforced tapered end-notched flexure tests for interlaminar strength determination (FE & exp.)
Azzam, A. Li, W. [96]				3 pt. bending of cross-ply CFRP (exp).
Chen et al. [43]			x	3-point bending (FE)
Helali et al. [97]		x	x	Tensile and bending configuration comparing average vs. complete layup (FE & exp.)
Huang et al. [99]			x	3 pt. bending w CZE (FE, no exp.)
Petrescu et al/ [102]				3 pt. bending at varrious span lengths to determine flexural modulus (exp.)
Niezgoda, T. & Derewońko, A. [38]	x	x		3 pt. bending multi-scale (FE & exp.)
Mujika, F. [103]				Analytical 3 pt. vs. 4 pt. bending test correction (exp.)
Akram et al. [138]	x			2D JC-orthogonal cutting on Al 6061-T6 (FE & exp.)
Ng, E. & Aspinwall, D.K. [139]	x			2D JC-orthogonal cutting on AISI H13 (FE & exp.)
Jomaa et al. [18]	x			HSM 2D JC-orthogonal AL-AA7075-T651 (FE. vs exp.)
Roy et al. [140]				Feed rate effect on orthogonal UD-CFRP (90°) cutting experiments (exp.)
Bhatnagar et al. [108]		x		Iosipescu shear & orthogonal cutting (exp.)
Koplev et al. [19]				UD-orthogonal w/ quick-stop (exp.)

Author	FE Scale			Analysis
Gobivel et al. [45, 126]			x	Macro 2d orthogonal cutting CFRP w/o interface modelling (FE & exp.)
Mahdi, M. & Zhang, L. [50]		x		2D orthogonal cutting w/ user-defined constitutive model (FE & exp.)
Lasri et al. [127]		x		2D orthogonal cutting w/ alternative failure criteria (FE vs. exp. from literature)
Arola, D. & Ramulu, M. [20]	x			2D orthogonal (FE. vs exp.)
Sakuma, K. & Masafumi, S. [21]				UD-orthogonal GFRP (exp.)
Nayak, D. [141, 142]	x		x	2D UD-orthogonal (FE vs. exp.)
Abena et al. [125]			x	2D orthogonal cutting of UD-CFRP w/ CZM interface (FE & exp.)
He et al. [129]		x		3D orthogonal cutting of UD-CFRP w/o CZM interface; damage initiation present, no chip evolution (FE & exp.)
Alaiji et al. [52]		x		3D orthogonal cutting of UD-CFRP; damage initiation present, no chip evolution (FE & exp.)
Dandekar, C.R. & Shin, Y.C. [44]	x			2D orthogonal cutting of UD-CFRP with CZM interface and fibre VUMAT (FE & exp.)
Xu, J. & El Mansori, M. [143]	x			CFRP/Ti orthogonal cutting model with affected interface zone (FE & exp.)
Wang et al. [144]			x	3D orthogonal cutting of UD-CFRP (FE & exp.)
Shchurov et al. [145]		x		Smoothed particle hydrodynamics 3D orthogonal cutting of 4340 alloy-steel, AL6061-T5 composite (FE vs. exp. from literature)
Kim, D. & Ramulu, M. [26]				Drilling graphite bismaleimide titanium stacks (exp.)
Shyha, I.S.E.M. [11, 112, 122, 123]				UD & woven multi-tool drilling (exp.)
Ducobu et al. [54]		x		3D orthogonal cutting of Ti6Al4V using CEL model (exp.)

Author	FE Scale			Analysis
Garrick, R. [9]				Drilling with PCD, CFRP/Ti (exp.)
Ho-Cheng, H. & Dharan, C.K.H. [24]				Analytical delamination when drilling
Iliescu et al. [25]				Phenomenological model of thrust force vs. tool life (exp.)
Teti, R. [6]				Composites machining review
Lissek et al. [106]				Drilling induced delamination qualification (exp.)
Gao et al. [47]				3D drilling CFRP using plastic deformation model
Merino-Pérez et al. [111]				Cutting speed and constituents vs forces in drilling CFRP (exp.)
Karpat, Y. & Bahtiyar, O. [113]				CFRP drill geometry analysis (exp.)
Wang et al. [114]				Coated carbide drills tool wear vs. drilling forces (exp.)
Faraz et al [115]				Cutting edge rounding tool wear criterion drilling CFRP (exp.)
Jain, S. & Yang, D.C.H. [118]				Analytical expressions determine subcritical thrust force for delamination free CFRP drilling; incorporates variable, stepped-down feed rate through thickness (exp.)
Won, M.S. & Dharan, C.K.H. [116]				Analytical model for delamination reduction using pilot hole advantage when drilling CFRP (exp.)
Zitoune et al. [120]				Process parameters drilling CFRP/AL stack (exp.)
Brinksmeier, E. & Janssen, R. [121]				Process parameter optimization of CFRP/Ti/AL drilling with multi-tool geometry (exp.)
Kahwash et al. [124]				FRP composite machining modelling review
Zhang et al. [146]				Exit defect assessment when drilling CFRP (exp.)
Eneyew, E. & Ramulu, M. [147]				Hole quality assessment when drilling UD-CFRP (exp.)

Author	FE Scale			Analysis
Isbilir, O. & Ghassemieh, E. [131]			x	3D drilling of Titanium alloy (Ti6Al4V) (FE & exp.)
Abdelhafeez et al. [58]		x		3D CEL drilling of titanium & aluminum stack (FE & exp.)
Debnath et al. [148]				Innovative tool design for drilling CFRP (exp.)
Chakrapani, P. & Sekar, V. [149, 51]			x	Friction coefficient and failure model influence on 3D drilling of GFRP (FE & exp.)
Giasin et al [53]			x	3D drilling of AL2024-T3 using JC (FE & exp.)
Giasin et al. [49]		x		3D drilling of GLARE (fibre-metal) laminate w/ CZM (FE & exp.)
Zenia et al. [130]		x		2D & 3D orthogonal & drilling of CFRP w/ CZM (FE & exp.)
Usui et al. [46]		x		3D orthogonal w/ CZM & drilling of CFRP (FE & exp.)
Phadnis et al. [150]		x		FE CFRP/AL drilling model (no interface/CZM) (FE & exp.)
Phadnis et al. [128]	x			FE CFRP drilling model w/ interface/CZM (FE & exp.)

Chapter 3

Non-linear material characterization of CFRP with FEM utilizing cohesive surface considerations validated with effective tensile test fixturing

Complete citation:

P. Hale and E. Ng. "Non-linear material characterization of CFRP with FEM utilizing cohesive surface considerations validated with effective tensile test fixturing". In: Materials Today Communications 23 (2020). pp 1-15.

Non-linear material characterization of CFRP with FEM utilizing cohesive surface considerations validated with effective tensile test fixturing

This chapter is a copy of the paper published in *Materials Today Communications* journal. This paper evaluates modelling considerations for accuracy, regarding material characterization of CFRP with varying fiber orientations with respect to loading and thickness. The paper describes an improved fixturing tool for the experiments, that is incorporated into the simulations, which more accurately predicts the experiments. A key aspect outlined in the paper is the inclusion of cohesive surfaces between ply instances that better predicts the nonlinear loading response observed of the CFRP laminates.

Authors: Patrick Hale, Eu-gene Ng

Submitted to the *Materials Today Communications* journal

Published December, 2019

Abstract

Modelling the effect of fibre orientation in carbon fibre reinforced plastic (CFRP) on mechanical behavior is critical for component design and manufacturing process optimization. The objectives of this paper are to simulate the mechanical properties of CFRP to fracture and design a tensile test rig that could induce fracture at the specimen gauge section consistently. Finite element solver ABAQUS Explicit was used to simulate the effects of mass/time scaling, different failure models and cohesive surfaces. Failure models evaluated were Hashin, MCT, LaRC02, maximum strain, Tsai-Wu, Tsai-Hill, Christensen and Puck. The fibre orientations investigated were parallel, 45° and perpendicular to the tensile loading condition. Extensive design of the tensile test rig was briefly described. Experimental results showed that with the newly designed test rig, the failure occurred in the gauge region, regardless of the fibre orientation. When the fibre orientation was parallel to the tensile load, all the failure models show similar rate of force increment with respect to displacement. Puck's failure model most accurately predicts the fracture force and displacement versus experimental data. With fibre orientations at 45° and 90°, the maximum strain and LaRCO2 failure models were more suitable in terms of accuracy and simulation convergence. Incorporating cohesive surfaces between instances to predict nonlinearity in the loading response is critical. Significant reduction in failure force was predicted when test was setup at angles between parallel to 45°. The model was capable of predicting the effects of fibre orientation and laminate thickness on fracture force agreeing with published experimental results.

3.1 Introduction

In automotive and aerospace industries the interaction of different material components during assembly may require drilling holes to facilitate bolting sections together. Stack-Ups are laminated carbon fibre reinforced polymers (CFRP) generally by aluminum and/or titanium sections. Due to the different fracture mechanics for each material, the drilling of these through holes is no easy task. Prior to the Finite Element Modelling (FEM) work on Stack-Ups, the CFRP is effectively modelled in tensile and bending setups to accurately and efficiently predict material response and failure in common modes.

Time consuming and costly testing is required to determine material parameters used to accurately represent a CFRP sample for design calculations and end use. To avoid purposeless testing many researchers have adapted the Association for Testing Materials (ASTM) D3039/D3039M-17 geometry when determining material strengths. Nirbhay et al. and Krishnamoorthy studied different FEM modelling setups using this geometry [1, 2]. Creatively in 1977, Arcan developed a unique disc geometry that when loaded in tension, at various angles with respect to the primary fibre direction and could determine principal material stresses [3]. The original geometry required significant material per test and was therefore modified to a reduced size. Hajjar and Haj-Ali used a modified Arcan fixture to determine shear stiffness and its non-linear stress-strain response [4]. Work developed further using this geometry to determine energy based fracture toughness and complex 3D behaviour [5, 6]. Alternatively Hallett and Wisnom modelled progressive damage using a notched geometry to control and correlate failure at the notch [7]. Lapczyk and Hutado studied a damage evolution law based on Hashin's work for initiation and an energy based damage evolution to predict notch sensitivity [8]. Despite the ideal material properties of a CFRP composite they are quite susceptible to damage caused during manufacturing, assembly, or in service. Zappalorto and Carraro worked to quantify the stress concentration factor of orthotropic plates, thus improving the understanding of notch sensitivity and controlling the location of failure [9].

The ASTM standardized tensile test method for polymer matrix composite materials, inclusive of CFRP, is designation D3039/D3039M-17 [10]. The designated acceptable failure locations by ASTM are shown in Figure 3.1. Many modes of failure illustrated are not useful if the measurement tools are not capturing the failure in the chosen gauge section; any failure that is not designated with a second character Gage (G) would be outside the intended failure region and unable to capture the strain at failure. Authors commonly describe the damage first initiating in the tabbed region rather than the intended gauge region [11, 12]. Coguill and Adams studied tabs and specimen geometry extensively describing no one specimen configuration can be optimal for ultimate tensile performance of unidirectional specimens [13]. Numerous fixturing techniques and sample geometries have been studied including rectangular, wishbone, notched and the disc geometry created by Arcan.

Experimentally, the tensile tests used a standard planar wishbone specimen as referenced from ASTM E 8/E 8M using the sheet-type for serrated wedge grips; referred to as *Geometry I* [14]. When unidirectional (UD) CFRP is loaded parallel to the fibres in a tensile test, the loads experienced can be ten orders greater than when loaded perpendicular to the fibre. Significant gripping pressure is required for these tests to prevent slipping during the loading, frequently resulting in compressive damage on the CFRP samples in the gripping area prior to failure in the gauge

First Character

Failure Type	Code
Angled	A
Edge delamination	D
Grip/tab	G
Lateral	L
Multi-mode	M(xyz)
Long splitting	S
Explosive	X
Other	O

Second Character

Failure Type	Code
Inside grip/tab	I
At grip/tab	A
<1W from grip/tab	W
Gage	G
Multiple areas	M
Various	V
Unknown	U

Third Character

Failure Type	Code
Bottom	B
Top	T
Left	L
Right	R
Middle	M
Various	V
Unknown	U

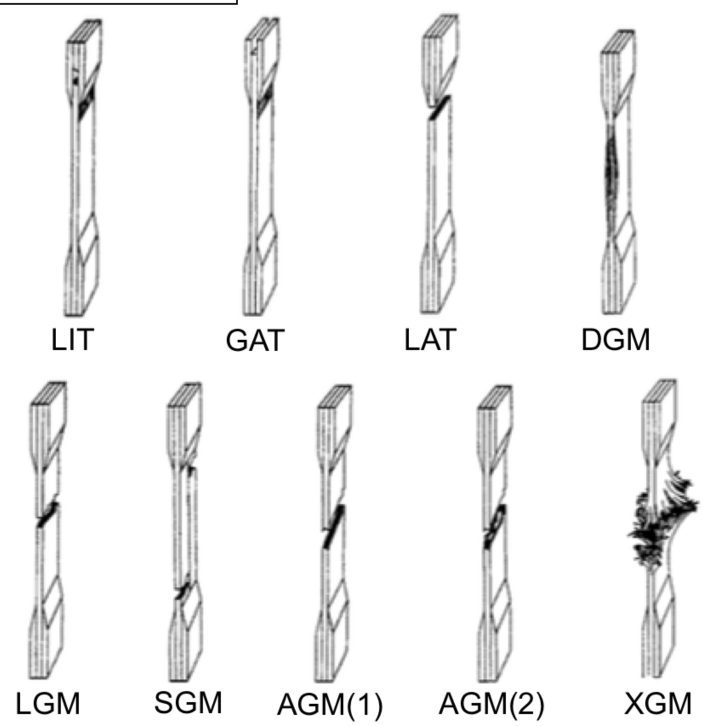

Figure 3.1: Tensile test failure codes [10]

region. Continuing further, the wishbone geometry was exaggerated, to control failure location in the intended location, after noticing a geometry Kobayashi et al. used when testing carbon composite strengths at high temperatures [15]. As a result, a newly designed gripping method was developed to induce compressive forces on critical sections in the gripping regions, yet not induce damage and greatly improve consistency of the fracture tests.

FE modelling of fibre reinforced polymers (FRP's) hinges on the failure model developed by Hashin [16] that encompasses of four failure modes, which are i) matrix tension, ii) matrix compression, iii) fibre tension and iv) fibre compression failure. Significant work has developed numerous other failure models including LaRC02 [17], Max Strain, Max Stress, Tsai-Wu [18], Tsai-Hill [19], Christensen [20], Puck [21] and a Multi-Continuum Theory (MCT) [22] failure criterion, which are described in Table 4.1.

The ABAQUS damage initiation model, based on Hashin's failure criteria, requires the i) longitudinal tensile and compressive strength, ii) the transverse tensile and compressive strength and iii) the longitudinal and transverse shear strength. It also requires a variable alpha, which is the contribution of the shear strength to the fibre tensile failure mode as modified in Hashin [3].

Table 3.1: Failure models and criterion for FRP composites

Model	Failure model modes	
Hashin	Fibre Tension (F.T.)	$\left(\frac{\sigma_{11}}{S_{11}^{+}}\right)^2 + \alpha\left(\frac{\sigma_{12}^2+\sigma_{13}^2}{S_{12}^2}\right) \geq 1.0$
	Fibre Compression (F.C.)	$\left(\frac{\sigma_{11}}{S_{11}^{-}}\right)^2 \geq 1.0$
	Matrix Tension (M.T.)	$\frac{(\sigma_{22}+\sigma_{33})^2}{(S_{22}^{+})^2} + \frac{\sigma_{23}^2-\sigma_{22}\sigma_{33}}{S_{23}^2} + \frac{\sigma_{12}^2+\sigma_{13}^2}{S_{12}^2} \geq 1.0$
	Matrix Compression (M.C.)	$\left[\left(\frac{S_{22}^{-}}{2S_{23}}\right)^2 - 1\right]\left(\frac{\sigma_{22}+\sigma_{33}}{S_{22}^{-}}\right) + \frac{(\sigma_{22}+\sigma_{33})^2}{4S_{23}^2} + \dots$ $\dots + \frac{\sigma_{23}^2-\sigma_{22}\sigma_{33}}{S_{23}^2} + \frac{\sigma_{12}^2+\sigma_{13}^2}{S_{12}^2} \geq 1.0$
MCT	Fibre	$\pm A_1^f (I_f^1)^2 + A_4^f I_4^f = 1$ $I_1^f = \sigma_{11}^f$ $I_4^f = (\sigma_{12}^f)^2 + (\sigma_{13}^f)^2$
	Matrix	$\pm A_1^m (I_1^m)^2 - \pm A_2^m (I_2^m)^2 + A_3^m I_3^m + \dots$ $\dots + A_4^m I_4^m - \pm A_5^m I_1^m I_2^m = 1$ $I_1^m \equiv \sigma_{11}^m$ $I_2^m \equiv \sigma_{22}^m + \sigma_{33}^m$ $I_3^m \equiv (\sigma_{22}^m)^2 + (\sigma_{33}^m)^2 + 2(\sigma_{23}^m)^2$ $I_4^m \equiv (\sigma_{12}^m)^2 + (\sigma_{13}^m)^2$
LaRC02	F.T.	$FI_F = \frac{\epsilon_{11}}{\epsilon_1^T}, \epsilon_1^T = \frac{X^T}{E_{11}}$
	F. C. with M. C.	$FI_F = \left(\frac{\sigma_{22}^m}{Y^T}\right)^2 \left(\frac{\tau_{12}^m}{S^L}\right)^2$
	F. C. with M. T.	$FI_F = \left\langle \frac{\lvert\tau_{12}^m\rvert + \eta^L \sigma_{22}^m}{S^L} \right\rangle$
	M. T.	$FI_M = \left(\frac{\sigma_{22}}{Y^T}\right)^2 + \left(\frac{\tau_{12}}{S^L}\right)^2$
	M. C.	$FI_M = \left(\frac{\tau_{eff}^T}{S^T}\right)^2 + \left(\frac{\tau_{eff}^L}{S^L}\right)^2$
	M. Biaxial C.	$FI_M = \left(\frac{\tau_{eff}^m{}^T}{S^T}\right)^2 + \left(\frac{\tau_{eff}^m{}^L}{S^L}\right)^2$
Puck	Fibre Tension	$\frac{1}{\epsilon_{1T}}\left(\epsilon_1 + \frac{v_{f12}}{E_{f1}} m_{\sigma f}\sigma_2\right) = 1$
	Fibre Kinking	$\frac{1}{\epsilon_{1T}}\left(\epsilon_1 + \frac{v_{f12}}{E_{f1}} m_{\sigma f}\sigma_2\right) = 1 - (10\gamma_{21})^2$
	Inter-Fibre Failure A.	$\sqrt{\left(\frac{\tau_{21}}{S_{21}}\right)^2 + \left(1 - p_{\perp\vert\vert}^{(+)} \frac{Y_T}{S_{21}}\right)^2 \left(\frac{\sigma_2}{Y_T}\right)^2} + \dots$ $\dots + p_{\perp\vert\vert}^{(+)} \frac{\sigma_2}{S_{21}} = 1 - \left\lvert \frac{\sigma_1}{\sigma_{1D}} \right\rvert$
	Inter-Fibre Failure B.	$\frac{1}{S_{21}}\left(\sqrt{\left(\tau_{21}^2 + \left(p_{\perp\vert\vert}^{(-)}\sigma_2\right)^2} + p_{\perp\vert\vert}^{(-)} \frac{\sigma_2}{S_{21}}\right) = 1 - \left\lvert \frac{\sigma_1}{\sigma_{1D}} \right\rvert$
	Inter-Fibre Failure C.	$\frac{1}{\left(2\left(1+p_{\perp\perp}^{(-)}\right)\right)}\left(\left(\frac{\tau_{21}}{S_{21}}\right)^2 + \left(\frac{\sigma_2}{R_{\perp\perp}^A}\right)^2\right)\frac{R_{\perp\perp}^A}{(-\sigma_2)} = 1 - \left\lvert \frac{\sigma_1}{\sigma_{1D}} \right\rvert$
Max Strain	$\left(\frac{\epsilon_{11}}{\epsilon_{11}^{max+}}, \frac{\epsilon_{11}}{\epsilon_{11}^{max-}}, \frac{\epsilon_{22}}{\epsilon_{22}^{max+}}, \frac{\epsilon_{22}}{\epsilon_{22}^{max-}}, \frac{\epsilon_{12}}{\epsilon_{12}^{max-}}\right) \geq 1.0$	

A macro-mechanical approach treats the FRP as an equivalent homogeneous material (EHM). In the past EHM models were not able to identify material constituents' damage nor fibre-matrix interactions however with Multi-Continuum Theory (MCT) EHM model capabilities have increased. The composite stress state within the representative volume element (RVE) are calculated and are critical to predict damage and material failure versus a homogenized average stress and strain. LARC02 identifies fibre failure and matrix cracking in UD composites using six failure modes, which are i) fibre failure in tension, ii) fibre compressive failure with matrix compression, iii) fibre compression failure with matrix tension, iv) matrix tension, v) matrix compression and vi) matrix experiencing biaxial compression. Most significant, once any of the six failure indices are greater than 1.0, the fibre or matrix has failed. This facilitates element deletion and model convergence in transverse loading conditions. Tsai-Wu and Tsai-Hill are quadratic, stress-based criterion that do not distinguish between failure modes; Tsai-Hill formulation gives more emphasis on the shear contribution. During matrix dominated loading a small contribution of stress to the overall failure strength can cause damage evolution convergence issues. The Christensen criterion utilizes the six fundamental strengths of the composite material to identify two different failure modes in the matrix and fibre. The Puck criterion identifies fibre failure and inter-fibre failure in a unidirectional composite. The inter-fibre failure is the formulation for the matrix damage depending on the plane of loading. In ABAQUS, to utilize failure criteria alternative to the built-in Hashin method for FRP's, a user-defined material subroutine must be implemented. This can be accomplished using Helius Progressive Failure Analysis (PFA) software.

In this study, repeatable, accurate experimental tensile testing is achieved via an effectively redesigned fixture for FRP tensile tests. A thorough parametric study was conducted to effectively model a CFRP composite using commercial finite element software ABAQUS. A sensitivity analysis regarding element type, mesh convergence, scaling techniques, damage initiation and evolution methods were studied with limitations described. Convergence of damage evolution dominated by transverse loading was determined to be limited to specific failure models. The significance of modelling multiple ply layups using cohesive surface interactions demonstrates the ability to capture the nonlinear loading response of the sample when loaded in various fibre orientations.

3.2 Experimental Work

The UD CFRP samples were machined from sheets made by ACP Composites Inc. The manufacturer mechanical properties are described in Table 3.2. These are produced using an Autoclave curing process at high temperature and pressure to ensure a repeatable, high-quality panel with minimal voids, waves or buildups. The CFRP is made from a pre-impregnated unidirectional layup with 60% fibre volume.

Table 3.2: Standard Modulus (SM) CFRP - material properties [23]

SM UD CFRP	0°	90°
Longitudinal Modulus (GPa)	135	10
Transverse Modulus (GPa)	10	135
In-plane Shear Modulus (GPa)	5	5
Major Poisson's ratio	0.3	0.3
Ultimate (Ult.) Tensile Strength (MPa)	1500	50
Ult. Comp. Strength (MPa)	1200	250
Ult. In-plane Shear Strength (MPa)	70	70
Ult. Tensile Strain	1.05	0.5
Ult. Comp. Strain	0.85	2.5
Density (g/cm^3)	1.6	

All CFRP samples and the machining of the fixturing was completed in house on a 3-axis HAAS CNC mill. The CFRP samples were machined with a Kennametal down-cut style, 6 flute, diamond coated endmill. Standard 2-flute, high-helix carbide endmills were used for machining aluminum. The UD CFRP was purchased in 12"x36" panels and machined further into repeatable 6"x6" sections. The sections were aligned with the HAAS axis and then machined at 0°, 45° and 90° to minimize any variability in sample fibre direction.

Preliminary tensile tests found inconsistencies with the failure location of the standard tensile test geometry. Regardless of the carbon fibre orientation, the fracture did not occur within the gauge area, as shown in Figure 3.2 a). Common serrated wedge grips unfortunately induce concentrated compressive damage on the sample due to the significant gripping force required when loading the CFRP samples to fracture. ASTM-D3039 describes adding tabs as needed [10]. An exhaustive 74 page report titled Tabbing Guide for Composite Test Specimens exists to provide information regarding tab design and application [24]. Tab materials must be selected with great consideration to adhesion and toughness versus stiffness that will lead to nonlinearity in response [25]. Mehar et al. describes tab design as an art that affects coupon strength [26]. Sadeghian et al. uses epoxy tabs to prevent premature failure near coupon ends [27] although others note steel, aluminum, carbon fibre and epoxy as possible options [28, 29]. UD fibre reinforced polymers (FRP) are susceptible to notch sensitivity due to the great longitudinal strength, but comparatively low shear strength. Extensive design work and experiments were preformed to improve the fixturing and sample geometry to improve repeatability of the tensile tests while avoiding tabs.

A NASA supported report by Worthem tested five geometries to reduce stresses leading to unintended failure between the gauge section and the tab region [25]. To prevent this, a newly designed gripping method was developed to induce compressive forces on critical sections in the gripping regions, yet not induce damage and greatly improved consistency in fracture tests, shown in Figure 3.3 a) and b). The new fixturing jig was designed to position the samples for a tensile test while inducing compressive stress on the radius of curvature. The ratio of grip width to gauge width was increased in the modified geometry from 3:2 to 4:1. The sample gauge width in Geometry I was 12.5 mm. In Geometry II and III it is 4.76 mm with a grip width four times that. The radius of curvature to gauge width ratio was increased from 1:1 to 4:1. The intention is to drastically reduce the effect of the grips on the failure of the tensile specimen. This was accomplished by promoting failure in the gauge area, at a decreased load, with a reduction in stress concentrations near the radius. Details of Geometry III is shown in Figure 3.2 c).

The new jig design is made of Aluminum and positions the sample parallel to the loading direction. Rather than using common serrated wedge grips that induce significant concentrated compressive damage on the sample, the sample naturally sits in the jig and is subject to a progressive compressive force on the arced region as it is loaded in tension. UD fibre reinforced polymers (FRP) are susceptible to notch sensitivity due to the great longitudinal strength, but comparatively low shear strength. Most revolutionary, the new jig helps prevent premature failure due to the notch sensitivity by subjecting this region to compressive forces in the arced regions.

The geometry III specimens, with use of the new jig, demonstrated improved consistency in fracture, shown in Figure 3.3 c). The sample geometry and new fixturing allowed for the Aramis camera to capture strain to failure and the force-displacement results were repeatable. Inspired by improvements of the modified geometry and

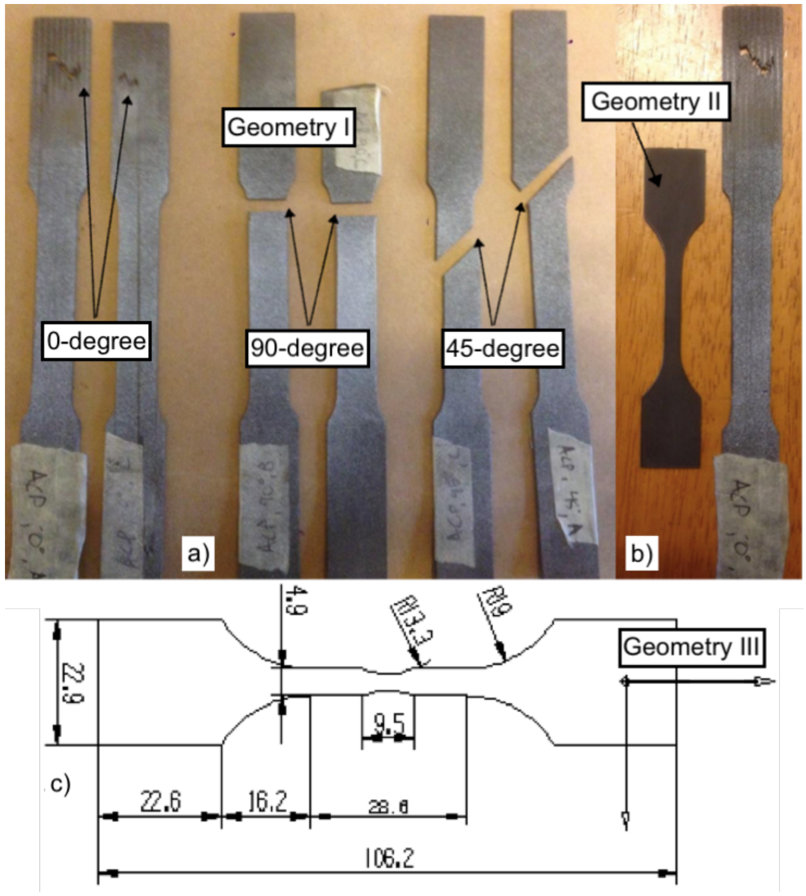

Figure 3.2: a) Standard tensile test failure inconsistencies b) Geometry II comparison c) Geometry III schematic

notched tensile tests described in literature [3] a specific notch radius was machined into new samples in the gauge region. The geometry was modified to promote a more specific failure location by including a notched region in the gauge section. This directly focused failure in the desired locations and improved consistency of the material results further.

The 0°, 45°and 90° samples were tested five times to ensure repeatability and the results were averaged. These tests were previously completed for the original wishbone ASTM geometry and the initial modified geometry is shown in Figure 3.2

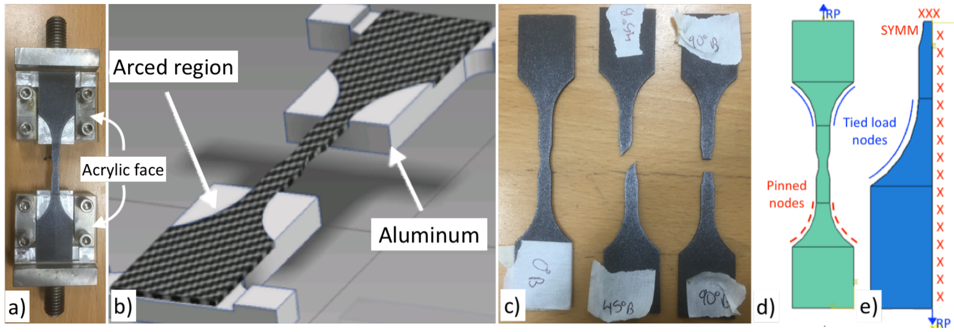

Figure 3.3: a) New tensile jig setup b) CAD - CFRP positioned in grips c) Geometry III: 0°, 45°, 90° fractures d) Full FE model e) 1/4 FE model used with cohesive surface modelling

b), prior to *Geometry III* as detailed in Figure 3.2 c). The tensile tests were loaded into the Instron Dual Column Universal Testing system and loaded at a separation of 0.25 mm/min. Displacement accuracy is the greater of ± 0.02 mm or 0.15% of displacement. Load accuracy is ± 0.5% of reading down to 1/200 of load cell capacity, ± 1.0% of reading from 1/200 to 1/500 of the load cell capacity [30]. The 90° samples average failure was recorded at 155N which is between the 1/200 to 1/500 of the load capacity range and therefore the latter of the accuracies applies. Strain was measured using digital image correlation (DIC), a technique that uses a high speed camera to trace particular points on the samples surface; points randomly distributed by spraying the sample with a white speckled paint. Using the commercial digital correlation software, produced by Aramis, the strain is calculated. The two cameras - offering 3D surface imaging - record surface strain at 6 megapixel and 25 Hz with a minimum measurement area or 10x8 mm [31].

3.3 FE modelling considerations

To represent a fibre reinforced polymer in FEA using ABAQUS requires density, elastic properties and damage modelled by Hashin's four failure criteria. Furthermore a VUMAT module was used to model other failure criteria. For anisotropic fibre reinforced composites, ABAQUS models damage by an initiation and evolution criteria. Generally, CFRP materials exhibit elastic-brittle behaviour and four failures are considered with Hashin's damage mode, which are i) fibre rupture in tension, ii) fibre buckling and kinking in compression, iii) matrix cracking and transverse tensions and shearing, and iv) matrix crushing under transverse compression and shear.

Table 3.3: Comprehensive FEA modelling analysis

Study	Parameter/Cases
Phase I - Through thickness	Number of elements through thickness of sample 1, 2, 3, 4, 5, 6
Phase II - Scaling	Mass scaling - Modifying minimum time step increment 1e-2, 1e-3, 1e-4, 1e-5, 1e-6, none Time sclaing - Modifying analysis duration and loading rate 1x, 10x, 100x, 100x*
Phase III - Failure models	ABAQUS-Hashin 0°, 45°& 90° VUMAT (Puck, MCT, LaRC02, Chris., Max Strain, Hashin) 0°, 45°& 90°
Phase IV - Cohesive surfaces	MAXS damage init. & displacement damage evol. 0°, 45°& 90°

Variables	Phase I	Phase II-A	Phase II-B	Phase III	Phase IV
Through thickness	In Study	4	4	Failure model	Cohesive model
Mass scaling	1.0e-4	In Study	5.e-5		
Time scaling	10x	10x	In Study		
Initial model settings	MCT failure criterion with damage evolution based on instantaneous degradation using 10% time delay. All other model parameters described earlier are maintained throughout study unless identified.				

The model utilizes ABAQUS' Explicit solver with boundary conditions applied to the arced surfaces of the tensile geometry, as shown in Figure 3.3 d). At one end, the pair of arced surfaces are pinned (dashed line) and cannot translate. At the other end the velocity constraint replicating the tensile test extension of 0.25 mm/min longitudinally is applied. In the quarter symmetry model, which is used later with cohesive surface modelling for computational benefit, symmetric boundary conditions are applied in the XY and YZ planes, as shown in Figure 3.3 e).

The velocity is applied to the reference node (RP) and a tied equation constraint is used to transfer the velocity and thereby displacement of the reference node to the arced regions, which was similar to the experimental loading condition with the new fixtures shown in Figure 3.3 a). This avoids any contact interactions between rigid body members representing the fixturing and the tensile geometry, which allows for more efficient output of resulting forces and displacements via the one reference node. The analysis used continuum shell elements (SC8R), which are 8-node quadrilateral in-plane general purpose elements, with reduced integration and enhanced hourglass control. The plane stress assumption is accurately made with use of fibre-reinforced composites. The planar geometry is thin with stress acting along its plane and the ply layup amplifies this, dividing the planar geometry into ten thinner planar sections. Material failure is assumed to be dominated by longitudinal (fibre), transverse (matrix) and in-plane shear strengths and not in the tertiary (thickness) axis. To achieve accurate material representation regarding the through thickness geometry, solid or continuum shell elements should be used and not conventional shell elements. The reduced integration promotes computational efficiency by reducing the number of Gaussian co-ordinates when solving the numerical integration to calculate the stiffness matrix. With reduced integration, the stiffness of an element is reduced. To avoid distorted elements, hourglass control is used however this control adds additional artificial energy to the analysis and should be kept less than ten percent, in order to maintain realistic stiffness [32].

Failure models and progressive damage techniques were studied to determine the most effective with respect to accuracy of prediction, convergence and efficiency. Without convergence, FE models render useless for machining simulations as damage evolution and element deletion is a necessity. To develop an efficient base model before investigating the damage initiation and evolution capabilities of CFRP FE modelling, a parametric study isolated key modelling inputs individually, while all other model inputs were fixed. Table 4.3 describes the parameters investigated during each phase of analysis including i) number of through thickness elements, ii) mass scaling and time scaling iii) the study of the various failure models and iv) the incorporation of cohesive surface interactions between instances. Prior to carrying out Phase I, a mesh refinement analysis was carried out optimizing computational time in comparison to failure force prediction.

3.3.0.1 Phase I - Through thickness

To accurately model the ply interaction and progressive failure of the CFRP, certain considerations must be made including the number of through thickness elements used. In Figure 3.4, a mesh with 1 element and a mesh with six elements through the thickness of the sample is illustrated. The resulting computational expense of adding elements through the thickness of the geometry ranging from one to six was studied as shown in Table 4.3. By applying four elements in the through thickness region, a deviation of only 0.51% exists for the ultimate force prediction with a computational savings of 12 hours or 33% versus six elements being modelled through the thickness of the sample. Considering the experimental variation, a deviation in prediction of 0.51% is deemed acceptable.

3.3.0.2 Phase II - Scaling techniques

In ABAQUS, the minimum stable time increment for an explicit dynamic analysis is expressed in Equation 3.1.

$$\Delta t = L^e / c_d \ , \quad and \ \ c_d = \sqrt{\frac{E}{\rho}} \tag{3.1}$$

L^e is the characteristic length element and c_d is the dilatational wave speed of the material. E is the Young's modulus of the material and ρ is the density of the material [33]. To improve computational efficiency explicit dynamic models can utilize time scaling and mass scaling techniques. The dynamic effects induced by changing the loading time, or inertial effects resulting from increased density to increase the time increment, must remain insignificant. The benefit of employing mass scaling is the time step limit applies to the smallest elements first until satisfied and therefore if appropriately used will not have significant impact the results, just reduce the

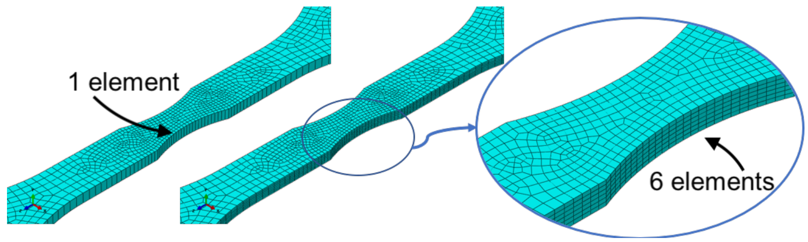

Figure 3.4: Through thickness: 1 versus 6 elements

computation time.

The loading response for the various mass scaling cases controlled by increasing the minimum time step (T.S.) in the explicit analysis. The ultimate failure force prediction was within 2.8% when using the 5.0e-4s minimum time step versus a 1.0e-4s minimum time step. Model computation time was 6.43 hours for the 5.0e-4s time step versus 24.98 hours for the 1.0e-4s time step. It is recommended to reduce the minimum time step to 1.0e-4s for final model evaluations to ensure the prediction accuracy, however for the continuation of the model parameters sensitivity study 5.0e-4s will suffice.

The effect of time scaling was studied involving an accelerated loading rate versus the 1 mm/min rate of the experiment. Figure 3.5 shows the effect of time scaling on the force-displacement response. The FEM tensile test time period was decreased from two minutes (120 s) to 1.2 s, which is a reduction of 100x. The velocity was manipulated to ensure an equivalent magnitude of displacement.

By reducing the loading time through time scaling, while maintaining an equivalent load displacement, a reduction in computation time from 47.29 hours to 0.52 hours can be achieved. The 1.2 s scaled model is greatly impacted by this time scaling, resulting in a difference in prediction by 9.06%, which was reduced to 3.62% for the 12.0 s setup. Shown in Figure 3.5, when time scaling is too significant as seen in the 1.2 second model, a harmonic wave propagates through the loading response. Similarly, when mass scaling was applied too aggressively a harmonic response developed. The mass scaling should be reduced to negate this response and can be achieved by reducing the mass scaling time step by half an order of magnitude (5.0e-4s to 1.0e-4s). The increased loading rate can cause damage to propagate through the sample and

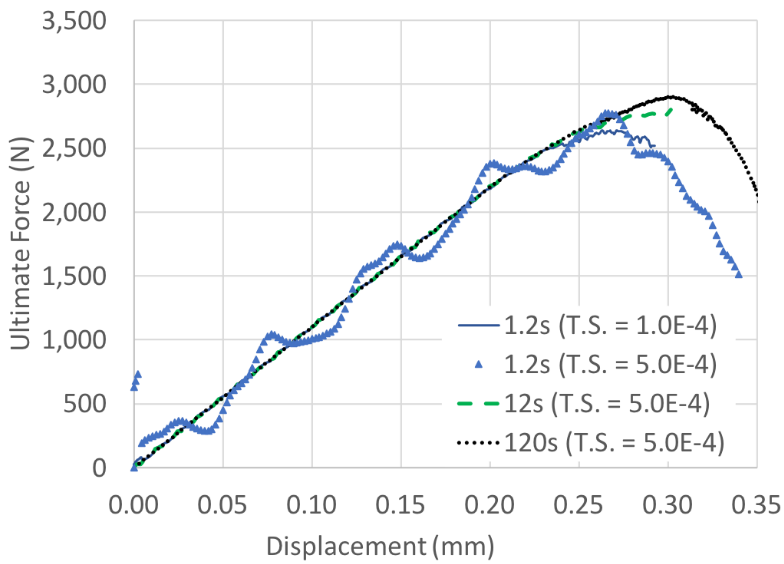

Figure 3.5: Time scaling load response

evolve prematurely.

Tensile and bending tests are regularly studied at low strain rates (0.001-0.0001 s^{-1}), however machining operations generally involve strain rates above $100s^{-1}$. Kwon et al. demonstrated the 0° tests having no sensitivity to strain rate [34]. The 90° samples demonstrate an increase of 53% in modulus and 80% in failure strength. For the 45° tests, a 50% increase in elastic modulus and 75% increase in failure strength. Further more, an increase in non-linearity was noticed. In this study, the CFRP material is modelled as linear-elastic, strain rate insensitive with material degradation. Viscoelsasticity is not considered as no experimental data was attained to verify this at this stage. The application of time scaling is investigated to utilize computational advantage with consideration to avoid altering the material response induced by strain rate dependency.

3.3.0.3 Phase III - Failure models

Using the criteria described regarding mesh refinement, through-thickness-elements, mass scaling and time scaling, an investigation was carried out to understand the effect of different damage initiation criteria. The initial response of a fibre reinforced composite material in ABAQUS is modelled as linear-elastic until the onset of damage. The effective stress tensor is used to evaluate the initiation of damage is shown in Equation 3.2.

$$\hat{\sigma} = M\sigma, \qquad and \;\; M = \begin{bmatrix} \frac{1}{(1-d_f)} & 0 & 0 \\ 0 & \frac{1}{(1-d_m)} & 0 \\ 0 & 0 & \frac{1}{(1-d_s)} \end{bmatrix} \tag{3.2}$$

where σ is the true stress and M is the damage operator. The internal damage variables for the fibre (d_f), the matrix (d_m) and shear (d_s) are determined from the damage variables outlined, depending on the specific failure criteria used. The failure models evaluated fit in two categories. The first, is built into the ABAQUS solver that uses Hashin's four failure modes: matrix tension, matrix compression, fibre tension, fibre compression. The second category requires a customized VUMAT subroutine utilizing Helius PFA and was used to model MCT, Hashin, Max Stress, Max Strain, Puck, Christensen and LaRC02. The initial loading responses up to 0.2 mm are quite similar to the experiment shown in Figure 3.6. The ABAQUS Hashin model illustrates an instantaneous failure resulting from a different set damage evolution parameters used in Abaqus. The Max Strain criteria is based on a ratio of current strain in relation to a critical strain and reaches the material limit prematurely. LaRC02, Tsai-Wu Tsai-Hill, Christensen, and MCT are all dependent on the stress in the fibre direction reaching the failure strength and therefore resemble one another. The Puck model involves the strain in the fibre direction, but also a contribution of the transverse stress and a transverse stress coefficient, resulting in a delayed progression of failure resulting in the most accurate prediction of the experiment. Failure models for unidirectional composites loaded parallel to fibres are efficient, as they control the material failure and element deletion. The differences and limitations of these models will be more clearly made when loaded in the shear and transverse directions when failure is controlled by the matrix damage progression.

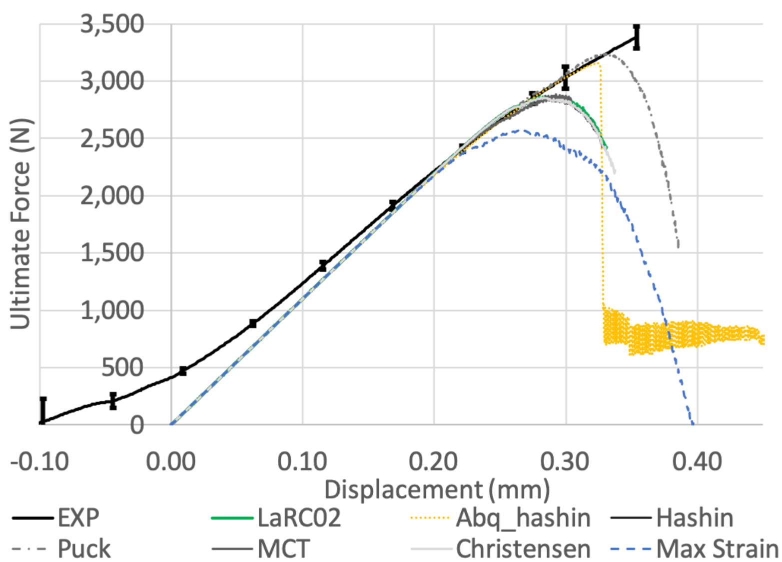

Figure 3.6: 0° failure model analysis

3.3.1 Phase IV - Cohesive surface modelling

To capture the nonlinear loading response of the CFRP, the tensile geometry is divided into multiple instances representing the plies of the CFRP. Between the instances cohesive surface interactions are created as shown in Figure 3.7. The tensile sample has a thickness of 1.1 mm and was divided into 10 sections to represent the ply thickness. In addition, node sets are created on the top and bottom surfaces to be used as cohesive interactions. Highlighted in Figure 3.7 is the ply 1 bottom surface and ply 2 top surface cohesive interaction. A General Contact explicit interaction must be created with included pairs set to All* with self [33]. To alleviate some of the computational expense brought on by the inclusion of cohesive surfaces, a quarter model utilizing symmetry in the YZ and YX planes was developed. After the symmetric boundary conditions were applied, a velocity condition was applied to a reference point, which was tied to a set of loading nodes as done with the full model.

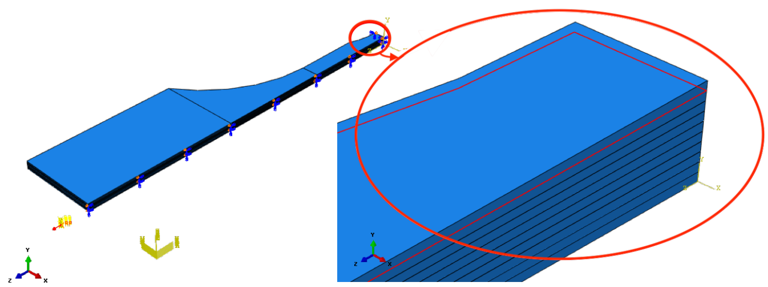

Figure 3.7: 1/4 tensile model with cohesive surfaces

To model the cohesive surfaces, a contact property must be created and include three main properties, which are normal behaviour, cohesive behaviour and damage. Normal behaviour determines the contact behaviour in the normal direction and is controlled by the “hard" contact pressure overclosure relationship. The cohesive behaviour allows for any slave nodes that experience contact, whether initially or after some loading, to be controlled by a traction-separation behaviour. The most computationally efficient method in ABAQUS is to have an uncoupled behaviour using stiffness in the normal, secondary and tertiary axis (K_{nn}, K_{ss} and K_{tt}) and the separations in the normal, first shear and secondary shear are denoted by δ_n, δ_s and δ_t respectively. Therefore, the elastic behaviour of the contact stress, t, is shown in Equation 3.3 [33].

$$t = \begin{pmatrix} t_n \\ t_s \\ t_t \end{pmatrix} = K\delta = \begin{pmatrix} K_{nn} & K_{ns} & K_{nt} \\ K_{ns} & K_{ss} & K_{st} \\ K_{nt} & K_{st} & K_{tt} \end{pmatrix} \begin{pmatrix} \delta_n \\ \delta_s \\ \delta_t \end{pmatrix} \tag{3.3}$$

The damage modelling parameters are the most influential of the cohesive surface modelling factors. It involves identifying a damage initiation point and controlling the damage evolution. After much investigation, the damage initiation criteria used is a maximum stress (MAXS) criteria and is expressed as follows in Equation 3.4.

$$MAXS = max\left\{ \frac{\langle t_n \rangle}{t_n^o}, \frac{t_s}{t_s^o}, \frac{t_t}{t_t^o} \right\} \tag{3.4}$$

The peak values when using MAXS criteria of the contact stress in the normal, first shear and secondary shear are denoted by t_n^o, t_s^o and t_t^o. Damage is initiated when the ratio of the current contact stress in the normal, secondary and tertiary axis reach one. When this occurs, the damage evolution will be initiated whereby the stiffness of the cohesive surface will be degraded. To control the damage evolution a damage variable, D, evolves from zero to one. There are two methods used to model the damage evolution, specifying a failure separation or an energy-based separation. To gain understanding on the effect of cohesive surface damage evolution modelled by failure energies or an effective separation, extensive FE work learned that cohesive failure controlled by an effective separation to be more computationally stable [17, 35, 33]. The stiffness is represented by Equation 3.5.

$$K_{nn} = K_{ss} = K_{tt} = \alpha E_{33}^{PLY} / t^{PLY} \tag{3.5}$$

where α is a parameter with a suggested value of 50, t^{PLY} is the thickness of the bonded plies and E_{33}^{PLY} is the normal Modulus of the CFRP; this suggests that the stiffness is $5.0x10^6 N/mm^3$ [36]. The stiffness is purely a guideline that is stiff enough to provide load transfer, but not too stiff that unauthentic fluctuations occur in the output [35]. The initial strength estimate should represent the normal strength of the ply, shown in Equation 3.6.

$$\frac{S_{12}^{PLY} + S_{23}^{PLY}}{2} = S_s = S_t = 70MPa \tag{3.6}$$

The damage evolution was set to a displacement of 0.01 mm with a linear softening. The cohesive interaction significantly increases the ability to capture the nonlinear loading response frequently overlooked in FEA analysis.

3.4 Results & Discussion

The strain data captured by the 3D Aramis camera and force-displacement data from the Instron were analyzed providing force, stress and strain results for the 0°, 90° and 45° fibre layup direction tensile tests.

3.4.1 0° fibre layup orientation

Figure 3.8 shows the experimental results for the 0° layup direction tensile tests. On the primary axes the stress-strain relationship is plotted and on the secondary axes the force-displacement is plotted. The load peaked at 3379.9 N at a displacement of 0.3912 mm. The standard deviation error is shown in Figure 3.8, with an average error throughout the load response of 46.64 N (max 207.53 N) for the 0° tests. The new grips' design required time to allow the samples to seat into the arcs via the tensile loading, generating a nonlinear initial force response. This nonlinear period can vary slightly, depending on the initial positioning of the samples in the grips, but is easily overcome by adjusting the displacement by an offset to synthesize the tests. Strain measurement from the Aramis system outputs a time stamp and global strain value with respect to an averaged area in the gauge region.

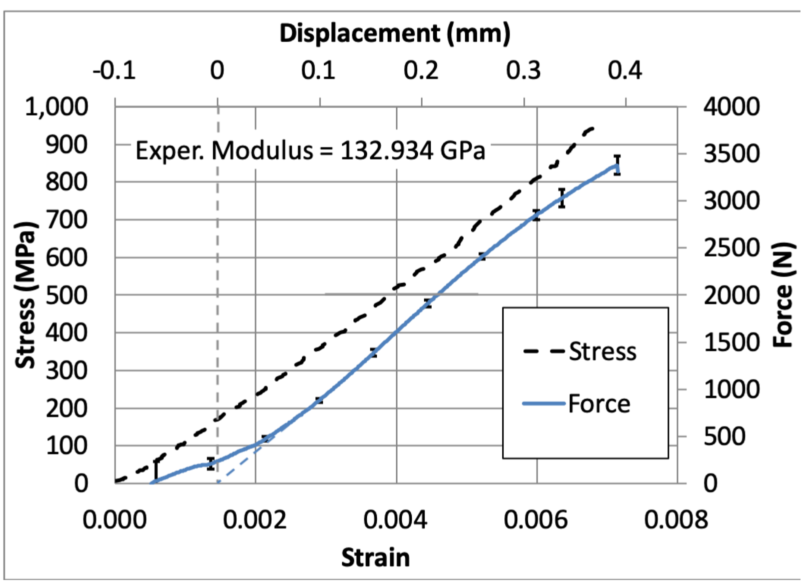

Figure 3.8: 0° experimental results: stress-strain & force-displacement

The Instron outputs a similar timestamp, displacement and the corresponding force. Strain outputs were adjusted for position, averaged and a third order polynomial was fit to the curve with a correlation coefficient of 0.9973, to disregard variation in the recording.

Figure 3.9 illustrates the damage state variable progression. SDV2 designates the progression of damage in the matrix. In Figure 3.9 a) the SDV2 output is describing the matrix damage progression where in the focused area (red) complete matrix damage has occurred. Subsequently in Figure 3.9 b) at the same time step the initiation of fibre damage has begun (SDV1). Figure 3.9 c) illustrates the damage progression one step prior to gross rupture and finally the sample rupture with element deletion in Figure 3.9 d).

Figure 3.10 compares the experimental force-displacement plot compared with the VUMAT-Puck fibre reinforced polymer FE model. The new grips described earlier induce compression to the arc region, which prevents premature failure. The nonlinear section of the experimental curve, shown as the "nonlinear grip-effect" region, is a result of the sample compressing into the redesigned grips. The displacement is then shifted to approximate what would otherwise be an initial linear load response. Although Figure 3.10 demonstrates an agreeable response to the experimental loading,

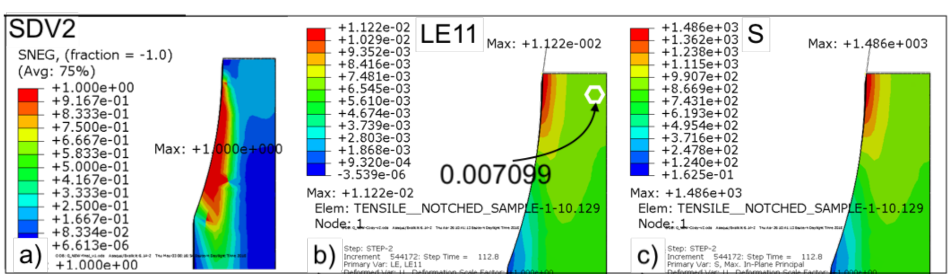

Figure 3.9: Damage variable progression for 0° FEM sample [a) SDV2=1.0 b) SDV1 initiation c) SDV2 prior to element deletion d) SDV1 at element deletion

an error within 8.33% in displacement and 6.66% with respect to peak load, greater than 0.2 mm (40%) of the loading expires before the FEM prediction begins to resemble the experimental loading response. Specifically, only the nonlinearity towards failure is well represented.

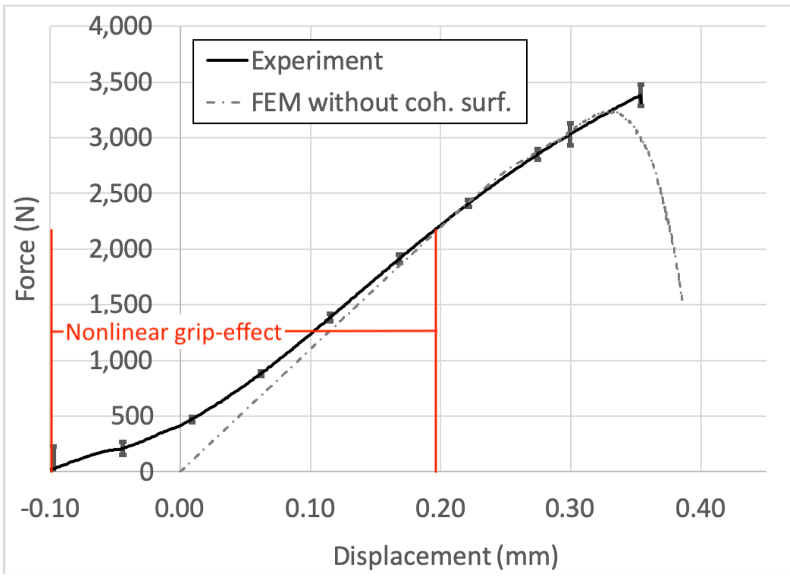

Figure 3.10: 0° force-displacement response versus FEA

Figure 3.11 shows the VUMAT model output of matrix failure (SDV2), strain and stress field respectively one step prior to failure. Figure 3.12 a) and b) shows the experimental strain field on the sample prior to failure and failure respectively for comparison. The failure location predicted by the FE model is similar to that observed by the Aramis camera as shown in Figure 3.12 c). The FE predicted Young's Modulus was 133.353 GPa, which was similar to that acquired experimentally, which was 132.934 GPa.

Figure 3.11 c) shows the stress distribution one step prior to failure and a concentrated stress magnitude of 1486 MPa, which was similar to that measured by the manufacturer of 1500 MPa [23]. The simulated stress magnitude for the sample was

946.4 MPa, which agrees well with the stress acquired experimentally of 945.5 MPa. The experimental stress was calculated by dividing the maximum load by the gauge area. The failure location prediction in comparison to the rupture caught by the Aramis camera, initiate at the notch and grow in the same manner. The experimental strain at the last frame prior to failure shows a strain in the gauge (notch) region of 0.00681, shown in Figure 3.12 a). In Figure 3.11 b) the simulated gauge region strain is 0.007099 and is in good agreement with the global strain data output from the experimental results.

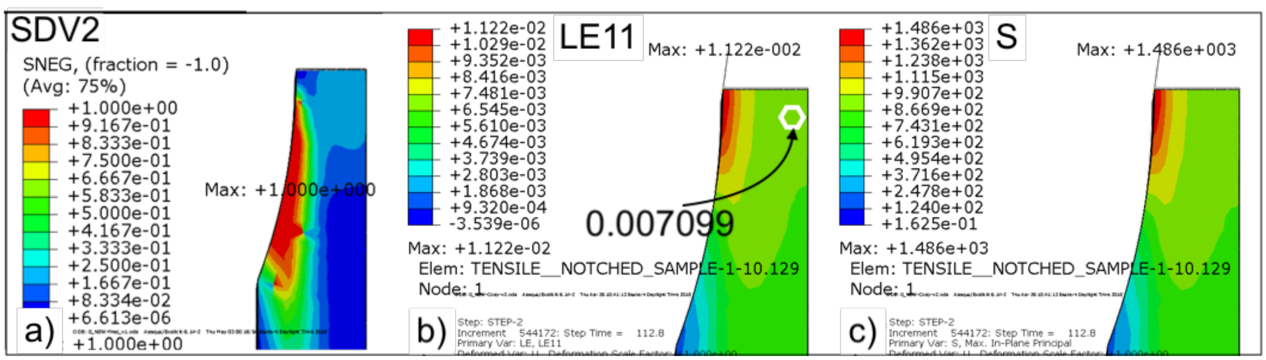

Figure 3.11: a) SDV2 b) Strain prior to failure c) Stress prior to failure

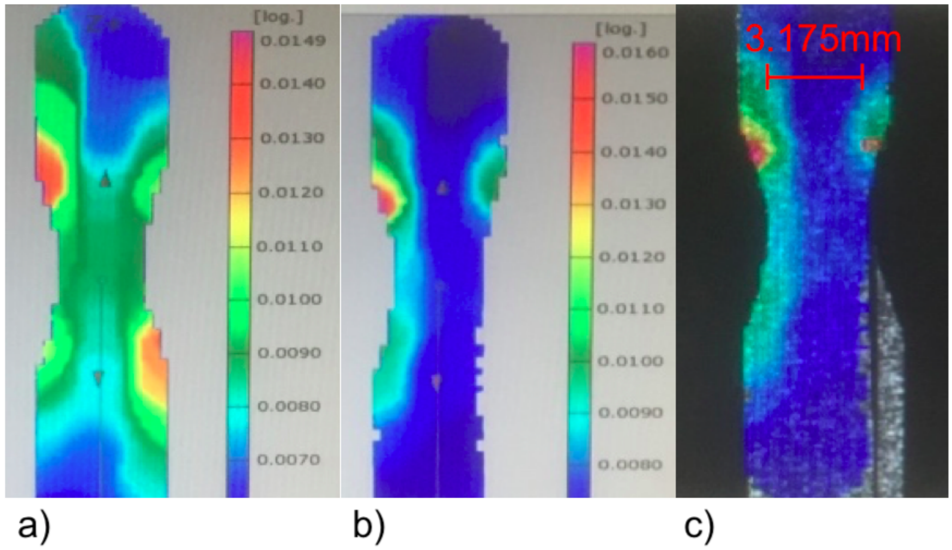

Figure 3.12: Aramis strain: a) frame 430 b) frame 431 c) frame 431

3.4.2 0° Multi-instance, 1/4 model with cohesive surfaces

Cohesive modelling considerations between plies is studied, accomplished by cohesive zones or cohesive surfaces. Published papers neglecting the cohesive interactions due to the computational expense [1, 37, 38] or unrealized benefits [39] is common. Giliol et al. reported that no delaminating occurred and results replicated a model using a perfect TIE constraint between plies, that only output cohesive failure after the CFRP had failed [39]. This outcome was a result of incorrect cohesive interaction property assignment, specifically the damage initiation state of the cohesive traction was too high. Marzi et al. [40], has shown cohesive modelling to have significant effect on the realistic loading response of the UD CFRP sample even at higher velocities.

The inclusion of a cohesive surface between the instances greatly improved the loading response of the FEM is shown in Figure 3.13. The response is within 6.34% in displacement failure and 3.69% with respect to peak load. Most significantly, the load response resembles the curve as early as 0.07 mm (20%) into loading with the inclusion of interface modelling, diminishing the nonlinear grip-effect. The model without cohesive surfaces using the VUMAT and Puck failure criteria, dashed line shown in Figure 3.10, does not represent the experimental loading well with an inflated loading response. In comparison, the simulation with the inclusion of cohesive interfaces accurately predicts the experimental data.

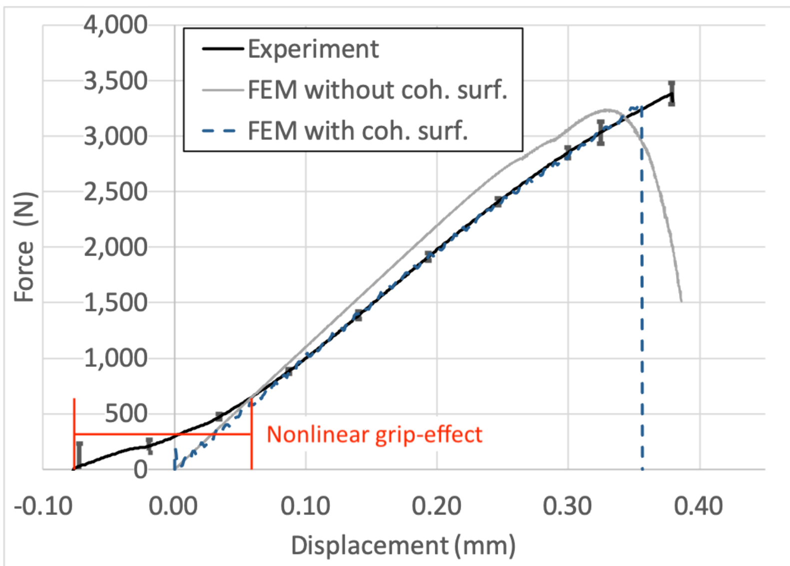

Figure 3.13: 0° FEM response with cohesive surface interaction

3.4.3 90° fibre layup orientation

Figure 3.14 shows the linear elastic loading response of Puck, Hashin, MCT, LaRC02, Christensen and Max Strain for 90° tensile simulations nearly replicating one another. This is a result of the matrix material response during damage evolution using the same elastic theory, only differing when considering damage evolution for the matrix. The critical factor is the ability for the model to converge towards failure during the damage evolution stage. This was only accomplished when modelling with a maximum strain criterion and partially by LaRC02 but solver diverged.

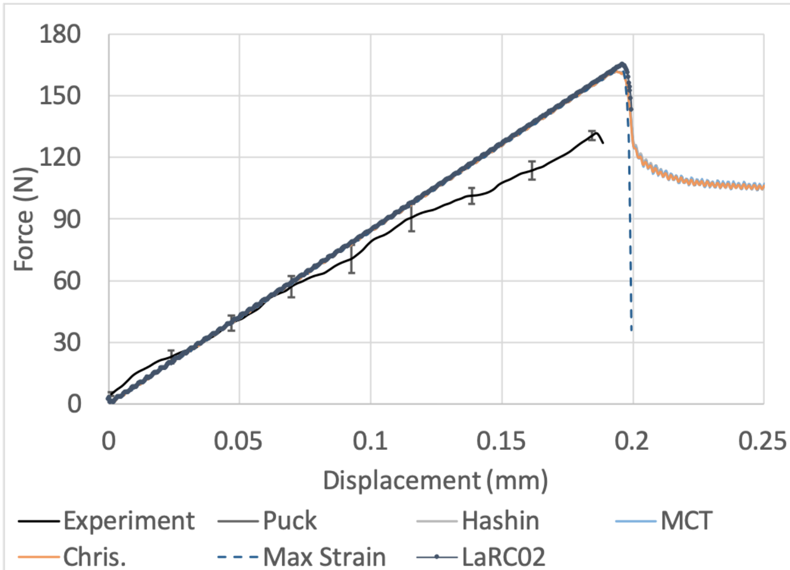

Figure 3.14: 90° failure model analysis

The inability to converge is controlled by the failure mode and involves deleting failed elements. Convergence issues will occur as the sample will never fail, supporting zero load or element deletion. Instead a post-failure stiffness continues infinitely preventing the element deletion. Once the stress on an element is large enough to cause matrix damage, the stiffness of this element reduces to a post-failure stiffness. The material will follow a degradation of stiffness process, based on a time-period or energy release. Once the degradation of stiffness of the element has occurred, the element cannot bear load (at least no more than the post-failure stiffness allows) and therefore the stress in the element will never increase enough to cause failure based in the fibre direction. This convergence issue occurs at any significantly off-angle loading, especially between 45° to 90°.

The Maximum Strain failure criteria uses the maximum absolute value of the following individual failure indices shown in Equation 3.7.

$$\left| \frac{\epsilon_{11}}{\epsilon_{11}^{max+}}, \frac{\epsilon_{11}}{\epsilon_{11}^{max-}}, \frac{\epsilon_{22}}{\epsilon_{22}^{max+}}, \frac{\epsilon_{22}}{\epsilon_{22}^{max-}}, \frac{\epsilon_{12}}{\epsilon_{12}^{max-}} \right| \geq 1 \tag{3.7}$$

A ratio of the current increment strain in a principle vector direction (*longitudinal* ϵ_{11}, *transverse* ϵ_{22}, *shear* ϵ_{12}) and the maximum strain at failure for that vector direction, is evaluated. The maximum values are determined from the provided strengths (failure stresses), material moduli and Poisson's ratio and therefore is an efficient failure criterion, especially when geometry and loading are not complex.

3.4.4 90° Multi-instance, 1/4 model with cohesive surfaces

The cohesive modelling setup described in the 0°, quarter model, was implemented with a rotation of the ply layup so the fibres would be perpendicular to the loading for the 90° setup. Despite the successful modelling of the nonlinearity for the 0 deg tensile simulations, a result largely due to the use of multiple ply layups, nonlinearity was not initially captured with the 90° FE models. With matrix-fibre composites, the matrix damage initiation and evolution lead to fracture. When the fibres are parallel to loading the fibres withstand significant load as the matrix damage evolves. The outer instance will damage prior to the middle of the specimen. These contributions lead to the successful modelling of the nonlinear response of the 0° tests and was shown in Figure 3.13. The 90° tests are not controlled by the fibre damage. The coupon experiences fracture because of a failure in the matrix. Due to the computational benefit, the matrix is modelled as an isotropic linear-elastic material, generally preceding fibre damage. The inclusion of cohesive modelling between instances with damage allows the model to capture non-linearity in the loading response as the matrix damages.

It was discovered the initial stiffness and failure strength of the cohesive interface was too high in this orientation, as the failure in the interface only occurred after matrix failure. To induce any nonlinearity into the load response for the 90° samples the damage initiation of the interface must precede the matrix damage. Shown in Figure 3.15, is an improved simulated material response with the inclusion of cohesive surfaces. Without the cohesive surfaces a linear response predicted does not represent the experimental response recorded. The Young's modulus prediction compared to the experimentally determined modulus is improved from a 17.7% difference without cohesive surfaces to a 3.6% difference with the inclusion of cohesive surfaces.

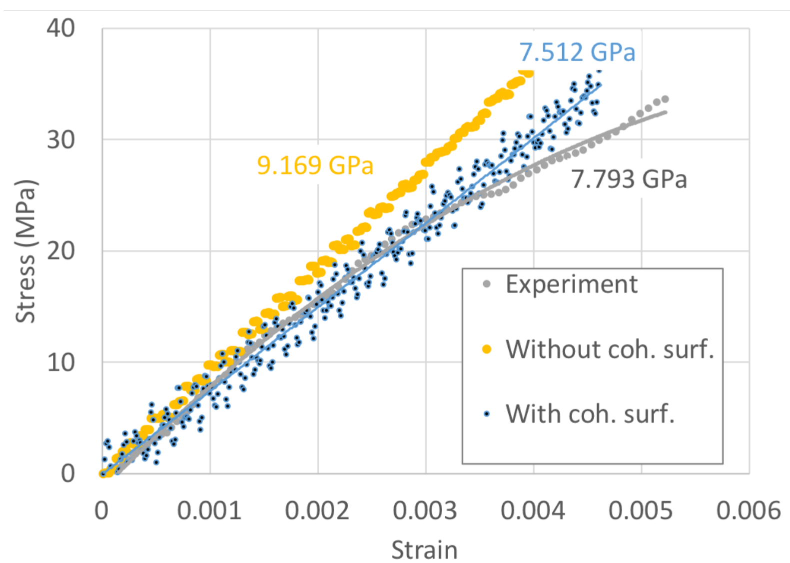

Figure 3.15: 90° stress-strain

3.4.5 45° fibre layup orientation

The FE model shows good correlation to the results captured by the Instron tensile machine and Aramis camera. In Figure 3.16 a) the Max In-plane Stress output in the gauge region one frame prior to failure is 70.42 MPa, compared to 66.15 MPa determined experimentally. The sample failure captured with the Aramis camera shown in Figure 3.16 b) and the Figure 3.16 c) illustrating the predicted sample failure with element deletion (SDV1) resemble one another well.

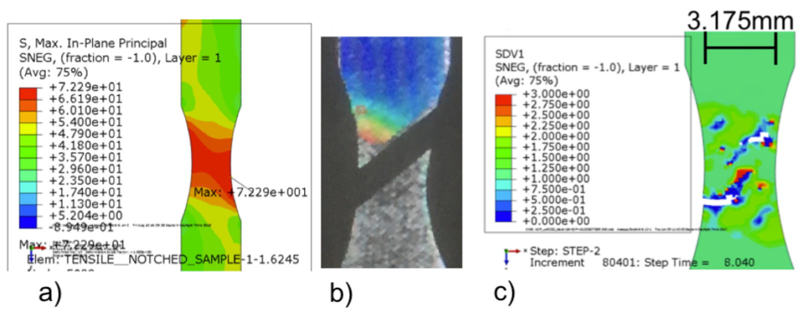

Figure 3.16: a) FEM In-plane stress b) Aramis Strain c) FEM SDV1 failure

Figure 3.17 shows the 45° fibre layup simulated loading response representing the experiment well. The ability to converge to failure was achieved by Max Strain and the LaRC02 model. Maximum Strain over predicted rupture due to the inability to capture mixed-mode failure contributions in loading. This is captured when using the LaRC02 failure model.

The LaRC02 model defines the matrix damage in tension as shown in Equation 3.8.

$$FI_M = \Big(\frac{\sigma_{22}}{Y^T}\Big)^2 + \Big(\frac{\tau_{12}}{S^L}\Big)^2 \tag{3.8}$$

where Y^T is the transverse tensile failure strength, S^L is the longitudinal shear failure strength and FI_M is the failure index for the matrix. Failure is based on a combination of the matrix loading in the transverse and shear directions. The LaRC02 failure model accurately represents the 45° fibre layup direction tensile test most accurately with damage evolution and element deletion.

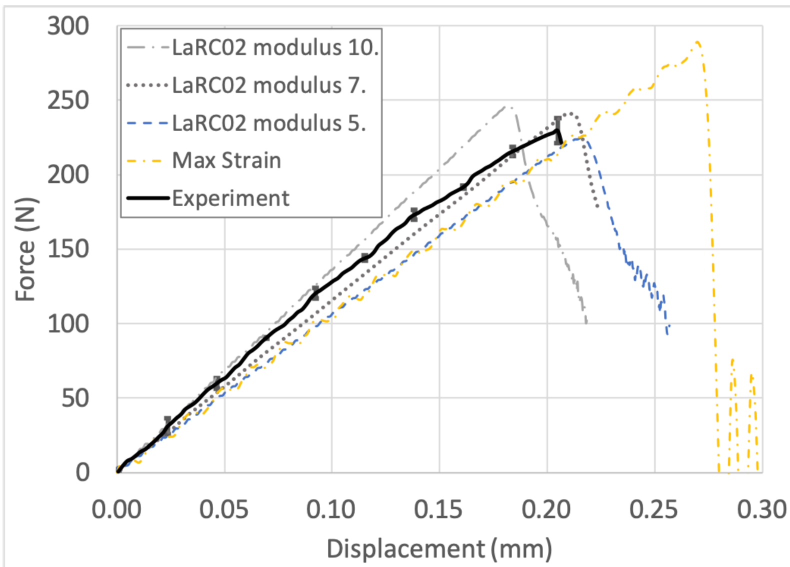

Figure 3.17: 45° failure models & alternative modulus

The loading response was studied as the shear modulus was manipulated between 5 and 10 GPa. The manufacturer magnitude is 5 GPa and the modulus from the 45° tensile test is 10.38 GPa. Figure 3.17 shows the improved loading response in the FEA prediction with an increased shear modulus. The 10 GPa modulus most closely predicts the initial loading however the nonlinear response is not captured. This cannot be modelled without the inclusion of cohesive surfaces with damage inclusion.

3.4.6 45° Multi-instance, 1/4 model with cohesive surfaces

The initial cohesive interaction was created and applied to surfaces between the ten individual instances. The stiffness was created based on the epoxy modulus divided by the thickness of the interaction layer multiplied by an alpha coefficient set to fifty as recommended by ABAQUS literature [33]. The damage initiation was set to the epoxy failure strength and the evolution was set to 0.01 mm displacement controlled by an exponential softening [36].

To capture nonlinearity the cohesive interaction damage must be initiated prior to the matrix damage progression, which controls the failure of non-parallel fibre to loading setups. The damage initiation was set to a failure stress of 70 MPa determined by Equation 3.6, however cohesive damage was not preceding matrix failure in the 45° simulations.

By reducing the cohesive failure stress that controls the damage initiation, the model better resembled the experiments and cohesive damage was initiated prior to the matrix. The result of the damage initiation and evolution preceding the matrix damage has greatly improved the material response prediction, specifically the ability to capture the nonlinearity in the loading response shown in Figure 3.18.

The initial loading response and cohesive damage initiation improved the model prediction, however damage evolution parameters were not fully optimized. Shown in Figure 3.18, the cohesive damage initiated at a lower stress, the damage evolution progresses earlier leading to premature failure prediction. These parameters require more sensitivity analysis to fully predict the failure.

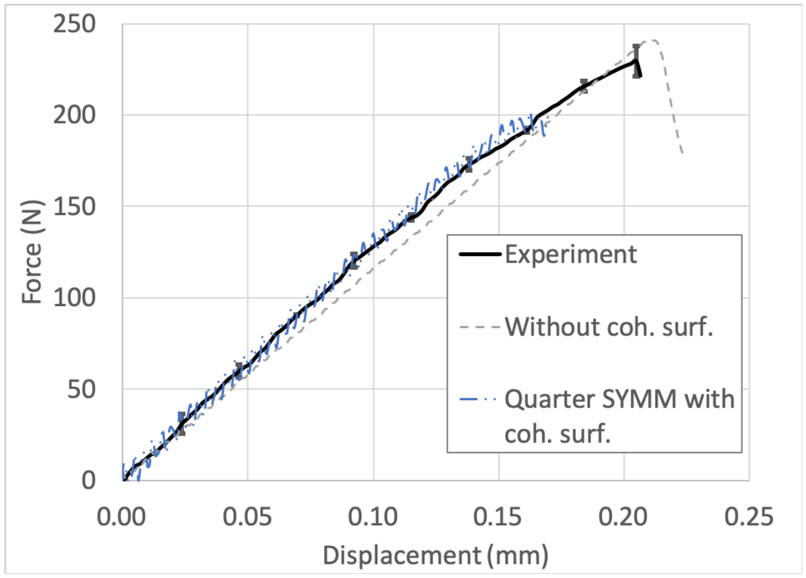

Figure 3.18: 45° force-displacement with cohesive surfaces

3.5 Nonlinear grip-effect verification

Validation of the nonlinear gripping region is achieved by the inclusion of rigid body surfaces used to represent the arced fixturing setup described. These rigid body surfaces, shown in Figure 3.19, require time to compress on the arced regions of the CFRP sample, causing a nonlinear response as the sample settles into the fixturing. This was first observed during the 0° fibre layup tensile experiments force-displacement output and hypothesized as the cause.

Geometry and FE modelling parameters including cohesive surface interaction between instances was maintained from section 3.4.2 0° - Multi-ply with cohesive surfaces. Friction has been noted by Russell et al. to be insensitive between 0.1-0.3 and was set with a penalty contact regime using a coefficient of friction of 0.3 [41]. The CFRP should not penetrate into the rigid surfaces. A "Hard" pressure over-closure contact minimizes the penetration of the slave surface (CFRP) into the

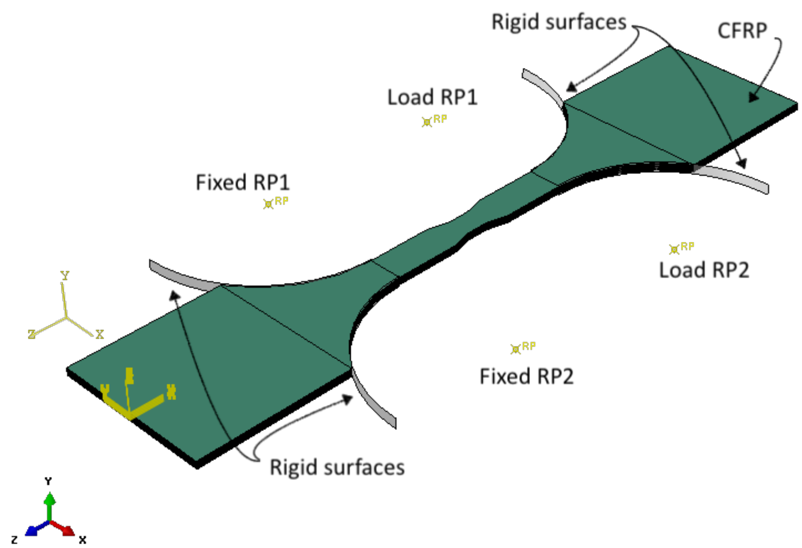

Figure 3.19: Tensile setup incorporating fixturing represented by rigid surfaces

master surface (Rigid surfaces) [33]. A summary of the model parameters used is shown in Table 3.4.

Without the inclusion of the rigid surfaces the initial nonlinear twenty percent of the loading observed from experiments was not captured, shown in Figure 3.13. In Figure 3.20, the FEA reaction force prediction accurately represents the experiment results including the sample settling into the fixture. Future work should verify contact interactions between the CFRP and fixturing in this area. Observing the FEM stress profile in the region could lead to new insights and further improve fixturing setup.

Figure 3.21 details the effect of fibre layup orientation on force-displacement response. The force magnitude and displacement were the highest when the fibre orientation was at 0°. As the fibre orientation increases to 90°, both force magnitude and displacement decreases. Similar trend was observed by Srbova et.al. [42] when experimentally investigating the effect of fibre orientation on uniaxial tensile loading

Table 3.4: Non-linear grip verification model parameters

Parameters	
Cohesive surfaces	Yes
Number of plies	10
Symmetry	No
Fixturing tool	Rigid surfaces with contact properties
Contact between plies	Cohesive with damage
Contact with tool	Hard with friction
Mesh size (mm)	0.250
Mass scaling (T.S. seconds)	1.0e-04
Time scaling	1x (120.0 s)
Bulk viscosity	Default
Failure Model	LaRC02
Matrix post stiffness failure	0.1 (Default)
Fibre post stiffness failure	1.0e-06 (Default)

configuration to fracture.

Figure 3.22 shows the effect of fibre layup orientation on simulated failure force between 0° to 90°. Also shown in the secondary axis of Figure 3.22 is the failure force normalized to the 0° fibre orientation. This was calculated by taking the magnitude of the respective failure force, in its respective fibre orientation, divided by the failure force of the 0° fibre orientation. A ∼50% reduction in failure force for the 5° layup compared to 0° fibre orientation (parallel to the loading direction) is observed. This shows that the 0° fibre orientation has a substantial effect on the failure force. However, when the fibre orientation was between 45° to 90°, the failure force simulated was insensitive to fibre orientation. This was because the matrix material dominated the response. Figure 3.22 also detailed results on failure force relative from 0° fibre orientation performed by Sadeghian et.al. [27] whom studied the nonlinear behavior of CFRP laminates of varying orientation. The experimental and numerical results also showed that the substantial reduction in failure force was

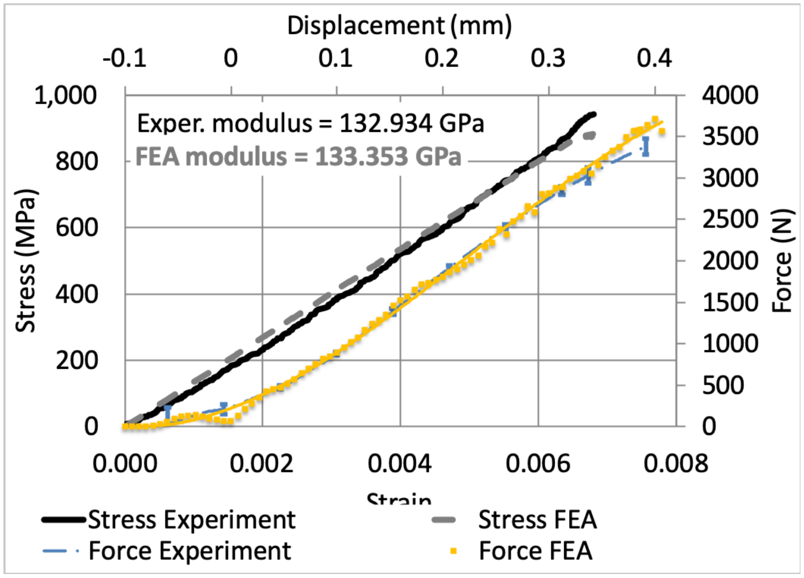

Figure 3.20: 0° experimental results: stress-strain & force-displacement

observed when the fibre layup orientation increased from 0° to 30°. Beyond 30°, the failure force plateaued.

To further test the effectiveness and versatility of the model developed in this research, the thickness of the laminate was modelled and compared with experimental results published by [26, 27, 43]. Figure 3.23 shows a bi-linear output for 0° UD-CFRP for three laminate thicknesses from the model developed in this research and those acquired experimentally by Sadeghian et.al. [27]. The normalized force per unit thickness, relative to the maximum force per unit thickness, was calculated by dividing the fracture force by the laminate thickness, then by the maximum force per unit thickness. Both the simulated results and those published by Sadeghian et.al. showed a bi-linear relationship, which highlights the strength of the laminate is not a unilinear relationship to thickness. When the thickness of the laminate was less than ~2 mm, a reduction in force per unit thickness is developed. The change in force per unit thickness plateaus when compared to laminate thickness greater than 2 mm. This

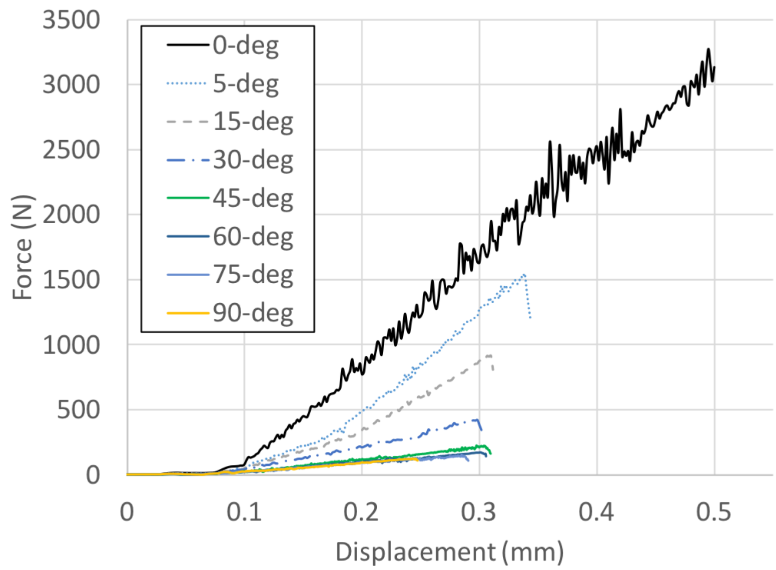

Figure 3.21: Effect of fibre layup orientation on force-displacement response

demonstrates a bi-linear relationship and the capability of the FE model to predict this trend. Inannucci et.al. [43] also found a bi-linear relationship on the effect of laminate thickness on force per unit thickness. Inannucci et.al. experimentally investigate the thickness of the laminate at 3 mm, 6 mm and 10 mm. When the thickness was increased from 3 mm to 6 mm, the force per unit thickness increased proportionally. However, beyond 6 mm, the increase was not proportional. This further shows that the FE model with inclusion of cohesive surface interfaces is capable of predicting varying fibre orientation loading responses and the strength to thickness relationship.

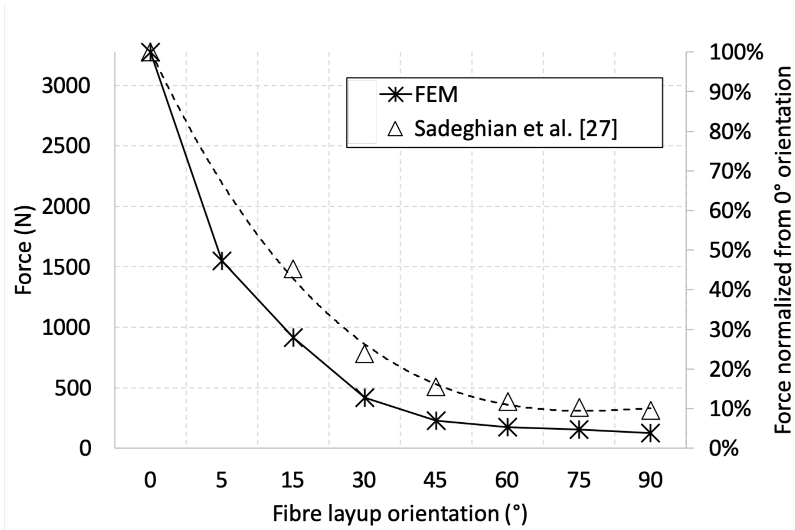

Figure 3.22: Effect of fibre layup orientation on failure force and relative to 0° fibre orientation

3.6 Conclusions

The development of an effective tensile test fixture combined with the use of a modified planar wishbone geometry greatly improved the repeatability and accuracy of the force-displacement and strain data recorded experimentally. This also greatly improved the control of the failure location which is most critical when using the ARAMIS 3D scanning camera to capture strain with a particularly small range of view.

When CFRP samples are subject to loading in a primary directions (fibre, matrix and shear), element size in the mesh was less sensitive than anticipated. Accurate, computationally efficient models can be achieved with element lengths of 0.375-0.5 mm for planar tensile tests. Loading a CFRP sample in a tension focuses loading in the ply and shows minimal dependence on the number of elements through the thickness of the geometry. Computational expense is reduced when the through thickness

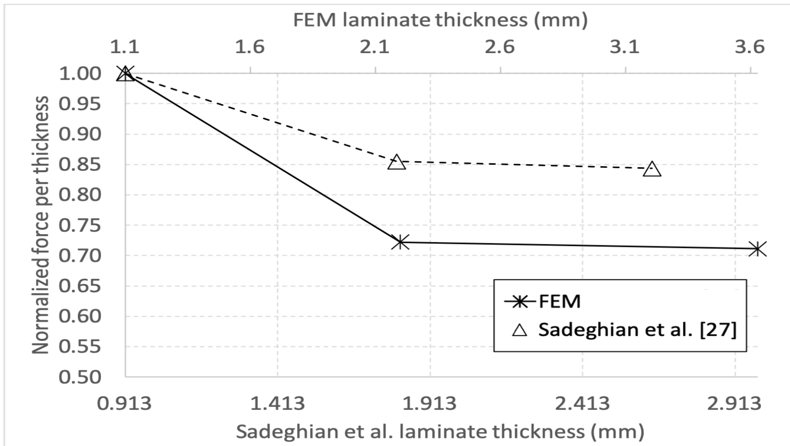

Figure 3.23: Effect on UD-CFRP laminate thickness for 0° fibre orientation normalized to maximum force per unit thickness.

element count is four or less, while maintaining accuracy. Mass scaling is the most critical factor regarding a models computational efficiency versus accuracy relationship. Variable mass scaling to a desired time step can reduce the computation time from years to minutes, but will have a drastic negative effect on the loading response accuracy. Consideration must be made to minimize the inertial effects caused by the increased density of the elements when implementing mass scaling. Utilizing the CFRP's insensitivity to strain rate allows for time scaling to be implemented resulting in more computational savings. Further, when loading non-parallel to the fibre orientation, the matrix material dominates the material response. Only Maximum Strain and LaRC02 failure effectively capture damage evolution in these off-fibre loading orientations.

With the inclusion of multi ply instances laminated by cohesive interactions capable of damage evolution, the nonlinear loading response recorded from the experiments was predicted with strong resemblance. The 45° and 90° fibre layup samples' failure is controlled by matrix damage evolution. The inclusion of cohesive surface modelling improved the ability to develop nonlinearity in the loading response once damage initiation strengths were optimized. The facilitation for the contribution of damage between instances derived a nonlinear response that is commonly not captured or assumed linear-elastic.

The enhancements made experimentally, in combination with the effective modelling techniques employed, significantly improved the effectiveness of the tests and the material representation in FEA. Work modelling the arced fixturing device using rigid surfaces verified the non-linear gripping region described. To further develop the cohesive surface modelling a three-point bending analysis should be studied at various fibre orientations to aid in accurately modelling the break-in and break-out delamination damage when drilling CFRP the cohesive interaction prediction is critical. With accurate representation of the CFRP material and its interlaminar cohesive nature effective machining simulations can be developed. The model was also capable of predicting the effects of fibre orientation and laminate thickness on fracture force, which was similar to published experimental results.

References

[1] M. Nirbhay, A. Dixit, R.K. Misra, and H.S. Mali. “Tensile Test Simulation of CFRP Test Specimen using Finite Elements”. In: *Procedia Materials Science* 5 (2014), 267 − 273.

[2] K. Krishnamoorthy and T. Sasikumar. “Analysis and Characterization of Tensile Property of the Composite Specimen using Ansys”. In: *International Journal of Applied Engineering Research* 11 (2016), 380 − 384.

[3] M. Arcan, Z. Hashin, and A. Voloshin. "Method to Produce Uniform Plane-Stress States with Applications to Fiber-Reinforced Materials". In: *Experimental Mechanics* Vol. 18, No. 4 (1978), 141 − 146. URL: https://doi.org/10.1007/BF02324146.

[4] R. El-Hajjar and R. Haj-Ali. "In-Plane Shear Testing of Thick-Section Pultruded FRP Composites using a Modified Arcan Fixture". In: *Composites Part B: Engineering* Vol. 35B, No. 5 (2004), 421 − 428. URL: http://dx.doi.org/10.1016/j.compositesb.2003.12.004.

[5] J. Tessmer, D. Hartung, and L. Aschenbrenner. "Mechanics of Composites in Lightweight Structures: Efficient Testing and Computation Accounting for Complex 3D Behaviour". In: *Proceedings of the 26th International Congress of the Aeronautical Sciences* 2 (2008), 1 − 9.

[6] M. Nikbakht and N. Choupani. "Fracture Toughness Characterization of Carbon-Epoxy Composite using Arcan". In: *International Journal of Aerospace and Mechanical Engineering* Vol. 2, No. 4 (2008), 247 − 253. URL: doi.org/10.5281/zenodo.1059685.

[7] S.R. Hallett and M.R. Wisnom. "Experimental Investigation of Progressive Damage and the Effect of Layup in Notched Tensile Tests". In: *J. Compos. Mater. (USA)* 40.2 (2006), pp. 119–41. ISSN: 0021-9983. URL: http://dx.doi.org/10.1177/0021998305053504.

[8] I. Lapczyk and J.A. Hurtado. "Progressive Damage Modeling in Fiber-Reinforced Materials". In: *Composites Part A: Applied Science and Manufacturing* Vol. 38, No. 11 (2007), 2333 − 2341. URL: https://doi.org/10.1016/j.compositesa.2007.01.017.

[9] M. Zappalorto and P.A. Carraro. "An Engineering Formula for the Stress Concentration Factor of Orthotropic Composite Plates". In: *Composites Part B:*

Engineering 68 (2015), 51 − 58. URL: `http://dx.doi.org/10.1016/j.compositesb.2014.08.020`.

[10] ASTM International. *ASTM D3039 / D3039M-17, Standard Test Method for Tensile Properties of Polymer Matrix Composite Materials*. West Conshohocken, PA, USA, 2017. DOI: 10.1520/D3039_D3039M-17.

[11] K.J. Wong, X.J. Gong, S. Aivazzadeh, and M.N. Tamin. "Tensile Behaviour of Anti-Symmetric CFRP Composite". In: *Procedia Engineering* 10 (2011), 1865 − 1870. URL: `https://doi.org/10.1016/j.proeng.2011.04.310`.

[12] R.J. Coguill and D.F. Adams. "Selection of the Proper Wedge Grip Surface for Tensile Testing Composite Materials". In: *Proceedings of the 44th International SAMPE Symposium and Exhibition* 44 (1999).

[13] R.J. Coguill and D.F. Adams. "Tabbed Axial Tensile Specimen Configurations for Unidirectional Composites". In: *Proceedings of the 45th International SAMPE Symposium and Exhibition* 45 (2000).

[14] ASTM International. *ASTM E8 / E8M-16a, Standard Test Methods for Tension Testing of Metallic Materials*. West Conshohocken, PA, USA, 2016. DOI: 10.1520/E0008_E0008M-16A.

[15] H. Kobayashi, K. Goto, H. Hatta, M. Koyama, and H. Fukuda. "Tensile Strength of Carbon-Carbon Composites at High Temperature up to 2773K". In: *Proceedings of the 17th International Conference on Composite Materials, ICCM-17, Edinburgh, United Kingdom* (2009).

[16] Z. Hashin. "Failure Criteria for Unidirectional Fiber Composites". In: *Journal of Applied Mechanics* Vol. 47, No. 2 (1980), 329 − 334. URL: `http://dx.doi.org/10.1115/1.3153664`.

[17] D.R. Ambur, N. Jaunky, and C.G. Davila. "Progressive Failure of Composite Laminates using LaRC02 Criteria". In: *Collection of Technical Papers - AIAA/ASME/ASCE/AHS/ASC Structures, Structural Dynamics and Materials Conference* 2 (2004), 898 − 913.

[18] S.W. Tsai and E.M. Wu. "A General Theory of Strength for Anisotropic Materials". In: *Journal of Composite Materials* 5 (1971), 58 − 80. URL: http://dx.doi.org/10.1177/002199837100500106.

[19] S.W. Tsai. "Strength Theories of Filamentary Structures". In: *Fundamental Aspects of Fiber Reinforced Plastic Composites* 5 (1968), 3 − 11.

[20] R.M. Christensen. "Tensor Transformations and Failure Criteria for the Analysis of Fiber Composite Materials". In: *Journal of Composite Materials* Vol. 22, No. 9 (1988), 874 − 897. URL: https://doi.org/10.1177/002199838802200906.

[21] A. Puck and H. Schurmann. "Failure Analysis of FRP Laminates by Means of Physically Based Phenomenological Models". In: *Failure Criteria in Fibre-Reinforced-Polymer Composites* (2004), 264 − 297. URL: http://dx.doi.org/10.1016/B978-008044475-8/50011-1.

[22] M.R. Garnich. "A Multicontinuum Theory for Structural Analysis of Composite Materials". PhD thesis. University of Wyoming, 1996.

[23] ACP Composites. *Carbon Firer Uni Laminates*. 2014. Accessed: 6/2015.

[24] D.O. Adams and D.F. Adams. *Tabbing Guide for Composite Test Specimens*. Tech. rep. UTAH Univ. Salt Lake City Dept. of Mechanical Engineering, US Department of Transportation Federal Aviation Administration, DOT/FAA/AR-02/106., 2002.

[25] D. W. Worthem. *Flat Tensile Specimen Design for Advanced Composites*. Tech. rep. Sverdup Technology Inc., National Aeronautics, and Space Administration, NASA CR-185261, 1990.

[26] A. Mehar, G.M.S. Ahmed, G.P. Kumar, Md.A. Rahman, and M.A. Qayum. "Experimental Investigation and FE Analysis of CFRP Composites". In: *Materials Today: Proceedings* Vol. 2, No. 4 (2015). 4th International Conference on Materials Processing and Characterization, 2831 – 2839. URL: https://doi.org/10.1016/j.matpr.2015.07.297.

[27] P. Sadeghian, A.R. Rahai, and M.R. Ehsani. "Effect of Fiber Orientation on Nonlinear Behavior of CFRP Composites". In: *Journal of Reinforced Plastics and Composites* 28.18 (2009), 2261 – 2272. URL: https://doi.org/10.1177/0731684408092065.

[28] J.M.F. Paiva, S. Mayer, and M. Rezende. "Comparison of Tensile Strength of Different Carbon Fabric Reinforced Epoxy Composites". In: *Materials Research* Vol. 9, No. 1 (2006), 83 – 89. DOI: 10.1590/S1516-14392006000100016.

[29] G. Belingardi, D. S. Paolino, and E. G. Koricho. "Investigation of Influence of Tab Types on Tensile Strength of E-Glass/Epoxy Fiber Reinforced Composite Materials". In: *Procedia Engineering* 10 (2011), 3279 – 3284. URL: https://doi.org/10.1016/j.proeng.2011.04.541.

[30] Instron. *Dual Column Tabletop Models 3360*. MA, USA, 2017. URL: http://www.instron.us/-/media/literature-library/products/2011/06/3300-series-table-model.pdf?la=en-US. Accessed: 2016-7-20.

[31] GOM Aramis. *ARAMIS Adjustable*. NC, USA, 2017. URL: https://www.gom.com/metrology-systems/aramis/aramis-adjustable.html. Accessed: 2017-12-05.

[32] R.S. Sandhu and K.J. Singh. “Reduced Integration for Improved Accuracy of Finite Element Approximations”. In: *Computer Methods in Applied Mechanics and Engineering* Vol. 14, No. 1 (1978), 23 − 37. URL: http://dx.doi.org/10.1016/0045-7825(78)90011-7.

[33] Dassault Systemes. *ABAQUS/CAE User's Guide, from ABAQUS 6.14 Online Documentation*. 2014.

[34] J. Kwon, J. Choi, H. Huh, and J. Lee. “Evaluation of the Effect of the Strain Rate on the Tensile Properties of Carbon and Epoxy Composite Laminates”. In: *Journal of Composite Materials* Vol. 51, No. 22 (2017), 3197 −3210. URL: https://doi.org/10.1177/0021998316683439.

[35] Autodesk Helius PFA. *Theory Manual*. 2016. URL: http://help.autodesk.com/view/ACMPAN/2016/ENU/?guid=GUID-1FEC4707-77A9-4FA4-BA2D-60B7444A1359.

[36] P.P. Camanho, A. Turon, C.G. Davila, and J. Costa. “An Engineering Solution for Mesh Size Effects in the Simulation of Delamination Using Cohesive Zone Models”. In: *Engineering Fracture Mechanics* Vol. 74, No. 10 (2007), 1665 − 1682. URL: http://dx.doi.org/10.1016/j.engfracmech.2006.08.025.

[37] V. Daghigh, M. Soroush, K. Nikbin, and A. Simoneau. “Finite Element Modeling of Tensile and Bending on Fiber Reinforced Polymer Composites”. In: *The 3rd International Conference on Composites: Characterization, Fabrication and Application* (2012), Tehran, Iran.

[38] L.F. Chen, L. Chen, and G. Zhang. “Finite Elemental Simulation on Flexural Process of Carbon Fiber/Epoxy Composite Laminates”. In: *Advanced Materials Research* 332-334 (2011), 1105 − 1108. URL: https://doi.org/10.4028/www.scientific.net/amr.332-334.1105.

[39] A. Gilioli, A. Manes, and M. Giglio. "Evaluation of the Effects of the Numerical Modelling Choices on the Simulation of a Tensile Test on CFRP Composite". In: *Procedia Structural Integrity* 8 (2018), 33 − 42. URL: `https://doi.org/10.1016/j.prostr.2017.12.005`.

[40] S. Marzi, A. Rauh, and R.M. Hinterholzl. "Fracture Mechanical Investigations and Cohesive Zone Failure Modelling on Automotive Composites". In: *Composite Structures* 111 (2014), 324 − 31. URL: `http://dx.doi.org/10.1016/j.compstruct.2014.01.016`.

[41] B.P. Russell, T. Liu, N.A. Fleck, and V.S. Deshpande. "Quasi-static Three-point Bending of Carbon Fiber Sandwich Beams With Square Honeycomb Cores". In: *Journal of Applied Mechanics* Vol. 78, No. 3 (2011), p. 15. URL: `http://dx.doi.org/10.1115/1.4003221`.

[42] H. Srbova, T. Kroupa, and R. Zemcik. "Identification of the Material Parameters of a Unidirectional Fiber Composite Using a Micromodel". In: *Materials and technology* 46 (2012), pp. 431–434.

[43] L. Iannucci, S. Del Rosso, P.T. Curtis, D.J. Pope, and P.W. Duke. "Understanding the Thickness Effect on the Tensile Strength Property of Dyneema® HB26 Laminates". In: *Materials* Vol. 11, No. 8 (2018), p. 1431. URL: `https://doi.org/10.3390/ma11081431`.

3.7 Nomenclature

ϵ	Strain
σ_{11}	Longitudinal stress (MPa)
$\sigma_{22} = \sigma_{33}$	Transverse stress (MPa)
E	Young'sModulus (GPa)
$\sigma_{12} = \sigma_{13}$	Longitudinal shear stress (MPa)
σ_{23}	Trasverse shear stress (MPa)
v	Poisson's ratio
S_{11}, S_{22}	Long. & Trans. material strengths (MPa)
S_{12}, S_{23}	Shear material strengths (MPa)
f, m, c	Fibre, Matrix, Composite
α	Contribution of shear variable ($0 \leq \alpha \leq 1$)
L^e	Characteristic Length Element
c_d	Dilatational Wave Speed
E_F	Flexural Modulus (MPa)
L	Support Span (mm)
b	Width of sample
h	Height of sample
m	Slope of the linear portion of the load-displacement curve (N, mm)
I	Moment of Inertia
I_j^m	Trans-isotropic matrix invariants
$j = 1, 2, 3, 4$	Matrix average stress state
p	Slope of fracture envelope
I_i^f	Trans-isotropic fibre invariants
$i = 1, 4$	Fibre average stress state
A_i^m, A_i^f	Adjustable coefficients
F_i, F_{ij}	Failure coefficients defined by strengths
Y_T, Y_C	Tensile and compressive strength (MPa)

Chapter 4

Three-point bending analysis with cohesive surface interaction for improved delamination prediction and application of CFRP composites

Complete citation:

P. Hale and E.Ng. “Three-point bending analysis with cohesive surface interaction for improved delamination prediction and application of carbon fibre reinforced plastics composites”. In: Modelling and Simulation in Materials Science and Engineering 28.3 (2020) pp 1-28.

Three-point bending analysis with cohesive surface interaction for improved delamination prediction and application of CFRP composites

This chapter is a copy of the paper published in *Modelling and Simulation in Materials Science and Engineering* journal. This paper evaluates modelling considerations for accuracy, regarding material characterization of CFRP specifically focusing on the cohesive interactions between plies. The paper describes consideration for larger radius punch to promote failure on the bottom-tension side of the bending setup; this so the Aramis strain camera could accurately record laminate failure. Small span-to-thickness considerations provided a failure dominated by interlaminar shear failure causing delamination, versus large span-to-thickness configurations where failure is dominated by normal stresses. This unique observation is significant to predicting delamination in other loading conditions such as drilling. Finally, the model capability is evaluated versus material responses described in literature for multi-fiber orientation setups and cross-ply layup configurations.

Authors: Patrick Hale, Eu-gene Ng

Submitted to the *Modelling and Simulation in Materials Science and Engineering*

Published January, 2020

Abstract

Carbon fibre reinforced plastic laminates were loaded through to fracture in a three-point bending configuration, to gain understanding of the cohesive interaction between plies and validate mechanical properties and predictive capability of the FE model. The effect of mesh refinement, scaling techniques, failure models and cohesive surfaces were investigated. Fibre orientations investigated were parallel, 45° and perpendicular to the loading. Experimental results showed a larger radius punch promoted failure on the intended bottom side, tensile stresses region, allowing for the Aramis strain camera to record the failure. When the fibre orientation was perpendicular to the punch load, all failure models show similar rate of force increment with respect to displacement. No difference in failure prediction is observed for the different 0° models, except for a 4.18% under prediction by LaRC02 compared to the experiment. With fibre orientations at 45° and 90°, the Maximum Strain and LaRCO2 failure models were more suitable in terms of accuracy and convergence. Incorporating cohesive surfaces between instances improve nonlinearity prediction of 45° and 90° layups. Small span-to-thickness ratio analysis predicts interlaminar shear failure, delamination, versus large span-to-thickness ratio determine normal stresses to dominate failure in laminate. Multi-fibre orientation and cross-ply layups successfully predict material response described in literature.

4.1 Introduction

Carbon fibre reinforced plastics' (CFRP) high strength, stiffness and customization has great appeal for many applications ranging from aerospace, automotive and sport. Critical for component design and manufacturing process optimization, is the ability to model the effect of fibre orientation on the mechanical behavior of CFRP. The many failure modes involved with CFRP, most specifically delamination, adds to the complexity of the material response prediction. To effectively utilize these materials in components in automotive and aerospace applications, thorough understanding of the material loading response, through failure, must be well understood. To optimize production of these materials, specifically when machining, the fracture mechanics of the CFRP including damage initiation and evolution must be accurately represented. CFRP material loading response research will promote the machining models' effectiveness.

In a CFRP part, the matrix material is used to protect the component from environment and transfer load between the fibers [1]. Many related factors make accurately representing the stiffness response of a CFRP coupon difficult from processing techniques, dispersion and layout of the fibre and matrix, to the interfacial structure between the two constituents [2]. Bending tests provide useful mechanical properties for the CFRP including the flexural modulus, the shear loading and a greater understanding and ability to represent the cohesive interactions between the plies. All are useful properties for characterizing a CFRP material, specifically when studying more complex machining environments. Drilling setups can utilize these insights in an attempt to capture and reduce break-in and break-out damage of the CFRP sample.

Described in a British Standards document “Plastics-Determination of flexural properties" [3], tensile tests are quite cumbersome for brittle materials. Three-point bending tests are preferred due to advantages in sample production, testing repeatability, negated notch sensitivity and predictable failure location. Further, with recommendations made by Mujika [4], the flexural modulus is corrected regardless of the three or four-point bending test and is therefore determined with confidence.

Experimentally, when a unidirectional (UD) CFRP coupon is loaded in tension a non-linear response is observed resulting from damage in the matrix and the interface between the matrix and fibres or plies. This nonlinearity increases as the angle between fibre orientation and the loading direction in the UD-CFRP is increased. Frequently in literature [5, 6, 7], a CFRP has a linear, elastic material response followed by damage initiation and evolution based on time, displacement, or energy; omitting the non-linear response observed experimentally. This representation is not sufficient as it neglects the inter-ply interactions and the prefailure damage in the matrix that contributes to a nonlinear response. To accurately capture the non-linear response of the CFRP coupon, the inclusion of multiple ply layups and most importantly the cohesive interaction between the plies must be modelled.

Finite element (FE) modelling of fibre reinforced polymers (FRP) hinges on the failure model developed by Hashin [8] that encompasses four failure modes, which are i) matrix tension, ii) matrix compression, iii) fibre tension and iv) fibre compression failure. Significant work has developed numerous other failure models. C. Davilla, working at NASA, developed a six-mode failure criteria denoted LaRC02 [9], Max Strain, Max Stress, Tsai-Wu [10], Tsai-Hill [11], Christensen [12], Puck [13] and a Multi-Continuum Theory (MCT) [14] failure criterion, which are described in Table

4.1.

The ABAQUS damage initiation model, based on Hashin's failure criteria, requires the i) longitudinal tensile and compressive strength, ii) the transverse tensile and compressive strength and iii) the longitudinal and transverse shear strength. It also requires a variable alpha, which is the contribution of the shear strength to the fibre tensile failure mode as modified in Hashin [8].

A macro-mechanical approach treats the FRP as an equivalent homogeneous material (EHM). In the past EHM models were not able to identify material constituents' damage nor fibre-matrix interactions however with Multi-Continuum Theory (MCT) EHM model capabilities have increased. The composite stress state within the representative volume element (RVE) are calculated and are critical to predict damage and material failure versus a homogenized average stress and strain [15].

Expanding from Hashin's four failure modes, LaRC02 identifies fibre failure and matrix cracking in UD composites using six failure modes, which are i) fibre failure in tension, ii) fibre compressive failure with matrix compression, iii) fibre compression failure with matrix tension, iv) matrix tension, v) matrix compression and vi) matrix experiencing biaxial compression. Once any of the six failure indices are greater than 1.0, the fibre or matrix has failed. Significantly, rather than the matrix failure preceding the fibre failure with the Hashin setup, these independent failure indices facilitate element deletion and model convergence in transverse loading conditions.

Tsai-Wu and Tsai-Hill are quadratic, stress-based criterion that do not distinguish between failure modes. Tsai-Hill formulation gives more emphasis on the shear contribution. During matrix dominated loading, a small contribution of stress relative to the overall ply failure strength is created, preventing damage evolution and element deletion. This limits the effectiveness of the model. The Christensen criterion utilizes the six fundamental strengths of the composite material to identify two different failure modes in the matrix and fibre. The Puck criterion identifies fiber failure and inter-fiber failure in a unidirectional composite. The inter-fiber failure is the formulation for the matrix damage depending on the plane of loading.

In Abaqus, to utilize alternative failure criteria other than the built-in Hashin model, a user-defined material subroutine must be implemented. This can be accomplished using Helius Progressive Failure Analysis (PFA) software.

Table 4.1: Failure models and criterion for FRP composites [16]

Model	Failure model modes	
Hashin	Fibre Tension (F.T.)	$\left(\frac{\sigma_{11}}{S_{11}^{+}}\right)^2 + \alpha\left(\frac{\sigma_{12}^2+\sigma_{13}^2}{S_{12}^2}\right) \geq 1.0$
	Fibre Compression (F.C.)	$\left(\frac{\sigma_{11}}{S_{11}^{-}}\right)^2 \geq 1.0$
	Matrix Tension (M.T.)	$\frac{(\sigma_{22}+\sigma_{33})^2}{(S_{22}^{+})^2} + \frac{\sigma_{23}^2-\sigma_{22}\sigma_{33}}{S_{23}^2} + \frac{\sigma_{12}^2+\sigma_{13}^2}{S_{12}^2} \geq 1.0$
	Matrix Compression (M.C.)	$\left[\left(\frac{S_{22}^{-}}{2S_{23}}\right)^2 - 1\right]\left(\frac{\sigma_{22}+\sigma_{33}}{S_{22}^{-}}\right) + \frac{(\sigma_{22}+\sigma_{33})^2}{4S_{23}^2} + \dots$ $\dots + \frac{\sigma_{23}^2-\sigma_{22}\sigma_{33}}{S_{23}^2} + \frac{\sigma_{12}^2+\sigma_{13}^2}{S_{12}^2} \geq 1.0$
MCT	Fibre	$\pm A_1^f (I_f^1)^2 + A_4^f I_4^f = 1$ $I_1^f = \sigma_{11}^f$ $I_4^f = (\sigma_{12}^f)^2 + (\sigma_{13}^f)^2$
	Matrix	$\pm A_1^m (I_1^m)^2 - \pm A_2^m (I_2^m)^2 + A_3^m I_3^m + \dots$ $\dots + A_4^m I_4^m - \pm A_5^m I_1^m I_2^m = 1$ $I_1^m \equiv \sigma_{11}^m$ $I_2^m \equiv \sigma_{22}^m + \sigma_{33}^m$ $I_3^m \equiv (\sigma_{22}^m)^2 + (\sigma_{33}^m)^2 + 2(\sigma_{23}^m)^2$ $I_4^m \equiv (\sigma_{12}^m)^2 + (\sigma_{13}^m)^2$
LaRC02	F.T.	$FI_F = \frac{\epsilon_{11}}{\epsilon_1^T}, \epsilon_1^T = \frac{X^T}{E_{11}}$
	F. C. with M. C.	$FI_F = \left(\frac{\sigma_{22}^m}{Y^T}\right)^2 \left(\frac{\tau_{12}^m}{S^L}\right)^2$
	F. C. with M. T.	$FI_F = \left\langle \frac{\lvert\tau_{12}^m\rvert+\eta^L\sigma_{22}^m}{S^L} \right\rangle$
	M. T.	$FI_M = \left(\frac{\sigma_{22}}{Y^T}\right)^2 + \left(\frac{\tau_{12}}{S^L}\right)^2$
	M. C.	$FI_M = \left(\frac{\tau_{eff}^T}{S^T}\right)^2 + \left(\frac{\tau_{eff}^L}{S^L}\right)^2$
	M. Biaxial C.	$FI_M = \left(\frac{\tau_{eff}^m{}^T}{S^T}\right)^2 + \left(\frac{\tau_{eff}^m{}^L}{S^L}\right)^2$
Puck	Fibre Tension	$\frac{1}{\epsilon_{1T}}\left(\epsilon_1 + \frac{v_{f12}}{E_{f1}} m_{\sigma f}\sigma_2\right) = 1$
	Fibre Kinking	$\frac{1}{\epsilon_{1T}}\left(\epsilon_1 + \frac{v_{f12}}{E_{f1}} m_{\sigma f}\sigma_2\right) = 1 - (10\gamma_{21})^2$
	Inter-Fibre Failure A.	$\sqrt{\left(\frac{\tau_{21}}{S_{21}}\right)^2 + \left(1 - p_{\perp\Vert}^{(+)}\frac{Y_T}{S_{21}}\right)^2\left(\frac{\sigma_2}{Y_T}\right)^2} + \dots$ $\dots + p_{\perp\Vert}^{(+)}\frac{\sigma_2}{S_{21}} = 1 - \left\lvert\frac{\sigma_1}{\sigma_{1D}}\right\rvert$
	Inter-Fibre Failure B.	$\frac{1}{S_{21}}\left(\sqrt{\left(\tau_{21}^2 + \left(p_{\perp\Vert}^{(-)}\sigma_2\right)^2} + p_{\perp\Vert}^{(-)}\frac{\sigma_2}{S_{21}}\right) = 1 - \left\lvert\frac{\sigma_1}{\sigma_{1D}}\right\rvert$
	Inter-Fibre Failure C.	$\frac{1}{\left(2\left(1+p_{\perp\perp}^{(-)}\right)\right)}\left(\left(\frac{\tau_{21}}{S_{21}}\right)^2 + \left(\frac{\sigma_2}{R_{\perp\perp}^A}\right)^2\right)\frac{R_{\perp\perp}^A}{(-\sigma_2)} = 1 - \left\lvert\frac{\sigma_1}{\sigma_{1D}}\right\rvert$
Max Strain	$\left(\frac{\epsilon_{11}}{\epsilon_{11}^{max+}}, \frac{\epsilon_{11}}{\epsilon_{11}^{max-}}, \frac{\epsilon_{22}}{\epsilon_{22}^{max+}}, \frac{\epsilon_{22}}{\epsilon_{22}^{max-}}, \frac{\epsilon_{12}}{\epsilon_{12}^{max-}}\right) \geq 1.0$	

Research by Huang et al. [17] used cohesive elements but were not validated by experiments. Ullah et al. studied dynamic bending tests of woven CFRPs using cohesive elements, described sensitivity to the size of cohesive zone elements that needs to be optimized in the interface region [18]. Ullah et al. studied woven composites under large-deflection and compared experimental results to a 2D FE model highlighting the interface zone cohesive elements were highly sensitive to mesh and stiffness magnitudes [19]. Petrescu et al. determined the flexural modulus of UD-CFRP samples using various span lengths, noting bending tests should be used preferentially for brittle materials for which tensile tests are difficult [2, 3]. Naresh et al. study the effect of fibre orientation in bending on CFRP and glass-fibre-reinforced-polymers (GFRP). Naresh et al. described fibre-matrix debonding for the 0°, 45° and 90°, setups and increased flexural strain due to delamination hindering crack propagation for cross-ply layups [20]. Niezgoda and Derewonko create a macro-micro scale FE model using beam elements to represent the fibre constituent reducing the computational cost by 60% versus the micro-scale model [21].

This research investigates the improved FEM representation of three-point bending tests when modelled with multi-ply layups and the cohesive interaction with damage between them. In this study, repeatable, accurate experimental three-point bending testing is achieved by use of an increased sized punch. This ensures fracture initiates on the bottom surface in tension so the Aramis strain camera can record the fracture. A thorough study was conducted to effectively model a CFRP composite using commercial finite element software ABAQUS. A sensitivity analysis regarding element type, mesh convergence, scaling techniques, damage initiation and evolution methods were studied with limitations described. Convergence of damage evolution dominated by transverse loading was determined to be limited to specific failure models and was discussed in detail in section Phase V - Experimental versus alternative FE failure criteria. The significance of modelling multiple ply layups using cohesive surface interactions demonstrates the ability to capture the nonlinear loading response of the sample when loaded in various fibre orientations and the samples' sensitivity to delamination between plies.

4.2 Experimental work

The UD-CFRP samples were machined from sheets made by ACP Composites Inc. The manufacturer estimated technical properties are described in Table 4.2 [22]. These samples are produced using an Autoclave curing process at high temperature and pressure to ensure a repeatable, high-quality, panel with minimal voids, waves or buildups. The CFRP is made from a pre-impregnated unidirectional layup with 60% fibre volume.

All CFRP samples and the production of the punch was created in house on a 3-axis mill. The CFRP samples were machined with a 6 flute, diamond coated endmill. The UD-CFRP was purchased in 12"x36" panels and machined further into repeatable 6"x6" sections. The sections were aligned with the machine axis and then machined at 0°, 45°, and 90°, to minimize any variability in sample fibre direction.

The initial bending setup shown in Figure 4.1 a) involves two supports with a diameter of 8.5 mm and a circular punch with a 6.5 mm diameter with the supports span held at 29.6 mm. Preliminary tests showed that the samples' fracture for the 0°, experiments were failing in compression on the top side of the surface due to the concentrated load. The strain and force-displacement data correlated well, but to capture the strain at fracture with the Aramis camera, failure would need to occur on the bottom surface. A modified bending setup was created with a newly designed punch with a greater diameter of 12.5 mm as shown in Figure 4.1 b). This reduced the loading concentration in the sample caused by the loading of the small diameter punch, leading to failure in tension on the underside of the CFRP test sample.

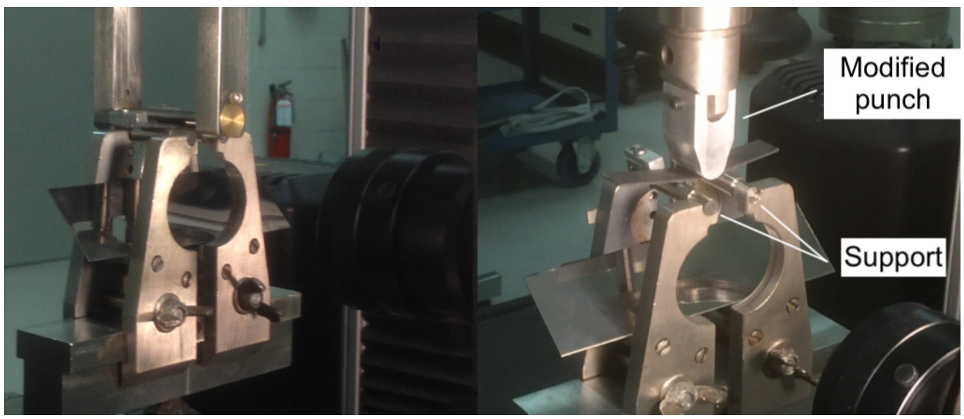

Figure 4.1: a) Initial 3-point bending b) Modified punch 3-point bending experimental setups

Table 4.2: Standard Modulus (SM) CFRP - material properties [22]

SM UD-CFRP	0°	90°
Longitudinal Modulus (GPa)	135	10
Transverse Modulus (GPa)	10	135
In-plane Shear Modulus (GPa)	5	5
Major Poisson's ratio	0.3	0.3
Ultimate (Ult.) Tensile Strength (MPa)	1500	50
Ult. Comp. Strength (MPa)	1200	250
Ult. In-plane Shear Strength (MPa)	70	70
Ult. Tensile Strain	1.05	0.5
Ult. Comp. Strain	0.85	2.5
Density (g/cm^3)	1.6	

The Aramis camera was used to measure the strain of the bottom-outer surface and the load and displacement output was recorded simultaneously. To facilitate the strain measurement, the camera was positioned in line with a mirror at 45°, reflecting onto the bottom surface of the coupon. Several test samples were used to verify the camera and machine calibration. Following this, samples at 0°, 45°, and 90°, fibre orientation, with respect to the punch, were loaded through failure.

The Instron Dual Column Universal Testing system was used to facilitate the three-point bending experimental setup shown in Figure 4.2 a). The modified punch punch shown in Figure 4.2 b) was loaded at 1 mm/min. Displacement accuracy is stated by manufacturer as the greater of +/- 0.02 mm or 0.15% of displacement. Load accuracy is +/- 0.5 % of reading down to 1/200 of load cell capacity, +/- 1.0 % of reading from 1/200 to 1/500 of the load cell capacity [23]. The 90°, samples average failure was recorded at 155 N which is between the 1/200 to 1/500 of the load capacity range and therefore, the latter of the accuracies applies. The Aramis 3D camera records surface strain at 6MP and 25 Hz with a minimum measurement area or 10x8 mm [24].

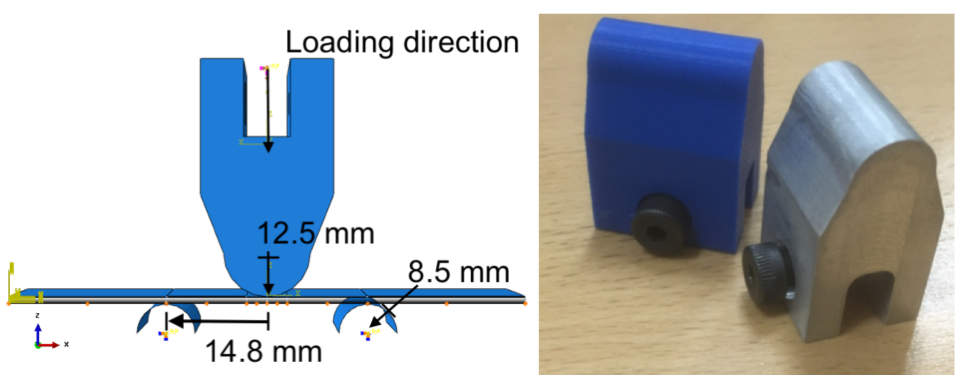

Figure 4.2: a) Three-point bending setup b) Modified punch

Difficulties controlling the fracture location of the fibre reinforced polymers (FRP) described in tensile experiments [16] are not encountered with bending tests. The fracture occurred in the gauge region below the punch and experimental data was efficiently captured, shown in Figure 4.3. The force of the sample is plotted against the displacement of the punch. The average of these tests was then compared to the FE model. The stress is then determined via bending theory and plotted versus the measured strain.

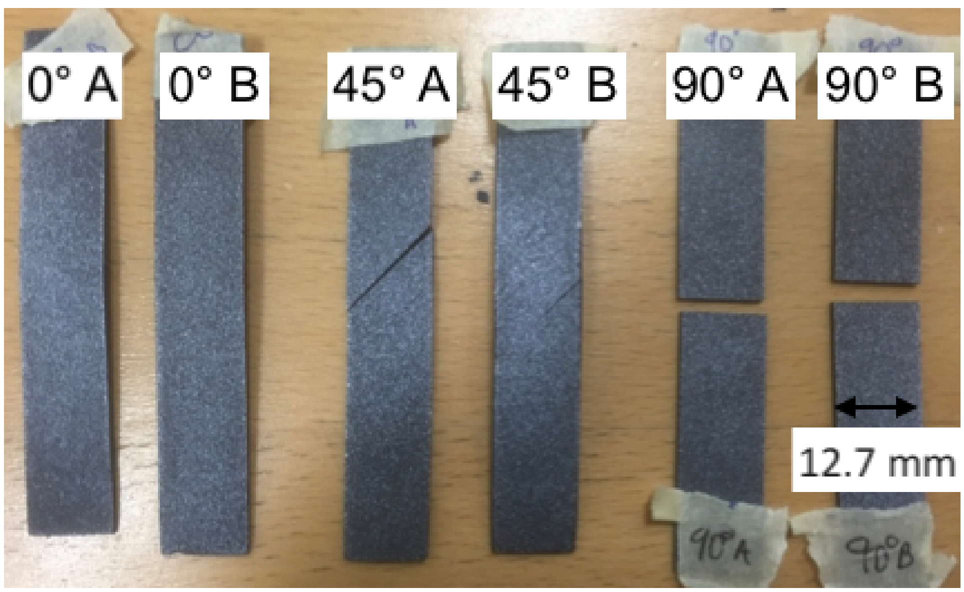

Figure 4.3: Experimental samples (0°, 45°, 90°,)

4.3 FEA Modelling

The three-point bending FE model represents the experimental setup using two rigid support surfaces and one rigid indenter surface used to provide the loading into the workpiece, as shown in Figure 4.4. The rigid members are three-dimensional surfaces, while the workpiece sample is modelled as one 3D deformable member, subdivided with 10 plies using a composite layup manager and a thickness of 0.11 mm per ply. Material properties for the CFRP were determined through the tensile experiments and FE models, results are detailed in [16]. Symmetry in the YZ plane was utilized to reduce the computation time by splitting the workpiece in half, thereby assuming only one support and half an indenter.

Referring to Figure 4.4, the x-axis shown would be parallel to the fibres for the 0° tests. When the fibres are parallel to the y-axis (into page) the 90 degree setup is achieved and at 45° to the x-axis, in the x-y plane, for the 45 degree tests. To control the loading in the model, two reference points were created, one for the indenter (RP) and the other for the support ($RP_{support}$). Using an equation constraint, the indenter nodes will be controlled by the reference point (RP). Similarly, the support nodes are controlled by the reference point ($RP_{support}$). The equation constraint maps a set of nodes to a specific node (usually a reference point), via a coefficient. When the coefficient is equal to -1, the node set moves identical to the reference point based on the set degrees of freedom.

When this setup is used, the load constraints become more efficiently applied. A fixed encastre constraint ($U1 = U2 = U3 = UR1 = UR2 = UR3 = 0$) is applied to the support reference point. There is symmetry applied to the model via the YZ plane and to the newly created edge at the bottom of the indenter ($XSYMMU1 = UR1 = UR3 = 0$) as shown in Figure 4.4. The loading velocity in the negative z-axis direction at the 1 mm/min rate is applied to the indenter reference point (RP).

Elements progress through damage evolution and fail, were allowed to be removed. To allow the indenter and the newly exposed elements to contact one another an

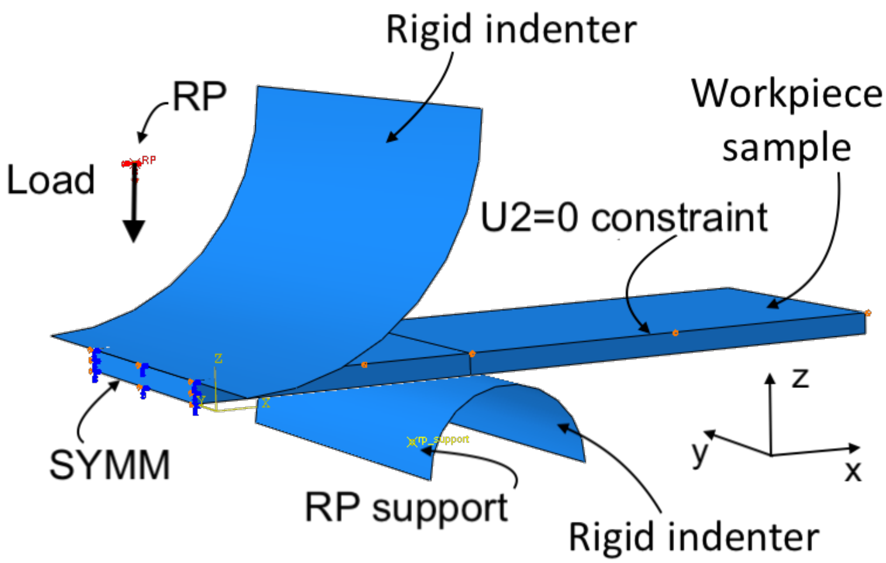

Figure 4.4: Bending FEA setup

interior node set must be created. This is done by creating an element set based on the CFRP sample node set and adding the parameter interior. The contact regime must be expanded to include the new surfaces created and is accomplished using a Global property assignment that is generally programmed as frictionless. The Global property assignment is required for the internal surface creation. The frictionless assignment is used to reduce computational time for the rest of the model. The specific property assignment is applied to the surface interactions between the support and CFRP and the indenter and CFRP, which used friction and a hard contact property to prevent penetration of the master and slave surfaces. This allows the internal newly formed surfaces to interact with the associated friction forces programmed with the contact property.

Failure models and progressive damage techniques have been studied to determine the most effective in terms of accuracy, convergence and efficiency. Without convergence, FE models render useless as damage evolution and element deletion is a necessity in this research. Furthermore, cohesive modelling considerations between plies is studied accomplished by cohesive zones or cohesive surfaces. Marzi et al. [25], has shown cohesive modelling to have significant effect on the realistic loading response of the UD-CFRP sample.

4.3.1 Cohesive surface modelling

To capture the nonlinear loading response of the CFRP resulting from matrix and delamination damage, the geometry is divided into plies with cohesive surface interactions considered. The bending sample has a thickness of 1.1 mm and was divided into 10 sections to represent the ply thickness. Node sets are created on the top and bottom surfaces to be used for cohesive interactions. Highlighted in Figure 4.5, is the ply n bottom surface and ply $n+1$ top surface cohesive interaction for the 10 plies. A General Contact-Explicit interaction must be created [26]. A global property assignment must be applied in addition to the individual property assignments between the two plies to facilitate the interior node set creation for eroding elements.

To alleviate some computational time brought on by the inclusion of cohesive surfaces, symmetry is applied. First, the YZ symmetry halves the model as described in the base model. Rather than using the original specimen width of 12.7 mm a 1 mm wide unit width specimen was modelled. Further applying symmetry in the ZX plane, the 1 mm specimen is reduced to a 1/3 mm wide sample symmetric in the ZX plane on both sides. After the symmetric boundary conditions were applied, a velocity condition was applied to a reference point, which was tied to a set of loading nodes as done with the base model.

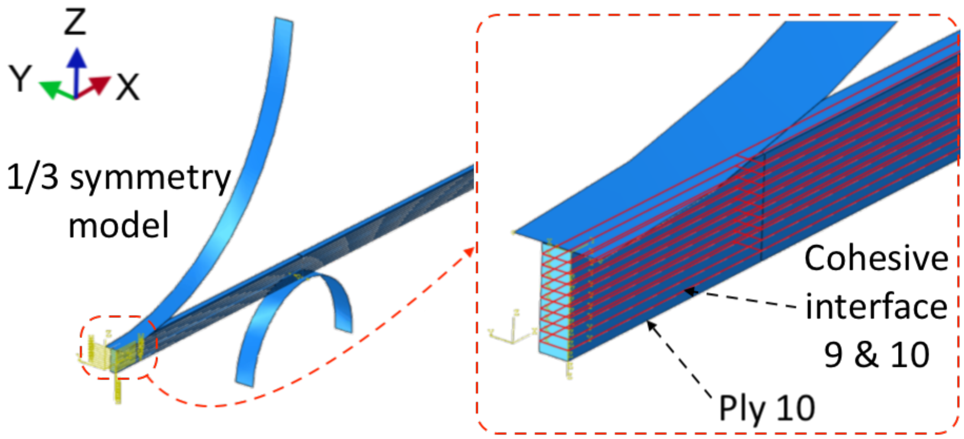

Figure 4.5: Symmetric (1/3) unit thickness model

To model the cohesive surfaces, a contact property is created including three main properties: normal behaviour, cohesive behaviour and damage. Normal behaviour determines the contact behaviour in the normal direction and is controlled by the “hard" contact pressure overclosure relationship. The cohesive behaviour allows for any slave nodes that experience contact, whether initially or after some loading, to be controlled by a traction-separation behaviour. The most computationally efficient method in ABAQUS is to have an uncoupled behaviour using stiffness in the normal, secondary and tertiary axis (K_{nn}, K_{ss} and K_{tt}) and the separation displacements in the normal, first shear and secondary shear directions are denoted by δ_n, δ_s and δ_t respectively. Therefore, the elastic behaviour of the contact stress, t, is shown in Equation 4.1 [26].

$$t = K\delta \tag{4.1}$$

The damage modelling parameters are the most influential of the cohesive surface modelling factors. It involves identifying a damage initiation point and controlling the damage evolution. After much investigation, the damage initiation criteria used is a maximum stress (MAXS) criteria and is expressed as follows in Equation 4.2.

$$MAXS = max\left\{\frac{\langle t_n \rangle}{t_n^o}, \frac{t_s}{t_s^o}, \frac{t_t}{t_t^o}\right\} \tag{4.2}$$

When using MAXS criteria, the peak values of the contact stress are the normal, and two shear tractions along the local 1- and 2-directions, denoted by t_n^o, t_s^o and t_t^o respectively. Once the ratio of the current contact stress in the normal, secondary and tertiary axis reach one, the damage has been initiated. The $\langle\rangle$ symbol is the Macaulay bracket allowing for integration over a discontinuous curve [26]. The discontinuous curve occurs because a purely compressive state causes no stress that would separate the cohesive surface and therefore no damage.

Once damage is initiated, the damage evolution will be initiated whereby the stiffness of the cohesive surface will be degraded. To control the damage evolution a damage variable, D, evolves from zero to one. There are two methods used to model the damage evolution, specifying a failure separation or an energy-based separation. After extensive work, and affirming common difficulties highlighted by researchers for developing failure energies values, the failure will be controlled by an effective separation at complete failure, relative to the initiation of damage [9, 15, 26]. The stiffness is represented by Equation 4.3.

$$K_{nn} = K_{ss} = K_{tt} = \alpha E_{33}^{PLY} / t^{PLY} \tag{4.3}$$

where α is a parameter with a suggested value of 50, t^{PLY} is the thickness of the bonded plies and E_{33}^{PLY} is the normal Modulus of the CFRP; this suggests that the stiffness is 1.76e6 MPa. Described by Helius PFA, the stiffness is of magnitude stiff enough to provide load transfer, but not too stiff that unauthentic fluctuations occur in the output. The initial strength estimate should represent the normal strength of the ply, shown in Equation 4.4.

$$\frac{S_{12}^{PLY} + S_{23}^{PLY}}{2} = S_s = S_t = 70MPa \tag{4.4}$$

The damage evolution was set to a displacement of 0.001 mm with a linear softening. The cohesive interaction significantly increases the ability to capture the non-linear response frequently overlooked in FE analysis.

To develop an efficient base model before investigating the damage initiation and evolution capabilities of CFRP modelling, a parametric study isolated key modelling inputs individually, while all other model inputs were fixed. Table 4.3 describes the parameters investigated during each phase of analysis including: Phase I - mesh refinement, Phase II - number of through thickness elements, Phase III - mass scaling and Phase IV - time scaling. This work precedes the study of the various failure models and the incorporation of cohesive surface interactions between plies, which are discussed in Phase V and Phase VI.

Table 4.3: Comprehensive FEA modelling analysis

Study	Parameter/Cases
Phase I - Mesh refinement	Minimum element size in gauge region 0.1 mm - 0.5 mm (5 cases)
Phase II - Through thickness	Number of elements through thickness of sample 1, 2, 3, 5, 6
Phase III - Mass scaling	Modifying minimum time step increment $1 \cdot 10^{-3}$, $1 \cdot 10^{-4}$, $1 \cdot 10^{-5}$, $5 \cdot 10^{-6}$, $1 \cdot 10^{-6}$, NONE
Phase IV - Time scaling	Modifying analysis duration and loading rate 1x, 10x, 100x, 100x*
Phase V - Failure models	ABAQUS-Hashin 0, 45 & 90 degree VUMAT (Puck, MCT, LaRC02, Max Strain, Hashin) 0°, 45°,& 90°,
Phase VI - Cohesive surfaces	MAXS damage init. & Displacement damage evol. 0°, 45°,& 90°,

4.3.2 Phase I - Mesh refinement

Edge pairs were created to apply seeding and modify element size in the model, illustrated in Figure 4.6. Through five separate analysis, the edge seeds were refined. In the critical gauge section of the bending test edge A, the most refined seeding was 0.1 mm with a bias expanding to 0.15 mm away from the centre. For the fifth setup, the most coarse mesh, edge A was seeded with 0.5 mm spreading to 0.75 mm away from centre. A similar method of refinement was applied to the other edge pairs and is tabulated in Table 4.4.

The 0° , bending test loading response for the five meshed models is shown in Figure 4.7. The coarsest model investigated included 2470 elements and completed in 8.34 hours. The most refined model involved 62080 elements and would take 124.36 hours however the model was stopped after 63.2 hours at the initiation of failure.

Table 4.4: Three-point bending mesh convergence; seed size (mm)

Edge	Bias	Mesh I	Mesh II	Mesh III	Mesh IV	Mesh V
Total number of elements		62080	15360	11578	3840	2470
Computation time (Hours)		124.36	63.83	31.83	20.37	8.34
Force (N)		372.21	377.00	375.18	285.11*	358.84
A	Single	0.1-0.15	0.2-0.3	0.3-0.45	0.4-0.6	0.5-0.75
B	None	0.1	0.2	0.3	0.4	0.5
B2	None	0.1	0.2	0.3	0.4	0.5
B3	None	0.25	0.5	0.75	1.0	1.25
C	Single	0.15-0.5	0.3-1.0	0.45-1.5	0.6-2.0	0.75-2.5
D	Single	0.5-1.0	1.0-2.0	1.5-3.0	2.0-4.0	2.5-5.0
E	None	# of elements is 5				

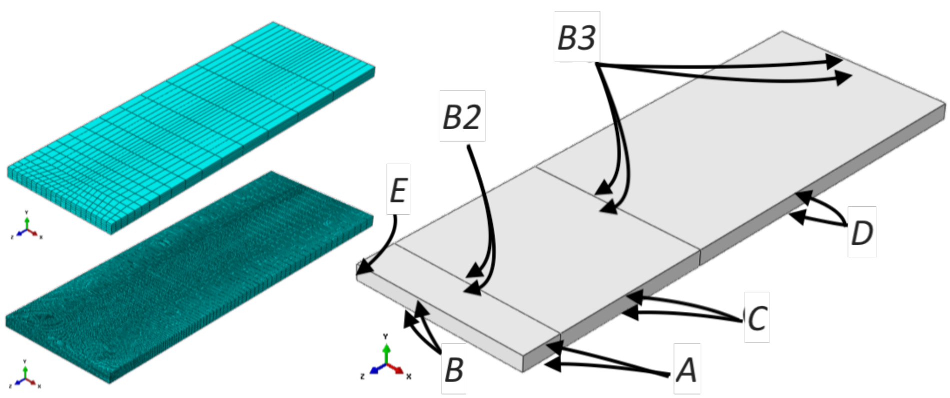

Figure 4.6: Mesh refinement edge seeding

Mesh III balances computational expense and model accuracy referencing the convergence of failure prediction through mesh refinement. Mesh III has 11578 elements and a CPU time of 31.83 hours. With one additional iteration of mesh refinement there is an increase to 15360 elements and a computation time of 63.83 hours, which was an increase in computation time by 100.5%. The model prediction of maximum reaction force prior to failure is within 0.48% or 1.8N for these two models. This difference is smaller than the variance in sample geometry and is therefore not significant versus the computational savings.

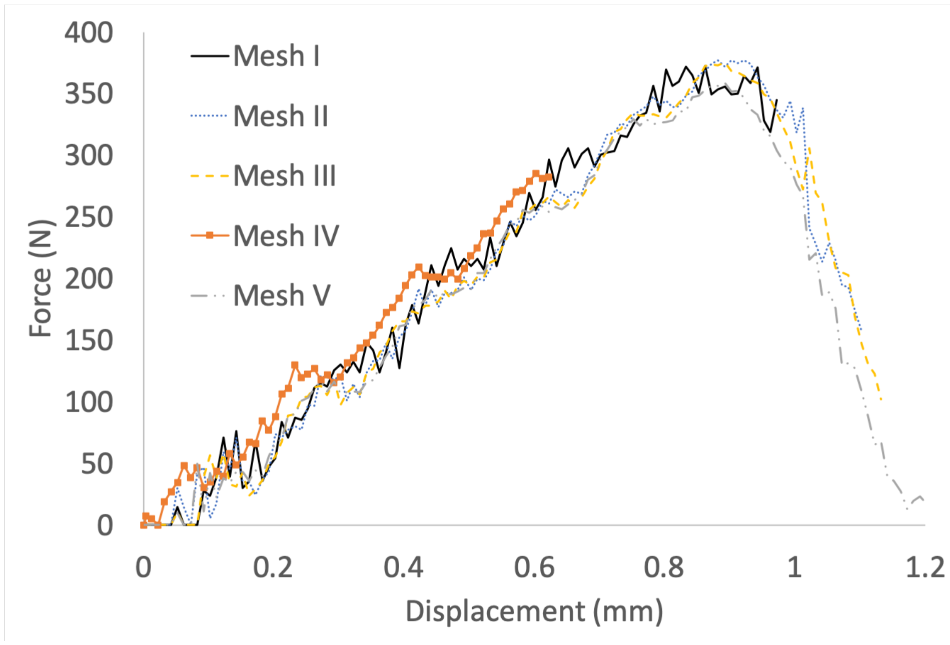

Figure 4.7: Effect of mesh refinement on displacement versus force response

4.3.3 Phase II - Through thickness element count

When the fibre-reinforced composites are subject to loading, the stress induced in the specimen is focused in the plane rather than through the thickness. This is due to the stacked ply structure with CFRPs, shown in Figure 4.5 dividing the planar geometry into ten thinner planar sections, the planar geometry is thin compared to the width and length of the specimen. Material failure is dominated by longitudinal (fibre), transverse (matrix) and in-plane shear strengths and not by stress in the tertiary (thickness) axis. To achieve accurate material representation regarding the through thickness geometry, solid or continuum shell elements should be used and not conventional shell elements. To accurately model the ply interaction and progressive failure of those plies, the appropriate number of elements through the thickness should be determined.

In Figure 4.8, the resulting convergence on failure prediction by adding elements through the thickness of the geometry is illustrated. With one element modelled through the thickness of the geometry the failure force is 367.4 N versus a failure force prediction of 378.9 N when six elements are modelled. This is a difference in prediction of 3.03%. The fracture prediction with five elements through the thickness is within 0.99% of the prediction with six elements through the thickness. This is an acceptable difference as the variation in the geometry of the samples for the experiments was greater and results in a reduction in computation.

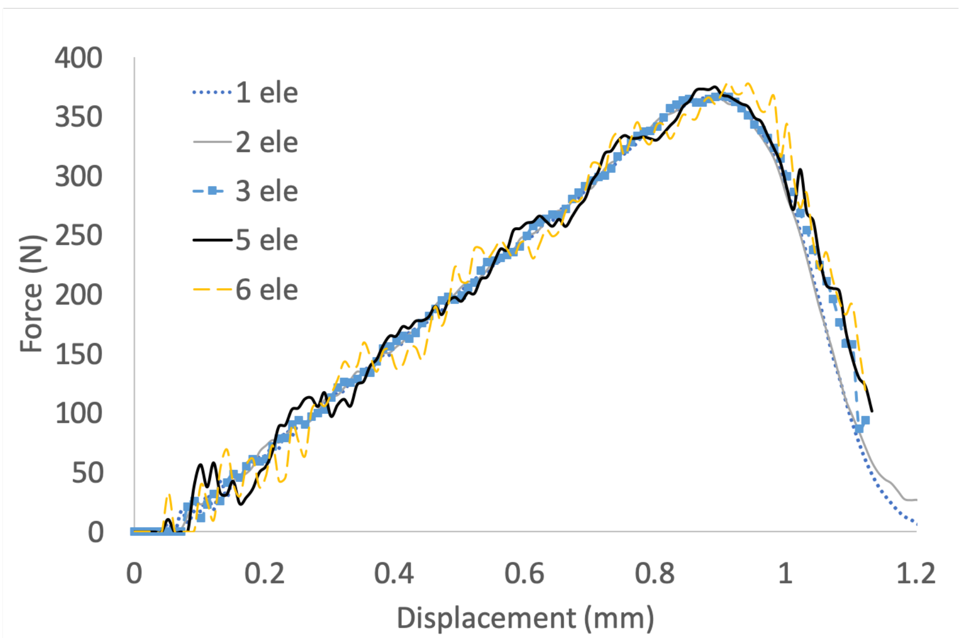

Figure 4.8: Effect of through thickness element count on displacement versus force response

4.3.4 Phase III - Mass scaling

Scaling an analysis is a necessary technique with failure prediction in explicit models, especially involving models with refined mesh creation and numerous damage state variables. Scaling techniques can be applied though time scaling and mass scaling. In ABAQUS, the minimum stable time increment for an explicit dynamic analysis is expressed in Equation 4.5. The dilatational wave speed is given in Equation 4.6.

$$\Delta t = L^e / c_d \tag{4.5}$$

$$c_d = \sqrt{\frac{E}{\rho}} \tag{4.6}$$

With a characteristic element length based on the model mesh refinement and the dilatational wave speed based on material properties of the CFRP, the stable time increment is approximately $1.0 \cdot 10^{-9} s$. This would result in a model requiring years to complete the computation. This is not economical and therefore motivation to validate the use of scaling in the FE model. The benefit of employing mass scaling, is the time step limit, applies to the smallest elements first until satisfied. Therefore, if appropriately used will not have significant impact the results, just reduce the computation time. In quasi-static analysis where strain rate is low, the kinetic energy of the model is low compared to the internal energy of the model. Accuracy can be maintained by mass scaling while keeping the kinetic energy of the model to less than 10% of the internal energy [26].

Illustrated in Figure 4.9, adding mass scaling based on a target time increment size of $1.0 \cdot 10^{-5} s$, an unwanted harmonic response is produced in the force-displacement plot resulting in an over prediction of failure by 4.40% and a model computation time of 20.42 hours.

Due to the increased mass the load output of the CFRP is altered in response to the changes in the models mass and inertia. When modelling with a target time

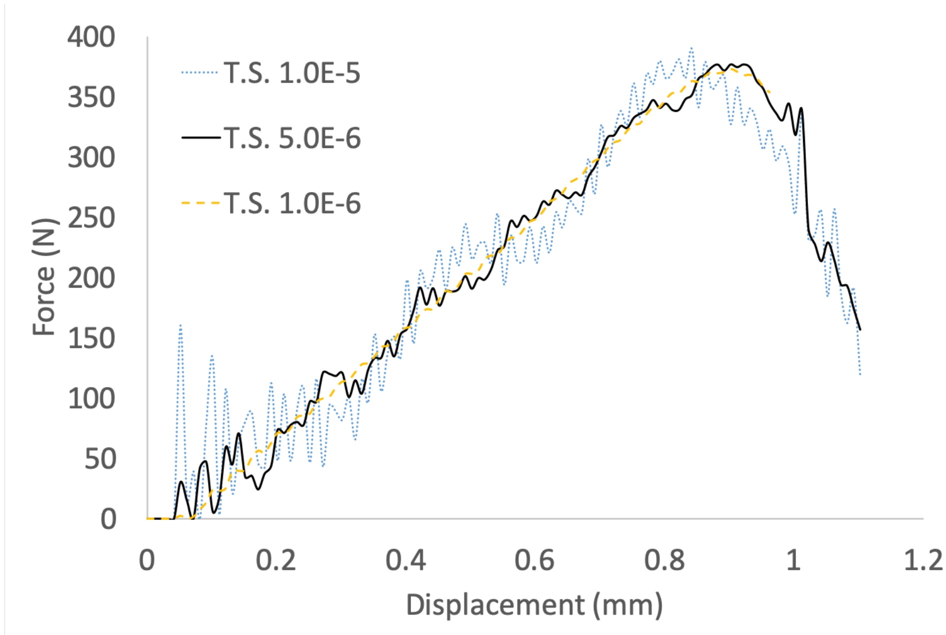

Figure 4.9: Effect of mass scaling on displacement versus force response

increment step (T.S) of $1.0{\cdot}10^{-6}s$ the commutation time increases by nearly seven times to 142.7 hours, but reduces the unwanted harmonic response. To find an appropriate material response and computational expense, the ideal T.S. is suggested at $5.0{\cdot}10^{-6}s$. This magnitude balances accuracy versus computation expense and ensures the artificially increased density does not alter the loading response. The outcome is a computational time of 37.4 hours and a deviation of only 1.01% in the overall fracture force prediction. Notice the significant reduction in the harmonic response of the loading with this target increment shown in Figure 4.9. Without the use of mass scaling the identical model would take 2.82 years to complete.

4.3.5 Phase-IV - Time scaling

Time scaling provides computational benefits by increasing the loading rate rather than using the natural time of the experiment, a loading rate of 1 mm/min. In Figure 4.10, the simulated time decreases from 120.0 seconds (s) to 1.2 s, a reduction of 100 times. The velocity constraint was manipulated to ensure an equivalent amount of displacement. By reducing the loading time and maintaining an equivalent load displacement, a reduction of computation time from 172.5 hours to 35.6 hours is achieved.

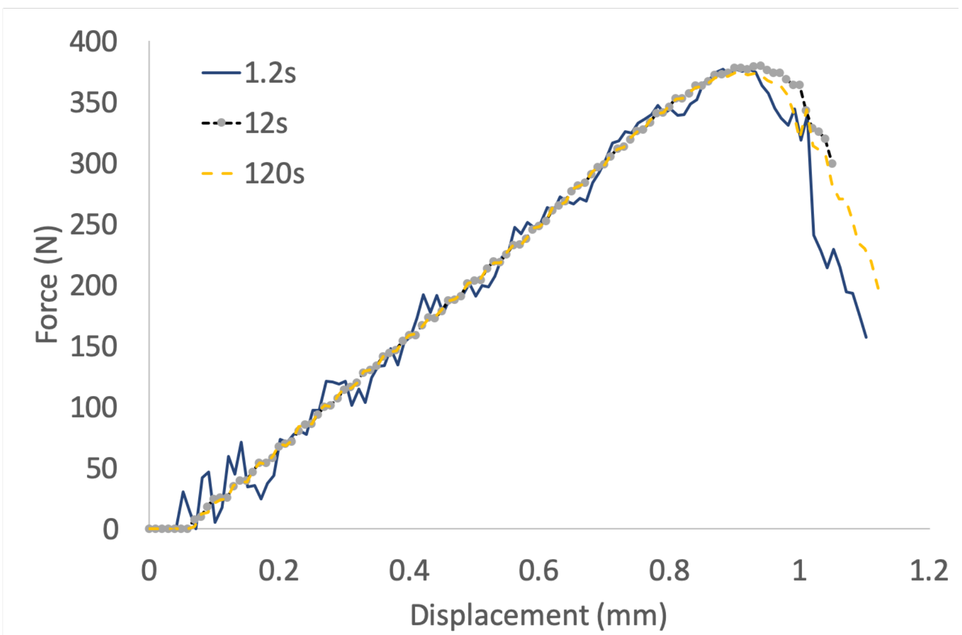

Figure 4.10: Effect of time scaling on displacement versus force response

To ensure an accurate comparison of the effect of time scaling, the mass scaling factor must be reduced accordingly. In Figure 4.11, notice the unwanted harmonic response during loading for the 1.2 s setup which used mass scaling set to a target time step (T.S.) increment of $1.0{\cdot}10^{-4}s$. When the mass scaling is reduced, the time scaling has very little effect on the loading response. Notice the improved response in the alternative setup using the same loading time of 1.2 s, however reduced mass scaling to a target time increment of $1.0{\cdot}10^{-6}s$. Overall, a 1.68% difference in failure force prediction is observed between the 120 s and 12 s setups and a 0.13% difference between the 120 s and 1.2 s setups when effectively time and mass scaled (1.2 s T.S. = $1.0{\cdot}10^{-6}s$, 12.0 s T.S. = $1.0{\cdot}10^{-5}s$, 120.0 s T.S. = $1.0{\cdot}10^{-4}s$). A combination of time scale by an order of ten and mass scaling to a minimum T.S. of $1.0{\cdot}10^{-5}s$ is used in models studied moving forward.

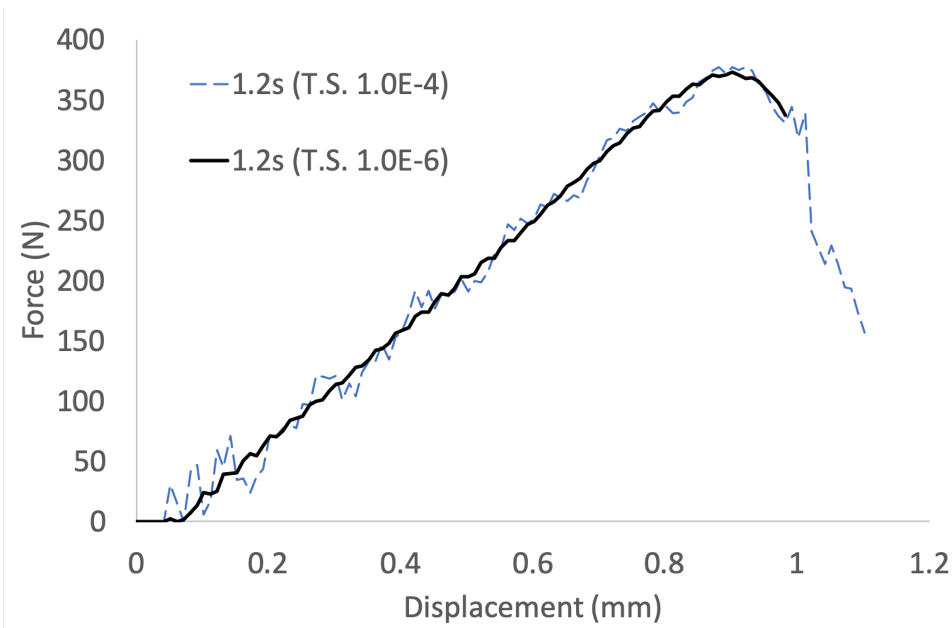

Figure 4.11: Effect of time scaling on displacement versus force response with adjusted mass scaling

By completing the investigation of the mesh convergence, through thickness element count, mass scaling and time scaling techniques a highly accurate, efficient three-point bending model has been developed. Following on from here, a comparison of various failure models were studied to determine their effectiveness in predicting failure.

4.4 Results & Discussion

4.4.1 Phase V - Experimental versus alternative FE failure criteria

In Figure 4.12, the 0° fibre layup three-point bending test simulations using various FRP failure criteria, described in Table 4.1, are plotted. For a particular failure criterion shown in Table 4.1, damage initiation is satisfied based on the response to the loading configuration in the FE model. To avoid any model tuning and facilitate model convergence, damage evolution was controlled by default instantaneous degradation settings (matrix post-failure stiffness 0.1 and fibre post-failure stiffness 0.01). The instantaneous degradation, a misnomer, reduces the strength of the elements to the post-stiffness values over a time period; this was consistent throughout an investigation based on the loading rate. The loading in this orientation, with the bending punch perpendicular to the fibres, demonstrates the anisotropic nature of the UD-CFRP, with great strength and failure controlled by the elastic-brittle fibre; minimal matrix effect. With a fibre dominated loading, the material responses are similar as the various FRP models use the same linear-elastic fibre response prior to damage. The difference is the failure prediction modelled by damage initiation and damage evolution. The failure models from Table 4.1, determines the point at which damage is predicted to initiate and continues until the criteria has been satisfied for the given failure index. The loading response prior to damage is purely elastic and identical between modes. The evolution parameters determine how the model converges towards failure. The damage evolution parameters were the same for each model in this investigation.

In Figure 4.12, the force-displacement prediction from the FE models, versus the 0° fibre orientation experiment, demonstrates good agreement. There is no difference between the failure prediction of the MCT, Hashin and Puck models, as illustrated in Figure 4.12 and differ from the fracture force of the experiment by 3.13%. The LaRC02 model under predicts the failure by 4.18% and the Max Strain prediction is 5.71% greater. The harmonic loading response prevalent in Figure 4.12, is due to the assertive scaling techniques used and is minimized for final model creation.

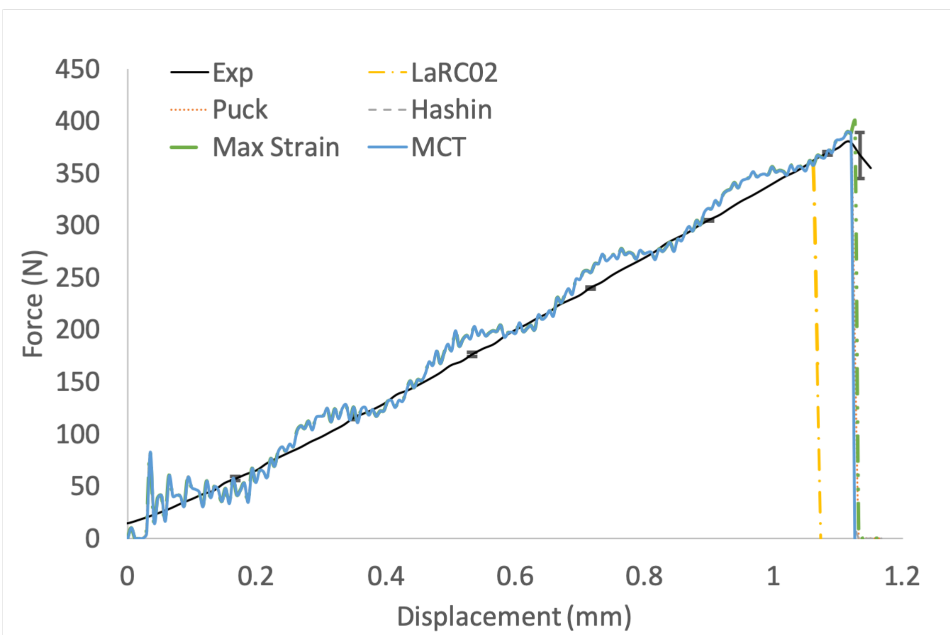

Figure 4.12: Comparison between failure models and experimental on displacement versus force response with 0° fibre orientation

Figure 4.13 shows the displacement-force diagram for 45° fibre orientation under a bending configuration. The loading response demonstrates good agreement in the loading versus displacement rate. The Max Strain failure model drastically underestimates the failure prediction, however, effectively models the fracture event fully with element deletion. MCT, Hashin and Puck failed to model the fracture event and continue to load indefinitely. The inability to converge on a loading response with the deletion of failed elements, is controlled by the failure mode. If the damage evolution is initiated by the matrix failing, followed by the fibre failure, convergence will not occur for shear and transverse loading situations. This is shown in Figure 4.14 Set I: iii, iv, v with no element deletion even when extreme displacements of greater than 2.0 mm are reached. An infinite symbol is marked on Figure 4.13 to illustrate the inability to predict failed elements and trigger element deletion for the MCT, Hashin and Puck failure models.

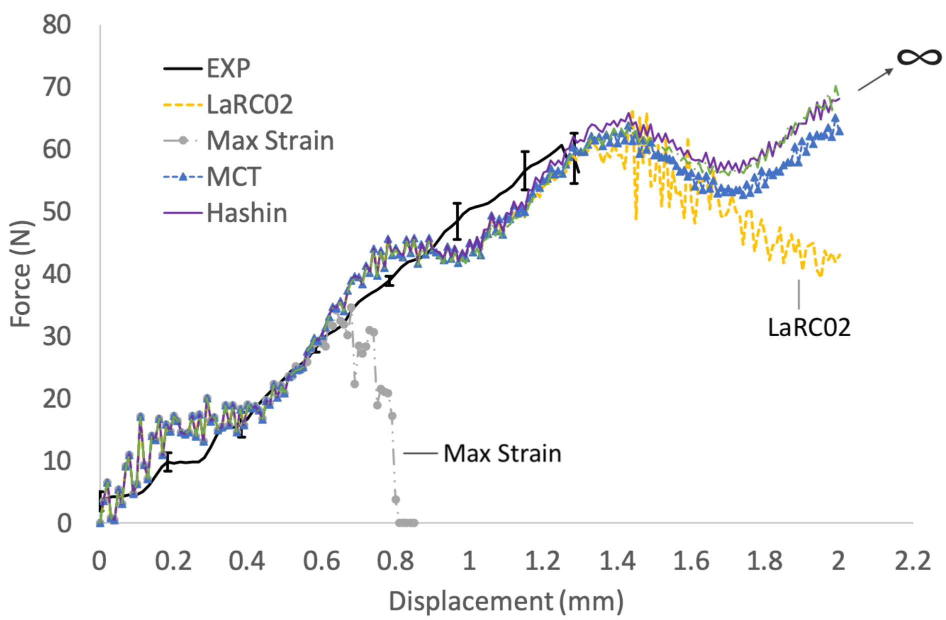

Figure 4.13: Comparison between failure models and experimental on displacement versus force response with 45° fibre orientation

When the stress on an element is large enough to cause matrix damage, the stiffness of this element reduces to a post-failure matrix stiffness. The material will follow a degradation of stiffness process, based on a time-period or energy release. Once the degradation of stiffness of the element has occurred, the element cannot bear load, at least no more than the post-failure stiffness allows. Therefore, the stress in the element will never increase enough to cause failure in the fibre and hence no deletion will occur. This convergence issue occurs at any significantly off-angle loading (45° to 90°) and no element deletion will be initiated. The LaRC02 successfully predicted material response and progressed through failure with element deletion; model timed out but did not suffer convergence issues.

Analogous to the 45° bending models, the loading response of the 90° fibre layup bending experiments are well represented as shown in Figure 4.15. The inability to capture the fracture with the MCT, Hashin and Puck models is experienced again. This is shown in Figure 4.14 Set II: iii, iv, v with no element deletion even when extreme displacements of greater than 2.0 mm are reached. The Max Strain model under predicts failure unacceptably, whereas the LaRC02 failure model accomplishes failure prediction well with respect to displacement and failure load. A 15.1% difference in displacement and a 0.3% difference in failure force was observed with the LaRC02 model. The larger difference in the failure displacement prediction was a result of the harmonic loading response. While the experiment was reaching critical load for the 90° configuration, the FE response was in the trough portion of the wave response, experiencing a reduced load, thereby delaying the onset of damage. To negate this effect, mass scaling techniques will be reduced while concurrently incorporating symmetry simplifications in the model to reduce computational expense.

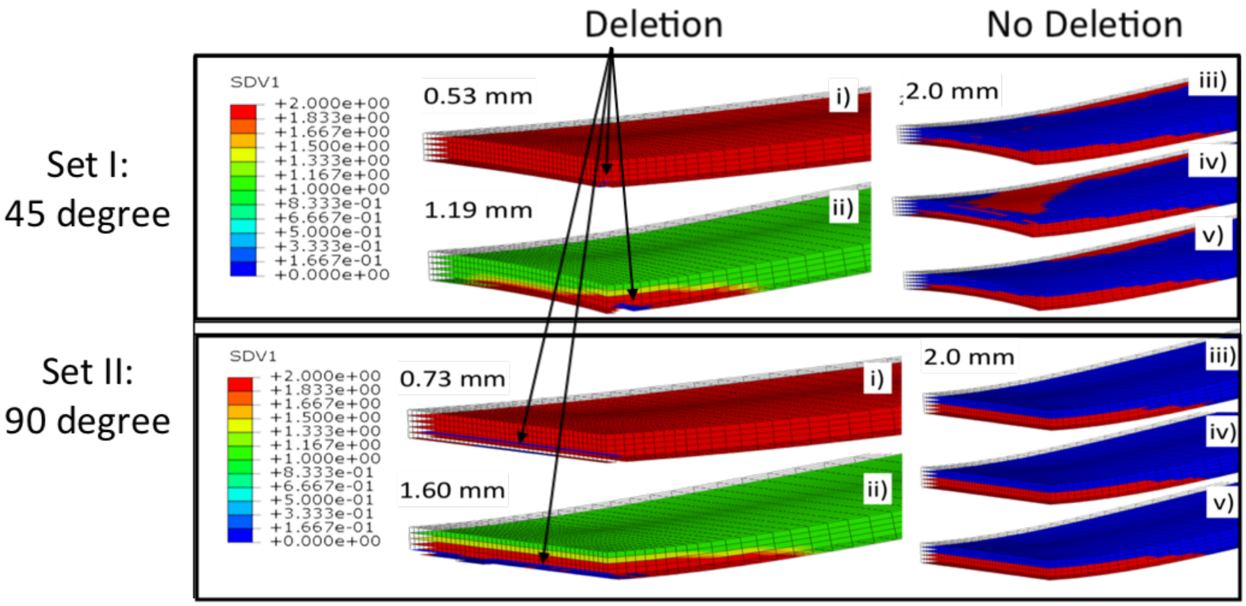

Figure 4.14: Set I: 45° SDV1 element deletion: i) Max Strain, ii) LaRC02, iii) Set II: 90° SDV1 element deletion: i) Max Strain, ii) LaRC02, iii) MCT iv) Hashin, v) Puck

FE modelling of matrix-fibre composites damage theory initiates with matrix damage initiation and evolution preceding fibre breakage. When the fibres are parallel to loading, 0° the fibres withstand significant load as the matrix damage evolves. The outer plies will damage prior to the middle of the specimen. These contributions lead to the successful modelling of the nonlinear response of the CFRP sample. The 45° and 90° tests are not controlled by the fibre damage. The coupon experiences fracture because of a failure in the matrix in the transverse loading direction. Due to the computational benefit, the matrix is commonly modelled as an isotropic linear-elastic material, negating the ability to capture nonlinearity in the prediction, although observed in experiment. By incorporating cohesive modelling between plies, with the inclusion of damage, the non-linear response in the matrix could be predicted.

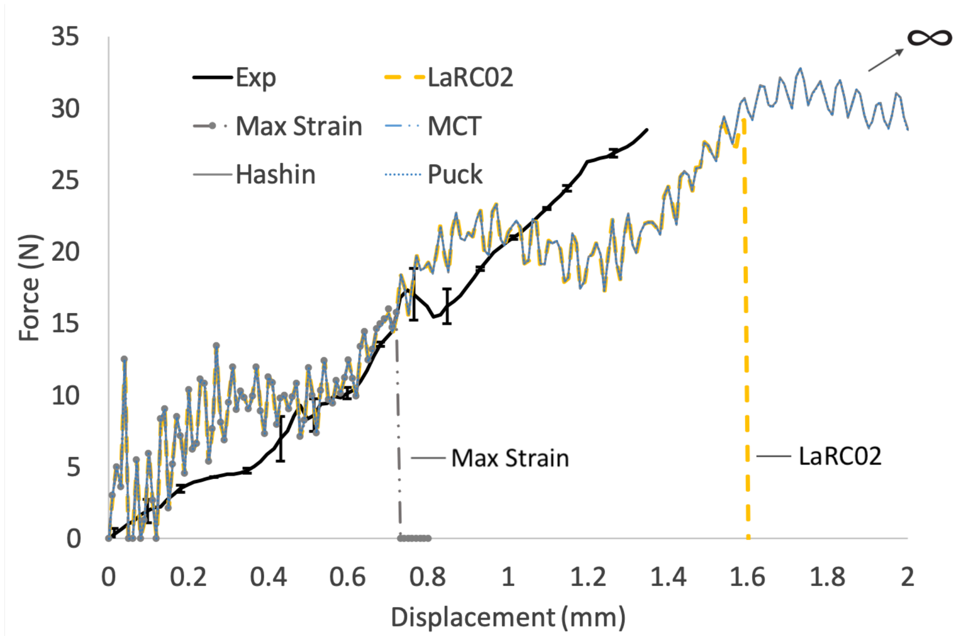

Figure 4.15: Comparison between failure models and experimental on displacement versus force response with 90° fibre orientation

4.4.2 Phase VI - Results of cohesive modelling utilizing unit thickness

In prior research, the inclusion of cohesive surfaces between the CFRP plies in FE modelling had significant effect on the accuracy of the tensile loading prediction [16]. The break-in and break-out damage when drilling fibre reinforced composites can only be predicted if the cohesive surface interaction is accurately modelled. The three-point bending test is an ideal load configuration to validate these modelling parameters. The cohesive material properties are shown in Table 4.5.

Friction has been noted by Russell et al. to be insensitive between 0.1-0.3 [27]. A "Hard" pressure over-closure contact minimizes the penetration of the slave surface

Table 4.5: Cohesive modelling parameters [27, 26]

Friction	0.3
Pressure Over-closure	Hard
Damage initiation = MAXS	70, 70, 70 (MPa)
Damage evolution = Displacement	0.001
Damage stabilization	0.002

into the master surface; the CFRP should not penetrate into the supports or indenter [26]. The Maximum Stress criteria and displacement damage evolution control described earlier was selected. The modulus of elasticity (E_F) is calculated using the tangent from the load displacement plot following Equation 4.7 [2, 28].

$$E_F = \frac{L^3 \cdot m}{4 \cdot b \cdot h^3} = \frac{m \cdot L^3}{48 \cdot I} \ , \tag{4.7}$$

where L is the span length, m is the linear slope of the load-displacement relationship, b is the width, h is the thickness and I is the second moment of area. Based on the experimental setup and the relationship shown in Equation 4.7 a flexural modulus of elasticity of 128.275 GPa is determined. In comparison, the tensile modulus determined by experiments in [16] was 132.934 GPa and a manufacturer reported modulus of 135 GPa [22].

In Figure 4.16, the Aramis strain output is illustrated in comparison to the strain output from the FEA. The maximum strain based on the International Organization for Standardization (ISO) standard bending theory is 0.00890. The FEA output strain (LE11) is 0.008307. This resulted in a difference of 6.66%. The computational efficiency gained by utilizing the symmetric unit thickness approach allows for the mass scaling to be reduced. The LaRC02 model response without incorporating cohesive surface interactions between plies is effected by this harmonic output; it is

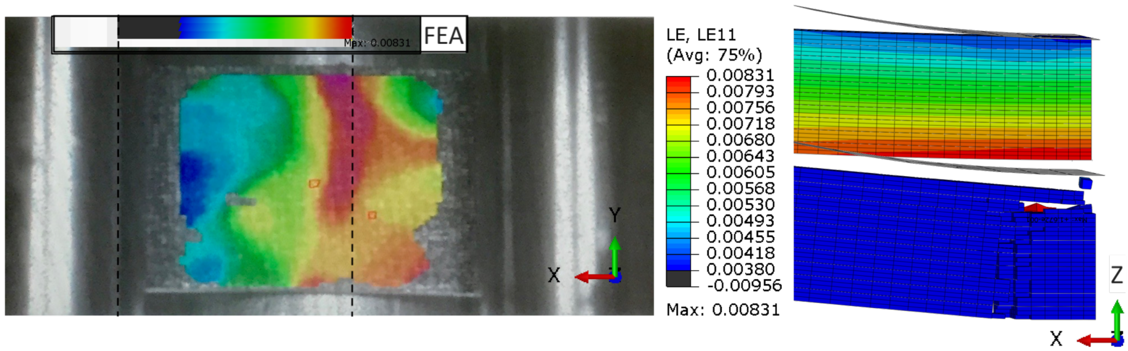

Figure 4.16: 0° with unit thickness versus Aramis strain capture

plotted in Figure 4.17 as FEM without cohesive surface. Figure 4.17 illustrates the LaRC02 FE model with cohesive surfaces predicting the CFRP material response very well in addition to reducing the unwanted harmonic response. Reaffirmed by Figure 4.18, highlighting the similarities of stress-strain prediction between FEA and experiments.

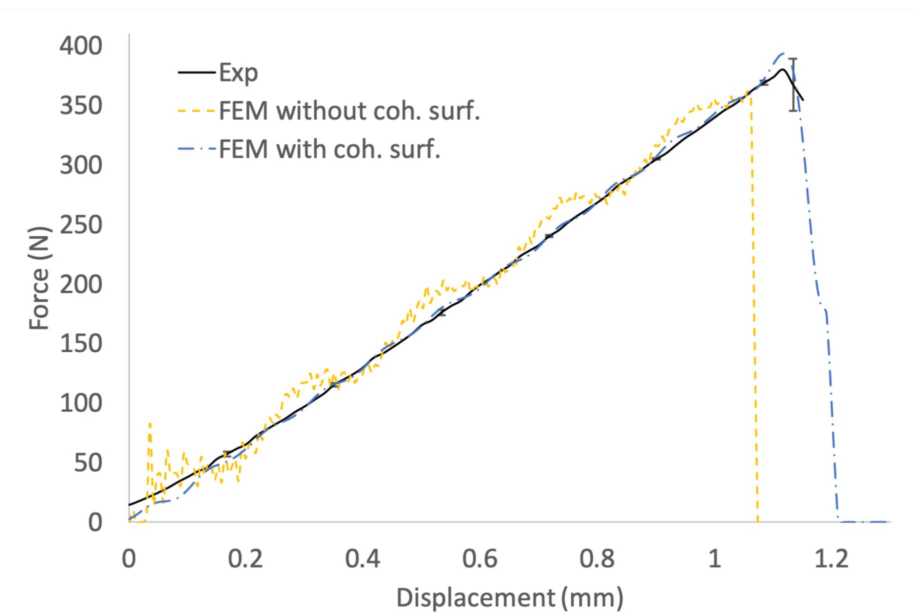

Figure 4.17: Force-displacement response with 0° fibre orientation unit thickness

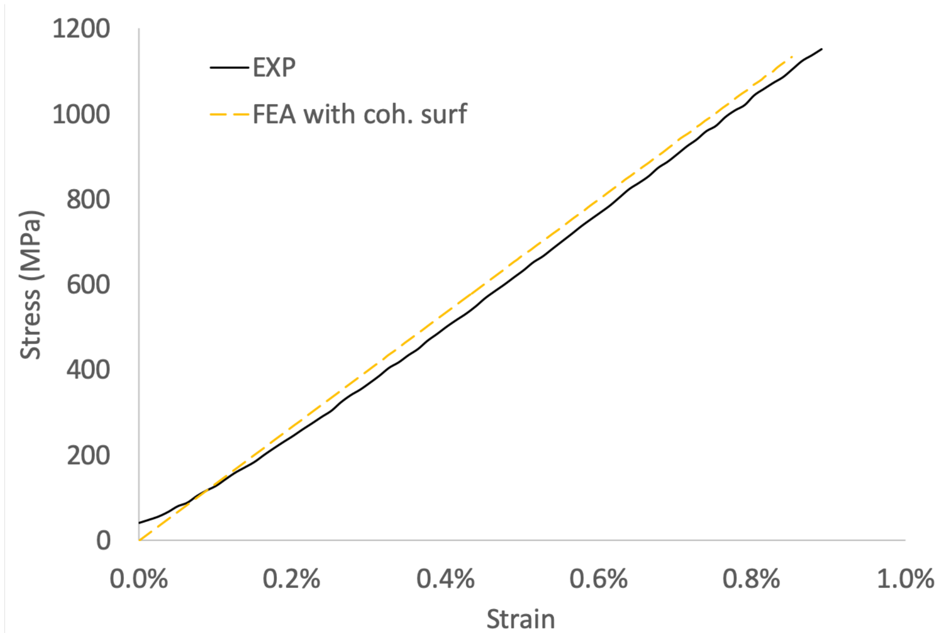

Figure 4.18: Stress-strain response with 0° fibre orientation unit thickness

Figure 4.19 shows the force-displacement material response for the 45° fibre layup three-point bending FE model with the inclusion of cohesive surfaces. The prediction does slightly underestimate the final failure which is a result of a number of correlated factors. The strengths of the CFRP and the damage initiation and evolution of the cohesive surfaces may be too low contributing to a slight underestimation of failure prediction. However, the loading response is well represented.

The sensitivity of the damage initiation variable of the cohesive interaction is less sensitive for the 0° fibre layups. The contact stress was varied from 1 to 75 MPa, however the cohesive damage initiated after the laminate damage. The 90° response shown in Figure 4.20 is relatively linear up to failure in comparison to the response of the 45° layup, shown in Figure 4.19. Figure 4.20 shows the 90° LaRCO2 failure model with cohesive surfaces, which agrees well with the 90° three-point bending

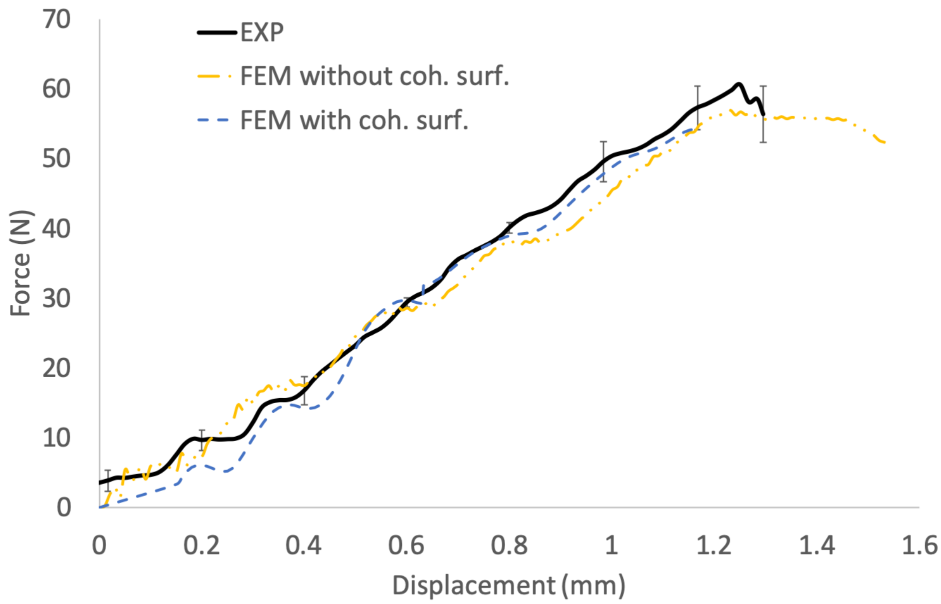

Figure 4.19: Force-displacement response with 45° fibre orientation unit thickness

experiments. By incorporating a unit thickness model and reducing the mass scaling applied, the loading response avoids underestimating the force approaching failure (1.0 to 1.6 mm displacement). This caused a delay in loading for the LaRCO2 (without cohesive surfaces) model resulting in an exaggerated displacement at failure. With the computational savings and reduced mass scaling, the LaRCO2 symmetrical unit thickness model with cohesive surfaces predicts the material response well with respect to failure load and displacement significantly reducing the harmonic variation.

The 0, 45 and 90° multi-instance bending predictions with the incorporation of cohesive surfaces improved the predicted material response of the CFRP. The response for the 45° fibre layup three-point bending test is sensitive to both the matrix damage and a contribution of fibre strength. Therefore, the cohesion between the two interfaces is more critical. This in contrast to loading dominated by the fibre (0°) or the matrix (90°).

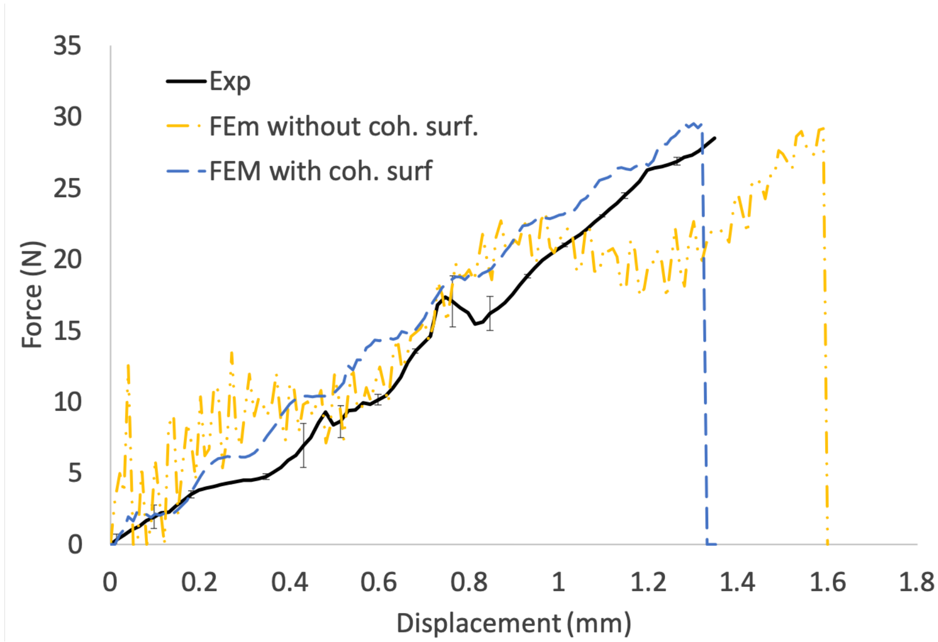

Figure 4.20: Force-displacement response with 90° fibre orientation unit thickness

4.4.3 Phase VII - Extension of model capabilities

Prediction of a material response and failure to a matrix dominated loading of unidirectional fibre reinforced polymers is difficult. The cause of this difficulty is a result of the matrix damage being only a precursor to fibre damage. The fibre damage controls the overall laminate failure. In Figure 4.21 a), b) and c) shows the bending loading of the 90° fibre orientation prior to matrix failure, matrix failure without the auxiliary (AUX) file and matrix failure with the AUX file respectively; the AUX file is an additional User Material file that can overwrite or add additional material properties and is specifically useful for material response prediction of transverse loading conditions, facilitating element deletion and therefore convergence with matrix failure otherwise not possible. Figure 4.21 b) showed the solution dependent state variable

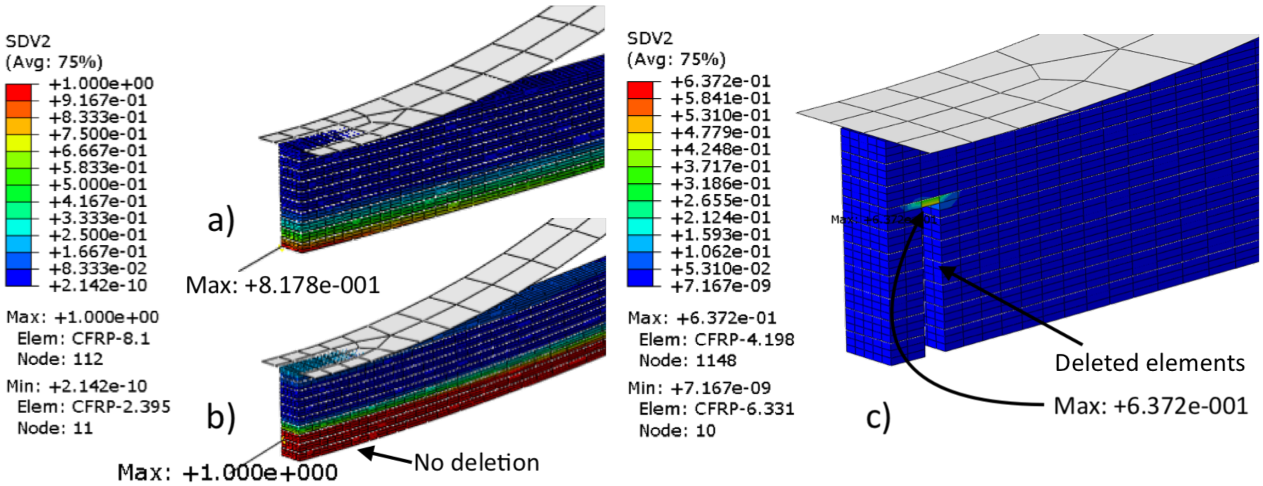

Figure 4.21: 90° a) Prior to matrix failure b) Matrix failure without AUX file, c) Matrix failure with AUX file

for the matrix failure, SDV2) has reached unity, elements should be deleted. Unfortunately, element deletion has not initiated yet. In bending, the matrix post-failure stiffness does not allow for the fibre to be loaded to a critical magnitude and therefore no element deletion occurs. A UD-CFRP loaded at a 45° orientation does predict element deletion, however closer investigation showed element deletion was not due to matrix failure, but instead fibre failure in compression on the top-side of the laminate.

To improve the limited modelling capabilities of most failure criteria when dominated by matrix loading, an additional material sub-file can be written to specifically control the element deletion based on the matrix damage response. To implement this, the auxiliary file (AUX) must be used with an element deletion set described.

The $SPILT$ criteria flags deletion based on the relationship shown in Equation 4.8:

$$\left(\frac{\langle\alpha\sigma^c_{22}\rangle}{S^+_{22}}\right)^2 + \left(\frac{\alpha\sigma^c_{12}}{S_{12}}\right)^2 + \left(\frac{\alpha\sigma^c_{13}}{S_{13}}\right)^2 \geq \theta \tag{4.8}$$

$$\alpha = \sqrt{\frac{1}{\psi^m}} \tag{4.9}$$

where ψ^m is the matrix failure criterion and θ is the element deletion threshold of magnitude $0 \leq \theta \leq 1$. Together, used in the relationship shown in Equation 4.9, the α parameter is determined. The *Split* criterion only considers σ^c_{22}, σ^c_{12} and σ^c_{13} which contribute to longitudinal Splitting. Lastly, the Macaulay brackets ensure the σ^c_{22} contributes to Splitting only when subject to tensile stresses; compressive stresses would not facilitate Splitting [15].

The AUX file has been implemented into an otherwise identical model as the one created for Figure 4.21 a). Figure 4.21 b) illustrates one increment prior to matrix failure (SDV2 $= 8.178 \cdot 10^{-1}$) before elements are deleted. Figure 4.21 c) one increment later, illustrates the elements successfully deleted from the model, identified by critical matrix damage and controlled using the *Split* criteria and element threshold deletion magnitude of 0.05.

Accurate material response prediction of a UD-CFRP coupon subject to three-point bending at 0°, 45°, and 90° can be achieved. However, a single damage initiation model still has great difficulty transitioning between fibre dominated loading, through shear dominated loading into matrix dominated loading.

Classical Beam Theory (CBM) describes the maximum normal stress and the maximum shear strength by the relationship shown in Equation 4.10 and 4.11 respectively:

$$\sigma_{max} = \frac{3P_{max}L}{2wt^2} \tag{4.10}$$

$$\tau_{max} = \frac{3P_{max}}{4wt} \tag{4.11}$$

where w and t are the width and thickness of the sample. A critical span-to-thickness relationship exists by dividing the normal stress by the interlaminar shear strength shown in Equation 4.12 [29, 30]:

$$\frac{\sigma_{max}}{\tau_{max}} = \frac{2L}{t} \tag{4.12}$$

Span-to-thickness ratios on the range ($L/t = 5 - 10$) will fail due to interlaminar shear (delamination) versus span-to-thickness ratios on the range ($L/t = 15 - 25$) will fail due to the normal stress applied [29]. With a ratio $L/t = 27$ the FE model failure is dominated by the normal stress, however the cohesive surfaces contribute to the material response.

Table 4.6 outlines the effect of span length in three-point bending on the material response of a UD-CFRP laminate. As [29] outlines, when $L/t = 15 - 25$, failure will be due to the normal stress applied. Column 3 ($L/t = 18.18$) describes a normal stress failure of 1196.98 MPa (1200 MPa by manufacturer) and a strain of 0.98% (1.05% by manufacturer). When the $L/t = 5 - 10$ [29] describes failure to be dominated by interlaminar shear. Column 1 & 2 ($L/t = 4.55$ & 9.09) determine an average shear strength of 68.13 MPa (manufacturer 70 MPa) and an average shear modulus of 4.11 GPa (manufacturer 5 GPa). Larger span versus thickness ratios shown in column 4 & 5 ($L/t = 26.91$ & 36.36) demonstrate the reduction in shear stress and dominance of normal stress. The FE model successfully identifies cohesive damage between instances for small spans when failure is dominated by interlaminar shear, prior to any element failure from normal stresses. This is in contrast to element failure being identified by material strengths, without any cohesive damage identified, for larger span setups. The results are quite agreeable with [29] descriptions that modifying the span-to-thickness ratio will facilitate an interlaminar shear failure or normal stress failure in the laminate. This reiterates the high value of a three-point bending test to be used for UD-CFRP laminate characterization. The span-to-thickness analysis should be extended to 45 and 90° UD-CFRP laminates.

Table 4.6: Material characterization versus span-to-thickness ratio (0 °)

L (mm)	5	10	20	29.6	40
L/t	4.55	9.09	18.18	26.91	36.36
δ (mm)	$7.99{\cdot}10^{-2}$	$2.00{\cdot}10^{-1}$	$5.93{\cdot}10^{-1}$	1.19	2.08
P (N)	1390.58	1147.38	613.13	407.68	316.98
σ_f (MPa)	678.68	1119.98	1196.98	1177.91	1237.64
ϵ_f	0.0211	0.0132	0.0098	0.0090	0.0086
τ (MPa)	74.66	61.60	32.92	21.89	17.02
E_f (GPa)	32.16	84.87	122.33	131.40	143.97
Shear Modulus (GPa)	3.54	4.67	3.36	2.44	1.98
t (mm)	1.1				
w (mm)	12.7				

Figure 4.22 shows the effect of fibre orientation on force to induce failure and failure force normalized with 0° fibre orientation. The AUX file was incorporated into the model. Fibre orientations included 0°, 5°, 15°, 30°, 45°, 60°, 75°,and 90°,. Model parameters from the prior unit thickness analysis were implemented including LaRC02 damage initiation and evolution criteria, cohesive surface interactions, in addition to the AUX file incorporating *Split* criteria. Figure 4.22 also shows similar experimental results determined by Sideridis et al. who studied various UD-CFRP layup orientations [30]. The 0° to 15° range of [30] and the FEM model from 0° to 5° show a minor insensitivity to fibre orientation on failure force. A characteristic not observed when a UD-CFRP laminate is loaded in tension, which suffers significant

immediate reduction [16].

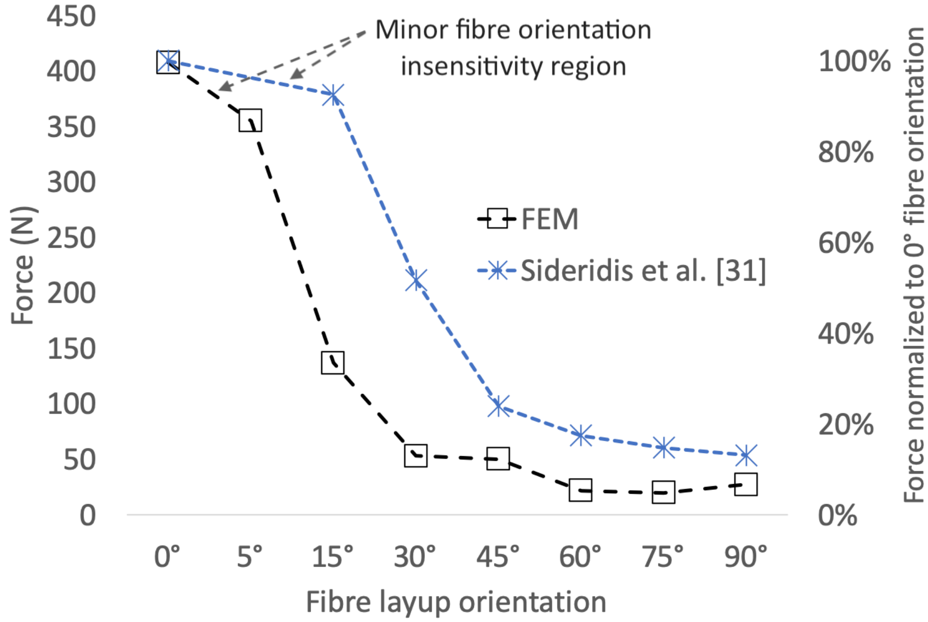

Figure 4.22: Failure force versus orientation: Three-point bending versus Sideridis et al. [30]

By incorporating the AUX file all models, including those dominated by matrix failure, were able to successfully predict failure with element deletion. A 66.4% reduction in failure force is predicted for the 15° layup versus the 0° layup, which highlights the significance of layup orientation with respect to part function. When a CFRP coupon is subject to load with a fibre orientation between 60° to 90° the failure force is insensitive due to the matrix material dominating the response. This trend was shown by the model and experimental results carried out by Sideridis et al..

Naresh et al. studies five layups in bending including 0°, 45°, 90° and two cross-ply setups with stacking sequences $(45°,-45°)_s$ and $(45°, 0°, 90°, -45°)_s$. The unidirectional layups (0°, 45°, 90°) fracture from a fibre-matrix debonding and matrix cracking. The cross-ply layups fracture resulting from delamination [20]. Caminero et al. investigates these layups in addition to a (0°, 90°)$_s$ layup [29]. An increase in toughness and strain at peak load is observed for the cross ply layups [20, 29]. Figure 4.23 shows the peak force at failure relative to the 0° layup for [20, 29] versus the FE model. The FE model predicted a similar load response trend for the 0°, 45°, and 90° agreeing quite well with Caminero et al. and Naresh et al. The FE models with (45°, -45°)$_s$ and (45°, 0°, 90°, -45°)$_s$ layups predicted the increasing force trend, however are underestimated. The increased strain at failure is observed but not to the relative magnitude of [20, 29]. The thin laminate in the FE model does not facilitate the ability to absorb energy and suffer damage before final rupture, as the thick laminate in [20, 29] does. Determining an effective laminate thickness to capture the increased toughness of cross-ply layups should be investigated; [31] determined this to be as thick as 7 mm. The cohesive surface interaction of the cross-ply layups can then be better understood.

4.5 Conclusion

When CFRP samples are subject to loading in primary directions (fibre, matrix and shear), element size in the mesh was less sensitive than anticipated. Accurate, computationally efficient models can be achieved with element lengths of 0.2 mm nearest to the expected failure region and increasingly more coarse away from the failure. Failure when loading a CFRP sample in a three-point bending test is still dominated by failure in the plane of the plies and show minimal dependence on the

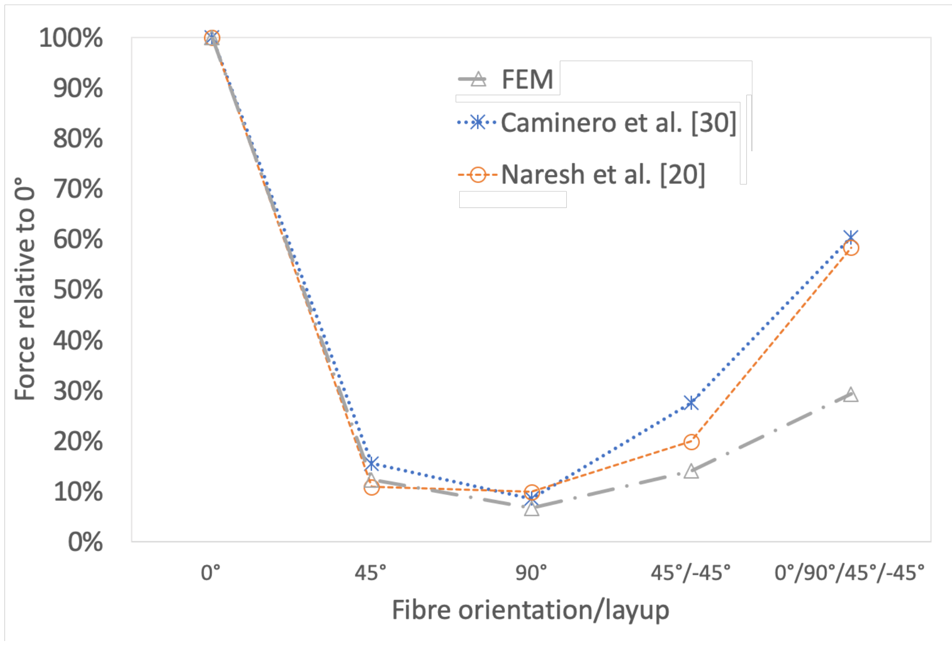

Figure 4.23: Force-displacement of various orientation and cross layups versus [20, 29]

number of elements through the thickness of the geometry. Computational expense is reduced when the through thickness element count is five or less, while maintaining accuracy. Mass scaling is the most critical factor regarding a models' computational efficiency versus accuracy. Variable mass scaling to a desired time step can reduce the computation time from years to minutes, but will have a drastic negative effect on the loading response accuracy. Consideration must be made to minimize the inertial effects caused by the increased density of the elements when implementing mass scaling. For the mesh refinement used in the FE model a mass scaling of less than $5.0{\cdot}10^{-6}s$ can be used without time scaling. Utilizing the CFRP insensitivity to strain rate allows for time scaling to be implemented resulting in more computational savings, however the mass scaling should be reduced accordingly as described.

With the inclusion of multi ply instances laminated by cohesive interactions capable of damage evolution, the nonlinear loading response recorded from the experiments was predicted with strong resemblance. The 45° and 90° fibre layup samples' failure is controlled by matrix damage evolution. The inclusion of cohesive surface modelling improved the ability to develop nonlinearity in the loading response once damage initiation strengths were optimized. The facilitation for the contribution of damage between plies derived a nonlinear response that is commonly not captured or assumed linear-elastic in other literature.

With appropriate punch design, in combination with the effective modelling techniques employed, significant improvements to the effectiveness of the tests and the material representation in FE models was made. This facilitated the ability to model multi-orientation and cross-ply layups successfully, which provides a tool to determine a layup for a particular strength and toughness requirement. With small span-to-thickness ratio the cohesive surface modelling successfully captured interlaminar shear damage (delamination) between plies. With large span-to-thickness ratio the FE model successfully predicted the experiments and was extended to predict various fibre orientations and cross-ply layups from literature. The cohesive surface modelling of three-point bending analyses should investigate the effect of laminate thickness further. This will further validate the material representation regarding laminate toughness, interlaminar shear strength and cohesive surface representation. The cross-ply layups' strength was underestimated versus literature due to the thin laminate geometry resulting in immediate laminate failure, versus a prolonged damage capable of absorbing energy during fracture. This cohesive interaction prediction is critical and directly relates to the break-in and break-out delamination damage when drilling CFRP. With accurate representation of the CFRP material and its interlaminar cohesive nature, effective machining simulations can be developed based on these findings.

References

[1] B.Z. Jang. *Advanced Polymer Composites: Principles and Applications*. Taylor & Francis, 1994. ISBN: 9780871704917.

[2] I. Petrescu, C. Mohora, and C. Ispas. "The Determination of Young Modulus for CFRP using Three Point Bending Tests at Different Span Lengths". In: *U.P.B. Sci. Bull., Series D* Vol. 75, No. 1 (2013), 121 − 128.

[3] International Organization for Standardization. "Plastics - Determination of Flexural Properties". In: (Dec. 2010), 1 − 19. ISO 178:2010.

[4] F. Mujika. "On the Difference Between Flexural Moduli Obtained by Three-Point and Four-Point Bending Tests". In: *Polymer Testing* Vol. 25, No. 2 (2006), 214 − 220. URL: `http://dx.doi.org/10.1016/j.polymertesting.2005.10.006`.

[5] A. Azzam and W. Li. "An Experimental Investigation on the Three-Point Bending Behavior of Composite Laminate". In: *IOP Conference Series: Materials Science and Engineering* Vol. 62, No. 1 (2014), 1 − 8. URL: `http://dx.doi.org/10.1088/1757-899X/62/1/012016`.

[6] M. Nirbhay, A. Dixit, R.K. Misra, and H.S. Mali. "Tensile Test Simulation of CFRP Test Specimen using Finite Elements". In: *Procedia Materials Science* 5 (2014), 267 − 273.

[7] J. Kwon, J. Choi, H. Huh, and J. Lee. "Evaluation of the Effect of the Strain Rate on the Tensile Properties of Carbon and Epoxy Composite Laminates". In: *Journal of Composite Materials* Vol. 51, No. 22 (2017), 3197 −3210. URL: https://doi.org/10.1177/0021998316683439.

[8] Z. Hashin. "Failure Criteria for Unidirectional Fiber Composites". In: *Journal of Applied Mechanics* Vol. 47, No. 2 (1980), 329 − 334. URL: http://dx.doi.org/10.1115/1.3153664.

[9] D.R. Ambur, N. Jaunky, and C.G. Davila. "Progressive Failure of Composite Laminates using LaRC02 Criteria". In: *Collection of Technical Papers - AIAA/ASME/ASCE/AHS/ASC Structures, Structural Dynamics and Materials Conference* 2 (2004), 898 − 913.

[10] S.W. Tsai and E.M. Wu. "A General Theory of Strength for Anisotropic Materials". In: *Journal of Composite Materials* 5 (1971), 58 − 80. URL: http://dx.doi.org/10.1177/002199837100500106.

[11] S.W. Tsai. "Strength Theories of Filamentary Structures". In: *Fundamental Aspects of Fiber Reinforced Plastic Composites* 5 (1968), 3 − 11.

[12] R.M. Christensen. "Tensor Transformations and Failure Criteria for the Analysis of Fiber Composite Materials". In: *Journal of Composite Materials* Vol. 22, No. 9 (1988), 874 − 897. URL: https://doi.org/10.1177/002199838802200906.

[13] A. Puck and H. Schurmann. "Failure Analysis of FRP Laminates by Means of Physically Based Phenomenological Models". In: *Failure Criteria in Fibre-Reinforced-Polymer Composites* (2004), 264 − 297. URL: http://dx.doi.org/10.1016/B978-008044475-8/50011-1.

[14] M.R. Garnich. "A Multicontinuum Theory for Structural Analysis of Composite Materials". PhD thesis. University of Wyoming, 1996.

[15] Autodesk Helius PFA. *Theory Manual*. 2016. URL: `http://help.autodesk.com/view/ACMPAN/2016/ENU/?guid=GUID-1FEC4707-77A9-4FA4-BA2D-60B7444A1359`.

[16] P. Hale and E.G. Ng. "Non-Linear Material Characterization of CFRP with FEM Utilizing Cohesive Surface Considerations Validated with Effective Tensile Test Fixturing". In: *Materials Today Communications* 23 (2020), 1 − 15. URL: `http://dx.doi.org/10.1016/j.mtcomm.2019.100872`.

[17] H. Huang, X. Ma, J. Qiao, and D. Yanhong. "Numerical Simulation of Failure Behaviors of CFRP Laminates on Hashin Model Coupled with Cohesive Elements". In: *IOP Conference Series: Materials Science and Engineering* Vol. 382, No. 3 (2018), 1 − 6. URL: `http://dx.doi.org/10.1088/1757-899X/382/3/032062`.

[18] H. Ullah, A.R. Harland, T. Lucas, D. Price, and V.V. Silberschmidt. "Finite-Element Modelling of Bending of CFRP Laminates: Multiple Delaminations". In: *Computational Materials Science* Vol. 52, No. 1 (2012), 147 − 156. URL: `http://dx.doi.org/10.1016/j.commatsci.2011.02.005`.

[19] H. Ullah, A.R. Harland, and V.V. Silberschmidt. "Damage Modelling in Woven-Fabric CFRP Laminates Under Large-Deflection Bending". In: *Computational Materials Science* 64 (2012), 130 − 135. URL: `http://dx.doi.org/10.1016/j.commatsci.2012.05.036`.

[20] K. Naresh, S. Krishnapillai, and V. Ramachandran. "Effect of Fiber Orientation on Carbon/Epoxy and Glass/Epoxy Composites Subjected to Shear and Bending". In: *Solid State Phenomena* 267 (2017), 103 − 108. URL: `http://dx.doi.org/10.4028/www.scientific.net/SSP.267.103`.

[21] T. Niezgoda and A. Derewońko. "Multiscale composite FEM modeling". In: *Procedia Engineering* Vol. 1, No. 1 (2009), 209 − 212. DOI: https://doi.org/10.1016/j.proeng.2009.06.049.

[22] ACP Composites. *Carbon Firer Uni Laminates*. 2014. Accessed: 6/2015.

[23] Instron. *Dual Column Tabletop Models 3360*. MA, USA, 2017. URL: http://www.instron.us/-/media/literature-library/products/2011/06/3300-series-table-model.pdf?la=en-US. Accessed: 2016-7-20.

[24] GOM Aramis. *ARAMIS Adjustable*. NC, USA, 2017. URL: https://www.gom.com/metrology-systems/aramis/aramis-adjustable.html. Accessed: 2017-12-05.

[25] S. Marzi, A. Rauh, and R.M. Hinterholzl. "Fracture Mechanical Investigations and Cohesive Zone Failure Modelling on Automotive Composites". In: *Composite Structures* 111 (2014), 324 − 31. URL: http://dx.doi.org/10.1016/j.compstruct.2014.01.016.

[26] Dassault Systemes. *ABAQUS/CAE User's Guide, from ABAQUS 6.14 Online Documentation*. 2014.

[27] B.P. Russell, T. Liu, N.A. Fleck, and V.S. Deshpande. "Quasi-static Three-point Bending of Carbon Fiber Sandwich Beams With Square Honeycomb Cores". In: *Journal of Applied Mechanics* Vol. 78, No. 3 (2011), p. 15. URL: http://dx.doi.org/10.1115/1.4003221.

[28] ASTM International. *Standard Test Method for Flexural Properties of Unreinforced and Reinforced Plastics and Electrical Insulating Materials*. West Conshohocken, PA, 2007, 1 − 11. DOI: 10.1520/D0790-17.

[29] M.A. Caminero, G.P. Rodríguez, and V. Muñoz. "Effect of Stacking Sequence on Charpy Impact and Flexural Damage Behavior of Composite Laminates". In: *Composite Structures* 136 (2016), 345 − 357. URL: https://doi.org/10.1016/j.compstruct.2015.10.019.

[30] E. Sideridis and G. A. Papadopoulos. "Short-Beam and Three-Point-Bending Tests for the Study of Shear and Flexural Properties in Unidirectional-Fiber-Reinforced Epoxy Composites". In: *Journal of Applied Polymer Science* Vol. 93, No. 1 (2004), 63 − 74. URL: https://doi.org/10.1002/app.20382.

[31] N. Carbajal and F. Mujika. "Determination of Compressive Strength of Unidirectional Composites by Three-Point Bending Tests". In: *Polymer Testing* Vol. 28, No. 2 (2009), 150 − 156. URL: https://doi.org/10.1016/j.polymertesting.2008.11.003.

4.6 Nomenclature

ϵ	Strain
σ_{11}	Longitudinal stress (MPa)
$\sigma_{22} = \sigma_{33}$	Transverse stress (MPa)
E	Young's Modulus (GPa)
$\sigma_{12} = \sigma_{13}$	Longitudinal shear stress (MPa)
σ_{23}	Trasverse shear stress (MPa)
v	Poisson's ratio
S_{11}, S_{22}	Long. & Trans. material strengths (MPa)
S_{12}, S_{23}	Shear material strengths (MPa)
f, m, c	Fibre, Matrix, Composite
α	Contribution of shear variable ($0 \leq \alpha \leq 1$)
L^e	Characteristic Length Element
c_d	Dilatational Wave Speed
E_F	Flexural Modulus (MPa)
L	Support Span (mm)
b	Width of sample
h	Height of sample
m	Slope of the linear portion of the load-displacement curve (N, mm)
I	Moment of Inertia
ψ^m	Matrix Failure Criterion (AUX)
θ	Element Deletion Threshold (AUX)
I_j^m	Trans-isotropic matrix invariants
$j = 1, 2, 3, 4$	Matrix average stress state
p	Slope of fracture envelope
I_i^f	Trans-isotropic fibre invariants
$i = 1, 4$	Fibre average stress state
A_i^m, A_i^f	Adjustable coefficients
F_i, F_{ij}	Failure coefficients defined by strengths
Y_T, Y_C	Tensile and compressive strength (MPa)

Chapter 5

3D Finite Element Model on Drilling of CFRP with Numerical Optimization and Experimental Validation

Complete citation:

P. Hale and E. Ng. “3D finite element model on drilling of cfrp with numerical optimization and experimental validation”. In: Materials 14.5 (2021). pp 1-22.

3D Finite Element Model on Drilling of CFRP with Numerical Optimization and Experimental Validation

This chapter is a copy of the paper published in *Materials* journal.

Authors: Patrick Hale, Eu-gene Ng

Submitted to the *Materials* journal

Published March, 2021

Abstract

When drilling Carbon Fibre Reinforced Plastic (CFRP) material achieving acceptable hole quality is challenging, while balancing productivity and tool wear. Numerical models are important tools for optimization of drilling CFRP material in terms of material removal rate and hole quality. In this research a macro-Finite Element (FE) model was developed to accurately predict the effect of drill tip geometry on hole entry and exit quality. The macro-mechanical material model was developed treating the Fiber Reinforced Plastic (FRP) as an Equivalent Homogeneous Material (EHM). To reduce computational time, numerical analysis was performed to investigate the influence of mass scaling, bulk viscosity, friction, strain rate strengthening and cohesive surface modelling. Consideration must be made to minimize the dynamic effects in the FE prediction. Experimental work was carried out to investigate the effect of drill tip geometry on drilling forces, hole quality and to validate the FE results. The geometry of the drills used were either double-point angle or a "candle-stick" profile. The 3D drilling model accurately predicts the thrust force and hole quality generated by the two different drills. Results highlight the improvement in predicted results with the inclusion of cohesive surface modelling. The force signature profile between the simulated and experimental results were similar. Furthermore, the difference between the predicted thrust force and those measured were less than 9%. When drilling with double angle drill tip, the inter-ply damage was reduced. This trend was observed in FE prediction.

5.1 Introduction

In aerospace and automotive industries, the interaction of different material components during assembly may require drilling holes to facilitate bolting sections together. Annually, 250 million twist drill bits are used in the US aerospace industry [1]. On the Airbus A350 it is estimated that 55000 holes are drilled to facilitate the assembly of one unit [2]. Composite plates with holes that have been moulded or drilled are susceptible to damage. Zitoune et al. demonstrated by loading parts under tension, that parts with drilled holes results in a 30% decrease in fracture strength [3]. Moulded holes are not always feasible and attaining positional and size tolerances becomes more cumbersome versus drilling, thereby creating motivation to improve the drilling process.

Contrary to the shear based cutting mechanism in ductile metals, CFRPs are dominated by a brittle crack propagation [4, 5]. In CFRPs the high thrust force resulting from the drill can cause peel-up and push-out effect on the workpiece, resulting in delamination of the ply. As drilling initiates, the work material is resisting the thrust force induced by the chisel edge of the tool. As the drill approaches the exit surface, there is little material to withstand this thrust force. Therefore, significant thrust force is transferred to the interface between the plies causing delamination under pure bending. By identifying the critical thrust force causing delamination, with respect to uncut thickness of the laminate, the feed rate should be modified throughout the progression of the drilling. Mainly, an aggressive feed at hole entrance to promote Material Removal Rate (MRR) and a reduced feed to mitigate delamination near the exit of the cut [6]. Adding to these considerations, tool wear increases the dynamic nature of the drilling process. Ismail et al. describes the unavoidable phenomenon which requires coolants, tool life monitoring and prediction, effective drill design geometry and optimal process parameters [7].

Vijayaraghvan outlines numerous considerations in modelling multilayer material machining which includes material modelling, contact, fracture criteria, adaptive meshing, element types, tool modelling [8]. Significant work has been done to investigate the drilling of CFRP materials, including reviews completed by Panchagnula et al. [9] and Lissek et al. [10] outlining the significance of process monitoring to ensure hole quality. Kahwash et al. highlighted the current practice of modelling the cutting process of CFRPs and the use of 2D orthogonal cutting due to its simplicity and computational advantage [11]. Liu et al. from experimental results on drilling of composite laminates concluded that the variation between materials' elastic modulus, affected the drilled hole diameters [12]. Computationally, Mahdi et al. studied mesh sensitivity, plane stress versus strain and rake angle. This research concluded that the rake angle had minimum effect. The effect of fibre angle when machining FRPs was successfully demonstrated [13]. Shyha et al. studied the effect of machining process parameters when drilling CFRP and determined drill geometry and feed rate were most critical [14]. Faraz et al. studied the effect of cutting edge rounding to predict and prevent increase drill loads and maintain hole quality [2].

Arola and Ramulu produced preliminary 2D orthogonal cutting models of graphite epoxy material and attained good correlation between predicted and experimental cutting force. However, poor agreement was found with thrust force [15]. An orthogonal 3D cutting model of CFRP was published by He et al. [16]. Strong variance in predicted cutting forces was described when using different failure criteria including

Hashin and Max Stress. Max Stress predicted cutting force reasonably where Hashin underestimated significantly. Predicted thrust force was significantly under-predicted by 75% difference when compared to experiments. He et al. described the thrust force predictions as an order of magnitude less than experiments as found in literature [17, 18]. No element removal or chip formation was captured. Lasri et al. describes the magnitude difference between experimental and modelled thrust force, captures damage, however does not show the removal of elements and chip formation progression; only the initiation [18].

Phadnis et al. compared drilling experiments to FEM model. Using X-ray microtomography drill entry and exit delamination damage was investigated [19]. Although exaggerated, the outer region of the delamination damage predicted in the FEA resembled experiments. The concern is the significant element removal of the failed cohesive elements at exit. Jain et al. [20], Lissek et al [10] and Won et al. [21] investigated the relationship between thrust force on hole quality with respect to delamination damage. Jain et al. discovered reduced thrust force along with delamination damage when the chisel width edge of the drill was decreased. Won el. al. noticed reduced thrust force measurements by pre-drilling the holes first. The results concluded that the magnitude of the thrust force critically affects the delamination damage of the CFRP.

The progression of damage experienced by an element is influenced by the cutting speed. The stable time increment in a FE analysis is governed by element size, bulk modulus and material density. The fine mesh and high stiffness of CFRP develops rigid elements that propagate a stress front through the CFRP creating premature damage. The bulk viscosity parameter can more accurately represent the material response by facilitating dampening, otherwise not well represented in the model. Garekani describes a FE model convergence sensitivity due to excessively distorted elements at certain cutting speeds. At high cutting speeds, models progress further before encountering convergence issues. When the cutting speed is reduced, a limited region exists where elements' material properties have been successfully degraded but the damage is not fully saturated and therefore elements cannot be removed [22]. For damage to be fully saturated the longitudinal damage must be satisfied, which is not always possible depending on the loading. Garekani suggests a max degradation parameter control less than unity to prevent this convergence issue. This facilitates convergence but does improve the material representation. Bulk viscosity parameters are frequently stated [23], with little description to why and how linear and quadratic viscosity parameters are determined or their influence on the model.

Conventional drilling experiments investigating cutting speed and CFRP constituents outlining significant importance of the matrix on the material response due to strain rate and thermal effects were studied by Merino-Perez et al. [24]. Merino-Perez et al. described a decline in the matrix ability to properly transfer load between fibres at high strain rates. Lasri et al. describes minimal strain rate dependence and a bouncing back effect reducing the overall depth of cut, with respect to the fibre material [18]. Using the split Hopkins bar technique, Lifshitz experimentally studied the interlaminar failure of CFRP at strain rates of 100-250 s^{-1} versus at static test conditions. The results showed an increase in strength by an average of 36% and modulus by 30% at the higher strain rate [25].

Giasin et al. created a 3D drilling model of a hybrid material made of stacked glass fibre/epoxy prepreg with aluminum sheets. The model predicted torque within

0.83-17.9% and thrust force within 3.2-53.2%. However, no delamination was identified and deemed negligible [26]. The effect of including cohesive surface in finite element modelling on the cutting of CFRP has been investigated by Dandekar et.al. [27], Abena et al. [28] and Lasri et al. [18] among others. Lasri et al. used a progressive failure stiffness degradation scheme when modelling orthogonal cutting to gain understanding on subsurface damage and its contribution on chip formation [18]. The inclusion of an interface zone between the constituents proved to have significant effect on delamination magnitude and fibre/matrix failure. 3D orthogonal and drilling model produced by Usui et al. captured delamination in various fibre orientations by using cohesive zone elements mapped to fracture planes defined by the Miller indices [29]. Zenia et al. developed similar research with an elasto-plastic damage model VUMAT that predicts interply damage and chip formation [30]. Isbilir et al. modelled the drilling process, including the inter-laminar damage, comparing a standard twist drill and step drill geometries [31]. Ply damage was modelled using Hashin's theory and delamination was based on a cohesive contact relationship. Isbilir et al. describes better model prediction capabilities with the inclusion of inter-laminar cohesive modelling.

The objective of this work was to progress the development of a macro FE drilling model, to be used as a tool to accurately test various drill geometries with reasonable computation time. To substantially reduce computational time, numerical analysis was preformed to investigate the influence of mass scaling, bulk viscosity, friction, strain rate strengthening and cohesive surface modelling, building on intra-ply and inter-ply progressive failure modelling techniques developed in [32, 33]. Experimental work was carried out to investigate the effect of of drill tip geometries on drilling forces, hole quality and to validate FE model prediction capabilities.

5.2 Experimental work

The pre-impregnated unidirectional CFRP panels were procured from ACP Composites Inc. using an autoclave curing process. The mechanical properties described by ACP Composites Inc. Acp24 are tabulated in Table 1.

Table 5.1: Standard Modulus (SM) CFRP - material properties [34]

SM UD-CFRP	0°	90°
Longitudinal Modulus (GPa)	135	10
Transverse Modulus (GPa)	10	135
In-plane Shear Modulus (GPa)	5	5
Major Poisson's ratio	0.3	0.3
Ultimate (Ult.) Tensile Strength (MPa)	1500	50
Ult. Comp. Strength (MPa)	1200	250
Ult. In-plane Shear Strength (MPa)	70	70
Ult. Tensile Strain	1.05	0.5
Ult. Comp. Strain	0.85	2.5
Density (g/cm^3)	1.6	

Two drill geometries were tested experimentally, named the CoroDrill (CD) CD854 and CD856, are shown in Figure 5.1 (a) and (b) respectively, after the drilling experiments were completed (Sandvik, Gimo, Sweden). The CD856 has a double-point angle, carbide geometry with diamond coating (N_2OC) that is designed to reduce delamination and splintering. The diamond coated (N_2OC) CD854 has a point geometry with additional spur edges on the circumference, designed to minimize burr formation when drilling Aluminum, detailed in Figure 5.1 (a). Both CD drills have a diameter of 4.7625 mm, incorporate small point angles (CD854 - 130°, CD856 - 120°) and high rake angles to reduce axial forces, critical for drilling thin walled structures [35]. Drill geometries were inspected with digital microscope, measuring key features from output frames. The CD854 drill incorporates additional spurs on the perimeter of the tool that score the circumference of the hole as detailed in Figure 5.1 a). This design is inspired by a Brad-Point drill commonly used in wood working to prevent fibre pull and tearing of the wood.

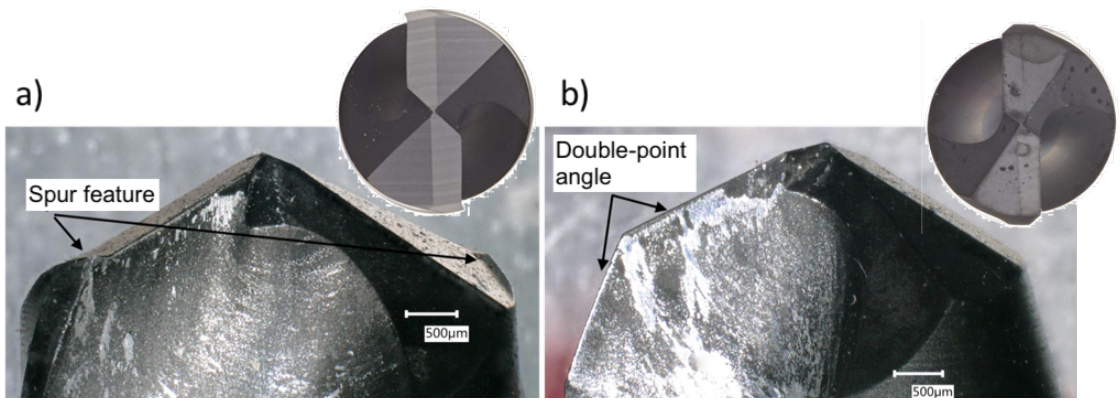

Figure 5.1: Drill geometries (a) CD854 and (b) CD856.

The drilling tests were carried out on a Fanuc controlled Matsuura LX-1, 3-axis vertical CNC machine (Matsuura Machinery Corporation, Fukui, Japan). Cutting forces were measured using a Kistler three component stationary piezoelectric dynamometer (type 9272, calibrated range: Fx = 0 - 3000 N, Fy = 0 - 3000 N, and Fz = 0 - 6000 N), connected to a series of charge amplifiers (type 5011A) (Kistler Group, Winterthur, Switzerland). Data acquisition was accomplished using an analogue to digital converter card connected to a high performance computer, which was capable of sampling at 200K samples per second per channel. Recordings were measured at 10kHz per channel. The drilling process was repeated five times to ensure repeatability. The machining parameters employed were 0.05 mm/rev and 60 m/min as recommended by the tool manufacturer.

5.3 Finite Element modelling considerations

A macro-mechanical approach treating the FRP as an Equivalent Homogeneous Material (EHM) was developed. The EHM model is based on Multi-Continuum Theory (MCT) which used a Representative Volume Element (RVE) to express the composite stress state as shown in Equation 5.1 [36],

$$\sigma^c = \frac{1}{V} \int_D \sigma(x, y, z) dV \tag{5.1}$$

where V is the total RVE and D is the fibre-matrix domain. The fibre and matrix average stress state is shown in Equation 5.2 and 5.3 respectively [36],

$$\sigma^f = \frac{1}{V_f} \int_{D_f} \sigma(x, y, z) dV \tag{5.2}$$

$$\sigma^m = \frac{1}{V_m} \int_{D_m} \sigma(x, y, z) dV \tag{5.3}$$

where V_f if the fibre RVE and V_m is the matrix RVE. The constituent average stress and strain for the fibre and matrix (σ^f, σ^m, ϵ^f, ϵ^m) are critical to predict damage and material failure versus a homogenized average stress and strain (σ^c, ϵ^c) [36]. When a FRP is subject to non-parallel loading with respect to the fibre orientation, failure is dominated by the matrix constituent. Damage should not be controlled by the fibre, nor should the matrix damage act only as a contribution to the homogenized composite material failure. This is a significant limitation of prior EHM modelling versus the MCT-EHM formulation. If a failure criterion is independent and based only on a matrix parameter, it can initiate element deletion.

FE modelling of Fibre Reinforced Polymers (FRPs) forms its basis on the failure model developed by Hashin [37] that encompasses four failure modes, which are i) matrix tension, ii) matrix compression, iii) fibre tension and iv) fibre compression failure. Significant work has developed numerous additional failure models including LaRC02 [38, 39], Max Strain, Max Stress, Tsai-Wu [40], Tsai-Hill [41], Christensen [42], Puck et al. [43] and a Multi-Continuum Theory (MCT) [44] failure criterion. The formulation and advantages of these failure models are described in previous literature [32, 33]. In this research a user-defined material subroutine was implemented into ABAQUS, to utilize failure criteria alternative to the built-in Hashin method for FRPs.

When damage is initiated, controlled by the failure model implemented, an instantaneous degradation method reduces the stiffness of the matrix and fibre from its original undamaged state to a user-defined value between zero and one. This degradation scheme is implemented instantaneously, or can be defined for a time period to improve the response prediction of fracture. This is an efficient degradation method, however can be sensitive to mesh size resulting in increased failure loads for coarse meshes and premature failure for refined mesh models. To avoid premature failure prediction of the CFRP loading response, techniques including damping applied through bulk viscosity, softening in contact interactions and enhanced element controls reducing stiffness, can be applied.

5.3.1 Finite Element Geometry and Boundary Conditions

The drilling FE model was designed to replicate the experimental setup using a rigid drill bit. Drill bits were designed in Siemens NX CAD, exported as step (.stp) files and imported into ABAQUS. The complex drill geometries require the use of tetrahedral 3D stress elements (C3D10M). The C3D10M are explicit, quadratic, modified elements with the deformation along the edge following a bi-linear interpolation versus a quadratic function. This modification creates an additional node in the middle of the edge of the element. The modified term refers to a unique formulation using a bi-linear interpolation. These elements cannot represent curved surfaces as well as the true second order elements, however gain computational efficiency [45]. Cyclic symmetry is not possible in ABAQUS Explicit models. As the tool revolves about the z-axis the interaction between the tool and workpiece would be cyclically symmetric except for the changing interaction between the tool face and fibre orientation. Symmetry in the XZ and YZ plane was utilized to reduce the workpiece to one quarter and thereby reduce the computation time, however still capturing a tool-fibre interaction ranging from 0° to 90 °.

The body elements and nodes for the drill are mapped to the reference point; load constraints are most efficiently applied with this setup. When drilling CFRP the loading velocity in the z-axis direction is 3.342 mm/s (feed = 0.05 mm/rev) and rotation is 420.0 rad/s (4010 RPM, 60 m/min cutting speed). Model boundary conditions are shown in Figure 5.2. The feed rate and cutting speed magnitudes are recommended by the tool manufacturer for the CoroDrill CD854 and CD856 drills [46].

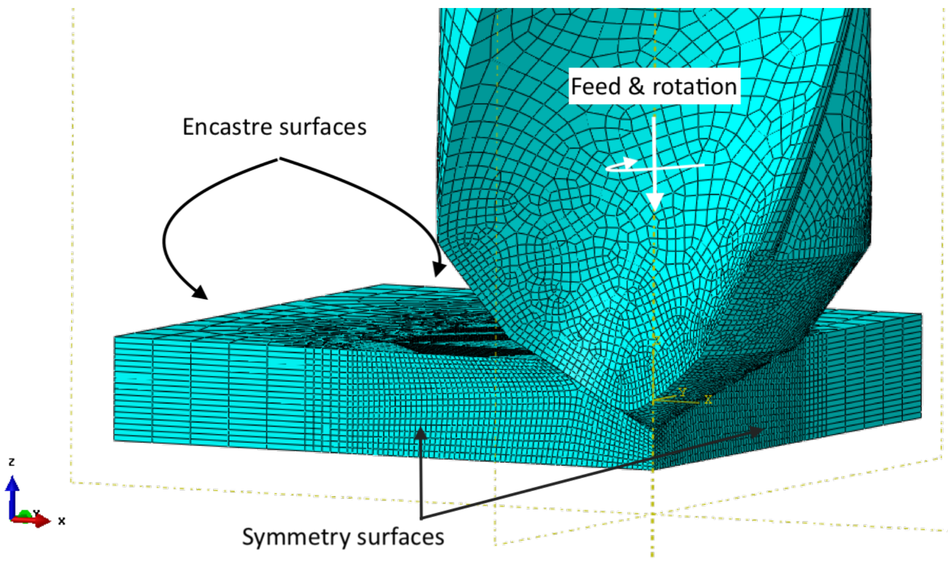

Figure 5.2: Model boundary conditions illustration.

A discrete rigid body converts the solid geometry to a shell body. The tip of the drill bit as shown in Figure 5.3. This negates the requirement of meshing the internal volume and focuses on the outer surface using a 4-node bi-linear rigid quadrilateral element (R3D4). This setup requires additional property assignment including the geometries' weight and rotational inertia. The approach reduced the number of elements from 67672 to only 6568 elements using the discrete rigid geometry.

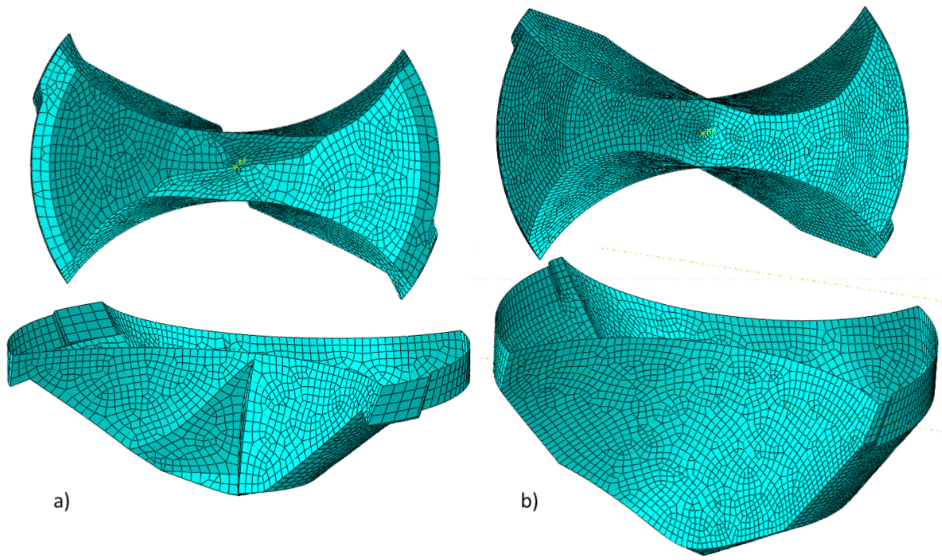

Figure 5.3: Discrete rigid (shell) body (a) CD854 (b) CD856.

The CFRP laminate workpiece was modelled as one 3D deformable member. The sample is subdivided with 10 plies to facilitate cohesive surface interactions. Material properties for the CFRP were determined and validated through tensile and three-point bending experiments and FE models at various fibre orientations [32, 33].

In the explicit analysis, the stable time increment decreases as Young's Modulus increases [45]. The tool in a machining simulation that is generally quite stiff and rigid compared to a workpiece can negatively effect the stable time increment. A discrete rigid body does not affect the global time increment, thereby can increase computational efficiency without significantly affecting the overall accuracy of the solution. Comparing identical models except for the described differences in the drill bit representation, the explicit time step for a deformable body with a rigid body constraint is 1.22x10^{-9} s, versus a discrete rigid body is 3.43x10^{-9} s. An increase in stable time increment of three times and reduction in computation time. The estimated memory required for the otherwise equivalent analyses reduces from 1.9

GB to 1.1 GB due to the reduced elements required for meshing the tool. The resultant force prediction is subjected to noise. The noise was generated by the high modulus of CFRP under high strain rate deformation together with element deletion leading to intermittent contact, and small modelling volume which provide minimal damping. Therefore, the resultant force is filtered with a Chebyshev type II filter.

5.3.2 Mass Scaling

The minimum stable time increment for an explicit dynamic analysis is expressed in Equation 5.4 [45],

$$\Delta t = L^e / c_d \ , \quad and \ \ c_d = \sqrt{\frac{E}{\rho}} \tag{5.4}$$

where L^e is the characteristic length element and c_d is the dilatational wave speed of the material. The dilatational wave speed requires Young's modulus (E) and the density (ρ) of the material [45].

With a characteristic element length of 10 - 100 μm the stable time increment is approximately 1.0x10^{-8} s to 1.0x10^{-9} s resulting in an extremely long model computation time involving 1.0x10^{6} s to 10x10^{7} s solution increments. To improve computational efficiency with explicit dynamic models, scaling techniques can be employed via time scaling or mass scaling. The dynamic effects induced by changing the loading time, or inertial effects resulting from increased density to increase the time increment, must remain insignificant. Mass scaling is achieved by increasing the density of the smallest elements, which modifies the wave speed and the resulting time step.

Table 5.2 compares mass scaled models controlled with a time step increment ranging from 2.5x10^{-6} s to no scaling. Without scaling the model would compute in 175 days. The mass in the system without scaling is 0.169 kg and increases to $\approx$ 6 kg at the most extreme scaling studied. Figure 5.4 compares the resulting thrust force with mass scaling controlled by the time step, on the range from 2.5x10^{-7} s to 7.5x10^{-8} s. A large oscillation response is generated by the increased mass in the model when heavily scaled, resulting in exaggerating the thrust force impact in the CFRP workpiece. The range bar in Figure 5.4 illustrates the oscillation magnitude. This produces a shock wave into the workpiece, with an exaggerated damage front.

Table 5.2: Effect of mass scaling.

Time step (sec.)	CPU time (days)	Complete (%)	Mass change (%)	Net weight (kg)
2.5x10^{-6} s	0.748	100	3.419E3	5.950172
1.0x10^{-6} s	0.962	100	5.469E2	1.093824
7.5x10^{-7} s	2.076	100	3.076E2	0.689199
5.0x10^{-7} s	3.086	100	1.366E2	0.400060
2.5x10^{-7} s	5.897	100	3.403E1	0.226627
1.0x10^{-7} s	13.128*	93.3	5.303	0.178053
7.5x10^{-8} s	19.615*	39.4	2.910	0.174007
1.096x10^{-8} s	174.669*	0.1	No Scaling	0.169087

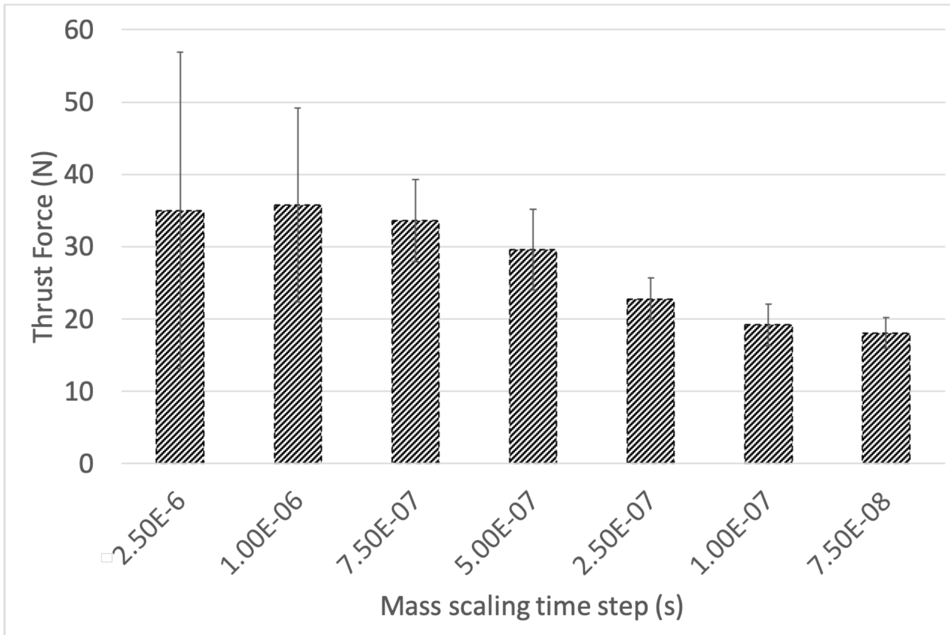

Figure 5.4: Effect of mass scaling on thrust force.

The 7.5x10^{-8} s time step resulted in a mass scaling of 2.91% and develops a smooth progression through the loading profile. However, this time step requires significant computational resources. The 1.0x10^{-7} s time step involving a 5.30% scaling reduces the computational burden by 3 days while avoiding a harmonically induced thrust force loading response. The time step of 2.5x10^{-7} s was used to investigate the effect of model input parameters on model response, seen in sections 3.3 to 3.6. For the 3D drilling model, a time step of 1.0x10^{-7} s was used.

5.3.3 Bulk Viscosity

When modelling high rate, dynamic situations, bulk viscosity applies damping with respect to the volumetric straining [45]. In an explicit analysis, the bulk viscosity is applied in a linear and quadratic form. The linear bulk viscosity is used to dampen the resonant in the highest element frequency and is expressed in Equation 5.5 [45],

$$p_1 = b_1 \rho c_d L^e \dot{\epsilon_{vol}} \tag{5.5}$$

where b_1 is the damping coefficient that defaults to 0.06 and $\dot{\epsilon_{vol}}$ is the volumetric strain rate. The quadratic bulk viscosity is used to distribute the shock front from a compressive load and prevent elements collapsing from the high velocity gradient and takes the form as shown in Equation 5.6 [45],

$$p_2 = \rho (b_2 L^e \dot{\epsilon_{vol}})^2 \tag{5.6}$$

where b_2 is the quadratic bulk viscosity coefficient with a default variable of 1.2 [45].

To understand and optimize the effect of linear and quadratic bulk viscosity have on the drilling simulation, a parametric study was carried out to investigate the effect of these parameters at two magnitudes and is tabulated in Table 5.3.

Table 5.3: Parametric study on bulk viscosity.

Phase I		
Bulk Viscosity Input b_1, b_2	Change in mass scaling (%)	Thrust Force (N)
0.1, 2.5	8.22	42.43
0.4, 2.5	93.1	56.01
0.7, 2.5	227	83.14
1.1, 2.5	492	139.62
Phase II		
Bulk Viscosity Input b_1, b_2	Change in mass scaling (%)	Thrust Force (N)
0.04, 0.8	-3.95	31.12
*0.06, 1.2	0.00	34.42
0.08, 1.6	3.95	36.61
0.10, 2.0	8.22	36.14

* Default parameters

Phase I outlines the significant impact the bulk viscosity parameters have on the drilling simulation. In comparison to the default magnitudes (0.06, 1.2), the predicted thrust force when the linear and quadratic viscosity parameters are set to 1.1, 2.5, is four times greater. The mass scaling for the model increases by a factor of 4.92 to maintain the time step of the analysis, affecting the load response of the tool. Figure 5.5 illustrates pre and post bulk viscosity damage induced into the workpiece. This is a unrealistic response demonstrating poor prediction capabilities due to incorrect, excessive bulk viscosity parameters. Shown in Figure 5.5 (b), the majority of material beneath the tool fractures causing a spike in the load output not observed with experiments.

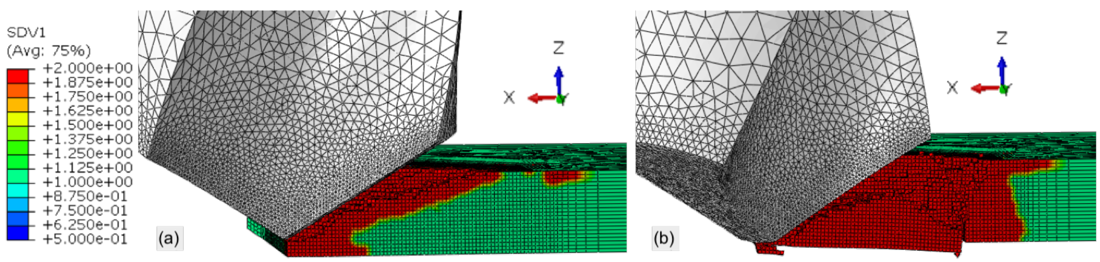

Figure 5.5: (a) Pre and (b) Post bulk viscosity induced damage when $b_1 = 1.1$ and $b_2 = 2.5$.

In Phase II, the bulk viscosity parameters were modified more closely with respect to the default parameters of 0.06 (linear), 1.2 (quadratic). Figure 5.6 illustrates the thrust force for the Phase II viscosity parameters studied. Case '0.04, 0.8' did not provide enough dampening to mitigate the oscillating response present in the loading profile. The default parameters develop a profile inclusive of a loading region with a constant tool engagement region and followed by a decrease in loading as the tool exits, as observed by experiments. An increase from the default parameters to '0.08, 1.6' predicts a similar response while reducing the oscillation output. The '0.1, 2.0' most effectively develops the loading response observed experimentally with the least oscillation in the predicted thrust force.

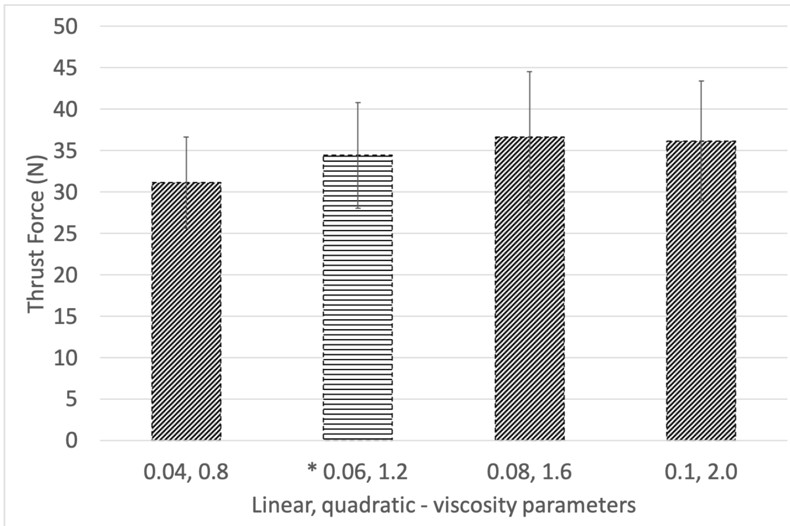

Figure 5.6: Effect of linear and quadratic bulk viscosity on simulated thrust force.

5.3.4 Friction

Friction opposes motion between surfaces in contact. As failed elements are removed from the modelled workpiece while drilling, new elements are exposed. An interior node set creation facilitates the contact between the tool and the newly exposed elements. Contact in an explicit FE model involves a general contact regime that can be enhanced identifying surface pairs.

Normal behaviour between the surfaces applies a “Hard" contact to prevent pressure-overclosure. The tangential behaviour applies a penalty friction formulation isotropically. Chardon et al. highlights the large variety in literature regarding the friction coefficient when machining CFRP, noting researchers using values ranging from 0.09 to 0.9 [47]. The penalty formulation uses Coulomb’s friction relationship that determines the maximum allowable shear stress across an interface as a function of the contact pressure. Once the magnitude of the shear stress surpasses the stick/slip point, the contacting surfaces slide [45]. Coulomb's friction relationship is given in Equation 5.7,

$$F_R = \mu F_N \tag{5.7}$$

where μ is the coefficient of friction and F_N is the normal force. Different coefficients of friction for static and kinetic contact exist, resulting in different static and kinetic friction forces. Neither static or kinetic frictions demonstrate high dependence on contact area between surfaces or roughness, but rather the pairing of materials [48].

Figure 5.7 (a) illustrates common damage experienced when drilling UD-CFRP including fuzzing and spalling [49]. Fuzzing refers to uncut fibres around the hole that develops when the angle between the fibre and the cutting velocity are *acute*. Spalling damage is a form of delamination resulting from the chisel-edge of the drill and develops further as a result of the cutting edges on the side of the drill [49]. Figure 5.7 illustrates the fibre damage (SDV1) output comparing friction coefficients (b) 0.35 and (c) 0.05. The damage observed in the model increased when a greater coefficient of friction was used. Shown in Figure 5.7 (b) and (c), using an identical arc for reference, the increased damage in addition to areas of fuzzing and spalling is noticeable in (b) when the greater friction coefficient is used.

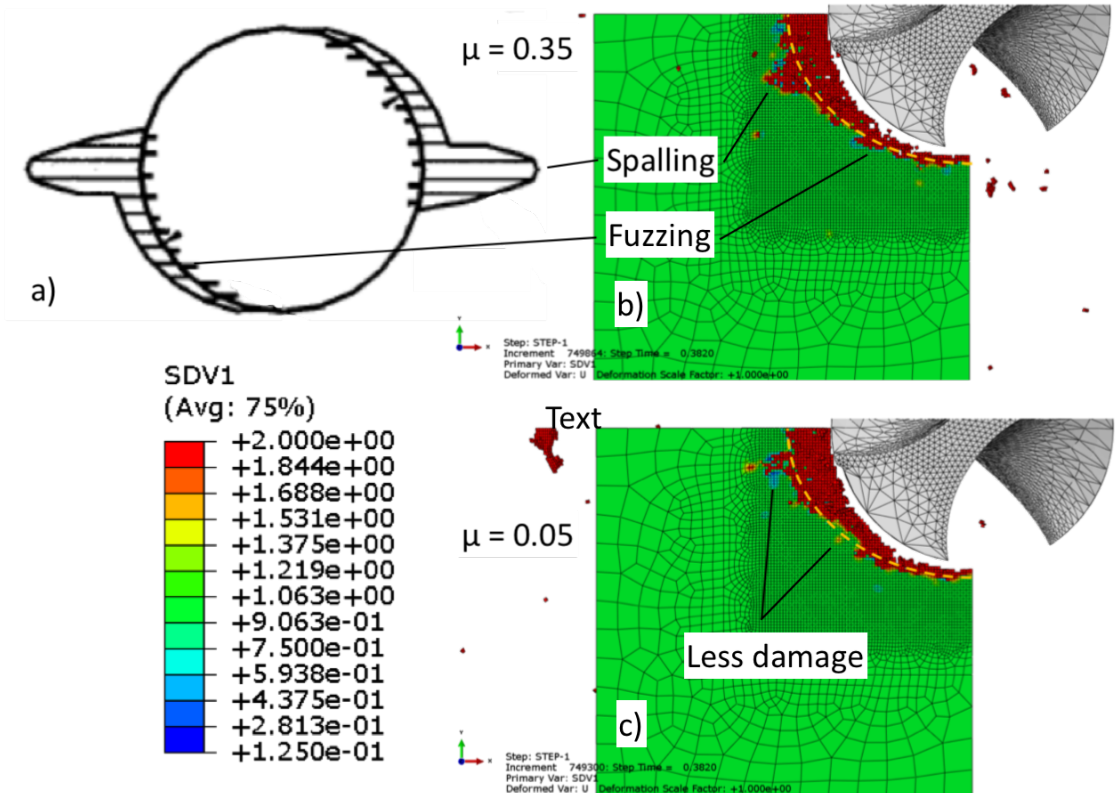

Figure 5.7: (a) Illustration of drilling induced damage by fuzzing and spalling [49] and SDV1 damage distribution at (b) 0.35 and (c) 0.05 coefficient of friction.

The effect of the friction coefficient on the FE drilling model thrust force and in-plane force is tabulated in Table 5.4. The magnitude of the predicted thrust force is not significantly influenced by the friction coefficient. Notable differences in the in-plane force-displacement profile are observed, shown in Figure 5.8, despite minimal change in magnitude as shown in Table 5.4. When the friction coefficient is 0.55, an unsteady oscillating load response develops and an increased in-plane force was observed. The 0.05 friction coefficient does not suffer an oscillating response, however a load spike is observed at the drilling exit. Modifying the friction coefficient changes the interaction between the tool and UD-CFRP. This influences the damage and force prediction, however no discernible, quantifiable relationship was determined. Prakash et al. studied friction coefficients from 0 to 1, noting the magnitude that most closely represents the experiments [50]. Rather than fitting the model, Chardon et al. performs experiments to capture the tribological conditions when machining CFRP and describes an apparent friction coefficient of 0.06 to 0.08 [47]. The drilling models in this research demonstrate improved prediction with low magnitude coefficients of friction agreeing well with [47]. Therefore, a friction coefficient of 0.1 was used in the drilling models.

Table 5.4: Friction coefficient study.

Friction coefficient	Thrust Force (N)	In-plane Force (N)
0.05	34.76	2.32
0.15	34.65	2.43
0.35	38.61	2.29
0.55	35.81	2.62

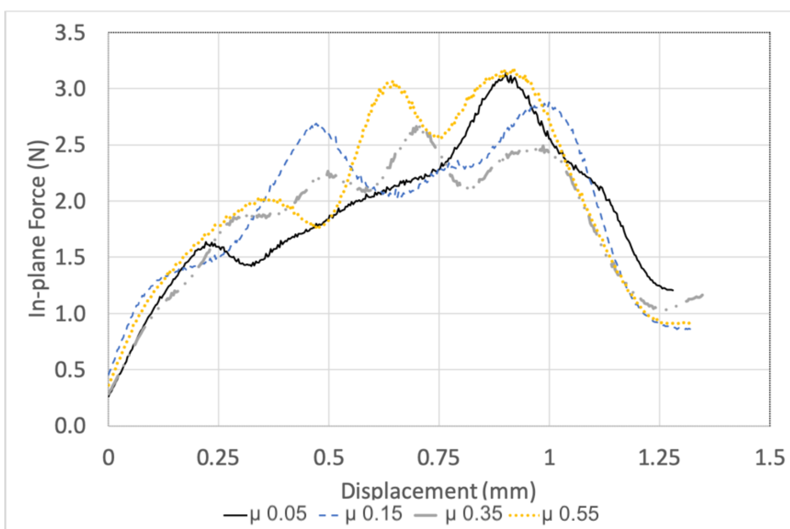

Figure 5.8: Effect of coefficient of friction on in-plane force displacement profile.

5.3.5 Strain Rate Strengthening

In drilling operations, the strain rate can be 1000 s^{-1} and therefore consideration should be made for the strain rate hardening experienced by the epoxy in a CFRP laminate. This is accomplished by invoking two additional user material variables in the VUMAT and are based on the relationship in Equation 5.8 [36],

$$S = S_0\left(1 + \zeta_m log_{10}\frac{\dot{\epsilon}}{\dot{\epsilon_0}}\right) \tag{5.8}$$

A sensitivity analysis regarding the matrix strain rate strengthening parameter was investigated. A model without matrix strain rate strengthening was compared against models setting the strengthening parameters to 0.01, 0.3, 0.5 and 0.99. Figure 5.9 shows the thrust force magnitude with and without strain rate strengthening of the matrix are plotted. The strain rate hardening parameter increases the loading response by 10.87%. The load-displacement response was insensitive to the magnitude of the strain hardening parameter (0.01 to 0.99) despite the relationship described in Equation 6.12. All models studied with the inclusion of the strengthening relationship output the same response. Although the sensitivity analysis was not conclusive, the 10.87% increase in thrust force prediction is in line with the experimental findings described by Lifshitz et al. [25]. Lifshitz et al. described a sensitivity of 1-3 times increase in modulus depending on the loading arrangement with respect to fibre orientation. Although many authors describe the fibre materials' insensitivity to strain rate [15, 17, 18], the matrix and inter-ply interaction demonstrates strain rate sensitivity and directly influence the transfer of load between the fibre and matrix [24].

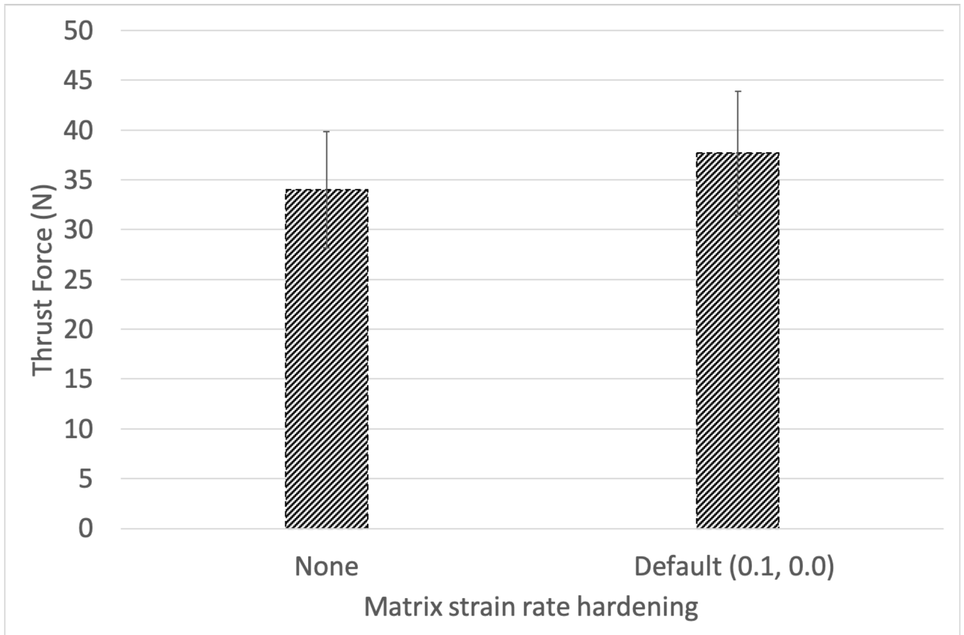

Figure 5.9: Matrix strain rate hardening

5.3.6 Cohesive surface modelling

When a UD-CFRP laminate is loaded in a principal direction such as tension, compression or bending, cohesive surface modelling is a useful mechanism that can facilitate more accurate prediction of the non-linearity in the CFRP material response. A linear-elastic fibre material that follows a damage degradation process cannot sufficiently capture this, reiterating the vitality of cohesive surfaces [32]. Incorporating non-linear material response prediction capabilities is seldom attempted in research due to the added modelling complexity and computational expense, despite experimental testing demonstrating its effect [51, 52].

To model the delamination damage when drilling a CFRP laminate, the geometry was divided into individual instances with cohesive surface interactions applied between them. The CFRP workpiece has a thickness of 1.1 mm and was divided into 10 sections to represent the ply thickness. Node sets are created for the top and bottom surfaces to be used with the cohesive interactions. Individual property assignments are created for the cohesive surface interactions based on prior experiments; details described in [32, 33].

A cohesive contact is modelled using normal behaviour, cohesive behaviour and damage behaviour properties. The damage modelling parameters are the most influential regarding the response of the cohesive surface interaction. This involves identifying a damage initiation point and controlling the damage evolution. Damage evolution will be initiated whereby the stiffness of the cohesive surface will be degraded. Failure separation criteria was controlled by an effective separation at complete failure, relative to the initiation of damage as discovered by [38, 36, 45]. Damage stabilization was applied.

Cohesive modelling between plies is an additional consideration that was implemented to predict the peel-up and break-out damage when drilling UD-CFRP laminates with various drill geometries. This damage has been shown to be most critical to determine a parts functionality [49, 53]. Figure 5.10 (a) and (b) details cohesive surface modelling that has damage initiation values based on the in-plane shear strength of 70 MPa and the transverse (90°) compressive strength of the CFRP of 250 MPa respectively. The damage initiation variable ranges from 0 representing no damage, to 1 representing that damage initiation is complete and damage evolution is initiated. If damage is initiated in the cohesive surface at an inaccurate, lesser strength, the damage will propagate too drastically between the plies, as shown in

Figure 5.10 (c). As the cohesive damage increases the laminate will become multiple, un-bonded plies that are substantially weaker than the original laminate, leading to laminate failure at a lesser strength. The damage initiation and evolution parameters must accurately predict the cohesive relationship. Otherwise unrealistic damage will result in poor model prediction capabilities, which was also concluded by [19]. Shown in Figure 5.10 (b) and (d), the 250 MPa cohesive surface damage initiation strength accurately predicts the damage induced by the thrust and rotation of the drill. Made clear in the figure is the importance of the cohesive bond between the stacking of the plies, which must resist the compressive, bending load induced by the drill and the shearing of the cohesive bond due to the rotation and therefore cutting of the tool.

5.4 Results & Discussion

Figure 5.11 shows thrust force with respect to the drill displacement measured experimentally when drilling CFRP with CD854 and CD856 drill bits. There is an increased thrust force of 22.3% experienced for the CD854, but a more immediate exit of the workpiece in comparison to the CD856. The immediate exit was observed as the thrust force signature came to zero at a drill displacement of 1.75 mm, due to the shallower axial drill tip geometry. The more immediate exit of CD854 drill from the CFRP laminate is due to the spur features that are positioned at the forefront of the drill axially and located at the periphery of the tool, radially. As these spurs exit the laminate in the axial direction, the majority of the hole has been cut radially. In contrast, the CD856 double-point angle results in a delayed, reducing load as it completes the drilling through the CFRP. The tool must travel deeper axially to allow

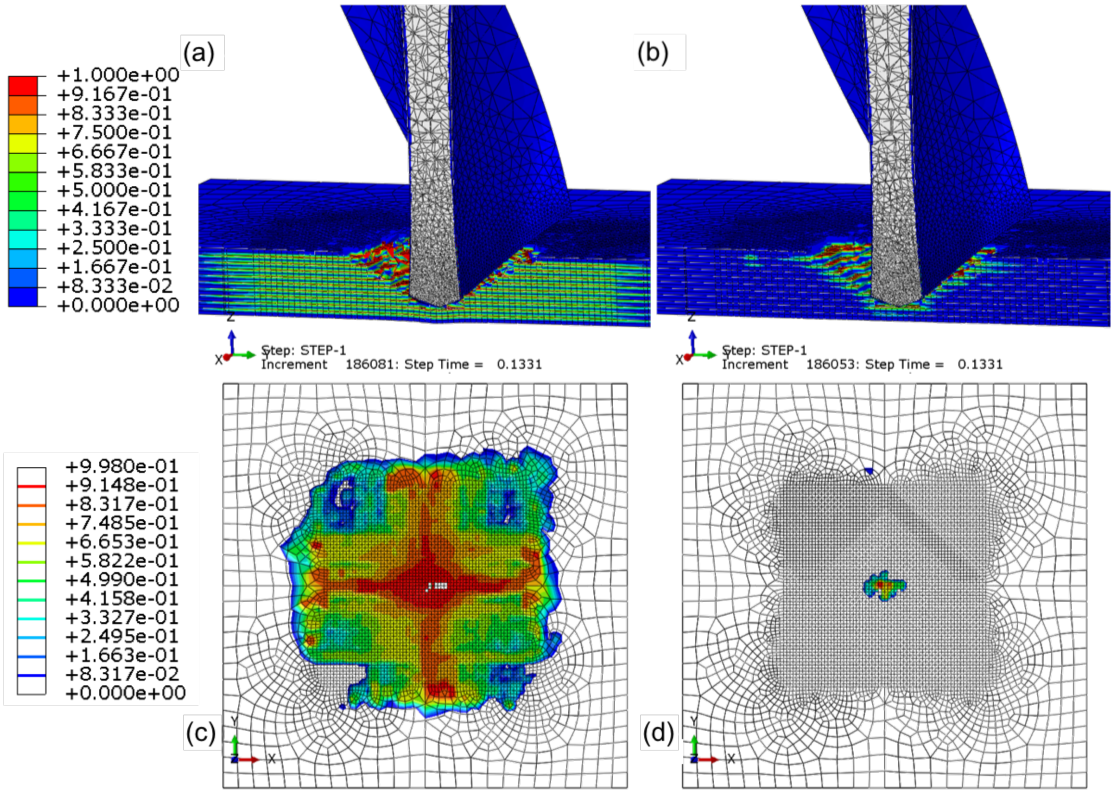

Figure 5.10: Cohesive damage when using MAXS Damage initiation at (a) 70 MPa and (b) 250 MPa. Cohesive damage between plies 9 and 10 (c) 70 MPa and (d) 250 MPa.

for the remainder of the diameter to be machined. This results in the CD856 double-point angle design experiences lower thrust force and agrees well with thrust profiles determined in research done by Li et al. who determined lower thrust and improved hole quality in comparison to standard twist drill geometries [54].

Figure 5.12 (a) and (b) shows the hole entry quality with CD854 and CD856 drills respectively. When drilling with CD854, the amount of fraying at the hole entry was noticeably minimized in comparison to the CD856. Geometrically, a more circular hole was generated with the CD854 versus the CD856. This is evident when the identical white-dashed reference circles were superimposed to the top of the drilled

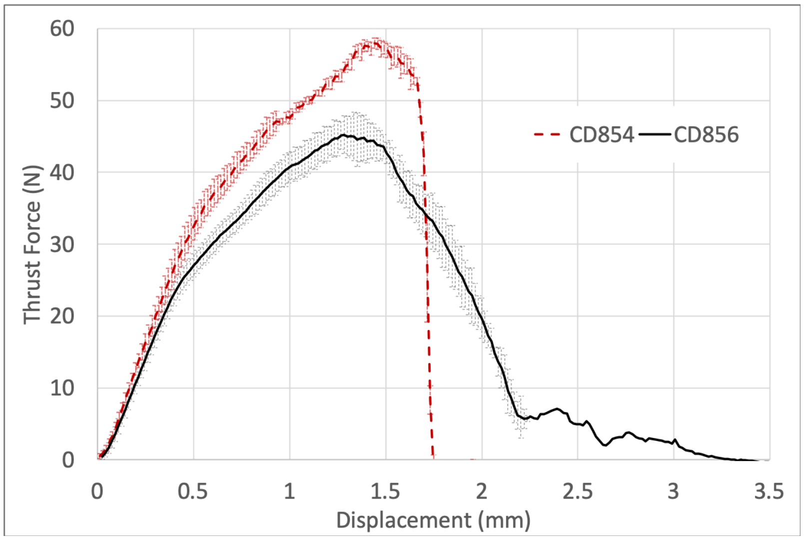

Figure 5.11: Experimentally measured thrust force signature of CD854 and CD856 versus drill displacement.

holes in Figures 5.12 (a) and (b).

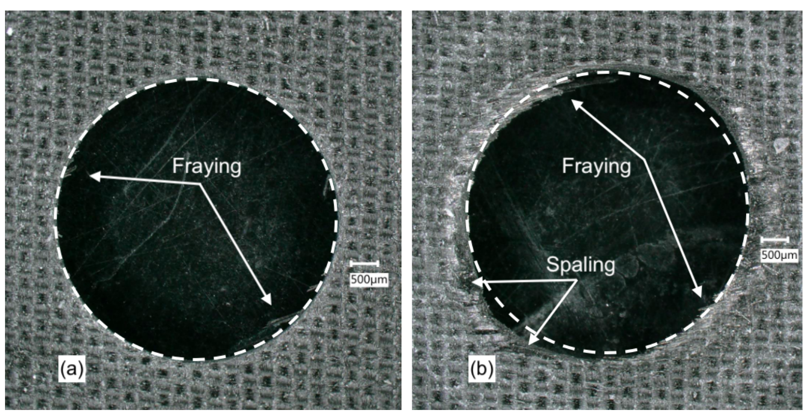

Figure 5.12: Hole entry quality when drilling with (a) CD854 and (b) CD856.

Figure 5.13 details a visual description of the hole entry drilled with CD854 and for the CD856 respectively. Significant fraying was observed at the hole entry when drilling with the CD856 as observed in Figure 5.13 (c). Xu et al. studied double-point angle drill geometries and described similar fraying and tearing defects as shown in Figure 5.13 (b) [55]. Figure 5.13 (a) details the depth profile of the holes. It was observed when drilling with CD856, undesired under-cutting of the hole wall is reduced when compared to the CD854 drill. Qui et al. also described increased fraying and burrs with the double-point angle drill versus the improved hole quality with the candle-stick geometry [56].

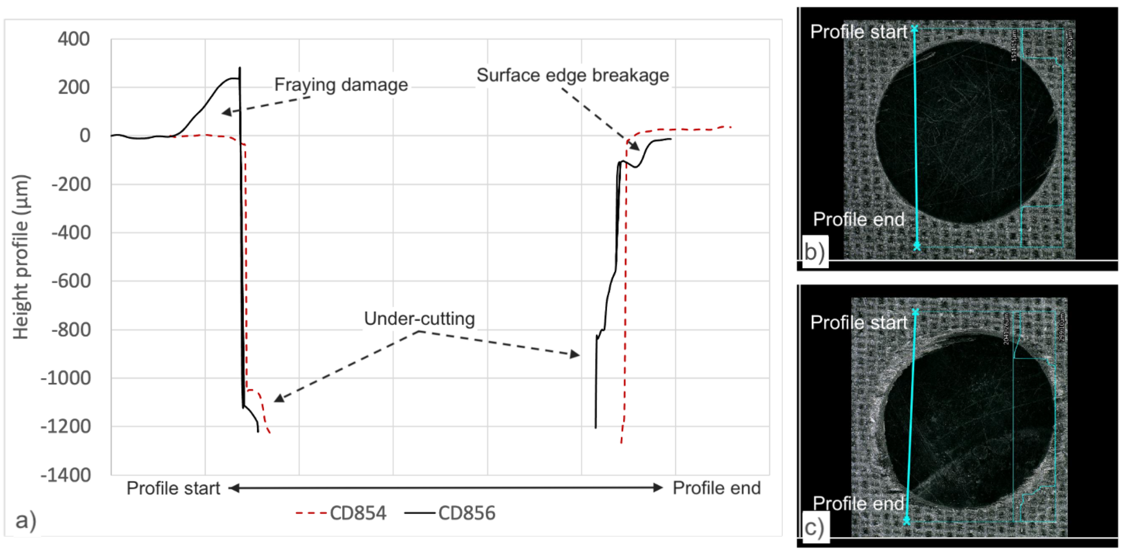

Figure 5.13: (a) Depth profile of the hole drilled with CD854 and CD856 drills, (b) visual of hole entry quality when drilling with CD854 drill, (c) visual of hole entry quality when drilling with CD856 drill.

Figure 5.14 (a) and (b) details the thrust force signature with respect to depth drilled with CD854 and CD856 drills respectively. The difference between the predicted and simulated maximum thrust force for CD854 and CD856 were 6.58% and 0.39% respectively. The modelled thrust force signature for CD854 was unable to predict the rapid decrease when the drill exits the CFRP. Instead a slower rate of decrease was shown. On the other hand, the predicted thrust force signature for the CD856 is similar to those acquired experimentally in both the drilling initiation and exit of the holes as shown in Figure 5.14 (b).

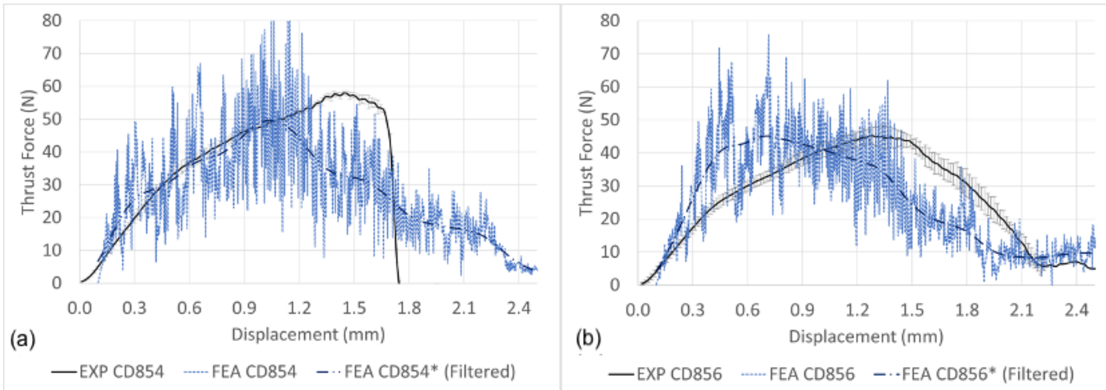

Figure 5.14: Experimental and predicted thrust force, (a) CD854, (b) CD856.

The thrust force signature prediction excluding and incorporating cohesive surface modelling together with experimental results are shown in Figure 5.15 (a) and (b) when drilling with CD854 and CD856 respectively. Shown in Figure 5.15 (a) and (b), the cohesive surfaces provide additional strength and dampening, preventing the compressive shock-wave to prematurely cause elements to fail in the FE model. As a result, the thrust output predicted a more realistic steady cutting zone, before more realistically exiting the CFRP laminate. When the cohesive surface modelling was not considered in the simulation this was not observed, reiterating the significance of incorporating the cohesive interaction in FE models. Effective cohesive surface modelling makes possible the observation of damage between plies and develops a more realistic material representation. The thrust profile prediction with cohesive surface interactions demonstrates better prediction in comparison to the experiments. Karprat et al. who studied various double-point angle drill geometries described similar observations [57, 58]. The cohesive surfaces develop a load profile that extends over a greater drilling displacement, reducing the amount of prematurely failed elements and more accurately predicts the experimental results. In comparison to the drilling experiments, the maximum thrust force predicted by the FE model is within 1.991% for the CD854 and 8.976% for the CD856 drill. However, one must consider the entire load profile prediction and understand there is room for improvement in the FE prediction.

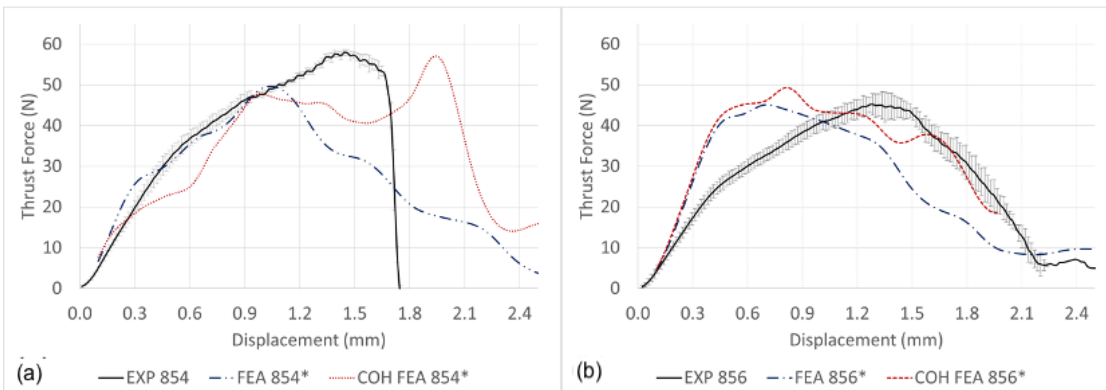

Figure 5.15: Experimental and predicted thrust force signature with cohesive (COH) surface modelling, (a) CD854, (b) CD856.

Figure 5.16 (a) and (b) details the damage initiation (CSMAXSCRT) of the cohesive surface when drilling with CD854 and CD856 respectively. The maximum stress criteria output magnitude ranges from 0 to 1. Zero signifying undamaged cohesive surfaces and one identifying damage evolution initiated. When drilling with CD854, more cohesive damage is observed when compared to CD856. The reduced cohesive damage is a result of the smaller double point angles feature found in the CD856 geometry. The smaller point angles reduce the thrust force induced into the CFRP, which lessens the bending and resulting delamination between the plies. This was observed experimentally by Ahmet et al. experimentally studied the relationship between point angle and delamination, and point angle and thrust force, through an analysis varying spindle speed and feed rate [59]. Most critical, the small point angle of 90° versus the 118° or 130° demonstrated the least delamination. The narrow point angle transforms the axial thrust force into radial compression. This transforms a portion of the axial, mode I - opening failure, to mode II - in-plane shear. More specifically, the axial thrust causing bending and delamination between the plies is reduced. This observation agrees with Su et al. who demonstrated by modifying the spur edge from axial to a double-point angle inspired spur edge, the thrust force included a radial component causing compression on the laminate hole-wall, thereby reducing delamination damage [60].

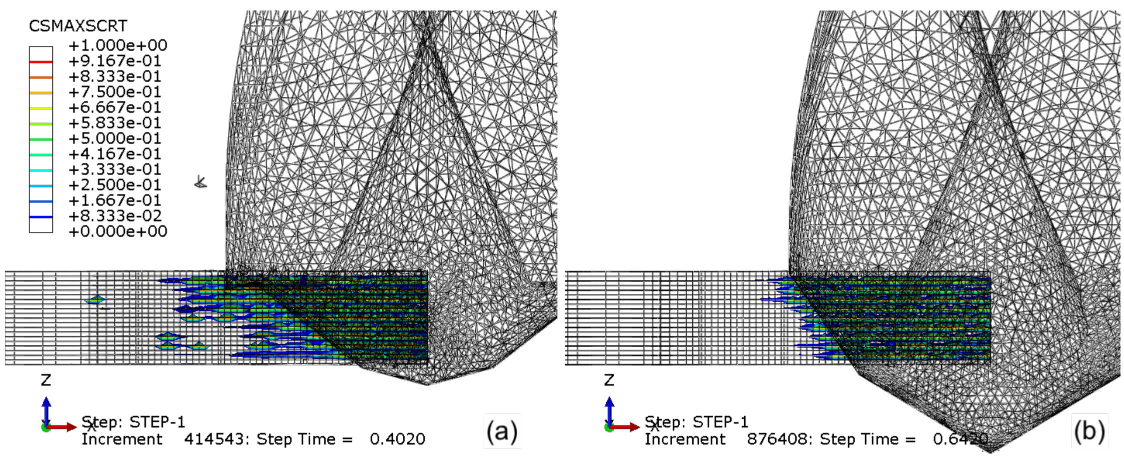

Figure 5.16: Damage initiation (CSMAXSCRT) of the cohesive surface when drilling with (a) CD854 and (b) CD856.

Implementing the cohesive interaction in the FEM model facilitates the ability to capture the delamination damage in the composite. This occurs at the entry and exit of the drilling in the UD-CFRP laminate and must be minimized to maintain the composites' integrity near the hole. This is especially true for thin walled composites. Thick composites have significant material, resulting in a greater second moment of inertia and a higher resistance to bending. However, the thick wall composite is still susceptible to delamination due to the mode I - opening, which is between plies as the tool exits the composite. Thin walled composites are prone to mode I - opening delamination near the entry and exit due to the decreased second moment of inertia.

The FE model developed in this research also predicts hole quality with respect to geometry. Figure 5.17 (a) and (b) details the total damage variable (SDV1) that controls element deletion. The CD854 with the candlestick geometry shown in Figure 5.17 (a), demonstrated a more precisely cut hole and parallel wall. The CD856 as shown in Figure 5.17 (b), demonstrated a less precisely cut wall with some damage resulting in element deletion radially into the laminate. This supports the hole quality results from experiments shown in Figure 5.12 (a) and (b). A precise hole being cut with the CD854 in Figure 5.17 (a) and more spaling and fraying observed by the CD856 hole shown in Figure 5.17 (b). The FEA results and observations experimentally validate the functionality of the spur cutting edge of the CD854, which creates a more precise cutting path resulting in a more accurate drilled hole geometry.

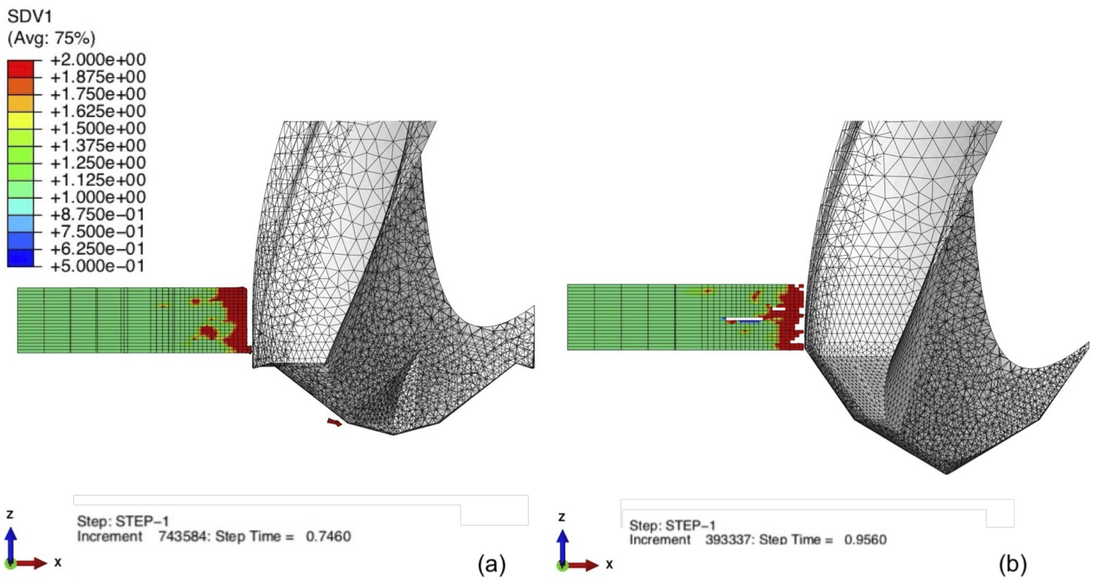

Figure 5.17: Hole quality when drilling with (a) CD854 and (b) CD856.

5.5 Conclusion

A macro 3D FE drilling model was presented that could be used as an accurate simulation tool to model the effects of drill geometries with reasonable computational time. Additionally, a numerical analysis was performed to investigate the influence of mass scaling, bulk viscosity, friction, strain rate strengthening and cohesive surface modelling. The following conclusions were made based on the definite boundaries and magnitude that was used in this investigation:

- Mass scaling has a substantial effect on computational time reduction. Consideration must be made to minimize the dynamic effects caused by the increased density of the elements when implementing mass scaling.

- Linear and quadratic bulk viscosity parameters can mitigate the noise generated during the simulation of CFRP laminate drilling. Effective selection of the bulk viscosity parameters can improve thrust force prediction with a marginal increase in computational time.

- Modelling the tool as a 3D surface, versus the rigid 3D body tool commonly used in literature, demonstrated computational advantage and accuracy in model prediction.

- When cohesive surface modelling was incorporated into the 3D drilling model, the predicted thrust force signature agrees better in terms of magnitude and profile when compared with those acquired experimentally.

- The 3D drilling model could accurately predict the thrust force and hole quality generated by two different drills. Simulated results show that with a double angle drill tip geometry, inter-ply damage was reduced. With the "candle-stick" drill tip, the hole quality was improved.

- In comparison to the drilling experiments, the maximum thrust force predicted by the FE model is within 1.991% for the CD854 and 8.976% for the CD856 drill.

- The CD854 "spur-edges" drills a higher quality hole, however the CD856 double-angle reduces delamination. Further investigation continues into the modification of the spur-edge to reduce inter-ply damage by promoting axial compression.

References

[1] E.P. DeGarmo, J.T. Black, and R.A. Kohser. *Materials and Processes in Manufacturing*. Wiley, 2003. ISBN: 9780471656531.

[2] A. Faraz, D. Biermann, and K. Weinert. "Cutting Edge Rounding: An Innovative Tool Wear Criterion in Drilling CFRP Composite Laminates". In: *International Journal of Machine Tools and Manufacture* Vol. 49, No. 15 (2009), 1185 − 1196. URL: http://dx.doi.org/10.1016/j.ijmachtools.2009.08.002.

[3] R. Zitoune, L. Crouzeix, F. Collombet, T. Tamine, and Y.H. Grunevald. "Behaviour of Composite Plates with Drilled and Moulded Hole Under Tensile Load". In: *Composite Structures* Vol. 93, No. 9 (2011), 2384 − 2391. URL: https://doi.org/10.1016/j.compstruct.2011.03.027.

[4] M.A. Karataş and H. Gökkaya. "A Review on Machinability of Carbon Fiber Reinforced Polymer (CFRP) and Glass Fiber Reinforced Polymer (GFRP) Composite Materials". In: *Defence Technology* Vol. 14, No. 4 (2018), 318 − 326. URL: https://doi.org/10.1016/j.dt.2018.02.001.

[5] H. Wang, H. Zhang, K. Goto, I. Watanabe, H. Kitazawa, M. Kawai, H. Mamiya, and D. Fujita. "Stress Mapping Reveals Extrinsic Toughening of Brittle Carbon Fiber in Polymer Matrix". In: *Science and Technology of Advanced Materials* Vol. 21, No. 1 (2020), 267 − 277. URL: https://doi.org/10.1080/14686996.2020.1752114.

[6] W. König, C. Wulf, P. Grass, and H. Willerscheid. "Machining of Fibre Reinforced Plastics". In: *CIRP Annals* Vol. 34, No. 2 (1985), 537 − 548. URL: https://doi.org/10.1016/S0007-8506(07)60186-3.

[7] S.O. Ismail, S. Sarfraz, M. Niamat, M. Mia, M.K. Gupta, D.Y. Pimenov, and E. Shehab. "Comprehensive Study on Tool Wear During Machining of Fiber-Reinforced Polymeric Composites". In: *Machining and Machinability of Fiber Reinforced Polymer Composites*. Singapore: Springer, 2021, 129 − 147. ISBN: 978-981-33-4153-1. URL: https://doi.org/10.1007/978-981-33-4153-1_5.

[8] A. Vijayaraghavan and D. Dornfeld. "Challenges in Modelling Machining of Multilayer Materials". In: (2005). UC Berkeley: Laboratory for Manufacturing and Sustainability, 1 − 8. URL: Permalink:~https://escholarship.org/uc/item/60k6x64r.

[9] K.K. Panchagnula and K. Palaniyandi. "Drilling on Fiber Reinforced Polymer/Nanopolymer Composite Laminates: A Review". In: *Journal of Materials Research and Technology* Vol. 7, No. 2 (2018), 180 − 189. URL: https://doi.org/10.1016/j.jmrt.2017.06.003.

[10] F. Lissek, J. Tegas, and M. Kaufeld. "Damage Quantification for the Machining of CFRP: An Introduction about Characteristic Values Considering Shape and Orientation of Drilling-induced Delamination". In: *Procedia Engineering* 149 (2016), 2 − 16. URL: https://doi.org/10.1016/j.proeng.2016.06.632.

[11] F. Kahwash, I. Shyha, and A. Maheri. "Modelling of Cutting Fibrous Composite Materials: Current Practice". In: *Procedia CIRP* 28 (2015), 52 − 57. URL: http://dx.doi.org/10.1016/j.procir.2015.04.010.

[12] D. Liu, Y.J. Tang, and W.L. Cong. "A Review of Mechanical Drilling for Composite Laminates". In: *Composite Structures* Vol. 94, No. 4 (2012), 1265 − 1279. URL: https://doi.org/10.1016/j.compstruct.2011.11.024.

[13] M. Mahid and L. Zhang. "A Finite Element Model for the Orthogonal Cutting of Fiber-Reinforced Composite Materials". In: *Journal of Materials Processing Technology* Vol. 113, No. 1-3 (2001), 373 − 377.

[14] I.S. Shyha, D.K. Aspinwall, S.L. Soo, and S. Bradley. "Drill Geometry and Operating Effects when Cutting Small Diameter Holes in CFRP". In: *International Journal of Machine Tools and Manufacture* Vol. 49, No. 12-13 (2009), 1008 − 1014. URL: https://doi.org/10.1016/j.ijmachtools.2009.05.009.

[15] D. Arola and M. Ramulu. "Orthogonal Cutting of Fiber-Reinforced Composites: a Finite Element Analysis". In: *International Journal of Mechanical Sciences* Vol. 39, No. 5 (1997), 597 − 613. URL: http://dx.doi.org/10.1016/S0020-7403(96)00061-6.

[16] Y.L. He, J.P. Davim, and H.Q. Xue. "3D Progressive Damage Based Macro-Mechanical FE Simulation of Machining Unidirectional FRP Composite". In: *Chinese Journal of Mechanical Engineering* Vol. 31, No.51 (2018), 1 − 16. URL: https://doi.org/10.1186/s10033-018-0250-5.

[17] D. Nayak, N. Bhatnagar, and P. Mahajan. "Machining Studies of UD-FRP Composites Part 2: Finitie Element Analysis". In: *Machining Science and Technology* Vol. 9, No. 4 (2005), 503 − 528. URL: https://doi.org/10.1080/10910340500398183.

[18] L. Lasri, M. Nouari, and M. El Mansori. "Modelling of Chip Separation in Machining Unidirectional FRP Copmposites by Stiffness Degradation Concept". In: *Composites Science and Technology* Vol. 69, No. 5 (2009), 684 − 692. URL: http://dx.doi.org/10.1016/j.compscitech.2009.01.004.

[19] V.A. Phadnis, F. Makhdum, A. Roy, and V.V. Silberschmidt. "Drilling in Carbon/Epoxy Composites: Experimental Investigations and Finite Element Implementation". In: *Composites Part A: Applied Science and Manufacturing* 47 (2013), 41 − 51. URL: https://doi.org/10.1016/j.compositesa.2012.11.020.

[20] S. Jain and D.C.H. Yang. "Delamination-Free Drilling of Composite Laminates". In: *Journal of Engineering for Industry* Vol. 116, No. 4 (1994), 475 − 481. URL: http://dx.doi.org/10.1115/1.2902131.

[21] M.S. Won and C.K.H. Dharan. "Chisel Edge and Pilot Hole Effects in Drilling Composite Laminates". In: *Journal of Manufacturing Science and Engineering* Vol. 124, No. 2 (2002), 242 − 247. URL: http://dx.doi.org/10.1115/1.1448317.

[22] A.H.A. Garekani. "Numerical Modeling of Orthogonal Cutting of Carbon Fibre Reinforced Polymer Composites". PhD thesis. University of British Columbia, 2016. URL: http://dx.doi.org/10.14288/1.0305793.

[23] X. Wang D.and He, Z. Xu, W. Jiao, F. Yang, L. Jiang, L. Li, W. Liu, and R. Wang. "Study on Damage Evaluation and Machinability of UD-CFRP for the Orthogonal Cutting Operation Using Scanning Acoustic Microscopy and the Finite Element Method". In: *Materials* Vol. 10, No. 2 (2017), p. 20. DOI: 10.3390/ma10020204. URL: https://doi.org/10.3390/ma10020204.

[24] J.L. Merino-Perez, R. Royer, E. Merson, A. Lockwood, S. Ayvar-Soberanis, and M.B. Marshall. "Influence of Workpiece Constituents and Cutting Speed on the Cutting Forces Developed in the Conventional Drilling of CFRP Composites". In: *Composite Structures* 140 (2016), 621 − 629. URL: http://dx.doi.org/10.1016/j.compstruct.2016.01.008.

[25] J.M. Lifshitz and H. Leber. "Response of Fiber-Reinforced Polymers to High Strain-Rate Loading in Interlaminar Tension and Combined Tension/Shear". In: *Composites Science and Technology* Vol. 58, No. 6 (1998), 987 − 996. URL: http://dx.doi.org/10.1016/S0266-3538(97)00226-1.

[26] K. Giasin, S. Ayvar-Soberanis, T. French, and V. Phadnis. "3D Finite Element Modelling of Cutting Forces in Drilling Fibre Metal Laminates and Experimental Hole Quality Analysis". In: *Applied Composite Materials* Vol. 24, No. 1 (2017), 113 − 137. URL: https://doi.org/10.1007/s10443-016-9517-0.

[27] C.R. Dandekar and Y.C. Shin. "Multiphase Finite Element Modeling of Machining Unidirectional Composites: Prediction of Debonding and Fiber Damage". In: *Journal of Manufacturing Science and Engineering* Vol. 130, No. 5 (2008). URL: http://dx.doi.org/10.1115/1.2976146.

[28] A. Abena, S.L. Soo, and K. Essa. "A Finite Element Simulation for Orthogonal Cutting of UD-CFRP Incorporating a Novel Fibre-Matrix Interface Model". In: *Procedia CIRP* 31 (2015), 539 − 544. URL: `http://dx.doi.org/10.1016/j.procir.2015.04.091`.

[29] S. Usui, J. Wadell, and T. Marusich. "Finite Element Modeling of Carbon Fiber Composite Orthogonal Cutting and Drilling". In: *Procedia CIRP* 14 (2014), 211 − 216. URL: `http://dx.doi.org/10.1016/j.procir.2014.03.081`.

[30] S. Zenia, L.B. Ayed, M. Nouari, and A. Delamézière. "An Elastoplastic Constitutive Damage Model to Simulate the Chip Formation Process and Workpiece Subsurface Defects when Machining CFRP Composites". In: *Procedia CIRP* 31 (2015), 100 − 105. URL: `http://dx.doi.org/10.1016/j.procir.2015.03.100`.

[31] O. Isbilir and E. Ghassemieh. "Numerical Investigation of the Effects of Drill Geometry on Drilling Induced Delamination of Carbon Fiber Reinforced Composites". In: *Composite Structures* 105 (2013), 126 − 133. URL: `https://doi.org/10.1016/j.compstruct.2013.04.026`.

[32] P. Hale and E.G. Ng. "Non-Linear Material Characterization of CFRP with FEM Utilizing Cohesive Surface Considerations Validated with Effective Tensile Test Fixturing". In: *Materials Today Communications* 23 (2020), 1 − 15. URL: `http://dx.doi.org/10.1016/j.mtcomm.2019.100872`.

[33] P. Hale and E.G. Ng. "Three-Point Bending Analysis with Cohesive Surface Interaction for Improved Delamination Prediction and Application of Carbon Fibre Reinforced Plastics Composites". In: *Modelling and Simulation in Materials Science and Engineering* Vol. 28, No. 3 (2020). URL: `http://dx.doi.org/10.1088/1361-651X/ab7054`.

[34] ACP Composites. *Carbon Firer Uni Laminates*. 2014. Accessed: 6/2015.

[35] Sandvik Coromant. *Composite Product Solutions*. 2010. URL: `https://www.sandvik.coromant.com/SiteCollectionDocuments/downloads/global/brochures/en-gb/C-2940-155.pdf`.

[36] Autodesk Helius PFA. *Theory Manual*. 2016. URL: `http://help.autodesk.com/view/ACMPAN/2016/ENU/?guid=GUID-1FEC4707-77A9-4FA4-BA2D-60B7444A1359`.

[37] Z. Hashin. "Failure Criteria for Unidirectional Fiber Composites". In: *Journal of Applied Mechanics* Vol. 47, No. 2 (1980), 329 − 334. URL: `http://dx.doi.org/10.1115/1.3153664`.

[38] D.R. Ambur, N. Jaunky, and C.G. Davila. “Progressive Failure of Composite Laminates using LaRC02 Criteria”. In: *Collection of Technical Papers - AIAA/ASME/ASCE/AHS/ASC Structures, Structural Dynamics and Materials Conference* 2 (2004), 898 − 913.

[39] C.G. Davila, P.P. Camanho, and C.A. Rose. “Failure Criteria for FRP Laminates”. In: *Journal of Composite Materials* Vol. 39, No. 4 (2005), 323 − 345. URL: https://doi.org/10.1177/0021998305046452.

[40] S.W. Tsai and E.M. Wu. “A General Theory of Strength for Anisotropic Materials”. In: *Journal of Composite Materials* 5 (1971), 58 − 80. URL: http://dx.doi.org/10.1177/002199837100500106.

[41] S.W. Tsai. “Strength Theories of Filamentary Structures”. In: *Fundamental Aspects of Fiber Reinforced Plastic Composites* 5 (1968), 3 − 11.

[42] R.M. Christensen. “Tensor Transformations and Failure Criteria for the Analysis of Fiber Composite Materials”. In: *Journal of Composite Materials* Vol. 22, No. 9 (1988), 874 − 897. URL: https://doi.org/10.1177/002199838802200906.

[43] A. Puck and H. Schurmann. “Failure Analysis of FRP Laminates by Means of Physically Based Phenomenological Models”. In: *Failure Criteria in Fibre-Reinforced-Polymer Composites* (2004), 264 − 297. URL: http://dx.doi.org/10.1016/B978-008044475-8/50011-1.

[44] M.R. Garnich. “A Multicontinuum Theory for Structural Analysis of Composite Materials”. PhD thesis. University of Wyoming, 1996.

[45] Dassault Systemes. *ABAQUS/CAE User’s Guide, from ABAQUS 6.14 Online Documentation*. 2014.

[46] Sandvik Coromant. *Machining Carbon Fibre Materials. User’s Guide.* Sandviken, Sweden, 2010, 1 − 63. URL: https://www.sandvik.coromant.com/sitecollectiondocuments/downloads/global/technical%5C%20guides/en-gb/c-2920-30.pdf.

[47] G. Chardon, O. Klinkova, J. Rech, S. Drapier, and J.M. Bergheau. “Characterization of Friction Properties at the Work Material/Cutting Tool Interface During the Machining of Randomly Structured Carbon Fibers Reinforced Polymer with Poly Crystalline Diamond Tool Under Dry Conditions”. In: *Tribology International* 81 (2015), 300 − 308. URL: https://doi.org/10.1016/j.triboint.2014.09.002.

[48] V. L. Popov. “Coulomb’s Law of Friction”. In: *Contact Mechanics and Friction: Physical Principles and Applications*. Berlin, Heidelberg: Springer, 2010, 133 − 154. ISBN: 978-3-642-10803-7. DOI: 10.1007/978-3-642-10803-7_10. URL: https://doi.org/10.1007/978-3-642-10803-7_10.

[49] H.J. Zhang, W.Y. Chen, D.C. Chen, and L.C. Zhang. "Assessment of the Exit Defects in Carbon Fibre-Reinforced Plastic Plates Caused by Drilling". In: *Key Engineering Materials* 196 (2001), 43 − 52. URL: https://doi.org/10.4028/www.scientific.net/KEM.196.43.

[50] C. Prakash and K.S. Vijay Sekar. "Influence of Friction Coefficient and Failure Model in 3D FEA Simulation of Drilling of Glass Fiber Reinforced Polymer Composites". In: *Advances in Manufacturing Processes* (2019), 81 − 90. URL: https://doi.org/10.1007/978-981-13-1724-8_8.

[51] S. Marzi, A. Rauh, and R.M. Hinterholzl. "Fracture Mechanical Investigations and Cohesive Zone Failure Modelling on Automotive Composites". In: *Composite Structures* 111 (2014), 324 − 31. URL: http://dx.doi.org/10.1016/j.compstruct.2014.01.016.

[52] X. Li, Y. Yan, L. Guo, and C. Xu. "Effect of Strain Rate on the Mechanical Properties of Carbon/Epoxy Composites Under Quasi-Static and Dynamic Loadings". In: *Polymer Testing* 52 (2016), 254 − 264. URL: https://doi.org/10.1016/j.polymertesting.2016.05.002.

[53] E.D. Eneyew and M. Ramulu. "Experimental Study of Surface Quality and Damage when Drilling Unidirectional CFRP Composites". In: *Journal of Materials Research and Technology* Vol. 3, No. 4 (2014), 354 − 362. URL: http://www.sciencedirect.com/science/article/pii/S2238785414000799.

[54] P. Li, X. Qiu, C. Li, Q. Niu, A. Chen, and T.J. Ko. "Hole Exit Damage and Tool Wear During the Drilling of CFRP with a Double-Point Angle Drill". In: *Journal of Mechanical Science and Technology* Vol. 33, No. 5 (2019), 2363 − 2370. URL: https://doi.org/10.1007/s12206-019-0436-5.

[55] C. Xu, Y. Wang, J. Xu, and X. Liu. "Design of Internal-Chip-Removal Drill for CFRP Drilling and Study of Influencing Factors of Drilling Quality". In: *The International Journal of Advanced Manufacturing Technology* Vol. 106, No. 5 (2020), 1657 − 1669. URL: https://doi.org/10.1007/s00170-019-04698-8.

[56] X. Qiu, P. Li, C. Li, Q. Niu, A. Chen, P. Ouyang, and T.J. Ko. "New Compound Drill Bit for Damage Reduction in Drilling CFRP". In: *International Journal of Precision Engineering and Manufacturing-Green Technology* Vol. 6, No. 1 (2019), 75 − 87. URL: https://doi.org/10.1007/s40684-019-00026-3.

[57] Y. Karpat and O. Bahtiyar. "Comparative Analysis of PCD drill Designs During Drilling of CFRP Laminates". In: *Procedia CIRP* 31 (2015), 316 − 321. URL: http://dx.doi.org/10.1016/j.procir.2015.03.094.

[58] Y. Karpat, B. Değer, and O. Bahtiyar. "Drilling Thick Fabric Woven CFRP Laminates with Double Point Angle Drills". In: *Journal of Materials Processing Technology* Vol. 212, No. 10 (2012), 2117 − 2127. URL: https://doi.org/10.1016/j.jmatprotec.2012.05.017.

[59] E. Kilickap A. Yardimeden and Y.H. Celik. "Effects of Cutting Parameters and Point Angle on Thrust Force and Delamination in Drilling of CFRP". In: *Materials Testing* 56 (2014), 1042 − 1048. URL: https://doi.org/10.3139/120.110666.

[60] Fei Su, Lei Zheng, Fujian Sun, Zhenhua Wang, Zhaohui Deng, and Xinyi Qiu. "Novel Drill Bit Based on the Step-Control Scheme for Reducing the CFRP Delamination". In: *Journal of Materials Processing Technology* 262 (2018), 157 − 167. ISSN: 0924-0136. DOI: https://doi.org/10.1016/j.jmatprotec.2018.06.037.

Chapter 6

Extending the Finite Element Drilling Model

FEM "Stack-Up" drilling study of fibre reinforced composite material laminated by Aluminum, validated with experiments.

6.1 Introduction

Stack-Ups are laminated carbon fibre reinforced polymers (CFRP) generally by aluminum and/or titanium sections. One step drilling operation requirements have led to the development of pneumatic, electric and robotic advanced drilling units to improve cutting efficiency and quality.

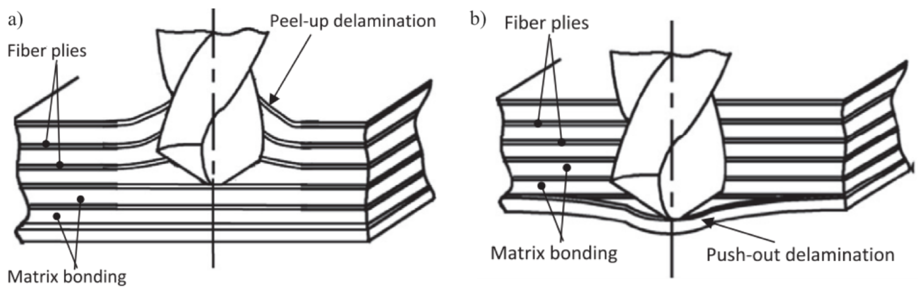

Figure 6.1: a) Peel-up effect b) Push-out effect [20]

With delamination, the drill movement of a distance dX is associated with the work done by the thrust force, F_A. This deflects the ply while promoting the inter-laminar crack. The energy related to this is represented by Equation 6.1:

$$G_{IC}dA = F_A dX - dU \tag{6.1}$$

where dU is the strain energy, dA is the increase in delamination crack area and G_{IC} is the mode I crack propagation energy per unit area. The drilling induced delamination is a function of the applied thrust force. Exceeding a critical amount, F_A, which the uncut thickness of the laminate cannot withstand causes delamination. Figure 6.2 illustrates the mechanism outlined by Equation 6.2:

$$F_A = \pi\sqrt{32G_{IC}M} = \pi\left[\frac{8G_{IC}Eh^3}{3(1-v^2)}\right]^{1/2} \tag{6.2}$$

where E is the Young's Modulus, v is the Poisson's ratio and M is the stiffness per unit width of the fibre-reinforced polymer (FRP). The relationship for M is given by Equation 6.3:

$$M = \frac{Eh^3}{12(1-v^2)} \tag{6.3}$$

A result of the thrust force, is the pure bending of the laminate causing delamination. The change in area, dA, is calculated in Equation 6.4 depending on the radius of delamination, a:

$$dA = \pi(a+da)(a+da) - \pi a^2 = 2\pi a da \tag{6.4}$$

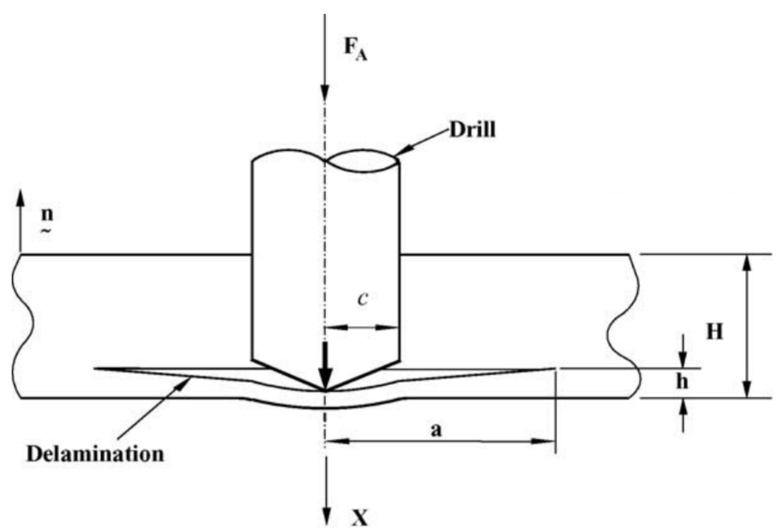

Figure 6.2: Delamination cause by twist drill [24]

By identifying the critical thrust force causing delamination, with respect to uncut thickness of the laminate, the feed rate should be modified throughout the progression of the cut. Mainly, an aggressive feed at initiation to promote material removal rate

(MRR) and a reduced feed to mitigate delamination near the exit of the cut.

When machining Stack-ups additional problems can be experienced such as: metallic chips causing damage on the drilled CFRP surface during chip evacuation, separation of plies allowing for the accumulation of metal chips and CFRP dust in the interface between materials, and hole size variation due to cutting efficiency and varying thermal expansion coefficients between materials. Simulating the machining process is an important endevour to predict damage or wear in the CFRP and tools, to maintain quality and cost expectations for part manufacture and to promote greater understanding of the cutting process, therefore contributing to advancements in tool design.

CFRP has been effectively modelled in tensile and bending setups to accurately and efficiently predict material response and failure in common modes [151, 152], however Finite Element Modelling (FEM) on Stack-Ups involves higher strain rates, complex tool design and various material interactions, therefore requiring specific modelling considerations. Vijayaraghvan described many of these considerations when modelling multi-layer-material machining, including material modelling, contact, fracture criteria, adaptive meshing, element types, tool modelling, etc. [104].

3D orthogonal and drilling model produced by Usui et al. captured delamination in various fibre orientations by using cohesive zone elements mapped to fracture planes defined by the Miller indices [46]. Giasin et al. developed a 3D drilling model of a hybrid material made of stacked glass fibre/epoxy prepreg with aluminum sheets [49]. The FE model provided torque measurement within 18% and thrust force within 52%. Xu and Mansori preformed experiments outlining machining quality when trimming CFRP/Ti stacks relies highly on fibre orientaiton and tool wear [119]. Zitoune et al.

preformed experimental tests on drilling stacks and determined thrust force of aluminum and titanium to be 2-3 times higher than CFRP and high feed rates increase circularity [120]. Phadnis et al. experimentally drilled Aluminum with CFRP stacks and compared with an FEA model. Results showed that a low feed rate, high cutting speeds reduced thrust force and torque [48]. Karpat et al. compared drill designs experimentally and highlighted that double point drill angles with long primary edge length show lower thrust force at exit however experience increased wear and confirms better tool performance at lower feeds [113]. Shyha et al. investigated hole quality utilizing one drill geometry with various coatings, coolant environments, cutting speeds and feed settings in addition to a dual level speed program, doubling the speed for Aluminum and CFRP versus the Titanium. Studying wet coolant versus spray mist coolant, Shyha et al. determined wet, high pressure coolant undersized holes 14-20 μm versus up to 120 μm with spray mist coolant [122]. Park et al. concluded that polycrystalline diamond (PCD) drills were superior to tungsten carbide (WC) drill. However, major chipping was noticed at the cutting edges when drilling titanium due to brittle nature of PCD. CFRP abraded the cutting edge, and titanium extended the flank wear due to carbide grain pullout when the titanium adhesion was removed [16]. Wang et al. studied the effect of tool wear in drilling CFRP, describes rapid dulling due to brittle nature of CFRP can be significantly reduced with ultra-hard diamond coating, however aluminum titanium nitride (AlTiN) did not, due to its oxidation during drilling. Insignificant change in torque was observed after 80 holes, however 3.5 times the thrust force with wear on uncoated and AlTiN coated [114]. Drilling Titanium, CFRP and Aluminum Shyha et al. demonstrated low cutting speed and feed under wet conditions were most ideal (less than 20/40 m/min & 0.05 mm/rev)

[123]. This feed is recommended for drilling stacks by multiple drill manufacturers including Sandvik [109], however this cutting speed is 1.5-3 times less than commonly recommended. Although tool life demonstrated 310 drilled holes, material removal has decreased and therefore productivity. Brinksmeier et al. experimentally studied the drilling of multi-layer composites consisting of CFRP, Titanium and Aluminum alloys and concluded that improved drill geometries, coatings and minimum quantity lubrication is critical [121].

Jain et al. preformed experiments regarding the reduced feed that support Hocheng et al. work. Jain et al. found 40-60% of the thrust force is created by the chisel edge and demonstrated by reducing the chisel width edge thrust force and thereby delamination was greatly reduced [118]. Further improvements focused on reducing the effect of the chisel edge of the drill to minimize thrust force were preformed by Won who studied the effect on forces with and without pre-drilled holes [116]. The pilot hole was shown to reduce thrust force significantly allowing for use of much higher feed force. Lissek et al. describes delamination is the most critical damage when drilling CFRP [106].

Won demonstrated that as the feed rate increased from 0.1 to 0.7 mm/rev for a 1/4" twist drill the thrust force increased nearly 5 times in magnitude; a feed rate greater than 0.1 mm/rev resulted in a thrust force greater than the critical force causing delamination damage. However, with the pre-drill thrust force increased only marginally and remained well under the critical thrust force value even at feeds of 0.7 mm/rev. Tsao and Hocheng continued this investigation identifying a process window for pre-drilled holes relating the ratio of the chisel edge length to pre-drilled hole diameter. As a result the critical thrust is reduced with a pre-drilled hole, therefore allowing for more assertive feed rates to be used [117].

The objective of this work is to develop an efficient, effective FE model validated by experimental work, which then provides the foreground reasoning to test alternative cutting speeds and feeds, tool geometries incorporating predrill, alternate frictions representing coatings and coolants, stacking sequences and other parameters that can improve the machining process of various CFRPs and Stack-ups.

6.2 FE modelling theory & considerations

6.2.1 UD-CFRP Material Behavior Model

A macro-mechanical approach treated the FRP as an equivalent homogeneous material (EHM). The EHM model based on Multi-Continuum Theory (MCT) uses a representative volume element (RVE) to express the composite stress state as shown in Equation 6.5:

$$\sigma^c = \frac{1}{V}\int_D \sigma(x,y,z)dV \tag{6.5}$$

where V is the total RVE and D is the fibre-matrix domain. The fibre and matrix average stress state is shown in Equation 6.6 and 6.7:

$$\sigma^f = \frac{1}{V_f}\int_{D_f} \sigma(x,y,z)dV \tag{6.6}$$

$$\sigma^m = \frac{1}{V_m}\int_{D_m} \sigma(x,y,z)dV \tag{6.7}$$

The constituent average stress and strain $(\sigma^f, \sigma^m, \epsilon^f, \epsilon^m)$ are critical to predict damage and material failure versus a homogenized average stress and strain (σ^c, ϵ^c) [153]. When a FRP is subject to loading non-parallel to the fibre orientation, failure is dominated by the matrix constituent. Damage should not be controlled by the fibre, nor should the matrix damage act only as a contribution to the homogenized composite material failure. This is a significant limitation of prior EHM modelling versus the MCT-EHM formulation. If a failure criterion is independent, based only on a matrix parameter, it can be evaluated and trigger element deletion.

When damage is initiated, controlled by the failure model implemented, an instantaneous degradation method reduces the stiffness of the matrix and fibre from its original undamaged state to a user-defined value between zero and one. This degradation scheme is implemented instantaneously, or can be defined for a time period to improve the response prediction of fracture. This is an efficient degradation method, however can be sensitive to mesh size resulting in increased failure loads for coarse meshes and premature failure for refined mesh models. To avoid premature failure prediction of the CFRP loading response, techniques including damping applied through bulk viscosity, softening in contact interactions and enhanced element controls reducing stiffness, can be applied.

To model the delamination damage when drilling a CFRP laminate, the geometry was divided into individual instances with cohesive surface interactions applied between them. The CFRP workpiece has a thickness of 1.1 mm and was divided into 10 sections to represent the ply thickness. Node sets are created for the top and bottom surfaces to be used with the cohesive interactions. Figure 6.3, the ply 1 bottom surface and ply 2 top surface of the cohesive interaction is shown.

A General Contact (Explicit) interaction was created with a Global Property

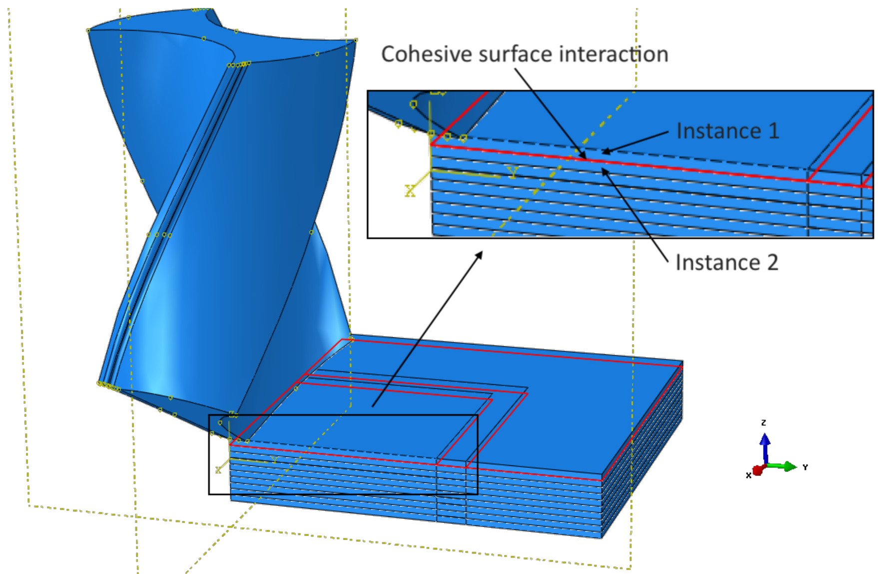

Figure 6.3: Cohesive surface interaction setup

assignment applied to the model. Individual property assignments between each pair of instances are defined. Symmetry is utilized in the geometry to reduce the CFRP laminate to one quarter helping to alleviate the computational expense brought on by the inclusion of cohesive surfaces.

To model the cohesive surfaces, a contact property is created including three main properties: normal behaviour, cohesive behaviour and damage behaviour. Normal behaviour determines the contact behaviour in the normal direction and is controlled by the "hard" contact pressure overclosure relationship. The cohesive behaviour allows for any slave nodes that experience contact, whether initially or after some loading, to be controlled by a traction-separation behaviour. The most computationally efficient method in ABAQUS is to have an uncoupled behaviour using stiffness in the normal, secondary and tertiary axis (K_{nn}, K_{ss} and K_{tt}) and the separations in the normal, first shear and secondary shear are denoted by δ_n, δ_s and δ_t. The elastic behaviour of the contact stress, t, is shown in Equation 6.8 [39]:

$$t = K\delta \tag{6.8}$$

The stiffness is represented by Equation 6.9:

$$K_{nn} = K_{ss} = K_{tt} = \alpha E_{33}^{PLY}/t^{PLY} \tag{6.9}$$

where α is a parameter with a suggested value of 50, t^{PLY} is the thickness of the bonded plies and E_{33}^{PLY} is the normal Modulus of the CFRP; this relationship suggests the stiffness is 1.76E6 MPa. The stiffness magnitude is non-physical and must be stiff enough to provide load transfer, but not too stiff that unauthentic fluctuations occur in the output [153]. The initial strength estimate should represent the normal strength of the ply based on Equation 6.10:

$$\frac{S_{12}^{PLY} + S_{23}^{PLY}}{2} = S_s = S_t \tag{6.10}$$

The damage modelling parameters are the most influential regarding the response of the cohesive surface interaction. This involves identifying a damage initiation point and controlling the damage evolution. The damage initiation criteria used is a maximum stress (MAXS) criteria and is expressed as follows in Equation 6.11:

$$MAXS = max\left\{\frac{\langle t_n \rangle}{t_n^o}, \frac{t_s}{t_s^o}, \frac{t_t}{t_t^o}\right\} \tag{6.11}$$

The peak values of the contact stress using MAXS are denoted by t_n^o, t_s^o and t_t^o. Once the ratio of the current contact stress in the normal, secondary and tertiary axis reach one, the damage has been initiated. At this point, the damage evolution will be initiated whereby the stiffness of the cohesive surface will be degraded. Failure separation criteria will be controlled by an effective separation at complete failure, relative to the initiation of damage [154, 153, 39]. Damage stabilization was applied with a viscosity coefficient of 0.001.

In drilling operations, the strain rate can be 1000 s^{-1} and therefore consideration should be made for the strain rate hardening experienced by the epoxy in a CFRP laminate. This is accomplished by invoking two additional user material variables in the VUMAT and are based on the relationship in Equation 6.12:

$$S = S_0\left(1 + \zeta_m log_{10}\frac{\dot{\epsilon}}{\dot{\epsilon_0}}\right) \tag{6.12}$$

where S_0 is the strength at a strain rate of $\dot{\epsilon_0} = 0.001s^{-1}$, ζ_m is the user material magnitude for matrix strain hardening. For reference, a matrix strength of 50 MPa and a $\zeta_m = 0.1$ results in a strength of 75 MPa when the strain rate ($\dot{\epsilon}$) is $100s^{-1}$. When the strain rate is increased to $1000s^{-1}$ the matrix strength becomes 80 MPa based on this relationship. An identical relationship to Equation 6.12 is formulated for the fibre material strain hardening effect, however this was not implemented due to insensitivity noted in literature [95, 140, 155].

6.2.2 Aluminium 6061 Material Behavior Model

The Johnson-Cook (JC) plasticity model can effectively predict the deformation of ductile metals at high strain rates experienced when machining [139]. To represent the ductile Aluminum material used in the drilling experiments the JC material model was implemented, shown by Equation 6.13:

$$\bar{\sigma} = (A + B\bar{\epsilon}^n)\left[1 + Cln\left(\frac{\dot{\bar{\epsilon}}}{\dot{\bar{\epsilon_0}}}\right)\right]\left[1 - \left(\frac{T - T_{room}}{T_{melt} - T_{room}}\right)^m\right] \tag{6.13}$$

where $\bar{\sigma}$ is the equivalent stress, $\bar{\epsilon}$ is the equivalent plastic strain, $\dot{\bar{\epsilon}}_0$ is the reference strain rate at 1.0 s^{-1} and $\dot{\bar{\epsilon}}$ is the plastic strain rate. The JC damage model is a cumulative damage law where the increment of equivalent plastic strain, $\Delta\bar{\epsilon}$ is divided by the equivalent strain at failure, $\bar{\epsilon_f}$; shown in Equation 6.14 [39]:

$$D = \sum \left(\frac{\Delta\bar{\epsilon}}{\bar{\epsilon_f}} \right) \tag{6.14}$$

The equivalent strain at failure takes the form of the following Equation 6.15:

$$\bar{\epsilon_f} = \left[D_1 + D_2 exp\left(D_3 \frac{P}{\bar{\sigma}} \right) \right] \left[1 + D_4 ln\left(\frac{\dot{\bar{\epsilon}}}{\dot{\bar{\epsilon}}_0} \right) \right] \left[1 + D_5 \left(\frac{T - T_{room}}{T_{melt} - T_{room}} \right) \right] \tag{6.15}$$

where $D_1 - D_5$ are described in Table 6.1.

Table 6.1: Aluminum 6061 - Johnson Cook Model Parameters [156, 157, 158, 138]

Initial yield stress, A (MPa)	324
Hardening modulus, B (MPa)	114
Strain hardening exponent, n	0.42
Strain rate coefficient, C	0.002
Reference strain rate	1.0 s^{-1}

Aluminum 6061 - Johnson Cook Damage Parameters	
Initial failure strain, D1	-0.77
Exponential factor, D2	1.45
Triaxiality factor, D3	-0.47
Strain rate factor, D4	0.0
Temperature factor, D5	0.0

6.2.3 Drilling Tool Consideration

These drill geometries use advanced design to provide specifically improved drilling function. Representing a tool as a discrete rigid body is an accurate model simplification, specially if the main focus is not modelling the deformation or stress distribution throughout the tool body. The drill was modelled as a discrete rigid body as the main focus is on modelling the deformation and stress distribution in the UD-CFRP and Al6061 "Stack-up" material. A discrete rigid body converts the solid geometry to a shell body. This negates the requirement of meshing the internal volume and focuses on the outer surface using a 4-node bi-linear rigid quadrilateral element (R3D4). This setup requires additional property assignment including the geometries' weight and rotational inertia. A reduction from 67672 elements with the deformable rigid geometry to only 6568 elements using the discrete rigid geometry is created.

To attain greater computational efficiency the drill geometry is considered rigid. Abaqus models rigid bodies using one of three techniques. These drill geometries cannot be represented by primitives, therefore analytical rigid is not an option. The second method uses a 3D deformable body with a rigid body constraint applied. The disadvantage of this method is the dramatic increase in elements due to the meshing of the interior of the drill with 3D modelling. The focus should be on the outer surface representation, not the interior volume.

There are three contrasting methods when creating rigid bodies in Abaqus. Analytically rigid requires the geometry to be modelled by the use of lines, arcs or other primitive CAD geometries. This body cannot be generated from primitives, therefore the analytically rigid representation is not possible.

A deformable body requires a 3D geometry to be created. In the interaction module, a rigid body constraint is made to a portion of an assembly, whereby the nodes and respective elements are controlled by one reference point. An advantage of this method is once the geometry is meshed and material properties are provided, the mass and inertia of the geometry can be determined within the model.

The disadvantage is the dramatic increase in elements due to the 3D modelling; unnecessary as the geometry is rigid, the focus should be on the outer surface representation, not the interior volume.

A deformable body controlled by a rigid constraint maps the nodes and elements of the instance to a reference point.

The discrete rigid body uses a reference node, generally assumed to be the centre of mass and requires the input of the mass and inertia of the instance. The moment of inertia is a measure of the resistance to angular acceleration and is defined as the integral of the "second moment" about an axis of all the elements of mass, dm, which compose the body [159]. The moment of inertia of a body of mass with a density and volume can be expressed as:

$$I = \rho \int_V r^2 dV \tag{6.16}$$

where ρ is the density and r is the radius relative to the instantaneous axis. The moment of inertia magnitudes for the drill geometries were estimated based on a cylinder of equal diameter and mass of the drill bit. The exact moment of inertia was determined via the FE software utilizing the volume and mass properties of the solid deformable body, prior to converting the body to discrete rigid.

The principal advantage to representing portions of a model with rigid bodies rather than deformable finite elements is computational efficiency. Element-level calculations are not performed for elements that are part of a rigid body. Although some computational effort is required to update the motion of the nodes of the rigid body and to assemble concentrated and distributed loads, the motion of the rigid body is determined completely by a maximum of six degrees of freedom at the rigid body reference node [39]. Figure 6.4 compares the 3D tri mesh versus the rigid body quad mesh that was used in the current research.

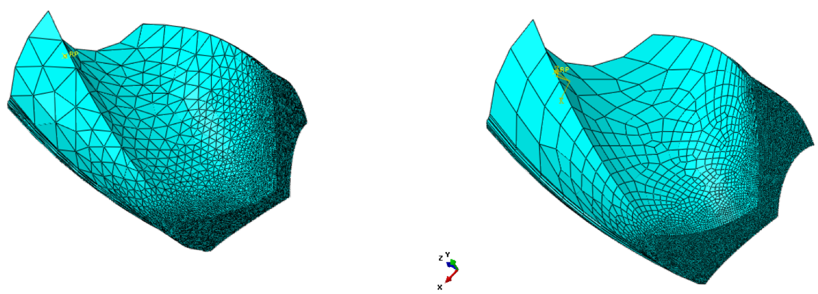

Figure 6.4: 3D tri mesh vs Rigid body quad mesh

In the explicit analysis, the stable time increment decreases as Young's Modulus increase. The tool in a machining simulation that is generally quite stiff and rigid compared to a workpiece can negatively effect the stable time increment. A discrete rigid body does not affect the global time increment, thereby can increase computational efficiency without significantly affecting the overall accuracy of the solution. Comparing identical models except for the described differences in the drill bit representation, the explicit time step for a deformable body with a rigid body constraint is 1.22E-9 seconds, versus a discrete rigid body is 3.43E-9 seconds. An increase in stable time increment of three times and reduction in computation time. The estimated memory required for the otherwise equivalent analyses reduces from 1.9GB to 1.1GB due to the reduced elements required meshing the tool.

6.2.4 Simulation Boundary Condition

To alleviate computational expense with preliminary models the CFRP workpiece was modified with a cut revolve operation to reduce the drilling time; the model simulates the drilling process engaged into the workpiece partially. This modification was present when studying mesh sensitivity, scaling techniques, bulk viscosity and strain rate hardening effect. Utilizing this cut revolve reduces the translation during the simulation and makes more immediate the interaction between the bulk of tool and the workpiece creating a reduction in computation by 40%. To capture the entry and exit of the tool with the workpiece and attain the full loading profile, the revolve cut will be abandoned.

With this modified geometry, a sweep meshing technique with an assigned stack direction and sweep paths most be selected. Figure 6.5 illustrates the importance of mesh controls. In Figure 6.5 b), the failure to apply the sweep path through the CFRP thickness results in thousands of additional elements, generally 1 μm in length. Avoiding mapped meshing is important, a subset of structured meshing, which leads to distorted elements with poor aspect ratio and a large, unnecessary number of elements created [39]. Worse still, the stable increment from equation 5.4, will be reduced by 50 times, thereby increasing the required computation time of the model.

The drilling FE model was designed to replicate the experimental setup using a rigid drill bits as described in the previous chapter.

Cyclic symmetry would reduce a model to a smaller rotational range with respect to the z-axis, the axis of cyclic symmetry. In Figure 6.5 a), one sixth of a model is highlighted with respect to the axis of symmetry. Unfortunately cyclic symmetry is

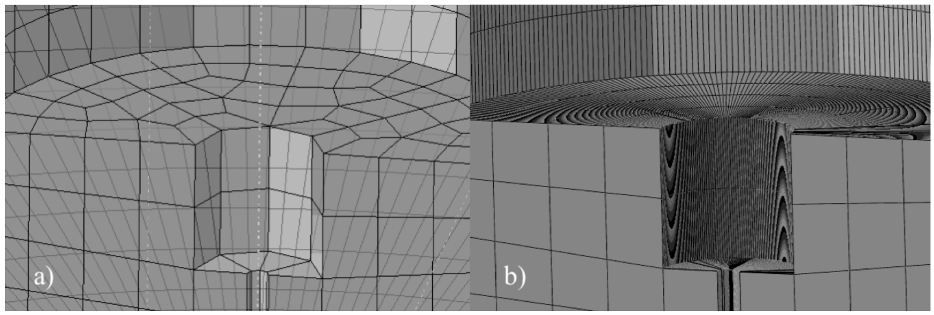

Figure 6.5: a) Properly defined Sweep Path through thickness b) Sweep Path through plane

not possible in Abaqus Explicit models. Shown in Figure 6.6, symmetry in the XZ and YZ plane can be utilized to reduce the workpiece to one quarter and thereby reduce the computation expense. Referring to Figure 6.6 b), the x-axis shown would be parallel to the fibres for the 0-degree reference.

A circular, planar workpiece geometry with cyclic symmetry controlled by the number of flutes on the drill could have great computational savings; half symmetry could be utilized for two flute drills, only one-third of the model is required for three flute drills and one-quarter for four flute drills, etc.

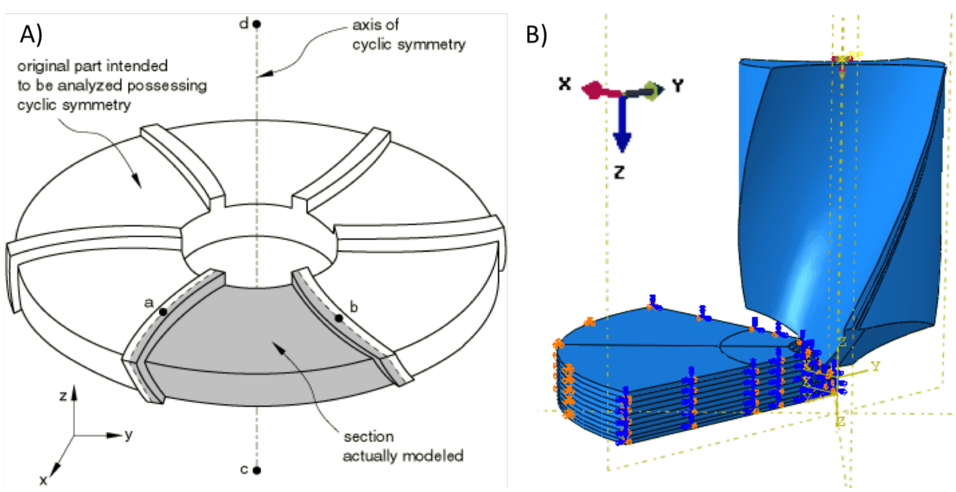

Figure 6.6: A) Cyclic symmetry example [39], B) FEA Drilling setup

The body elements and nodes for the drill are mapped to the reference point; load constraints are most efficiently applied with this setup. When drilling CFRP the loading velocity in the z-axis direction is 3.342 mm/s (feed = 0.05 mm/rev) and rotation is 420.0 rad/s (4010 RPM, 60 m/min cutting speed). The feed rate and cutting speed magnitudes are recommended by the tool manufacturer Sandvik for the CoroDrill (CD) 854 and CD856 drills [160].

The model input file model generated must be edited to consider the internal volume. As elements progress through damage evolution and fail the elements are removed. To allow the drilling tool and the newly exposed elements to contact one another, an interior node set must be created. This allows the internal newly formed surfaces to interact with the associated friction forces, including failing elements that have separated, representing chip fragments. This is achieved by duplicating the element set for the CFRP workpiece and adding the parameter *interior*. The contact regime must be expanded to include the new surfaces created and is accomplished using a mocked Global property assignment and the identification of initial surface contact interactions; see Appendix A for details. This allows the internal newly formed surfaces to interact with the associated friction forces, including failing elements that have separated, representing chip fragments.

6.2.5 Experimental Work

The UD-CFRP and Al 6061 “Stack-Up” material drilling drilling experiments were carried out on a Fanuc controlled Matsuura LX-1, 3-axis vertical CNC machine. Cutting forces were measured using a Kistler three component stationary piezoelectric dynamometer (type 9272, calibrated range: Fx = 0 - 3,000 N, Fy = 0 - 3,000 N, and Fz = 0 - 6,000 N), connected to a series of charge amplifiers (type 5011A, with a frequency limit of 200 kHz). Data acquisition was accomplished using an analogue to digital converter card connected to a high performance computer, which was capable of sampling at 200 KS/sec per channel. Recordings were measured at 10kHz per channel. The drills were tested five times per stack-up arrangement to ensure repeatability.

Table 6.2: Standard Modulus (SM) CFRP - material properties [33]

SM UD CFRP	0°	90°
Longitudinal Modulus (GPa)	135	10
Transverse Modulus (GPa)	10	135
In-plane Shear Modulus (GPa)	5	5
Major Poisson's ratio	0.3	0.3
Ultimate (Ult.) Tensile Strength (MPa)	1500	50
Ult. Comp. Strength (MPa)	1200	250
Ult. In-plane Shear Strength (MPa)	70	70
Ult. Tensile Strain	1.05	0.5
Ult. Comp. Strain	0.85	2.5
Density (g/cm^3)	1.6	

Drill geometries investigated were Sandvik (CoroDrill) CD854 & CD856, which were designed to reduce delamination and splintering. The diamond coated (N_2OC) CD854 has a point geometry with additional spur edges on the circumference, designed to minimize burr formation when drilling Aluminum. The CD856 has a double angle, carbide geometry with diamond coating (N_2OC) that is designed to reduce delamination and splintering. Both CD drills incorporate small point angles (CD854 - 130°, CD856 - 120°) and high rake angles to reduce axial forces, critical for thin walled surfaces [109]. The CD854 drill incorporates additional spurs on the perimeter of the tool that score the circumference of the hole. A design inspired by a Brad-Point drill commonly used in wood working to prevent fibre pull and tearing of the wood. Figure 6.7 illustrates the additional spur cutting edges created with the CD854 on the circumference of the drill geometry.

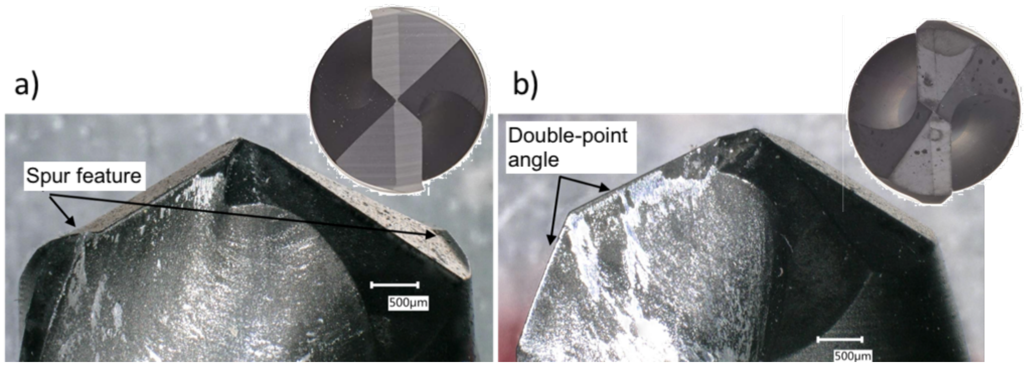

Figure 6.7: Sandvik CoroDrill geometries a) CD845 b) CD856

6.3 Results & Discussion

Figure 6.8 details the thrust force signatures for CD854 and CD856 when drilling through the top layers of UD-CFRP followed by Al 6061 beneath in a "Stack-Up" configuration. When drilling UD-CFRP only up to an initial depth of 1.1 mm, the CD854 load profile was approximately 20% higher than those generated by the CD856. This was because CD856 has a double-point angle design which experienced a lowered thrust force. Li et al. experimentally found similar trend when drilling UD-CFRP with standard twist drill geometries and compared with those double-point angles [161]. When drilling the Al 6061 portion of the 'Stack-Up' material higher thrust force was observed. However, CD856 with a double-point angle generated higher thrust force when compared with CD854, which trend was not similar when drilling UD-CFRP alone. At the hole exit, the CD856 thrust force signature showed a spike trend, which was not observed with CD854.

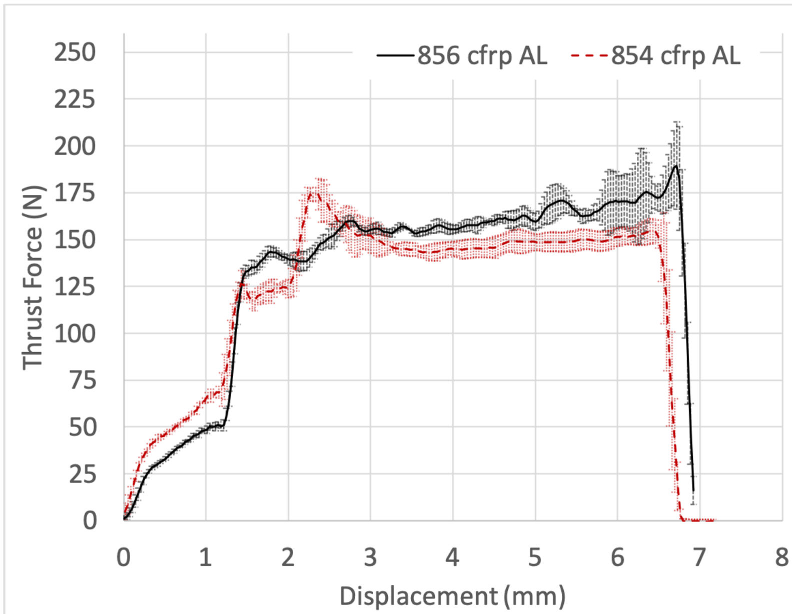

Figure 6.8: Experimentally measured thrust force signature when drilling UD-CFRP and Aluminium “Stack-Up” with CD854 and CD856 drills.

Figure 6.9 details a visual description of the hole entry surface of the Al 6061 drilled with CD854 and CD856. This surface was located at the interface between UD-CFRP and Al 6061. When drilling with CD856, there was a bulge deformation and sharp edge at the profile start and end regions respectively. Larger burr was observed when drilling with CD856. The hole entry burr profiles were like those observed by Hassan et al. [162] when drilling CFRP and Al2024 “Stack-Up” material. The spike in thrust force was associated with the larger burr as observed when drilling with CD856. CD854 did not generate a spike in the force signature, resulting in no burr or bulge deformation during hole entry to the aluminium. Banon et. al. also found similar trend on the effect of thrust force and interface burr height when drilling CFRP/TiAl4V stacks with a double point angle drill [163]. When drilling with high trust force, the workpiece material near the hole exit deflects more when compared to lower thrust force. This deflection would reduce the undeformed chip thickness results in larger burr height. Bonhin et.al [164] also made similar observation when drilling Stack-up combination of Al 2023 and glass fiber reinforced epoxy.

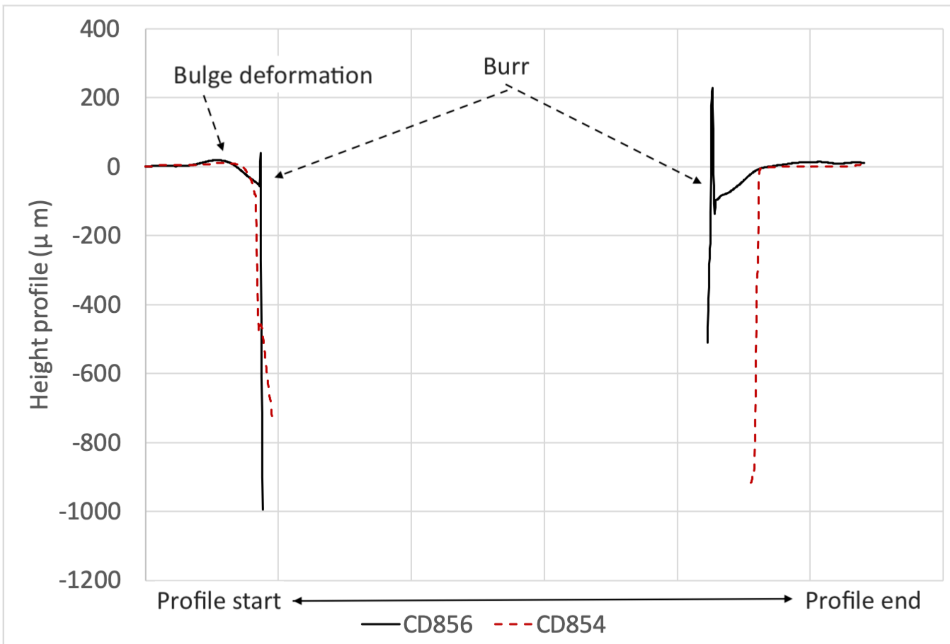

Figure 6.9: Aluminium hole entry profile at the interface of the UD-CFRP and aluminium when drilling with CD854 and CD856

Figure 6.10 shows the Lagrangian drilling model for the aluminium material. Elements exceeding the critical strain experience a damage evolution procedure leading to element deletions.

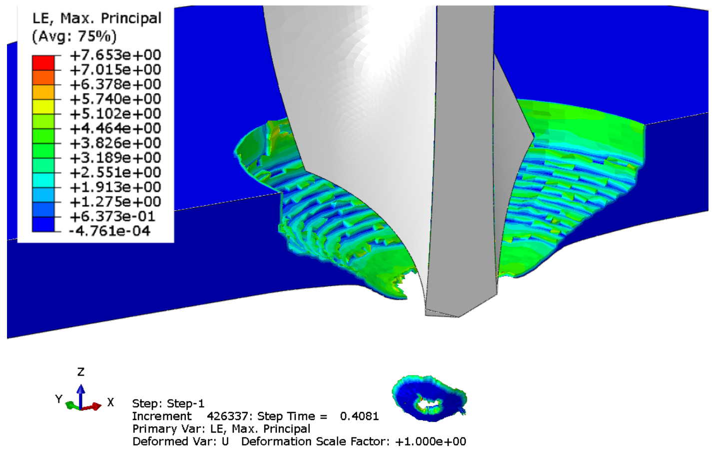

Figure 6.10: Principal strain distributions of the aluminium section when drilling UD-CFRP/aluminium "Stack-up" material with element deletion.

Figure 6.11 and 6.12 shows the simulated and measured force signature when drilling UD-CFRP and Al 6061 'Stack-Up' material with CD854 and CD856 respectively. The thickness of the Al 6061 section in the finite element model was halved to reduce computational time. This did not affect the results as the forces have reached quasi-steady state when drilling the Al 6061 section of the "Stack-Up" material. The predicted maximum thrust force for both CD854 and CD856 agreed well with those acquired experimentally. The model was also capable of capturing the thrust force trend when drilling on the CFRP and Al 60601 with CD854 and CD856. When drilling the Al 6061 portion of the "Stack-Up" material, the predicted trust force was higher with CD856 - approximately 180 N - versus the CD854, 150 N. This demonstrates good alignment with the experimental measurements, especially towards the exit of the Aluminum layer. In both Figure 6.11 and 6.12 a over prediction of the thrust force response thru the CFRP section is observed. This would be due to the support of the Aluminum backing layer.

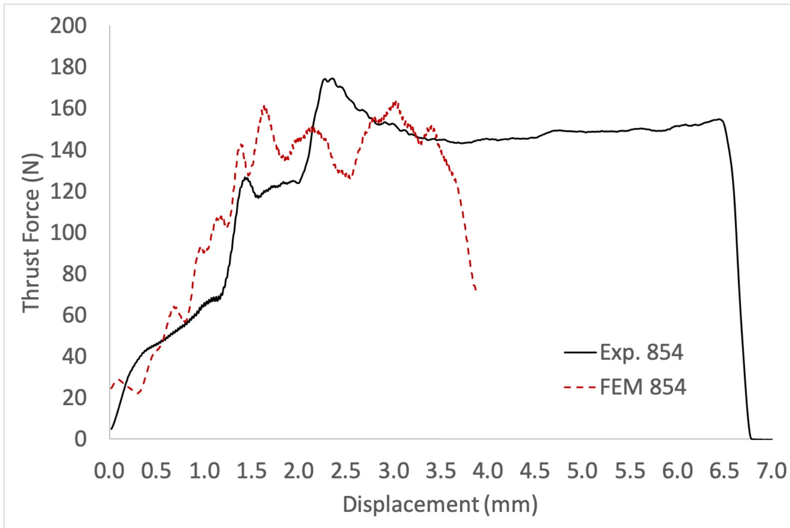

Figure 6.11: Simulated and measured force signature when drilling "Stack-Up" with CD854

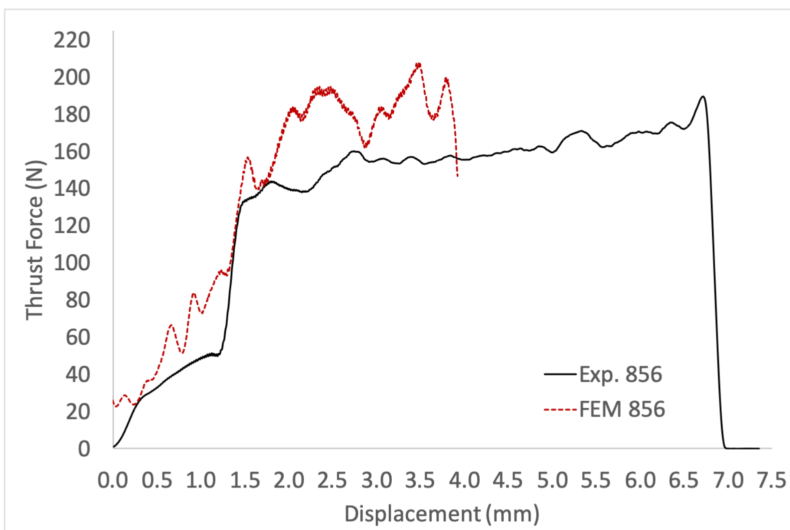

Figure 6.12: Simulated and measured force signature when drilling "Stack-Up" with CD856

6.4 Conclusion

A 3D finite element model was developed and presented for drilling “stack-up” material. Two different drill geometries were simulated and validated with experimental results. The following conclusions were made based on drilling of “Stack-up” material with two different drill geometries and bounded by the associated process parameters used.

The “Stack-up" drilling model predicted thrust force response well versus experiments. Specifically the spike in load created when transitioning between the UD-CFRP and Aluminum layer. Additionally, a reduction in thrust force was captured when drilling Aluminum with the CD854 versus the CD856. The CD856 double-angle geometry transforms the thrust from the drill more effectively into radial compression on the drilled wall of the laminate, reducing delamination damage in the UD-CFRP. When machining Aluminum, the double-angle geometry reduces the effective shearing action of the metal machining process. A greater thrust force is required for the CD856 versus CD854, resulting in a less effective tool when drilling “Stack-ups". This reaffirming the CD854 as an ideal tool for drilling FRPs and “Stack-ups".

Chapter 7

Conclusions & Future Work

There is no good idea that cannot be improved on.

Michael Eisner

The advantages for material characterization and customization of CFRP composites can serve to create a design less constrained by conventional guidelines and leading to an effective part creation. Due to the great quantity of design choices - fibre types, epoxy types, layup and weave options - significant considerations must be made by the engineer. To promote the utilization of CFRP composites numerical modelling, these models should be capable of successfully predicting the interaction and damage mechanics for a given scenario. In the future, destructive experimental characterization should only be required for verification of these models. Creating capable models is a very challenging task that researchers have studied for decades. There is an immense body of work available ranging from experimental to numerical modelling at the micro, meso and macro scale. Despite this work, engineers in practice are not fully utilizing these models due to their complexity or computational expense. The main endeavour of this research was to develop more effective material characterization techniques and to develop effective modelling tools that can accurately predict the damage mechanics of a CFRP laminate under various loading configurations. Moreover, modelling tools that can then be extended for use studying alternative material testing configurations, various machining processes and input parameters.

With increased computational power researchers have worked to model different loading configurations in three dimensions. Transitioning from micro-models focusing on constituent interactions and fracture mechanics, to macro-models focusing on process modelling and optimization. The orthotropic CFRP composite has many modes of failure, in the most basic sense including matrix cracking, fibre-matrix debonding and fibre breakage. To accomplish a 3D model, the fundamental modelling technique used in finite element modelling is the continuum damage mechanics (CDM) method. The numerically efficient method quantifies the evolution of the load, strain and effect on stiffness to determine strength, which is used to detect damage initiation and evolution. The CDM approach has been effectively applied to many macro-scale scenarios. In many situations a representative laminate level model can suffice including: normal loading configurations of UD-CFRP, symmetric-balanced cross-ply layups, symmetric weave composites represented as transversely isotropic. However, the inter-ply damage resulting from the decohesion of lamina's has detectable effect on the CFRP load response in many loading scenarios. The main focus of the modelling work was to effectively represent the CFRP composite in a meso-scale representation accounting for the inter-ply cohesive response, while maintaining an effective, computationally efficient FE tool to be utilized across many setups.

The following conclusions were made based on simulating the mechanical properties of CFRP to fracture and designing a tensile test rig that could induce fracture at the specimen gauge section consistently from Chapter 3:

- An effective tensile test fixture was developed with the use of a modified planar wishbone geometry. This design improved the repeatability and accuracy of the force-displacement and strain data substantially. With the implementation of such design, the position of the fracture region in the test samples were very consistent and repeatable. This is most critical when using the ARAMIS 3D scanning camera to capture strain with small spot size.

- Element size in the mesh was less sensitive then anticipated when CFRP samples were subjected to tensile loading in the plane strain deformation state. Accurate, computationally efficient models for planar tensile tests, element lengths of 0.375-0.5 mm can be utilized. When loading a CFRP sample in tension, the loading primarily affects the ply and showed minimal reliance on the number of elements across the thickness of the material. Computational costs can be reduced by limiting the number of elements through the thickness to four or fewer while maintaining accuracy.

- The most crucial factor affecting the computational efficiency-accuracy balance of models was mass scaling. Adapting the mass scaling to a desired time step can significantly decrease computation time from years to minutes, but it has a considerable negative impact on the accuracy of the loading response. To implement mass scaling effectively, measures must be taken to minimize the inertial effects caused by the increased density of elements.

- Exploiting the CFRP's insensitivity to strain rate enables time scaling to be implemented, resulting in further computational savings. Moreover, when loading the material in orientations non-parallel to the fiber direction, the matrix material becomes dominant in determining the material's response. Only the Maximum Strain and LaRC02 failure criteria effectively capture the evolution of damage in these off-fiber loading orientations.

- With the inclusion of multi-ply instances laminated by cohesive interactions capable of damage evolution, the experiments' nonlinear loading response was accurately predicted. The failure of samples with 45 and 90-degree fiber layups was primarily influenced by the evolution of matrix damage. The introduction of cohesive surface modeling enhanced the capacity to generate nonlinearity in the loading response, particularly after optimizing the initiation strengths of damage. This enabled the propagation of damage between instances, resulting in a nonlinear response that is typically overlooked or assumed to be linear-elastic.

Through the implementation of experimental improvements and effective modeling techniques, notable advancements were achieved in the efficiency of experimental tests and the accurate representation of materials in finite element analysis (FEA). The modeling of the arced fixturing device using rigid surfaces was successfully validated, confirming the presence of a non-linear gripping region as described.

To further enhance the cohesive surface modeling three-point bending analysis with varying fiber orientations was investigated to gain understanding regarding the initiation and propagation of delamination damage. By accurately representing the cohesive nature of interlaminar regions in CFRP materials, effective simulations for machining processes could be developed.

To gain understanding of the cohesive interaction between plies and validate mechanical properties and predictive capability of the FE model, CFRP laminates were loaded through to fracture in a three-point bending configuration. The following conclusions were drawn Chapter 4 of the current research:

- When subjecting CFRP samples to loading along the primary directions (fiber, matrix, and shear), the sensitivity of the mesh's element size was found to be lower than expected. Achieving accurate and computationally efficient models can be accomplished by utilizing element lengths of 0.2 mm in the proximity of the anticipated failure region, gradually transitioning to coarser elements further away from the failure zone.

- In a three-point bending test, failure of CFRP samples remains primarily governed by failure within the ply plane and demonstrates minimal dependence on the number of elements across the material's thickness. Computational costs can be reduced while maintaining accuracy by limiting the number of elements through the thickness to five or fewer.

- Among factors impacting the computational efficiency-accuracy trade-off, mass scaling plays a critical role. Employing variable mass scaling to achieve a desired time step can significantly decrease computation time from years to minutes. However, it has a notable negative impact on the accuracy of the loading response. Careful consideration is necessary to minimize the inertial effects resulting from the increased element density when implementing mass scaling.

- For the mesh refinement employed in the finite element (FE) model, a mass scaling of less than $5.0{\cdot}10^{-6}s$ can be utilized without time scaling. By leveraging CFRP's insensitivity to strain rate, time scaling can be implemented to achieve further computational savings.

- By incorporating multi-ply instances laminated through cohesive interactions capable of evolving damage, a remarkably similar nonlinear loading response to the experimental results was accurately predicted. The failure of samples with 45° and 90° fiber layups is predominantly influenced by the evolution of matrix damage. The utilization of cohesive surface modeling significantly enhanced the capacity to introduce nonlinearity in the loading response, especially after optimizing the strength of damage initiation. This facilitated the propagation of damage between plies, resulting in a nonlinear response that is often overlooked or assumed to be linear-elastic in existing literature.

- By employing appropriate punch design and implementing effective modeling techniques, significant enhancements were achieved in the effectiveness of tests and the accurate representation of materials in finite element (FE) models. This advancement enabled successful modeling of multi-orientation and cross-ply layups, providing a valuable tool for determining the optimal layup configuration based on specific strength and toughness requirements.
- For small span-to-thickness ratios, cohesive surface modeling proved successful in capturing interlaminar shear damage (delamination) occurring between plies. On the other hand, for large span-to-thickness ratios, the FE model accurately predicted experimental results and was further extended to predict various fiber orientations and cross-ply layups described in existing literature.
- It should be noted that the strength of cross-ply layups was underestimated compared to the literature due to the thin laminate geometry, which led to immediate laminate failure rather than prolonged damage capable of energy absorption during fracture.

Accurate prediction of cohesive interactions is crucial, particularly in relation to break-in and break-out delamination damage observed during CFRP drilling. With an accurate representation of CFRP material properties and interlaminar cohesive behavior, these findings pave the way for the development of effective machining simulations based on these insights.

An advanced macro 3D finite element (FE) drilling model was introduced, providing a reliable simulation tool capable of accurately capturing the impacts of various drill geometries while maintaining reasonable computational efficiency. Furthermore, a comprehensive numerical analysis was conducted to examine the effects of mass scaling, bulk viscosity, friction, strain rate strengthening, and cohesive surface modeling. The findings drawn from this investigation are based on well-defined parameters and their corresponding magnitudes, leading to the following conclusions:

- The implementation of mass scaling significantly reduces computational time, providing a notable reduction in overall processing duration. However, it is crucial to carefully manage and mitigate the dynamic effects stemming from the increased density of elements when applying mass scaling techniques.

- The inclusion of linear and quadratic bulk viscosity parameters proves effective in reducing noise generated during CFRP laminate drilling simulations. By carefully selecting appropriate bulk viscosity parameters, the prediction of thrust force can be improved with only a minor increase in computational time.

- By representing the tool as a 3D surface instead of the conventional rigid 3D body tool typically employed in simulations, exhibited notable computational benefits and enhanced accuracy in the prediction of model outcomes.

- When cohesive surface modelling was incorporated into the 3D drilling model, the predicted thrust force signature agrees better in terms of magnitude and profile when compared with those acquired experimentally.

- The 3D drilling model could accurately predict the thrust force and hole quality generated by two different drills. Simulated results show that with a double angle drill tip geometry, inter-ply damage was reduced. With the “candle-stick” drill tip, the hole quality was improved.

- In comparison to the drilling experiments, the maximum thrust force predicted by the FE model is within 1.991% for the CD854 and 8.976% for the CD856 drill.

- The CD854 "spur-edges" drills a higher quality hole, however the CD856 double-angle reduces delamination. Further investigation continues into the modification of the spur-edge to reduce inter-ply damage by promoting axial compression.

A meso-scale 3D drilling FE model was developed in this research to evaluate the effects of various drill geometries and process inputs, together with a reasonable computational time, was presented in Chapter 6. Additionally, a comprehensive resource was created outlining the magnitude of effect FE model considerations create, when developing a complex 3D drilling model for UD-CFRP laminates and “Stack-ups". In final, a quiver of tools were studied demonstrating the advantages of specific geometry features over a standard twist drill.

Numerous FE techniques and the associated advantages and costs were presented. The element removal of failed elements creates periodic voids between the tool and laminate resulting in intermittent contact and load profile. This, in addition to the inability of Coupled Eulerian Lagrangian models to complete without element deletion criteria - thereby negating the advantage of the CEL model - affirm the vitality of the mesh development. Although cyclic symmetry could not be implemented in an explicit analysis, symmetry was successfully applied reducing the model to one quarter. The computational advantage of discrete rigid tools, versus the common deformable body with rigid constraint, was outlined. The magnitude of effect of mass scaling was presented. Consideration must be made to minimize the inertial effects caused by the increased density of the elements when implementing mass scaling. The CFRP laminate is light in weight, stiff and small. The drilling operations is dynamic and at high speed. By effectively applying viscosity, with a marginal computational expense, an improved loading prediction can be achieved. Strain rate strengthening was applied utilizing an auxiliary material file, increasing the load profile by 10.9%. However, determining the sensitivity to the matrix strain rate strengthening parameter was not achieved. Friction in the CFRP drilling model is not a dominant consideration unless modelling “Stack-ups".

The FE model accurately predicted the increased thrust force developed by the CD854 versus the CD856 observed experimentally. When the laminate included multiple plies with cohesive interactions, 10 plies were modelled with 3 elements through the thickness. With the inclusion of multi-ply instances laminated by cohesive interactions capable of damage evolution, the loading response recorded from the experiments was predicted with strong resemblance and improved drill exit prediction. A reduction in inter-ply damage was predicted with the CD856, reaffirming the advantage of double-angle drill geometry function. The CD856 double-angle geometry transforms the thrust from the drill more effectively into radial compression on the drilled wall of the laminate, reducing delamination damage in the UD-CFRP. The “spur" cutting edge geometry of the CD854 demonstrated improved hole quality. Mesh refinement was limited to $60 - 75\mu mm$, therefore the FE model could not predict surface roughness and was limited to damage propagation prediction.

The “Stack-up" drilling model predicted thrust force response well versus experiments. Specifically the spike in load created when transitioning between the UD-CFRP and Aluminum layer. A reduction in thrust force was predicted when drilling

Aluminum with the CD854 versus the CD856, as observed experimentally. When machining Aluminum, the double-angle geometry of the CD856 reduces the effective shearing action of the metal machining process. A greater thrust force is required for the CD856 versus CD854, resulting in a less effective tool when drilling "Stack-ups". This reaffirming the CD854 as an ideal tool for drilling FRPs and "Stack-ups" as stated by the tool manufacturer Sandvik.

An accurate representation of the UD-CFRP material was achieved by facilitating the contribution of damage between plies. Effective FE material testing setups and 3D drilling models has been developed. The effective modelling techniques employed improve the material response prediction and can be applied to all material testing and machining configurations.

7.0.1 Future Work

To enhance the model's versatility and enable its effective application across a broader spectrum of loading scenarios and machining configurations, a few aspects warrant further investigation. These include:

- Strain-rate sensitivity of transverse and shear loading, and inter-ply cohesion
- Thermal sensitivity
- Alternative model considerations - smooth particle hydrodynamics (SPH)

UD-CFRP becomes strain rate sensitive when loading is focused in shear and transverse directions. In these instances the response is dominated by the matrix properties and the fibre-matrix interface response. Consideration was taken to investigating this material property, but proved insensitive via the VUMAT. A user-defined material file representing a piece-wise linear relationship between strain rate and matrix strengthening can be tabulated in the transverse, in-plane and out-of-plane shear directions. Accurate cohesive interaction prediction is critical as it directly relates to delamination damage. When drilling FRPs this results in pull-up and break-out damage at the entry and exit of the drill. A sensitivity analysis for matrix material strain rate strengthening is required.

Thermo-mechanical considerations of the drilling process would more accurately represent the machining process. When machining thick CFRP laminates and "Stack-ups" the frictional forces result in significant thermal loads. The matrix material is subject to thermal softening. The poor thermal conductivity of titanium layers results in thermal conductivity that can cause burning of the matrix and fuzzing on the drilled hole surface [165]. The high thermal conductivity of aluminum allows for the heat to diffuse quickly, thereby avoiding any softening of the CFRP [166]. The thermal stability to be dependent on the matrix functionality, cure temperature and fibre volume fraction, determining resins to degrade at temperature of 250°C [167].

Meshless numerical methods such as smoothed particle hydrodynamics (SPH) modelling shows promise overcoming well-known problems of FEM. The fixed relations between nodes and limitations to degrees of freedom creates challenges avoiding mesh distortion and solver error. This is combated using chip-separation criteria or element deletion techniques leading to intermittent workpiece-tool contact. SPH is based on a local interpolation between nodes where a continuum is discretized by a cloud of numerical integration points forming the basis of kernel functions [168]. SPH has been used to model the machining of homogeneous material [168, 169] and metal-metal composites [145]. Abena et al. develops a 3D orthogonal micro-macro cutting model first with FEM, implementing element deletion and describes the poor force prediction resulting from the intermittent contact. Then uses SPH to model the individual matrix and fibre constituents in the cutting area of focus and an EHM elsewhere. The model does not include any fibre-matrix interface, but an improved chip formation is described [125].

In terms of exploring the utilization of the developed 3D model, key areas of interest for further research encompass:

- Variable stepped/reduced feed rate strategy
- Vibration assisted drilling
- Pre-drill geometry & pre-drill diameter effect
- Pre-etched exit surface geometry & diameter

Delamination created by the thrust force of the drill results in the most detrimental damage when drilling CFRP [106]. The drill geometry and feed rate are the decisive factors relating to tool life and the resulting thrust force when drilling. Various stepped geometries have been studied experimentally and modelled, demonstrating a reduction in thrust force attributed to the reduced chisel edge [112]. Significant reduction in thrust force can be achieved by reducing the chisel width edge thereby reducing delamination [118]. Revolutionary drill geometries created by Debnath et al. [148] and modified in this research, demonstrate great promise to reduce thrust force when machining FRP laminates.

Additional improvement can be achieved by controlling the feed rate throughout the progression of the drilling. Variable feed rates when drilling composites demonstrates promising attributes including reduced thrust force, reduced fibre pull-out and improved hole surface quality [170, 171]. These improvements, generally thought to diminish productivity, are incorrect as more assertive feed rates can be used at the initiation of the drilling while the laminate has significant thickness, thereby maintaining MRR overall.

Incorporating vibration assisted drilling (VAD) has achieved high quality holes while reducing thrust force significantly [74, 150, 172]. VAD creates an intermittent cutting mechanism in the feed direction of the drill. Research has demonstrated the greater the cutting speed the larger the reduction found in thrust force utilizing ultrasonically assisted drilling (UAD)[150]. A parametric study determining the effect of frequency and amplitude of the VAD versus cutting speed and feed rate should be investigated using the FE model developed.

In an attempt to reduce the effect of the chisel edge of the drill to minimize thrust force the effect on cutting forces with and without pre-drilled holes has been studied [116]. The pilot hole was shown to reduce thrust force significantly allowing for use of much higher feed rates. By relating the ratio of the chisel edge length to pre-drilled hole diameter the thrust force was reduced with a pre-drilled hole, therefore allowing for more assertive feed rates to be used [117]. A parametric study determining the effect of various pre-drill geometries and diameters versus cutting speed and feed rate should be investigated using the FE model developed.

The pre-etched exit surface of a FRP laminate demonstrates promise, mitigating the expansion of damage at the exit of drilling [1]. This research needs to be extended in two streams. First, a tangibility study to determine if a drill geometry can be physically created and if so what limitations may exist within manufacturing such a drill. Second, an analysis to determine the ideal diameter and geometry of the etching.

Overall, an effective FE drilling model has been developed. There are many aspects that can be improved and there are many more areas it can be applied.

What is now proved was only once imagined.

William Blake

[1] See Appendix A *Extending the Finite Element Drilling Model: Part II.* The predrill-hypothesized drill reduced exit surface damage propagation. The notch creates a change in geometry that focuses the stress in the bottom surface ply, negating the radial expansion of the stress. This focuses the applied load from the drill, reducing thrust force and improving hole quality. The Debnath et al. redesigned geometry demonstrates reduced thrust force and improved hole quality, thereby enhancing a drill geometry already proven in experiments to be advantageous over a standard twist drill. The cutting edges on the periphery facilitate a hollow drill structure. The hollow drill structure facilitates future added functionality. Internal air/coolant channels can be incorporated to assist with chip evacuation. Alternatively, a predrill geometry could be more easily accommodated.

Bibliography

[1] Zoltek Toray Group. *The History of Carbon Fiber*. URL: http://zoltek.com/. Accessed 9/2013.

[2] D.M. Peters. *The New Steel-Carbon-Fiber-Reinforced Plastics: The Materials That May Revolutionise Aircraft Design*. Vol. 40, No. 2. 1968, 669 − 670.

[3] J. Gorss. "High Performance Carbon Fibers". In: *National Historic Chemical Landmark* (2003), 1 − 4.

[4] Toray Industries Inc. *What is Carbon Fiber?* URL: http://www.torayca.com/en/. Accessed 12/2017.

[5] C.T. Herakovich. *Mechanics of Fibrous Composites*. Wiley, 1997. ISBN: 978-0-471-10636-4.

[6] R. Teti. "Machining of Composite Materials". In: *CIRP Annals - Manufacturing Technology* Vol. 51, No. 2 (2002), 611 − 634. ISSN: 00078506. URL: http://dx.doi.org/10.1016/S0007-8506(07)61703-X.

[7] J.Y. Sheikh-Ahmad. *Machining of Polymer Composites*. New Yory, NY: Springer US, 2009, p. 315. ISBN: 978-0-387-35539-9.

[8] J. Pora. *Composite Materials in the Airbus A380 - From History to Future*. Tech. rep. France, 2002, 1 − 11.

[9] R. Garrick. "Drilling Advanced Aircraft Structures with PCD (Poly-Crystalline Diamond) Drills". In: *SAE Technical Papers* (2007). URL: http://dx.doi.org/10.4271/2007-01-3893.

[10] Anon. "Sky High Success for CVD Diamond Coated Tools". In: *Industrial Diamond Review* Vol. 67, No. 3 (2007), 69 − 70. ISSN: 00198145.

[11] I.S.E.M. Shyha. "Drilling of Carbon Fibre Reinforced Composites". PhD thesis. University of Birmingham, UK, 2010.

[12] D. Roquette, F. Meyer, and L. Herbeck. *High Volume Manufacturing of Carbon Fiber Reinforced Plastics for Body in White*. Germany: Voith Composites, Proceedings of the Conference Materialien des Karosseriebaus.

[13] C.D. Warren. *Low Cost Carbon Fiber Overview*. Tennessee, USA: Oak Ridge National Laboratory.

[14] G. List, M. Nouari, D. Gehin, S. Gomez, J.P. Manaud, Y. Le Petitcorps, and F. Girot. "Wear Behaviour of Cemented Carbide Tools in Dry Machining of Aluminium Alloy". In: *Wear* Vol. 259, No. 7-12 (2005), 1177 – 1189. URL: http://dx.doi.org/10.1016/j.wear.2005.02.056.

[15] P.D. Hartung, B.M. Kramer, and B.F. von Turkovich. "Tool Wear in Titanium Machining". In: *CIRP Annals - Manufacturing Technology* Vol. 31, No. 1 (1982), 75 – 80. URL: https://doi.org/10.1016/S0007-8506(07)63272-7.

[16] K.-H. Park, A. Beal, D.D.W. Kim, P. Kwon, and J. Lantrip. "Tool Wear in Drilling of Composite/Titanium Stacks using Carbide and Polycrystalline Diamond Tools". In: *Wear* Vol. 271, No. 11-12 (2011), 2826 – 2835. URL: http://dx.doi.org/10.1016/j.wear.2011.05.038.

[17] W.C. Chen. "Some Experimental Investigations in the Drilling of Carbon Fiber-Reinforced Plastic (CFRP) Composite Laminates". In: *International Journal of Machine Tools and Manufacture* 37.8 (1997), 1097 – 1108. URL: http://dx.doi.org/10.1016/S0890-6955(96)00095-8.

[18] W. Jomaa, O. Mechri, J. Levesque, V. Songmene, P. Bocher, and A. Gakwaya. "Finite Element Analysis of Serrated Chip Formation in Machining of 7075-T651 Aluminum Alloy". In: *IMPC 2016 - 28th International Mineral Processing Congress* 26 (2016), 446 – 458.

[19] A. Koplev, Aa. Lystrup, and T. Vorm. "Cutting Process, Chips, and Cutting Forces in Machining CFRP". In: *Composites* Vol. 14, No. 4 (1983), 371 – 376. URL: http://dx.doi.org/10.1016/0010-4361(83)90157-X.

[20] D. Arola and M. Ramulu. "Orthogonal Cutting of Fiber-Reinforced Composites: a Finite Element Analysis". In: *International Journal of Mechanical Sciences* Vol. 39, No. 5 (1997), 597 – 613. URL: http://dx.doi.org/10.1016/S0020-7403(96)00061-6.

[21] K. Sakuma and M. Seto. "Tool Wear in Cutting Glass-Fiber-Reinforced Plastics - The Relation Between Fiber Orientation and Tool Wear". In: *Bulletin of the JSME* Vol. 26, No. 218 (1983), 1420 – 1427. URL: http://dx.doi.org/10.1299/jsme1958.26.1420.

[22] A.K. Kaw. *Mechanics of Composite Materials*. Mechanical and Aerospace Engineering Series. Taylor & Francis, 1997. ISBN: 9780849396564.

[23] J. Destefani. "Hole in Four ... or More". In: Vol. 63 (2011). URL: https://www.ctemag.com/news/articles/hole-four-or-more.

[24] H. Ho-Cheng and C.K.H. Dharan. "Delamination During Drilling in Composite Laminates". In: *Journal of Engineering for Industry* Vol. 112, No. 3 (1990), 236 − 239. URL: https://doi.org/10.1115/1.2899580.

[25] D. Iliescu, D. Gehin, M.E. Gutierrez, and F. Girot. "Modeling and Tool Wear in Drilling of CFRP". In: *International Journal of Machine Tools and Manufacture* Vol. 50, No. 2 (2010), 204 − 213. URL: http://dx.doi.org/10.1016/j.ijmachtools.2009.10.004.

[26] D. Kim and M. Ramulu. "Drilling Process Optimization for Graphite/Bismaleimide-Titanium Alloy Stacks". In: *Composite Structures* Vol. 63, No. 1 (2004), 101 − 114. URL: http://dx.doi.org/10.1016/S0263-8223(03)00137-5.

[27] W.D. Callister. *Materials Science and Engineering: An Introduction, 6th Edition*. Wiley International Edition. Wiley, 2003. ISBN: 9780471224716.

[28] M.P. Groover. *Fundamentals of Modern Manufacturing: Materials, Processes, and Systems*. John Wiley & Sons, 2010. ISBN: 9780470467008.

[29] Carbon Fiber Gear. *Carbon Fiber Like You've Never Seen Before*. URL: https://blog.carbonfibergear.com/carbon-fiber-like-youve-never-seen-before/. Accessed 8/2018.

[30] NetComposites. *Woven Fabrics*. URL: https://netcomposites.com/guide-tools/guide/reinforcements/woven-fabrics/. Accessed 8/2018.

[31] TP Sathishkumar, S Satheeshkumar, and J Naveen. "Glass Fiber-Reinforced Polymer Composites - A Review". In: *Journal of Reinforced Plastics and Composites* Vol. 33, No. 13 (2014), 1258 ˘ 1275. DOI: 10.1177/0731684414530790.

[32] Advanced Fiber Systems DuPont. *Kevlar Aramid Fiber Technical Guide*. VA, USA, 2017. URL: https://www.dupont.com/content/dam/dupont/amer/us/en/safety/public/documents/en/Kevlar_Technical_Guide_0319.pdf.

[33] ACP Composites. *Carbon Firer Uni Laminates*. 2014. Accessed: 6/2015.

[34] H. Ullah, A.R. Harland, and V.V. Silberschmidt. "Damage Modelling in Woven-Fabric CFRP Laminates Under Large-Deflection Bending". In: *Computational Materials Science* 64 (2012), 130 − 135. URL: http://dx.doi.org/10.1016/j.commatsci.2012.05.036.

[35] J.M.L. Reis. "Effect of Temperature on the Mechanical Properties of Polymer Mortars". In: *Materials Research* 15 (2012), 645 − 649. DOI: 10.1590/S1516-14392012005000091.

[36] Soo-Jin Park and Min-Kang Seo. *Chapter 7 - Types of Composites*. Ed. by Soo-Jin Park and Min-Kang Seo. Vol. 18. Interface Science and Technology. Elsevier, 2011, pp. 501–629. DOI: https://doi.org/10.1016/B978-0-12-375049-5.00007-4.

[37] M. Shahbazi. "An Efficient Virtual Testing Framework to Simulate the Progression of Damage in Notched Composite Laminates". PhD thesis. University of British Columbia, 2017. DOI: http://dx.doi.org/10.14288/1.0354263.

[38] T. Niezgoda and A. Derewońko. "Multiscale composite FEM modeling". In: *Procedia Engineering* Vol. 1, No. 1 (2009), 209 − 212. DOI: https://doi.org/10.1016/j.proeng.2009.06.049.

[39] Dassault Systemes. *ABAQUS/CAE User's Guide, from ABAQUS 6.14 Online Documentation*. 2014.

[40] E.J. Barbero. *Finite Element Analysis of Composite Materials Using Abaqus, 1st Edition*. CRC Press, 2013. ISBN: 978-1-4665-1661-8.

[41] M. Nirbhay, A. Dixit, R.K. Misra, and H.S. Mali. "Tensile Test Simulation of CFRP Test Specimen using Finite Elements". In: *Procedia Materials Science* 5 (2014), 267 − 273.

[42] V. Daghigh, M. Soroush, K. Nikbin, and A. Simoneau. "Finite Element Modeling of Tensile and Bending on Fiber Reinforced Polymer Composites". In: *The 3rd International Conference on Composites: Characterization, Fabrication and Application* (2012), Tehran, Iran.

[43] L.F. Chen, L. Chen, and G. Zhang. "Finite Elemental Simulation on Flexural Process of Carbon Fiber/Epoxy Composite Laminates". In: *Advanced Materials Research* 332-334 (2011), 1105 − 1108. URL: https://doi.org/10.4028/www.scientific.net/amr.332-334.1105.

[44] C.R. Dandekar and Y.C. Shin. "Multiphase Finite Element Modeling of Machining Unidirectional Composites: Prediction of Debonding and Fiber Damage". In: *Journal of Manufacturing Science and Engineering* Vol. 130, No. 5 (2008). URL: http://dx.doi.org/10.1115/1.2976146.

[45] K. Gobivel, A. Roy, K.S. Vijaysekar, and S. Kumar. "Finite Element Simulation of the Machining Process with CFRP Material". In: *International Journal of Innovative Research in Science* Vol. 5, No. 3 (2014), 1326 − 1329.

[46] S. Usui, J. Wadell, and T. Marusich. "Finite Element Modeling of Carbon Fiber Composite Orthogonal Cutting and Drilling". In: *Procedia CIRP* 14 (2014), 211 − 216. URL: http://dx.doi.org/10.1016/j.procir.2014.03.081.

[47] F. Gao, X. Tian, S. Liu, and B. Li. "The Simulation on Drilling of Carbon Fiber Reinforced Plastic Composites". In: *Proceedings of the 2012 International Conference on Computer Application and System Modeling* (2012), 1215 − 1218.

[48] V.A. Phadnis, A. Roy, and V.V. Silberschmidt. "Finite Element Analysis of Drilling in Carbon Fiber Reinforced Polymer Composites". In: *Journal of Physics*: *Conference Series* Vol. 382, No. 1 (2012), 1 − 6. URL: http://dx.doi.org/10.1088/1742-6596/382/1/012014.

[49] K. Giasin, S. Ayvar-Soberanis, T. French, and V. Phadnis. "3D Finite Element Modelling of Cutting Forces in Drilling Fibre Metal Laminates and Experimental Hole Quality Analysis". In: *Applied Composite Materials* Vol. 24, No. 1 (2017), 113 − 137. URL: https://doi.org/10.1007/s10443-016-9517-0.

[50] M. Mahid and L. Zhang. "A Finite Element Model for the Orthogonal Cutting of Fiber-Reinforced Composite Materials". In: *Journal of Materials Processing Technology* Vol. 113, No. 1-3 (2001), 373 − 377.

[51] Prakash C. and Vijay Sekar K.S. "3D Finite Element Analysis of Drilling of Glass Fiber Reinforced Polymer Composites". In: *Advanced Science, Engineering and Medicine* Vol. 10, No. 3-5 (2018), 308 − 312. DOI: 10.1166/asem.2018.2125.

[52] R. El Alaiji, L. Larbi, and A. Bouayad. "3D Finite Element Modeling of Chip Formation and Induced Damage in Machining Fiber Reinforced Composites". In: *American Journal of Engineering Research* 4 (2015), 123 − 132.

[53] K. Giasin, A. Hodzic, V. Phadnis, and S. Ayvar-Soberanis. "Assessment of Cutting Forces and Hole Quality in Drilling Al2024 Aluminium Alloy: Experimental and Finite Element Study". In: *International Journal of Advanced Manufacturing Technology* Vol. 87, No. 5-8 (2016), 2041 − 2061. URL: http://dx.doi.org/10.1007/s00170-016-8563-y.

[54] F. Ducobu, E. Riviére-Lorphévre, and E. Filippi. "Finite Element Modelling of 3D Orthogonal Cutting Experimental Tests with the Coupled Eulerian-Lagrangian (CEL) Formulation". In: *Finite Elements in Analysis and Design* 134 (2017), 27 − 40. URL: http://www.sciencedirect.com/science/article/pii/S0168874X17301488.

[55] H. Ullah, A.R. Harland, T. Lucas, D. Price, and V.V. Silberschmidt. "Finite-Element Modelling of Bending of CFRP Laminates: Multiple Delaminations". In: *Computational Materials Science* Vol. 52, No. 1 (2012), 147 − 156. URL: http://dx.doi.org/10.1016/j.commatsci.2011.02.005.

[56] M. Zetterberg. "A Critical Overview of Machining Simulations in ABAQUS". MA thesis. Stockholm, Sweden: KTH Royal Institute of Technology, 2014.

[57] K. Hosseinkhani and E.G. Ng. "Finite Element Simulation of Cutting Process Under the Worn Tool Edge Geometries". In: *The International Journal of Advanced Manufacturing Technology* Vol. 116 (2021), 3991 − 4006. URL: https://doi.org/10.1007/s00170-021-07725-9.

[58] A.M. Abdelhafeez, S.L. Soo, D. Aspinwall, A. Dowson, and D. Arnold. "A Coupled Eulerian Lagrangian Finite Element Model of Drilling Titanium and Aluminium Alloys". In: *SAE International Journal of Aerospace* Vol. 9, No. 1 (2016), 198 − 207. URL: http://dx.doi.org/10.4271/2016-01-2126.

[59] J. Proudian. "Simulating Residual Stress in Machining; from Post Process Measurement to Pre-Process Predictions". MA thesis. Stockholm, Sweden: KTH Royal Institute of Technology, 2012.

[60] E.J. Barbero. *Introduction to Composite Materials Design, 3rd Edition*. CRC Press, 2017. ISBN: 9781315296470.

[61] D.R.B. de Melo. "Composite Structures Impact Simulation Behavior". Master's Thesis. Lisboa, Portugal: Instituto Superior Técnico, 2014.

[62] CAE Associates. *Why Worry About Hourglassing in Explicit Dynamics? Part I*. 2015. URL: https://caeai.com/blog/why-worry-about-hourglassing-explicit-dynamics-part-i. Accessed: 3/2019.

[63] R. Fragoudakis. "Failure Concepts in Fiber Reinforced Plastics". In: *Failure Analysis and Prevention*. IntechOpen, 2017. Chap. 6. DOI: 10.5772/intechopen.71822.

[64] D Purslow. *The Shear Properties of Unidirectional Carbon Fibre Reinforced Plastics and their Experimental Determination*. Aeronautical Research Council Current Paper ARC-CP-1381, 1977.

[65] Sergio S.C. "High Fidelity Simulations of Failure in Fiber-Reinforced Composites". PhD thesis. Polytechnic University of Madrid, 2014. URL: https://doi.org/10.20868/UPM.thesis.30310.

[66] M.W. Czabaj and J.G. Ratcliffe. "Comparison of Intralaminar and Interlaminar Mode I Fracture Toughnesses of a Unidirectional IM7/8552 Carbon/Epoxy Composite". In: *Composites Science and Technology* 89 (2013), 15 − 23. URL: https://doi.org/10.1016/j.compscitech.2013.09.008.

[67] M.N. Nahas. "Survey of Failure and Post-Failure Theories of Laminated Fiber-Reinforced Composites". In: *Journal of Composites Technology and Research* Vol. 8, No. 4 (1986), 138 − 53. URL: http://dx.doi.org/10.1520/CTR10335J.

[68] S.W. Tsai and E.M. Wu. "A General Theory of Strength for Anisotropic Materials". In: *Journal of Composite Materials* 5 (1971), 58 − 80. URL: http://dx.doi.org/10.1177/002199837100500106.

[69] K. Naresh, S. Krishnapillai, and V. Ramachandran. "Effect of Fiber Orientation on Carbon/Epoxy and Glass/Epoxy Composites Subjected to Shear and Bending". In: *Solid State Phenomena* 267 (2017), 103 − 108. URL: http://dx.doi.org/10.4028/www.scientific.net/SSP.267.103.

[70] Z. Hashin. "Failure Criteria for Unidirectional Fiber Composites". In: *Journal of Applied Mechanics* Vol. 47, No. 2 (1980), 329 − 334. URL: http://dx.doi.org/10.1115/1.3153664.

[71] J. Lemaitre and R. Desmorat. *Engineering Damage Mechanics: Ductile, Creep, Fatigue and Brittle Failures*. Springer, 2005. ISBN: 3540215034.

[72] B. Lawn and T.R. Wilshaw. *Fracture of Brittle Solids*. Cambridge Solid State Science Series. Cambridge University Press, 1993. ISBN: 9780521401760.

[73] M.L. Benzeggagh and M. Kenane. "Measurement of Mixed-Mode Delamination Fracture Toughness of Unidirectional Glass/Epoxy Composites with Mixed-Mode Bending Apparatus". In: *Composites Science and Technology* Vol. 56, No. 4 (1996), 439 − 49. URL: http://dx.doi.org/10.1016/0266-3538(96)00005-X.

[74] H. Hocheng and C.C. Tsao. "The Path Towards Delamination-Free Drilling of Composite Materials". In: *Journal of Materials Processing Technology* Vol. 167, No. 2 (2005), 251 − 264. URL: https://doi.org/10.1016/j.jmatprotec.2005.06.039.

[75] K. Krishnamoorthy and T. Sasikumar. "Analysis and Characterization of Tensile Property of the Composite Specimen using Ansys". In: *International Journal of Applied Engineering Research* 11 (2016), 380 − 384.

[76] ASTM International. *ASTM D3039 / D3039M-17, Standard Test Method for Tensile Properties of Polymer Matrix Composite Materials*. West Conshohocken, PA, USA, 2017. DOI: 10.1520/D3039_D3039M-17.

[77] R.J. Coguill and D.F. Adams. "Selection of the Proper Wedge Grip Surface for Tensile Testing Composite Materials". In: *Proceedings of the 44th International SAMPE Symposium and Exhibition* 44 (1999).

[78] K.J. Wong, X.J. Gong, S. Aivazzadeh, and M.N. Tamin. "Tensile Behaviour of Anti-Symmetric CFRP Composite". In: *Procedia Engineering* 10 (2011), 1865 − 1870. URL: https://doi.org/10.1016/j.proeng.2011.04.310.

[79] R.J. Coguill and D.F. Adams. "Tabbed Axial Tensile Specimen Configurations for Unidirectional Composites". In: *Proceedings of the 45th International SAMPE Symposium and Exhibition* 45 (2000).

[80] D.O. Adams and D.F. Adams. *Tabbing Guide for Composite Test Specimens*. Tech. rep. UTAH Univ. Salt Lake City Dept. of Mechanical Engineering, US Department of Transportation Federal Aviation Administration, DOT/FAA/AR-02/106., 2002.

[81] D. W. Worthem. *Flat Tensile Specimen Design for Advanced Composites*. Tech. rep. Sverdup Technology Inc., National Aeronautics, and Space Administration, NASA CR-185261, 1990.

[82] A. Mehar, G.M.S. Ahmed, G.P. Kumar, Md.A. Rahman, and M.A. Qayum. "Experimental Investigation and FE Analysis of CFRP Composites". In: *Materials Today: Proceedings* Vol. 2, No. 4 (2015). 4th International Conference on Materials Processing and Characterization, 2831 – 2839. URL: https://doi.org/10.1016/j.matpr.2015.07.297.

[83] P. Sadeghian, A.R. Rahai, and M.R. Ehsani. "Effect of Fiber Orientation on Nonlinear Behavior of CFRP Composites". In: *Journal of Reinforced Plastics and Composites* 28.18 (2009), 2261 – 2272. URL: https://doi.org/10.1177/0731684408092065.

[84] J.M.F. Paiva, S. Mayer, and M. Rezende. "Comparison of Tensile Strength of Different Carbon Fabric Reinforced Epoxy Composites". In: *Materials Research* Vol. 9, No. 1 (2006), 83 – 89. DOI: 10.1590/S1516-14392006000100016.

[85] G. Belingardi, D. S. Paolino, and E. G. Koricho. "Investigation of Influence of Tab Types on Tensile Strength of E-Glass/Epoxy Fiber Reinforced Composite Materials". In: *Procedia Engineering* 10 (2011), 3279 – 3284. URL: https://doi.org/10.1016/j.proeng.2011.04.541.

[86] H. Kobayashi, K. Goto, H. Hatta, M. Koyama, and H. Fukuda. "Tensile Strength of Carbon-Carbon Composites at High Temperature up to 2773K". In: *Proceedings of the 17th International Conference on Composite Materials, ICCM-17, Edinburgh, United Kingdom* (2009).

[87] M. Zappalorto and P.A. Carraro. "An Engineering Formula for the Stress Concentration Factor of Orthotropic Composite Plates". In: *Composites Part B: Engineering* 68 (2015), 51 – 58. URL: http://dx.doi.org/10.1016/j.compositesb.2014.08.020.

[88] S.R. Hallett and M.R. Wisnom. "Experimental Investigation of Progressive Damage and the Effect of Layup in Notched Tensile Tests". In: *J. Compos. Mater. (USA)* 40.2 (2006), pp. 119–41. ISSN: 0021-9983. URL: http://dx.doi.org/10.1177/0021998305053504.

[89] S.R. Hallett and M.R. Wisnom. "Numerical Investigation of Progressive Damage and the Effect of Layup in Notched Tensile Tests". In: *Journal of Composite Materials* Vol. 40, No. 14 (2006), 1229 − 1245. URL: http://dx.doi.org/10.1177/0021998305057432.

[90] I. Lapczyk and J.A. Hurtado. "Progressive Damage Modeling in Fiber-Reinforced Materials". In: *Composites Part A: Applied Science and Manufacturing* Vol. 38, No. 11 (2007), 2333 − 2341. URL: https://doi.org/10.1016/j.compositesa.2007.01.017.

[91] M. Arcan, Z. Hashin, and A. Voloshin. "Method to Produce Uniform Plane-Stress States with Applications to Fiber-Reinforced Materials". In: *Experimental Mechanics* Vol. 18, No. 4 (1978), 141 − 146. URL: https://doi.org/10.1007/BF02324146.

[92] R. El-Hajjar and R. Haj-Ali. "In-Plane Shear Testing of Thick-Section Pultruded FRP Composites using a Modified Arcan Fixture". In: *Composites Part B: Engineering* Vol. 35B, No. 5 (2004), 421 − 428. URL: http://dx.doi.org/10.1016/j.compositesb.2003.12.004.

[93] J. Tessmer, D. Hartung, and L. Aschenbrenner. "Mechanics of Composites in Lightweight Structures: Efficient Testing and Computation Accounting for Complex 3D Behaviour". In: *Proceedings of the 26th International Congress of the Aeronautical Sciences* 2 (2008), 1 − 9.

[94] M. Nikbakht and N. Choupani. "Fracture Toughness Characterization of Carbon-Epoxy Composite using Arcan". In: *International Journal of Aerospace and Mechanical Engineering* Vol. 2, No. 4 (2008), 247 − 253. URL: doi.org/10.5281/zenodo.1059685.

[95] J. Kwon, J. Choi, H. Huh, and J. Lee. "Evaluation of the Effect of the Strain Rate on the Tensile Properties of Carbon and Epoxy Composite Laminates". In: *Journal of Composite Materials* Vol. 51, No. 22 (2017), 3197 −3210. URL: https://doi.org/10.1177/0021998316683439.

[96] A. Azzam and W. Li. "An Experimental Investigation on the Three-Point Bending Behavior of Composite Laminate". In: *IOP Conference Series: Materials Science and Engineering* Vol. 62, No. 1 (2014), 1 − 8. URL: http://dx.doi.org/10.1088/1757-899X/62/1/012016.

[97] H.T. Helali and M. Grafinger. "The Precision of FEM Simulation Results Compared with Theoretical Composite Layup Calculation". In: *Composites Part B: Engineering* 95 (2016), 282 − 292. URL: https://doi.org/10.1016/j.compositesb.2016.04.003.

[98] International Organization for Standardization. "Plastics - Determination of Flexural Properties". In: (Dec. 2010), 1 − 19. ISO 178:2010.

[99] H. Huang, X. Ma, J. Qiao, and D. Yanhong. "Numerical Simulation of Failure Behaviors of CFRP Laminates on Hashin Model Coupled with Cohesive Elements". In: *IOP Conference Series: Materials Science and Engineering* Vol. 382, No. 3 (2018), 1 − 6. URL: http://dx.doi.org/10.1088/1757-899X/382/3/032062.

[100] Z.M. Huang and L. Liu. "Predicting Strength of Fibrous Laminates under Triaxial Loads only upon Independently Measured Constituent Properties". In: *International Journal of Mechanical Sciences* 79 (2014), 105 − 129. URL: http://dx.doi.org/10.1016/j.ijmecsci.2013.08.010.

[101] H. Ullah, A.R. Harland, T. Lucas, D. Price, and V. Silberschmidt. "Analysis of Nonlinear Deformations and Damage in CFRP Textile Laminates". In: *Journal of Physics: Conference Series* 305 (2011), 1 − 11. URL: https://dx.doi.org/10.1088/1742-6596/305/1/012045.

[102] I. Petrescu, C. Mohora, and C. Ispas. "The Determination of Young Modulus for CFRP using Three Point Bending Tests at Different Span Lengths". In: *U.P.B. Sci. Bull., Series D* Vol. 75, No. 1 (2013), 121 − 128.

[103] F. Mujika. "On the Difference Between Flexural Moduli Obtained by Three-Point and Four-Point Bending Tests". In: *Polymer Testing* Vol. 25, No. 2 (2006), 214 − 220. URL: http://dx.doi.org/10.1016/j.polymertesting.2005.10.006.

[104] A. Vijayaraghavan and D. Dornfeld. "Challenges in Modelling Machining of Multilayer Materials". In: (2005). UC Berkeley: Laboratory for Manufacturing and Sustainability, 1 − 8. URL: Permalink:~https://escholarship.org/uc/item/60k6x64r.

[105] K.K. Panchagnula and K. Palaniyandi. "Drilling on Fiber Reinforced Polymer/Nanopolymer Composite Laminates: A Review". In: *Journal of Materials Research and Technology* Vol. 7, No. 2 (2018), 180 − 189. URL: https://doi.org/10.1016/j.jmrt.2017.06.003.

[106] F. Lissek, J. Tegas, and M. Kaufeld. "Damage Quantification for the Machining of CFRP: An Introduction about Characteristic Values Considering Shape and Orientation of Drilling-induced Delamination". In: *Procedia Engineering* 149 (2016), 2 − 16. URL: https://doi.org/10.1016/j.proeng.2016.06.632.

[107] D. Liu, Y.J. Tang, and W.L. Cong. "A Review of Mechanical Drilling for Composite Laminates". In: *Composite Structures* Vol. 94, No. 4 (2012), 1265 − 1279. URL: https://doi.org/10.1016/j.compstruct.2011.11.024.

[108] N. Bhatnagar, N. Ramakrishnan, N.K. Naik, and R. Komanduri. "On the Machining of Fiber Reinforced Plastic (FRP) Composite Laminates". In: *International Journal of Machine Tools and Manufacture* Vol. 35, No. 5 (1995), 701 – 716. URL: http://dx.doi.org/10.1016/0890-6955(95)93039-9.

[109] Sandvik Coromant. *Composite Product Solutions*. 2010. URL: https://www.sandvik.coromant.com/SiteCollectionDocuments/downloads/global/brochures/en-gb/C-2940-155.pdf.

[110] Composites World. *Hole quality defined*. URL: https://www.compositesworld.com/articles/hole-quality-defined. (Accessed: 01.09.2016).

[111] J.L. Merino-Perez, R. Royer, E. Merson, A. Lockwood, S. Ayvar-Soberanis, and M.B. Marshall. "Influence of Workpiece Constituents and Cutting Speed on the Cutting Forces Developed in the Conventional Drilling of CFRP Composites". In: *Composite Structures* 140 (2016), 621 – 629. URL: http://dx.doi.org/10.1016/j.compstruct.2016.01.008.

[112] I.S. Shyha, D.K. Aspinwall, S.L. Soo, and S. Bradley. "Drill Geometry and Operating Effects when Cutting Small Diameter Holes in CFRP". In: *International Journal of Machine Tools and Manufacture* Vol. 49, No. 12-13 (2009), 1008 – 1014. URL: https://doi.org/10.1016/j.ijmachtools.2009.05.009.

[113] Y. Karpat and O. Bahtiyar. "Comparative Analysis of PCD drill Designs During Drilling of CFRP Laminates". In: *Procedia CIRP* 31 (2015), 316 – 321. URL: http://dx.doi.org/10.1016/j.procir.2015.03.094.

[114] X. Wang, P.Y. Kwon, C. Sturtevant, D.D.W. Kim, and J. Lantrip. "Tool Wear of Coated Drills in Drilling CFRP". In: *Journal of Manufacturing Processes* Vol. 15, No. 1 (2013), 87 – 95. URL: http://dx.doi.org/10.1016/j.jmapro.2012.09.019.

[115] A. Faraz, D. Biermann, and K. Weinert. "Cutting Edge Rounding: An Innovative Tool Wear Criterion in Drilling CFRP Composite Laminates". In: *International Journal of Machine Tools and Manufacture* Vol. 49, No. 15 (2009), 1185 – 1196. URL: http://dx.doi.org/10.1016/j.ijmachtools.2009.08.002.

[116] M.S. Won and C.K.H. Dharan. "Chisel Edge and Pilot Hole Effects in Drilling Composite Laminates". In: *Journal of Manufacturing Science and Engineering* Vol. 124, No. 2 (2002), 242 – 247. URL: http://dx.doi.org/10.1115/1.1448317.

[117] C.C. Tsao and H. Hocheng. "The Effect of Chisel Length and Associated Pilot Hole on Delamination When Drilling Composite Materials". In: *International Journal of Machine Tools and Manufacture* Vol. 43, No. 11 (2003), 1087 – 1092. URL: https://doi.org/10.1016/S0890-6955(03)00127-5.

[118] S. Jain and D.C.H. Yang. "Delamination-Free Drilling of Composite Laminates". In: *Journal of Engineering for Industry* Vol. 116, No. 4 (1994), 475 – 481. URL: http://dx.doi.org/10.1115/1.2902131.

[119] J. Xu and M. El Mansori. "Cutting Modeling of Hybrid CFRP/Ti Composite with Induced Damage Analysis". In: *Materials* Vol. 9, No. 1 (2016). URL: http://dx.doi.org/10.3390/ma9010022.

[120] R. Zitoune, V. Krishnaraj, and F. Collombet. "Study of Drilling of Composite Material and Aluminium Stack". In: *Composite Structures* Vol. 92, No. 5 (2010), 1246 – 1255. URL: http://dx.doi.org/10.1016/j.compstruct.2009.10.010.

[121] E. Brinksmeier and R. Janssen. "Drilling of Multi-Layer Composite Materials consisting of Carbon Fiber Reinforced Plastics (CFRP), Titanium and Aluminum Alloys". In: *CIRP Annals* Vol. 51, No. 1 (2002), 87 – 90. URL: https://doi.org/10.1016/S0007-8506(07)61472-3.

[122] I. Shyha, S.L. Soo, D.K. Aspinwall, S. Bradley, S. Dawson, and C.J. Pretorius. "Drilling of Titanium/CFRP/Aluminium Stacks". In: *Key Engineering Materials* 447-448 (2010), 624 – 633. URL: http://dx.doi.org/10.4028/www.scientific.net/KEM.447-448.624.

[123] I.S. Shyha, S.L. Soo, D.K. Aspinwall, S. Bradley, R. Perry, P. Harden, and S. Dawson. "Hole Quality Assessment Following Drilling of Metallic-Composite Stacks". In: *International Journal of Machine Tools and Manufacture* Vol. 51, No. 7-8 (2011), 569 – 578. URL: http://dx.doi.org/10.1016/j.ijmachtools.2011.04.007.

[124] F. Kahwash, I. Shyha, and A. Maheri. "Modelling of Cutting Fibrous Composite Materials: Current Practice". In: *Procedia CIRP* 28 (2015), 52 – 57. URL: http://dx.doi.org/10.1016/j.procir.2015.04.010.

[125] A. Abena, S.L. Soo, and K. Essa. "A Finite Element Simulation for Orthogonal Cutting of UD-CFRP Incorporating a Novel Fibre-Matrix Interface Model". In: *Procedia CIRP* 31 (2015), 539 – 544. URL: http://dx.doi.org/10.1016/j.procir.2015.04.091.

[126] K. Gobivel, K.S. Vijay Sekar, and G. Prabhakaran. "Finite Element Analysis of High-Speed Machining of CFRP Material". In: *Advances in Materials and Metallurgy* (2019), 137 – 147. URL: https://doi.org/10.1007/978-981-13-1780-4_15.

[127] L. Lasri, M. Nouari, and M. El Mansori. "Modelling of Chip Separation in Machining Unidirectional FRP Copmposites by Stiffness Degradation Concept". In: *Composites Science and Technology* Vol. 69, No. 5 (2009), 684 – 692. URL: http://dx.doi.org/10.1016/j.compscitech.2009.01.004.

[128] V.A. Phadnis, F. Makhdum, A. Roy, and V.V. Silberschmidt. "Drilling in Carbon/Epoxy Composites: Experimental Investigations and Finite Element Implementation". In: *Composites Part A: Applied Science and Manufacturing* 47 (2013), 41 − 51. URL: https://doi.org/10.1016/j.compositesa.2012.11.020.

[129] Y.L. He, J.P. Davim, and H.Q. Xue. "3D Progressive Damage Based Macro-Mechanical FE Simulation of Machining Unidirectional FRP Composite". In: *Chinese Journal of Mechanical Engineering* Vol. 31, No.51 (2018), 1 − 16. URL: https://doi.org/10.1186/s10033-018-0250-5.

[130] S. Zenia, L.B. Ayed, M. Nouari, and A. Delamézière. "An Elastoplastic Constitutive Damage Model to Simulate the Chip Formation Process and Workpiece Subsurface Defects when Machining CFRP Composites". In: *Procedia CIRP* 31 (2015), 100 − 105. URL: http://dx.doi.org/10.1016/j.procir.2015.03.100.

[131] O. Isbilir and E. Ghassemieh. "Finite Element Analysis of Drilling of Titanium Alloy". In: *Procedia Engineering* 10 (2011), 1877 − 1882. ISSN: 1877-7058. URL: https://doi.org/10.1016/j.proeng.2011.04.312.

[132] R. Zitoune, L. Crouzeix, F. Collombet, T. Tamine, and Y.H. Grunevald. "Behaviour of Composite Plates with Drilled and Moulded Hole Under Tensile Load". In: *Composite Structures* Vol. 93, No. 9 (2011), 2384 − 2391. URL: https://doi.org/10.1016/j.compstruct.2011.03.027.

[133] S.R. Hallett and M.R. Wisnom. "Experimental Investigation of Progressive Damage and the Effect of Layup in Notched Tensile Tests". In: *Journal of Composite Materials* Vol. 40, No. 2 (2006), 119 − 141. URL: http://dx.doi.org/10.1177/0021998305053504.

[134] T.J. De Vries. "Blunt and Sharp Notch Behaviour of Glare Laminates". PhD thesis. TU Delft, 2001. URL: https://repository.tudelft.nl/islandora/object/uuid:bd3b2294-e095-407d-bb8d-1c66f6651ae8?collection=research.

[135] A. Gilioli, A. Manes, and M. Giglio. "Evaluation of the Effects of the Numerical Modelling Choices on the Simulation of a Tensile Test on CFRP Composite". In: *Procedia Structural Integrity* 8 (2018), 33 − 42. URL: https://doi.org/10.1016/j.prostr.2017.12.005.

[136] L. Iannucci, S. Del Rosso, P.T. Curtis, D.J. Pope, and P.W. Duke. "Understanding the Thickness Effect on the Tensile Strength Property of Dyneema® HB26 Laminates". In: *Materials* Vol. 11, No. 8 (2018), p. 1431. URL: https://doi.org/10.3390/ma11081431.

[137] S. Marzi, A. Rauh, and R.M. Hinterholzl. "Fracture Mechanical Investigations and Cohesive Zone Failure Modelling on Automotive Composites". In: *Composite Structures* 111 (2014), 324 − 31. URL: http://dx.doi.org/10.1016/j.compstruct.2014.01.016.

[138] S. Akram, S. Jaffery, M. Khan, M. Fahad, A. Mubashar, and L. Ali. "Numerical and Experimental Investigation of Johnson-Cook Material Models for Aluminum (Al 6061-T6) Alloy Using Orthogonal Machining Approach". In: *Advances in Mechanical Engineering* Vol. 10, No. 9 (2018), 1 −14. URL: https://doi.org/10.1177/1687814018797794.

[139] E.G. Ng and D.K. Aspinwall. "Modelling of Hard Part Machining". In: *Journal of Materials Processing Technology* Vol. 127, No. 2 (2002), 222 − 229. URL: http://dx.doi.org/10.1016/S0924-0136(02)00146-2.

[140] Y.A. Roy, K. Gobivel, K.S.V. Sekar, and S.S. Kumar. "Impact of Cutting Forces and Chip Microstructure in High Speed Machining of Carbon Fiber and Epoxy Composite Tube". In: *Archives of Metallurgy and Materials* Vol. 62, No. 3 (2017), 1771 − 1777. DOI: 10.1515/amm-2017-0269.

[141] D. Nayak, N. Bhatnagar, and P. Mahajan. "Machining Studies of UD-FRP Composites Part 2: Finitie Element Analysis". In: *Machining Science and Technology* Vol. 9, No. 4 (2005), 503 − 528. URL: https://doi.org/10.1080/10910340500398183.

[142] D. Nayak, N. Bhatnagar, and P. Mahajan. "Machining Studies of Uni-Directional Glass Fiber Reinforced Plastic (UD-GFRP) Composites. Part 1: Effect of Geometrical and Process Parameters". In: *Machining Science and Technology* Vol. 9, No. 4 (2005), 481 − 501. URL: http://dx.doi.org/10.1080/10910340500398167.

[143] J. Xu and M. El Mansori. "Experimental Studies on the Cutting Characteristics of Hybrid CFRP/Ti Stacks". In: *Procedia Manufacturing* 5 (2016), 270 − 281. URL: https://doi.org/10.1016/j.promfg.2016.08.024.

[144] X. Wang D.and He, Z. Xu, W. Jiao, F. Yang, L. Jiang, L. Li, W. Liu, and R. Wang. "Study on Damage Evaluation and Machinability of UD-CFRP for the Orthogonal Cutting Operation Using Scanning Acoustic Microscopy and the Finite Element Method". In: *Materials* Vol. 10, No. 2 (2017), p. 20. DOI: 10.3390/ma10020204. URL: https://doi.org/10.3390/ma10020204.

[145] I.A. Shchurov, A.V. Nikonov, I.S. Boldyrev, and D.V. Ardashev. "SPH Modeling of Chip Formation in Cutting Unidirectional Fiber-Reinforced Composite". In: *Russian Engineering Research* Vol. 36, No. 10 (2016), 883 − 887. URL: https://doi.org/10.3103/S1068798X1610018X.

[146] H.J. Zhang, W.Y. Chen, D.C. Chen, and L.C. Zhang. "Assessment of the Exit Defects in Carbon Fibre-Reinforced Plastic Plates Caused by Drilling". In: *Key Engineering Materials* 196 (2001), 43 − 52. URL: https://doi.org/10.4028/www.scientific.net/KEM.196.43.

[147] E.D. Eneyew and M. Ramulu. "Experimental Study of Surface Quality and Damage when Drilling Unidirectional CFRP Composites". In: *Journal of Materials Research and Technology* Vol. 3, No. 4 (2014), 354 − 362. URL: http://www.sciencedirect.com/science/article/pii/S2238785414000799.

[148] K. Debnath, M. Sisodia, A. Kumar, and I. Singh. "Damage-Free Hole Making in Fiber-Reinforced Composites: An Innovative Tool Design Approach". In: *Materials and Manufacturing Processes* Vol. 31, No. 10 (2016), 1400 − 1408. URL: https://doi.org/10.1080/10426914.2016.1140191.

[149] C. Prakash and K.S. Vijay Sekar. "Influence of Friction Coefficient and Failure Model in 3D FEA Simulation of Drilling of Glass Fiber Reinforced Polymer Composites". In: *Advances in Manufacturing Processes* (2019), 81 − 90. URL: https://doi.org/10.1007/978-981-13-1724-8_8.

[150] V.A. Phadnis, F. Makhdum, A. Roy, and V.V. Silberschmidt. "Experimental and Numerical Investigations in Conventional and Ultrasonically Assisted Drilling of CFRP Laminate". In: *Procedia CIRP* 1 (2012), 455 − 459. URL: https://doi.org/10.1016/j.procir.2012.04.081.

[151] P. Hale and E.G. Ng. "Non-Linear Material Characterization of CFRP with FEM Utilizing Cohesive Surface Considerations Validated with Effective Tensile Test Fixturing". In: *Materials Today Communications* 23 (2020), 1 − 15. URL: http://dx.doi.org/10.1016/j.mtcomm.2019.100872.

[152] P. Hale and E.G. Ng. "Three-Point Bending Analysis with Cohesive Surface Interaction for Improved Delamination Prediction and Application of Carbon Fibre Reinforced Plastics Composites". In: *Modelling and Simulation in Materials Science and Engineering* Vol. 28, No. 3 (2020). URL: http://dx.doi.org/10.1088/1361-651X/ab7054.

[153] Autodesk Helius PFA. *Theory Manual.* 2016. URL: http://help.autodesk.com/view/ACMPAN/2016/ENU/?guid=GUID-1FEC4707-77A9-4FA4-BA2D-60B7444A1359.

[154] D.R. Ambur, N. Jaunky, and C.G. Davila. "Progressive Failure of Composite Laminates using LaRC02 Criteria". In: *Collection of Technical Papers - AIAA/ASME/ASCE/AHS/ASC Structures, Structural Dynamics and Materials Conference* 2 (2004), 898 − 913.

[155] S.L. Orton, V.P. Chiarito, C. Rabalais, M. Wombacher, and S.P. Rowell. "Strain Rate Effects in CFRP Used For Blast Mitigation". In: *Polymers* Vol. 6, No. 4 (2014), 1026 − 1039. URL: https://doi.org/10.3390/polym6041026.

[156] G.R. Johnson and W.H Cook. "A Constitutive Model and Data for Metals Subjected to Large Strains, High Strain Rates, and High Temperatures". In: *Proceedings of the Seventh International Symposium on Ballistics* (1983), 541 − 547.

[157] D.R. Lesuer, G.J. Kay, and M.M. LeBlanc. "Modeling Large Strain, High Rate Deformation in Metals". In: *Proceedings of the TMS Fall Meeting* (2001), 75 − 86.

[158] L.E. Schwer. "Aluminum Plate Perforation: A Comparative Case Study using Lagrange with Erosion, Multi-Material ALE, and Sooth Particle Hydrodynamics". In: *7th European LS-DYNA Conference* (2009), 1 − 28.

[159] R.C. Hibbeler. *Engineering Mechanics - Statics and Dynamics*. NJ, USA: Prentice Hall, 2006. ISBN: 978-0132215091.

[160] Sandvik Coromant. *Machining Carbon Fibre Materials. User's Guide.* Sandviken, Sweden, 2010, 1 − 63. URL: https://www.sandvik.coromant.com/sitecollectiondocuments/downloads/global/technical%5C%20guides/en-gb/c-2920-30.pdf.

[161] P. Li, X. Qiu, C. Li, Q. Niu, A. Chen, and T.J. Ko. "Hole Exit Damage and Tool Wear During the Drilling of CFRP with a Double-Point Angle Drill". In: *Journal of Mechanical Science and Technology* 33 (2019), 2363 − 2370. URL: https://doi.org/10.1007/s12206-019-0436-5.

[162] A.A. Hassan, S.L. Soo, D.K. Aspinwall, D. Arnold, and A. Dowson. "An Analytical Model to Predict Interlayer Burr Size Following Drilling of CFRP-Metallic Stack Assemblies". In: *CIRP Annals* 69 (2020), 109 − 112. URL: https://doi.org/10.1016/j.cirp.2020.04.038.

[163] F. Bañon, A. Sambruno, M. Batista, S. R. Fernandez-Vidal, and J. Salguero. "Study of the One-Shot Drilling of CFRP/Ti6Al4V Stacks with a Double Tip Angle Cutting-Tool Geometry". In: *AIP Conference Proceedings* 2113.1 (2019). URL: https://doi.org/10.1063/1.5112618.

[164] E.P. Bonhin, S.D. Müzel, E.S. Guidi, E.C. Botelho, and M.V. Ribeiro. "Influence of Drilling Parameters on Thrust Force and Burr on Fiber Metal Laminate (Al 2024-T3/Glass Fiber Reinforced Epoxy)". In: *Procedia CIRP* 101 (2021), 338 − 341. URL: https://doi.org/10.1016/j.procir.2021.02.035.

[165] J. Fernandez-Perez, J.L. Cantero, J. Diaz-alvarez, and M.H. Miguelez. "Hybrid Composite-Metal Stack Drilling with Different Minimum Quantity Lubrication Levels". In: *Materials* Vol. 12, No. 3 (2019). URL: http://dx.doi.org/10.3390/ma12030448.

[166] M. Montoya, M. Calamaz, D. Gehin, and F. Girot. "Numerical Simulation of Workpiece Thermal Field in Drilling CFRP/Aluminum Alloy". In: *Key Engineering Materials* Vol. 611 − 612 (2014), 1226 − 35. URL: http://dx.doi.org/10.4028/www.scientific.net/KEM.611-612.1226.

[167] A. Vanaja and R.M.V.G.K. Rao. "Fibre Fraction Effects on Thermal Degradation Behaviour of GFRP, CFRP and Hybrid Composites". In: *Journal of Reinforced Plastics and Composites* Vol. 21, No. 15 (2002), 1389 − 1398. URL: https://doi.org/10.1177/0731684402021015780.

[168] E. Uhlmann and E. Barth. "Smoothed Particle Hydrodynamics Simulation of the Machining Process of Inconel 718". In: *Procedia Manufacturing* 18 (2018), 1 − 11. URL: https://doi.org/10.1016/j.promfg.2018.11.001.

[169] F. Spreng and P. Eberhard. "Machining Process Simulations with Smoothed Particle Hydrodynamics". In: *Procedia CIRP* 31 (2015), 94 − 99. DOI: https://doi.org/10.1016/j.procir.2015.03.073. URL: https://doi.org/10.1016/j.procir.2015.03.073.

[170] M. Li, S.L. Soo, D.K. Aspinwall, D. Pearson, and W. Leahy. "Study on Tool Wear and Workpiece Surface Integrity Following Drilling of CFRP Laminates with Variable Feed Rate Strategy". In: *Procedia CIRP* 71 (2018), 407 − 412. URL: https://doi.org/10.1016/j.procir.2018.05.055.

[171] N. Yaşar and M. Günay. "Experimental Investigation on Novel Drilling Strategy of CFRP Laminates Using Variable Feed Rate". In: *Journal of the Brazilian Society of Mechanical Sciences and Engineering* Vol. 41, No. 3 (2019), 150 − 162. URL: http://dx.doi.org/10.1007/s40430-019-1658-2.

[172] F. Makhdum, L.T. Jennings, A. Roy, and V.V. Silberschmidt. "Cutting Forces in Ultrasonically Assisted Drilling of Carbon Fibre-Reinforced Plastics". In: *Journal of Physics: Conference Series* 382 (2012), 1 − 7. URL: https://dx.doi.org/10.1088/1742-6596/382/1/012019.

[173] ASTM International. *ASTM E8 / E8M-16a, Standard Test Methods for Tension Testing of Metallic Materials*. West Conshohocken, PA, USA, 2016. DOI: 10.1520/E0008_E0008M-16A.

[174] S.W. Tsai. "Strength Theories of Filamentary Structures". In: *Fundamental Aspects of Fiber Reinforced Plastic Composites* 5 (1968), 3 − 11.

[175] R.M. Christensen. "Tensor Transformations and Failure Criteria for the Analysis of Fiber Composite Materials". In: *Journal of Composite Materials* Vol. 22, No. 9 (1988), 874 – 897. URL: https://doi.org/10.1177/002199838802200906.

[176] A. Puck and H. Schurmann. "Failure Analysis of FRP Laminates by Means of Physically Based Phenomenological Models". In: *Failure Criteria in Fibre-Reinforced-Polymer Composites* (2004), 264 – 297. URL: http://dx.doi.org/10.1016/B978-008044475-8/50011-1.

[177] Instron. *Dual Column Tabletop Models 3360*. MA, USA, 2017. URL: http://www.instron.us/-/media/literature-library/products/2011/06/3300-series-table-model.pdf?la=en-US. Accessed: 2016-7-20.

[178] GOM Aramis. *ARAMIS Adjustable*. NC, USA, 2017. URL: https://www.gom.com/metrology-systems/aramis/aramis-adjustable.html. Accessed: 2017-12-05.

[179] R.S. Sandhu and K.J. Singh. "Reduced Integration for Improved Accuracy of Finite Element Approximations". In: *Computer Methods in Applied Mechanics and Engineering* Vol. 14, No. 1 (1978), 23 – 37. URL: http://dx.doi.org/10.1016/0045-7825(78)90011-7.

[180] P.P. Camanho, A. Turon, C.G. Davila, and J. Costa. "An Engineering Solution for Mesh Size Effects in the Simulation of Delamination Using Cohesive Zone Models". In: *Engineering Fracture Mechanics* Vol. 74, No. 10 (2007), 1665 – 1682. URL: http://dx.doi.org/10.1016/j.engfracmech.2006.08.025.

[181] B.P. Russell, T. Liu, N.A. Fleck, and V.S. Deshpande. "Quasi-static Three-point Bending of Carbon Fiber Sandwich Beams With Square Honeycomb Cores". In: *Journal of Applied Mechanics* Vol. 78, No. 3 (2011), p. 15. URL: http://dx.doi.org/10.1115/1.4003221.

[182] B.Z. Jang. *Advanced Polymer Composites: Principles and Applications*. Taylor & Francis, 1994. ISBN: 9780871704917.

[183] E. Hara, T. Yokozeki, H. Hatta, Y. Iwahori, and T. Ishikawa. "Out-Of-Plane Tensile Modulus of CFRP Laminates by 3-Point Bending Test". In: *Advanced Composite Materials* Vol. 24, No. 3 (2015), 221 – 237. URL: http://dx.doi.org/10.1080/09243046.2014.960145.

[184] ASTM International. *Standard Test Method for Flexural Properties of Unreinforced and Reinforced Plastics and Electrical Insulating Materials*. West Conshohocken, PA, 2007, 1 – 11. DOI: 10.1520/D0790-17.

[185] D.K. Shin, H.C. Kim, and J.J. Lee. "Numerical Analysis of the Damage Behavior of an Aluminum/CFRP Hybrid Beam Under Three Point Bending". In: *Composites Part B: Engineering* 56 (2014), 397 – 407. URL: http://dx.doi.org/10.1016/j.compositesb.2013.08.030.

[186] Jan Tessmer, Daniel Hartung, and Lars Aschenbrenner. "Mechanics of composites in lightweight structures: Efficient testing and computation accounting for complex 3D behaviour". In: *ICAS Secretariat - 26th Congress of International Council of the Aeronautical Sciences 2008, ICAS 2008* 2 (2008), pp. 3096–3077.

[187] M. Nikbakht and N. Choupani. "Fracture Toughness Characterization of Carbon-Epoxy Composite using Arcan". In: *International Journal of Aerospace and Mechanical Engineering* 2.4 (2008), pp. 247–253.

[188] D.P. Yan, T. Hilditch, H.A. Kishawy, and G. Littlefair. "On Quantifying the Strain Rate During Chip Formation When Machining Aerospace Alloy Ti-5553". In: *Procedia CIRP* 8 (2013). 14th CIRP Conference on Modeling of Machining Operations (CIRP CMMO), 123 – 128. URL: https://doi.org/10.1016/j.procir.2013.06.076.

[189] G. Chardon, O. Klinkova, J. Rech, S. Drapier, and J.M. Bergheau. "Characterization of Friction Properties at the Work Material/Cutting Tool Interface During the Machining of Randomly Structured Carbon Fibers Reinforced Polymer with Poly Crystalline Diamond Tool Under Dry Conditions". In: *Tribology International* 81 (2015), 300 – 308. URL: https://doi.org/10.1016/j.triboint.2014.09.002.

[190] F. Zemzemi, W. Bensalem, J. Rech, A. Dogui, and P. Kapsa. "New Tribometer Designed for the Characterisation of the Friction Properties at the Tool/Chip/Workpiece Interfaces in Machining". In: *Tribotest* Vol. 14, No. 1 (), 11 –25. URL: https://doi.org/10.1002/tt.50.

[191] C. Bonnet, F. Valiorgue, J. Rech, and H. Hamdi. "Improvement of the Numerical Modeling in Orthogonal Dry Cutting of an AISI 316L Stainless Steel by the Introduction of a New Friction Model". In: *CIRP Journal of Manufacturing Science and Technology* Vol. 1, No. 2 (2008), 114 – 118. DOI: https://doi.org/10.1016/j.cirpj.2008.09.006. URL: https://doi.org/10.1016/j.cirpj.2008.09.006.

[192] K.H. Dittrich and D. Oelsner. "Production and Characterization of Dry Lubricant Coatings for Tools on the Base of Carbon". In: *International Journal of Refractory Metals and Hard Materials* Vol. 20, No. 2 (2002), 121 – 127. URL: http://dx.doi.org/10.1016/S0263-4368(02)00010-0.

[193] W. König, C. Wulf, P. Grass, and H. Willerscheid. “Machining of Fibre Reinforced Plastics”. In: *CIRP Annals* Vol. 34, No. 2 (1985), 537 – 548. URL: https://doi.org/10.1016/S0007-8506(07)60186-3.

[194] E.P. DeGarmo, J.T. Black, and R.A. Kohser. *Materials and Processes in Manufacturing*. Wiley, 2003. ISBN: 9780471656531.

[195] R. Voss, L. Seeholzer, F. Kuster, and K. Wegener. “Cutting Process Tribometer Experiments for Evaluation of Friction Coefficient Close to a CFRP Machining Operation”. In: *Procedia CIRP* 66 (2017), 204 – 209. URL: https://doi.org/10.1016/j.procir.2017.03.225.

[196] V. L. Popov. “Coulomb’s Law of Friction”. In: *Contact Mechanics and Friction: Physical Principles and Applications*. Berlin, Heidelberg: Springer, 2010, 133 – 154. ISBN: 978-3-642-10803-7. DOI: 10.1007/978-3-642-10803-7_10. URL: https://doi.org/10.1007/978-3-642-10803-7_10.

[197] O. Cousigné, D. Moncayo, D. Coutellier, P. Camanho, and H. Naceur. “Numerical Modeling of Nonlinearity, Plasticity and Damage in CFRP-Woven Composites for Crash Simulations”. In: *Composite Structures* 115 (2014), 75 – 88. URL: https://doi.org/10.1016/j.compstruct.2014.04.017.

[198] S. Eskandari, F.M.A. Pires, P.P. Camanho, H. Cui, N. Petrinic, and A.T. Marques. “Analyzing the Failure and Damage of FRP Composite Laminates Under High Strain Rates Considering Visco-Plasticity”. In: *Engineering Failure Analysis* 101 (2019), 257 – 273. URL: https://doi.org/10.1016/j.engfailanal.2019.03.008.

[199] X. Li, Y. Yan, L. Guo, and C. Xu. “Effect of Strain Rate on the Mechanical Properties of Carbon/Epoxy Composites Under Quasi-Static and Dynamic Loadings”. In: *Polymer Testing* 52 (2016), 254 – 264. URL: https://doi.org/10.1016/j.polymertesting.2016.05.002.

[200] C.G. Davila, P.P. Camanho, and C.A. Rose. “Failure Criteria for FRP Laminates”. In: *Journal of Composite Materials* Vol. 39, No. 4 (2005), 323 – 345. URL: https://doi.org/10.1177/0021998305046452.

[201] N. Taniguchi, T. Nishiwaki, and H. Kawada. “Tensile strength of unidirectional CFRP laminate under high strain rate”. In: *Advanced Composite Materials* 16.2 (2007), pp. 167–180. DOI: 10.1163/156855107780918937. eprint: https://doi.org/10.1163/156855107780918937. URL: https://doi.org/10.1163/156855107780918937.

[202] H. Srbova, T. Kroupa, and R. Zemcik. “Identification of the Material Parameters of a Unidirectional Fiber Composite Using a Micromodel”. In: *Materials and technology* 46 (2012), pp. 431–434.

[203] Thomas Y. Hou and Xiao-Hui Wu. "A Multiscale Finite Element Method for Elliptic Problems in Composite Materials and Porous Media". In: *Journal of Computational Physics* 134.1 (1997), pp. 169–189. ISSN: 0021-9991. DOI: https://doi.org/10.1006/jcph.1997.5682. URL: http://www.sciencedirect.com/science/article/pii/S0021999197956825.

[204] Fei Su, Lei Zheng, Fujian Sun, Zhenhua Wang, Zhaohui Deng, and Xinyi Qiu. "Novel Drill Bit Based on the Step-Control Scheme for Reducing the CFRP Delamination". In: *Journal of Materials Processing Technology* 262 (2018), 157 – 167. ISSN: 0924-0136. DOI: https://doi.org/10.1016/j.jmatprotec.2018.06.037.

[205] H. Ullah, A.R. Harland, and V.V. Silberschmidt. "Damage Modelling in Woven-Fabric CFRP Laminates Under Large-Deflection Bending". In: *Computational Materials Science* 64 (2012), 130 – 135. URL: http://dx.doi.org/10.1016/j.commatsci.2012.05.036.

[206] A.H.A. Garekani. "Numerical Modeling of Orthogonal Cutting of Carbon Fibre Reinforced Polymer Composites". PhD thesis. University of British Columbia, 2016. URL: http://dx.doi.org/10.14288/1.0305793.

[207] M.R. Garnich. "A Multicontinuum Theory for Structural Analysis of Composite Materials". PhD thesis. University of Wyoming, 1996.

[208] M.A. Caminero, G.P. Rodríguez, and V. Muñoz. "Effect of Stacking Sequence on Charpy Impact and Flexural Damage Behavior of Composite Laminates". In: *Composite Structures* 136 (2016), 345 – 357. URL: https://doi.org/10.1016/j.compstruct.2015.10.019.

[209] E. Sideridis and G. A. Papadopoulos. "Short-Beam and Three-Point-Bending Tests for the Study of Shear and Flexural Properties in Unidirectional-Fiber-Reinforced Epoxy Composites". In: *Journal of Applied Polymer Science* Vol. 93, No. 1 (2004), 63 – 74. URL: https://doi.org/10.1002/app.20382.

[210] N. Carbajal and F. Mujika. "Determination of Compressive Strength of Unidirectional Composites by Three-Point Bending Tests". In: *Polymer Testing* Vol. 28, No. 2 (2009), 150 – 156. URL: https://doi.org/10.1016/j.polymertesting.2008.11.003.

[211] M.A. Karataş and H. Gökkaya. "A Review on Machinability of Carbon Fiber Reinforced Polymer (CFRP) and Glass Fiber Reinforced Polymer (GFRP) Composite Materials". In: *Defence Technology* Vol. 14, No. 4 (2018), 318 – 326. URL: https://doi.org/10.1016/j.dt.2018.02.001.

[212] H. Wang, H. Zhang, K. Goto, I. Watanabe, H. Kitazawa, M. Kawai, H. Mamiya, and D. Fujita. "Stress Mapping Reveals Extrinsic Toughening of Brittle Carbon Fiber in Polymer Matrix". In: *Science and Technology of Advanced Materials* Vol. 21, No. 1 (2020), 267 – 277. URL: https://doi.org/10.1080/14686996.2020.1752114.

[213] S.O. Ismail, S. Sarfraz, M. Niamat, M. Mia, M.K. Gupta, D.Y. Pimenov, and E. Shehab. "Comprehensive Study on Tool Wear During Machining of Fiber-Reinforced Polymeric Composites". In: *Machining and Machinability of Fiber Reinforced Polymer Composites*. Singapore: Springer, 2021, 129 – 147. ISBN: 978-981-33-4153-1. URL: https://doi.org/10.1007/978-981-33-4153-1_5.

[214] J.M. Lifshitz and H. Leber. "Response of Fiber-Reinforced Polymers to High Strain-Rate Loading in Interlaminar Tension and Combined Tension/Shear". In: *Composites Science and Technology* Vol. 58, No. 6 (1998), 987 – 996. URL: http://dx.doi.org/10.1016/S0266-3538(97)00226-1.

[215] O. Isbilir and E. Ghassemieh. "Numerical Investigation of the Effects of Drill Geometry on Drilling Induced Delamination of Carbon Fiber Reinforced Composites". In: *Composite Structures* 105 (2013), 126 – 133. URL: https://doi.org/10.1016/j.compstruct.2013.04.026.

[216] P. Li, X. Qiu, C. Li, Q. Niu, A. Chen, and T.J. Ko. "Hole Exit Damage and Tool Wear During the Drilling of CFRP with a Double-Point Angle Drill". In: *Journal of Mechanical Science and Technology* Vol. 33, No. 5 (2019), 2363 – 2370. URL: https://doi.org/10.1007/s12206-019-0436-5.

[217] C. Xu, Y. Wang, J. Xu, and X. Liu. "Design of Internal-Chip-Removal Drill for CFRP Drilling and Study of Influencing Factors of Drilling Quality". In: *The International Journal of Advanced Manufacturing Technology* Vol. 106, No. 5 (2020), 1657 – 1669. URL: https://doi.org/10.1007/s00170-019-04698-8.

[218] X. Qiu, P. Li, C. Li, Q. Niu, A. Chen, P. Ouyang, and T.J. Ko. "New Compound Drill Bit for Damage Reduction in Drilling CFRP". In: *International Journal of Precision Engineering and Manufacturing-Green Technology* Vol. 6, No. 1 (2019), 75 – 87. URL: https://doi.org/10.1007/s40684-019-00026-3.

[219] Y. Karpat, B. Değer, and O. Bahtiyar. "Drilling Thick Fabric Woven CFRP Laminates with Double Point Angle Drills". In: *Journal of Materials Processing Technology* Vol. 212, No. 10 (2012), 2117 – 2127. URL: https://doi.org/10.1016/j.jmatprotec.2012.05.017.

[220] E. Kilickap A. Yardimeden and Y.H. Celik. "Effects of Cutting Parameters and Point Angle on Thrust Force and Delamination in Drilling of CFRP". In: *Materials Testing* 56 (2014), 1042 – 1048. URL: https://doi.org/10.3139/120.110666.

[221] P. Hale and E.G. Ng. "3D Finite Element Model on Drilling of CFRP with Numerical Optimization and Experimental Validation". In: *Materials* Vol. 14, No. 5 (2021), 1 − 22. URL: http://dx.doi.org/10.3390/ma14051161.

Appendix A

Extending the Finite Element Drilling Model: Part II

Innovative tools comparison: FEM drill geometry study: pre-drill; literature; improved.

A.1 Introduction

Utilizing the FE model developed in prior work, innovative drills were studied to gain understanding of the effect of various drill geometries. The first tool shown in Figure A.1 a) incorporates a predrill geometry, which is based off the CD854. The predill replicates the CD854, but is scaled down to a 50% diameter (3/32" or 2.38125 mm). The innovative geometry created by Debnath et al. [148] (b) and the revised Debnath et al. (c) were setup identically to the CD854 and CD856 models as discrete rigid bodies.

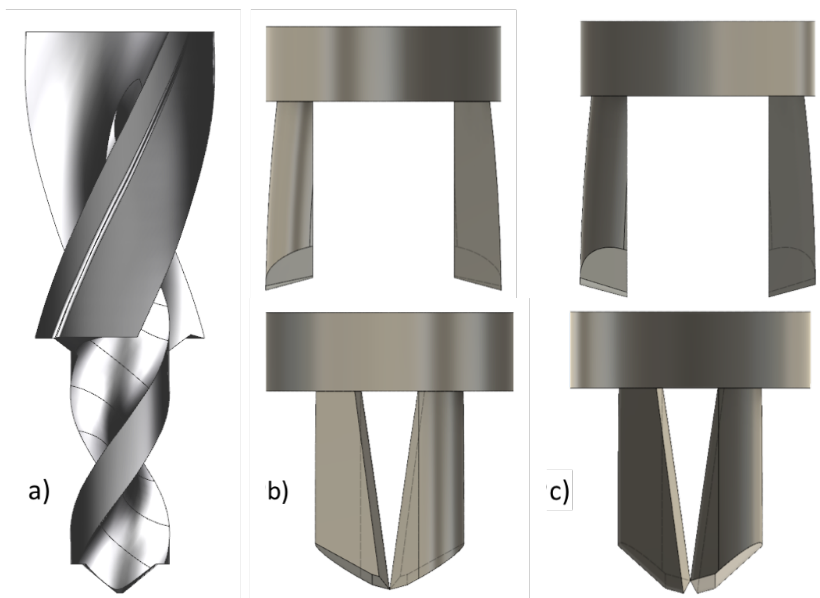

Figure A.1: a) Predrill geometry b) Innovative geometry [148] c) Revised Debnath et al.

A.1.1 Predrill Geometry Discussion

Due to the length of the predrill geometry (a) the analysis was divided into two stages for computational advantage. Figure A.2 a) shows Stage I positioning the predrill geometry at the top of the CFRP laminate surface. Stage II translates the tool in the axial direction, positioning it prior to the engagement of the secondary diameter, shown in Figure A.2 b).

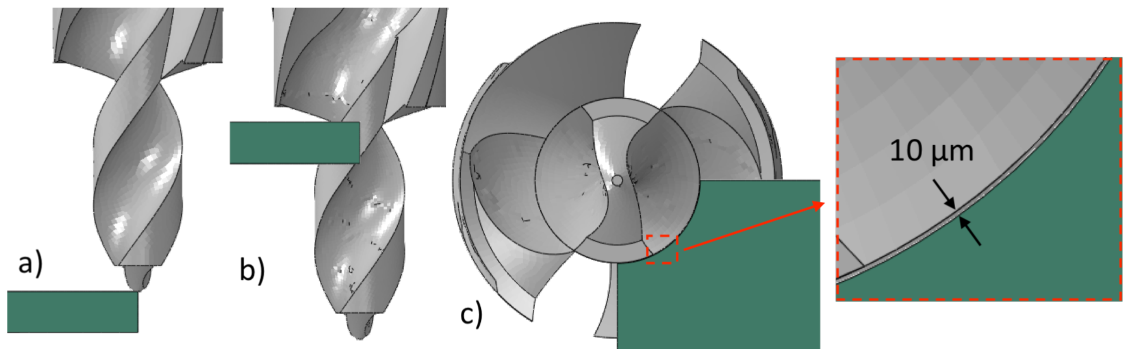

Figure A.2: a) Predrill Stage I b) Predrill Stage II side view c) Predrill Stage II bottom view

In Stage II a revolved cut is incorporated in the CFRP laminate to account for the deleted elements from the predrill of Stage I. There is an additional 10 μm gap to prevent pressure over-closure contact errors between the predrill and the CFRP material, shown in Figure A.2 c).

Adding to the function of the CD854 spur feature that scores the top surface of the CFRP laminate, a scored bottom-side CFRP laminate was additionally studied. The etching refers to a V-notched groove that is cut into the bottom surface via a hypothesized tool shown in Figure A.3 c). The V-notch is 0.11 mm (1 ply) in depth with a 45°angle. A revolve cut at 95% of the tool diameter (4.524 mm) is suggested. The V-notch geometry is shown in Figure A.3 a). The V-notch FE model setup and hypothesized tool are shown in Figure A.3 b) and c). The hypothesized tool acts as the predrill tool does. Initially, the wall of the drilled CFRP laminate would apply pressure keeping the cutting arm upright in a closed position. Once it drills through the CFRP laminate, the cutting arm, now free of the wall, would swing out due to the circumferential force. A retract movement of the drill in the axial direction would etch the bottom surface; similar to a pecking operation. Finally, the axial movement would reverse and the remainder of the hole could be drilled.

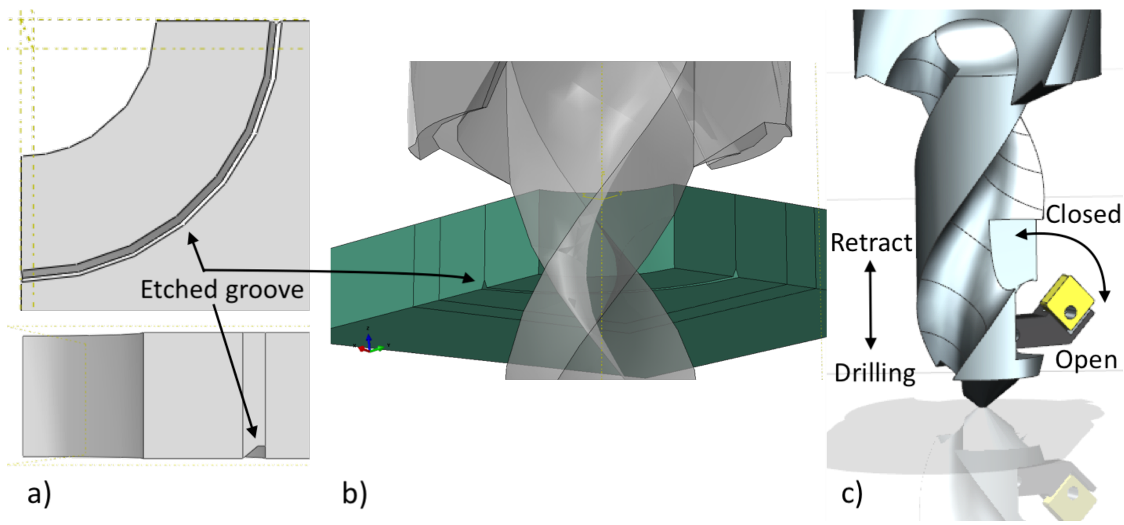

Figure A.3: a) V-notch geometry, b) V-notch FE setup, c) Hypothesized drill

Figure A.4 illustrates the thrust force for Stage I and II of the predrill model. The maximum thrust force from experiments with the 4.7625 mm CD854 drill was 58.22 N versus 50.68 N for the predrill setup (Stage I), a reduction of 12.95%. The average thrust force with respect to the bulk of the tool tip engaged in the laminate, was 54.87 N for the CD854 and 41.87 N for the predrill setup, resulting in a reduction of 23.69%. Stage II compares two models, with and without the etching of the exit surface. An 8.94% reduction in thrust force is predicted when the etching of the bottom surface is incorporated. This modification to the geometry facilitates the failure of the CFRP laminate controlling the damage propagation radially in the ply. The control is achieved by the geometry change of the etching, dampening the expansion of the stress when implemented.

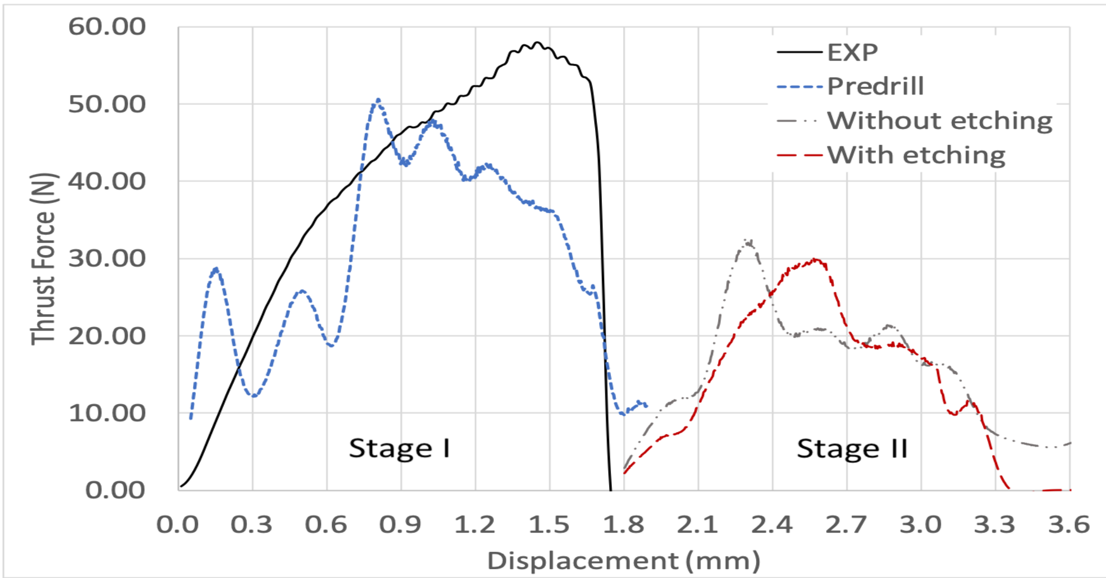

Figure A.4: Thrust force versus displacement: Stage I Pre-drill, Stage II with and without etching

Figure A.5 a) layers the etched matrix damage output (SDV2 = 1.0 grey) on top of the output without etching (SDV2 = 1.0 red). The red elements illustrate the increased damage propagation if etching is not applied. Figure A.5 b) illustrates the reduction in overall laminate damage (SDV1) at exit from drilling in Stage II. The reduction in thrust force at exit will reduce the spread of delamination damage at drill exit. Figure A.5 b) illustrates the complete laminate damage with etching (SDV1 = 2.0 black) and without (SDV1 = 2.0 red). Without etching, a significant increase in damaged elements (SDV1 > 1.0) illustrated in green, is predicted. A display group including the predrill tool and failed elements was created. The volume of damaged elements without etching is 1.36 mm^3 versus the reduced volume of 1.22 mm^3 with etching.

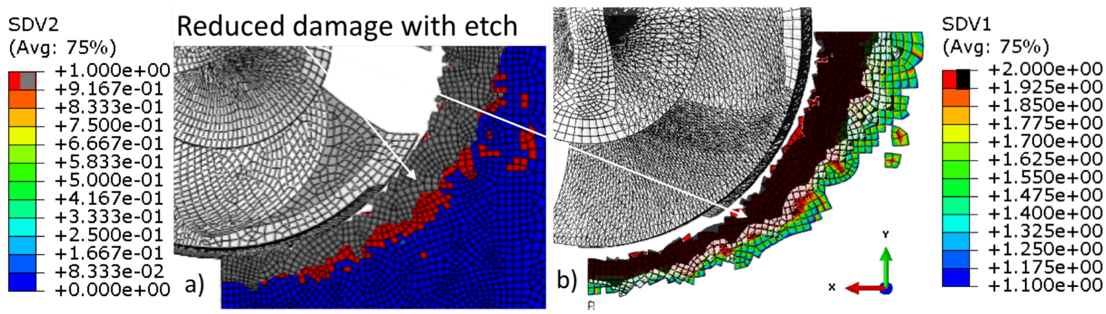

Figure A.5: With and without etching on exit surface a) Matrix damage (SDV2) b) Laminate damage (SDV1)

A.1.2 Innovative Geometry & Revised Debnath et al. Geometry

Debnath et al. created an innovative tool geometry, illustrated in Figure A.6, and determined an 80% and 82% reduction in thrust force when drilling through two different natural fibre-epoxy laminates versus a standard twist drill; one laminate was unidirectional, the other woven [148]. Debnath et al. noted improved hole quality with negligible defects such as fibre twisting, fibre pull-out and protruded fibres as found with the twist drill. The drill geometry demonstrates great improvements in quality and force reduction and was therefore created in CAD and simulated in the FE model for further investigation.

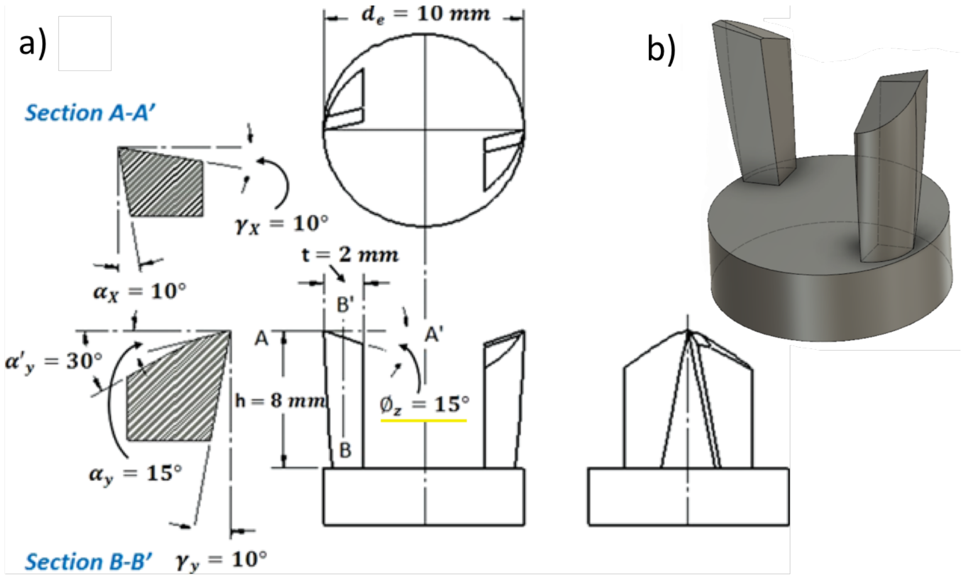

Figure A.6: a) Schematic innovative tool [148], b) CAD

Building on the advantages of the Debnath et al. drill geometry, a redesigned geometry was created that modified ϕ_z from 15°to -15°. The redesign is inspired to incorporate the benefits demonstrated by the CD856 drill. The Debnath et el al. geometry machines the periphery of the hole first. When the drill is engaged in the laminate, the thrust from the leading edge of the drill results in an axial and radial component. The radial force component has a vector towards the centre of the hole. This force component will induce tensile stress on the wall of the hole in the laminate. Tensile stress facilitates the growth of damage in a brittle FRP. When the ϕ_z is -15°the force component radially will create compressive forces on the laminate hole reducing the damage when drilling.

Figure A.7 i) illustrates the increased damage (red) with $\phi_z = 15°$, in comparison to the stable drilling response with $\phi_z = -15°$ shown in ii). The accelerated damage of the top surface damage is illustrated in Figure A.7 iii) versus iv); SDV1 entry surface damage for redesigned (compressive) drill is superimposed on top the entry surface damage for Debnath et al. drill at 2.0e-02 s. Figure A.8 illustrates the reduced damage on the exit surface for the redesigned drill (black) in comparison to the failed elements (red) from the Debnath et al. model.

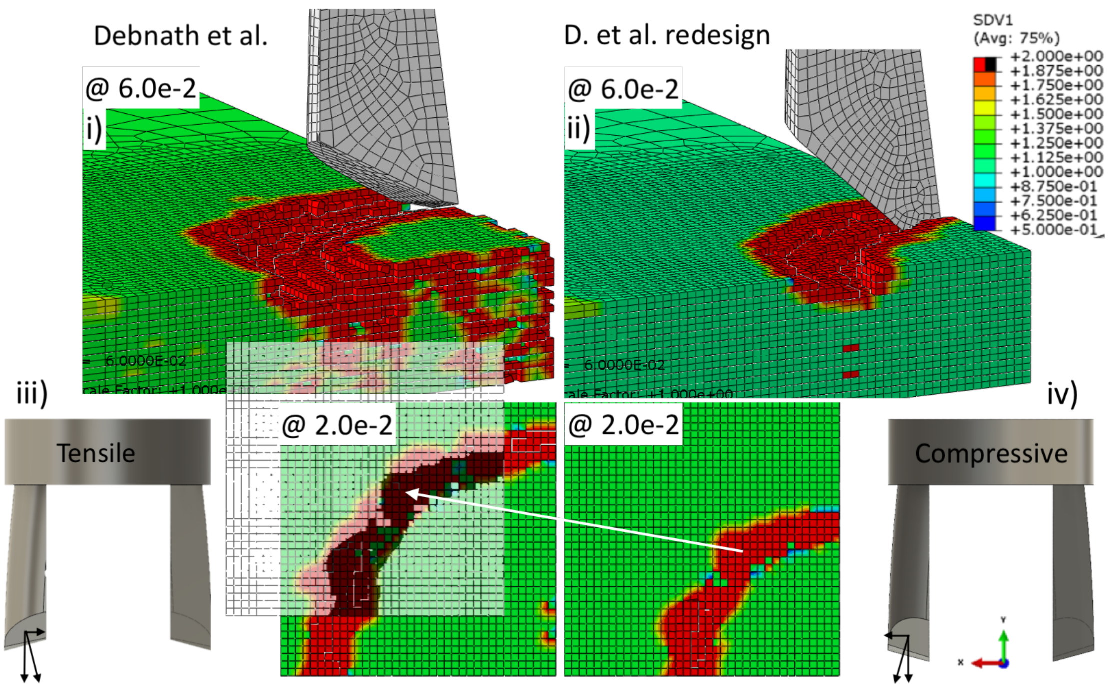

Figure A.7: Debnath et al. versus D. et al. redesign - SDV1 damage plot on entry surface

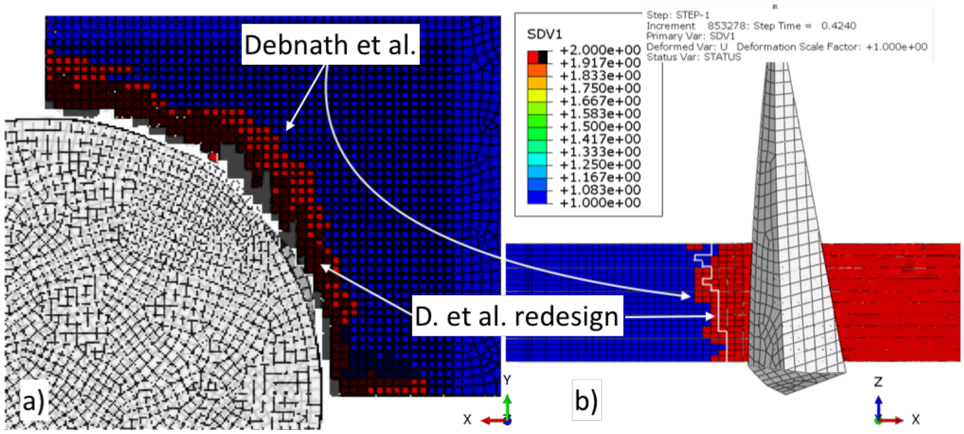

Figure A.8: Debnath et al. versus D. et al. redesign - SDV1 damage plot: a) bottom surface b) section view

Figure A.9 plots the predicted thrust force of the two drill geometries. The redesign requires similar thrust force with a marginal increase of 2.97% to drill through the UD-CFRP laminate. Integrating the thrust force-displacement curve, a reduction in cumulative energy required to drill is found with the redesign. One can appropriately hypothesize an increased tool life would result.

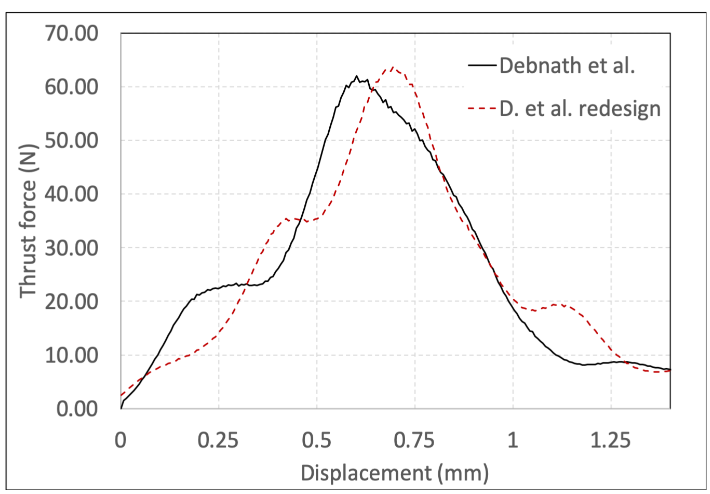

Figure A.9: Dednath et al. versus D. et al. redesign - thrust force (N) versus displacement (mm)

A.2 Conclusion

The objective of this work was to develop a macro FE model that could be used as a tool to accurately test various drill geometries, requiring a reasonable computation time. A quiver of tools were studied demonstrating the advantages of specific geometry features over a standard twist drill.

The predrill-hypothesized drill reduced exit surface damage propagation. The notch creates a change in geometry that focuses the stress in the bottom surface ply, negating the radial expansion of the stress. This focuses the applied load from the drill, reducing thrust force and improving hole quality.

The Debnath et al. redesigned geometry demonstrates reduced thrust force and improved hole quality, thereby enhancing a drill geometry already proven in experiments to be advantageous over a standard twist drill. The cutting edges on the periphery facilitate a hollow drill structure. The hollow drill structure promotes numerous added function. Internal air/coolant channel can be incorporated to assist with chip evacuation. A predrill geometry could be more easily accommodated.

An accurate representation of the UD-CFRP material was achieved by facilitating the contribution of damage between plies. An effective FE 3D drilling tool has been developed. The effective modelling techniques employed improve the effectiveness of the material response prediction from the drilling operation. UD-CFRP becomes strain rate sensitive when loading is focused in shear, or matrix directions. In these instances the response is dominated by the epoxy properties, which are strain rate dependent. Consideration was taken to investigating this material property, but can be studied further. Developing a sensitivity analysis for matrix material strain rate strengthening is required. Accurate cohesive interaction prediction is critical as it directly relates to the break-in and break-out delamination damage when drilling FRPs.

Appendix B

Internal surface creation

B.1 Without internal node creation

** INTERACTIONS

** Interaction: Int-2

*Contact, OP=New

*Contact Inclusions, ALL EXTERIOR

*Contact Property Assignment

, , IntProp-1

B.2 With internal node creation

*SURFACE, NAME=SURF1, TYPE=ELEMENT

,

WP1-1.WP1, INTERIOR

*end assembly

...

** INTERACTIONS

** Interaction: Int-2

```
*Contact, OP=New
*Contact Inclusions
SURF1,
*Contact Property Assignment
, , IntProp-1
```